

SOME ELECTROMAGNETIC FIELD PROBLEMS IN
D.C. MACHINES SUPPLIED FROM THYRISTORS

SUKHAMOY DAS, B.Sc, M.Tech, M.Sc.

A THESIS SUBMITTED FOR THE DEGREE OF
DOCTOR OF PHILOSOPHY

14 MAR 1978

621.3132 DAS
203626

UNIVERSITY OF ASTON IN BIRMINGHAM,
September, 1976

SUMMARY

This thesis presents a study of two electromagnetic problems in a d.c. machine.

Part (a)

Field analysis in the interpolar region of a d.c. machine operating on smooth voltage supply, using Schwarz-Christoffel transformation.

Part (b)

Experimental and theoretical study of eddy currents induced in the solid shell of a d.c. machine when carrying a pulsating component of a.c. flux which is the case when the d.c. machine is supplied from thyristors.

The work under part (a) is given below.

Chapter 1 outlines the principle of commutation process and reviews the problems of commutation analysis of a d.c. machine supplied from smooth voltage source, and discusses the work done by various investigators in this field. In Chapter 2 theoretical flux density distribution and toothpitch flux distribution under the compole, which are very important so far as the estimation of speed induced voltage in a commutating coil is concerned, are obtained in terms of machine dimension and field quantities, by solving the Laplacian field equation in the interpolar region with the help of Schwarz-Christoffel transformation. Theoretical investigation is made for three models, but none of them considers the armature slots. The effect of slots is taken into account with the help of a factor k_a obtained experimentally and discussed in Chapter 7. Non-linear multivariable optimisation technique is adopted

to find out the five w-plane constants from equations containing elliptic functions and elliptic integrals. This has been discussed in detail and its computer programme is given in the appendices.

Part (b) of the thesis is a different problem from part (a). After an introductory chapter which reviews the problems in the process of commutation arising from the eddy currents induced in the solid part of the magnetic circuits of a d.c. machine fed from controlled rectifiers, details of the test rig and instrumentations are written in Chapter 4, and discussion of the results of a series of experiments on a specially designed test machine are given in Chapters 5 and 7. Chapter 6 presents the theoretical analysis for the eddy currents induced in the solid shell due to the pulsating a.c. flux. Variable μ is taken into consideration with the help of Davies's formula $(\mu_r \mu_0)^{\frac{1}{2}} H = kI^m$. The discovery of power relationship between the fundamental flux reduction due to the induced eddy currents and the frequency of pulsation of a.c. flux within the range (25 Hz to 600 Hz) is written in Chapter 7. It is also discovered that the index 'm' is a function of the d.c. level of flux in the shell. Comparison of theoretical and experimental results are also given in Chapter 7.

Key words: 'Electromagnetic Field Problems - Thyristor Fed DC Machines'.

ACKNOWLEDGEMENTS

The author is deeply grateful to Professor E.J. Davies, Professor of Electrical Engineering in the University of Aston in Birmingham, who supervised the work on the eddy current problem in the shell, who was advisor for the work on the application of Schwarz-Christoffel transformation in the inter-polar region, and who has been a source of continuous advice and encouragement, and to Dr. I. Thomas who supervised the work on the application of Schwarz-Christoffel transformation in the inter-polar region, and who contributed through many helpful discussions.

His sincere thanks are also due to the following: Mr.N. Kerruish in the Mathematics Department, who checked the mathematical derivation.

Dr. A.L. Bowden, Mr. B. James, and Dr. P. Jackson, who provided many useful discussions.

All the technical staff of the Electrical Machines Centre, particularly Messrs. A.R. Stevenson, B. Harrison, L. Radford, J. Partlow, C. Partridge, and J. Lightfoot for their assistance with practical work.

All his friends, particular Messrs. B.Akhtar, M. Khair, N. Chavda, and v. Ghasi, who gave him the moral support. Parsons and Peebles who supplied the experimental machine. Miss Freeman who patiently typed the manuscript.

CONTENTS

<u>CHAPTER 1</u>	<u>Page No.</u>
SURVEY OF LITERATURE ON THE COMMUTATION PROBLEM IN D.C. MACHINES OPERATING ON A SMOOTH VOLTAGE SUPPLY.	5
1.1 Introduction.	5
1.2 Principle of Commutation.	6
1.3 Evaluation of Different Elements of the Voltage Current Matrix of the Commutating Coil.	13
1.3.1 Concept of Tooth Pitch Flux Distribution in the Interpolar Region for the Estimation of Speed Induced Voltages in the Commutating Coil and Scope for further work.	17
1.4 Coil Current during the Process of Commutation.	19
<u>CHAPTER 2</u>	
SCHWARZ-CHRISTOFFEL TRANSFORMATION AND THE FIELD PROBLEM IN THE INTERPOLAR REGION OF A D.C.MACHINE.	21
2.1 Introduction.	21
2.2 First Mathematical Model with Mainpole and Compole Both Extended to Infinity and Smooth Armature.	23
2.2.1 Discussion of the Theoretical Flux Density Distributions Obtained from the First Mathematical Model.	25
2.2.2 Tooth Pitch Flux Distribution.	27

	<u>Page No.</u>
2.3 Newton-Raphson Method	28
2.4 Second Model Without Mainpole.	29
2.4.1 Tooth Pitch Flux Distribution for the Second Model.	35
2.5 Third Mathematical Model.	36
2.5.1 Tooth Pitch Flux Distribution for the Third Model.	45
2.6 Conclusions.	45
2.7 Suggestions for Future Work.	47
 <u>CHAPTER 3</u>	
3.1 Survey of Literature on d.c. Machines Operating from Rectified a.c. Supply (with Special Reference to Commutation).	49
3.1.1 Introduction.	49
3.1.2 Some Investigations at the Earlier Stage.	49
3.1.3 Theoretical Investigations on d.c. Machines Supplied from Rectified a.c.	50
3.1.4 Development of SCR and Further Theoretical Investigations.	59
3.1.5 Lumped Circuit Impedance Representation for d.c. Machine.	73
3.1.6 Magnetic circuit of d.c. Machine and the a.c. Component of the Commutating Flux.	77
 <u>CHAPTER 4</u>	
DETAILS OF TEST MACHINE AND INSTRUMENTATION.	85
4. Introduction	85
4.1 Description of the Test Machine.	85

	<u>Page Number</u>
4.2 Details of the Test Rig.	87
4.3 Instrumentation of the Experimental Machine.	88
4.3.1 Shell Loop Search Coils.	88
4.3.2 Array of Search Coils in the Airgap at the Back of the Compole.	89
4.3.3 Tooth Pitch Search Coil.	90
4.3.4 Search Coils Around the Core of Interpole and on the Sideface of Compole.	90
4.3.5 Current Density Probes on the Surface of the Shell.	91
4.3.5.1 Calculation of Surface Current Density from the Probe Readings.	92
4.4.1 Measurement Techniques.	93
4.4.1.1 Flux Meter	93
4.4.1.2 Measurement of a.c. Flux.	93
4.5.1 Harmonic Analysis.	95
4.6 Preliminary Experiments.	96
4.6.1 Experiments to check the Magnetic Balancing in the Test Machine.	96
4.6.2 Brush Setting in the Magnetic Neutral Axis.	97
4.7 Measurement of Electrical Conductivity of the Steel used for Shell.	98
4.8 Superimposed a.c. - d.c. Supply.	98
4.8.1 Background to the Superposed a.c.-- d.c. Supply.	98

	<u>Page Number</u>
4.9 One Winding Parallel Circuits for Producing Superposed Steady and Periodic Fields in the Test Machine and the Simulation of Thyristor Fed d.c. Machine.	102
4.10 Details of the Variable Frequency a.c. Power Supply.	106
<u>CHAPTER 5</u>	
MEASURED EDDY CURRENT DISTRIBUTION ON THE SHELL SURFACE.	108
5.1 Introduction.	108
5.2 Eddy Current Distribution on the Surface of the Shell from the Experimental Evidence.	109
5.2.1 Experimental Results from the Current Density Probes.	109
5.2.2 Present Problem and Theoretical Investigation of Eddy Currents Induced in a Semi-infinite Slab by a δ -Function Coil Carrying a.c. Current.	113
5.2.3 A.c. Flux Tests in the Airgap at the back of the Compole using the Array of Search Coils.	116
5.2.4 D.c. Flux Test in the Airgap at the back of the Compole using the same Array of Search Coils.	117
5.2.5 Discussion of the Experimental Results obtained from the Search Coils and Current Density Probes.	118

5.2.6 Change in the Eddy Current Distribution in the Shell due to the Presence of Mainpoles in the Magnetic Circuit of d.c. Machines.	121
--	-----

CHAPTER 6

Theoretical Work on Eddy Currents Induced in the Solid Shell due to a.c. Excitation to the Compoles.	124
6.1 Introduction.	124
6.2 Mathematical Model.	125
6.3 Assumptions of the Theoretical Model.	126
6.4 Theoretical Deductions.	128
6.4.1 Eddy Current Distribution.	128
6.4.2 Magnetic Field Strength within the Shell.	134
6.4.3 Reaction mmf Due to the Eddy Currents Induced in the Shell.	135
6.4.4 Variable Permeability and Electro- magnetic Field Quantities.	138
6.4.4.1 Space Variation of μ_r in the Shell and the Surface Current Density.	141
6.4.4.2 Relationship between supply Frequency and mmf due to Eddy Currents with Constant Value of a.c. Excitation.	146

CHAPTER 7

FURTHER EXPERIMENTS AND VERIFICATION OF THE THEORETICAL RESULTS.	151
7.1 Introduction.	151
7.2 Measurements of Tooth-Pitch Flux Distribution.	151
7.2.1 Discussion and Conclusions.	152
7.3 Measurements of d.c. Flux Density in the Shell.	153
7.4 Experiments with Superposed a.c. - d.c. Supply and the Relationship Between the Supply Frequency and the a.c. Shell Flux with Different Levels of Steady and Pulsating Fluxes in the Shell.	154
7.4.1 Discussion and Conclusions.	161
7.4.2 Experiments Including Armature Reaction.	162
7.5 Discussion and Conclusions.	163

CHAPTER 8

SUGGESTIONS FOR FURTHER WORK.	166
REFERENCES.	170

APPENDIX 1

Evaluation of Elliptic Integrals of First and Second Kinds.	180
--	-----

APPENDIX 2

Evaluation of Elliptic Integrals of Third Kind.	182
--	-----

<u>APPENDIX 3</u>	<u>Page Number</u>
A.3.1 Comparison Between Elliptic Integrals and Simpson's Quadrature Formula.	185
A.3.2 Evaluation of Unknowns c, p, a , in the w plane using Multivariable Optimisation Technique.	187
<u>APPENDIX (4.COM.PRO.1)</u>	
Computer Programme to Evaluate g, A_1, d_1 , and d_2 , which Involve Elliptic Integrals and Functions when the Constants in the w Plane are Known.	195
<u>APPENDIX (4.COM.PRO.2)</u>	
Computer Programme to Find the Unknowns c, p, a , in the w Plane using Nonlinear Multivariable Optimisation Technique.	198
<u>APPENDIX (4.COM.PRO.3)</u>	
Computer Programme for Solving the Equation 6.80 of Chapter 6.	203
<u>APPENDIX (4.COM.PRO.4)</u>	
Computer Programme of Iterative Method of Calculating Variable μ on the Surface of the Shell for Various Odd Harmonic Current Sheets when the Physical Parameters of the Machine and a.c. Excitation to the Compole are given.	204
<u>APPENDIX (4.COM. PRO.5)</u>	
Computer programme for Harmonic Analysis.	206

APPENDIX 5

Page Number

A.5.1	The Constants A', a and b in terms of Known Quantities in the z plane.	208
A.5.2	The integration	209

$$A' \int \frac{\sqrt{(w-a)(w-b)}}{w(w+1)} dw$$

LIST OF PRINCIPAL SYMBOLS

a	constant, speed factor
$am(u, k) \equiv amu$	Amplitude u
$am^{-1}(y, k)$	inverse amplitude u
A'	constant
A	constant, vector potential
A_0	constant
$A_1 = A_L$	distance from compole edge to mainpole edge
$A_{\theta 2}$	vector potential in θ direction in region 2.
A_{z1}	fundamental component of linear current density in z direction.
b	constant, brush width.
b_0	width of the airgap at the back of the compole
B	constant, flux density.
B_{cp}	flux density in the interpole gap
c	constant
cnu	cosine amplitude u, Jacobian elliptic function.
C	constant
d	constant
d_0	thickness of the shell
d_1	half of the compole width.
d_2	width of the compole airgap.
dnu	delta amplitude u; Jacobian elliptic function.
D_A	armature diameter
D_C	commutator diameter.
e	instantaneous value of a.c. voltage.

e_a	instantaneous armature voltage drop
E	electric field strength
E_m	maximum value of a.c. voltage
E_r	speed induced voltage in the commutating coil due to the interpolar region flux wave.
E_{z3}	component of E in z direction in the shell.
$E(\phi, k) \equiv E(u)$	Legendre's incomplete elliptic integral of second kind.
f	frequency
F_1	fundamental mmf
F_e	eddy current reaction mmf
$F(\phi, k)$	incomplete elliptic integral of first kind.
g	mainpole airgap width
g'	compole airgap width
g_1	<i>Compole airgap</i>
H	magnetic field strength
H_x	component of H in x direction
H_{xsn}	time average of n th order <i>field</i> strength <i>in the x direction on the surface of the shell.</i>
H_{x3r}	resultant magnetic field strength in the shell in the x direction due to all the primary harmonic current sheets.
i	instantaneous value of a.c. current
I_a	current in armature conductor
j	$\sqrt{-1}$
J	current density
J_x	current density along x direction

J_{z3n}	eddy current density in the z direction in the shell due to the nth order primary harmonic current sheet.
J_{z3r}	resultant eddy current density flowing in the z direction in the shell due to all the primary harmonic current sheets.
k	constant, variable
K_1, K_2, K_3, K_4	constants
L	inductance
L	armature length
L_{cp}	axial length of compole
m	constant
n	harmonic order
N_t	number of turns in the armature coil.
P	$\sqrt{(\mu_0 \mu_r \omega a^2) / \rho}$
r, θ, z	cylindrical co-ordinate system
R	resistance
Re	real part of complex number
snu	sine amplitude u, Jacobian elliptic function
S_i	constant
S_t	Distance from mainpole tip to commutating pole tip.
t	time
t_{nu}	$\frac{snu}{cnu}$
T_i	constant
u	area unification factor

v_a	the peripheral speed of armature
V_a	armature counter voltage
V_{ab}	line to line voltage
V_m	instantaneous applied voltage
w	complex number $(u+jv)$
X_f	firing angle
X_s	stopping angle
X, Y, Z	Cartesian co-ordinate system
z	complex number $x + jy$
Z_s	number of armature conductors per slot
α	reciprocal of skin depth
β_x	distance moved through by commutator surface during commutation of x coil sides.
δ	skin depth of eddy current $\sqrt{\frac{2}{\sigma\mu_o\mu_r\omega}}$
Δ	operator
$\Delta\phi$	reduction in fundamental a.c. shell flux.
Δ_1	tooth pitch flux in first model (chapter 2)
Δ_2	tooth pitch flux in second model (chapter 2)
ϵ	infinitesimal small number.
ϕ	average value of fundamental a.c. shell flux.
ϕ_{av}	average value of a.c. flux
ψ	one of the axes in ξ plane or angle.
ξ	complex plane $(\phi+j\psi)$
λ	compole wavelength or $1/k_a$ value of the equivalent flux, per meter of embedded length established around the coil by a mmf of 1 amp-conductor in the slot.

τ	tooth pitch, time of commutation for a single coil
θ	angle
μ_0	permeability of free space
μ_r	relative permeability
μ	equals $\mu_0 \mu_r$
σ	electrical conductivity
ρ	electrical resistivity
ω	angular frequency equals $2\pi f$
Ω_{ci}	brush to bar contact resistances
$\pi(\phi, \alpha_3^2, k) \equiv \pi(u, \alpha^2)$	Legendre's incomplete elliptic integral of third kind.
$\}$	summation sign.

Subscripts

1, 2, 3	different regions (See Fig. 6.2)
av	average
e	eddy currents
i	to generalise any term
max	maximum
m	maximum
n	order of harmonic
r	resultant
r, θ , z	radial, angular, height
x, y, z	peripheral, radial, axial.

\sim below a symbol denotes complex vector.

\wedge above a symbol means vector quantity.

Abbreviation

a.c.	alternating current
d.c.	direct current
p.u.	per unit
cct.	circuit
e.m.f.	electromotive force, (volts)
m.m.f.	magnetomotive force (ampere turn)
p-p	peak to peak
r.m.s.	root mean square.
V.T.V.M.	Vacuum Tube Voltmeter.
C.R.O.	Cathode ray oscilloscope.

INTRODUCTION

The d.c. machine is one of the oldest machines and remains the most successful adjustable speed motor. Its use was limited because of the prevalence of a.c. power. Operation of d.c. motor from rectified a.c. was known since 1930 when the power tubes were developed, but the impact of thyristors, which is the most important development in the control of electric power in the past ten years, on d.c. motor drives has been particularly great because of good economic and technical combination between thyristor circuits and the d.c. motors. Drives using the combination are found from $\frac{1}{60}$ h.p. to 10,000 h.p. and in such diverse applications as trigger controlled electric drills, printing presses and steel rolling mills.

HISTORICAL BACKGROUND

In the early days of d.c. variable speed drives, the d.c. motor operated from a constant potential source was basically a variable field motor. In many plants the constant potential level could be adjusted to one or two fixed levels. Then the motor generator set (known as Ward-Leonard system) started to be used to produce the adjustable d.c. voltage source, and the system offered constant torque as well as constant h.p. characteristics. These were the first systems attempting to increase performance through increased speed range and accurate speed control. Various

regulating techniques were employed to control the generator field and the motor field. As the variable voltage systems grew in acceptance and as the performance criteria demanded from the machine and process increased, the need for a better motor was apparent. It became necessary to design a motor with improved mechanical performance (torque to inertia ratio), improved electrical performance. The machines were designed to take advantage of the technological changes in insulating materials, metals and better mechanical designs.

In the late 1950's and early 1960's the commercial uses of thyristors started. These silicon controlled rectifiers were first available at lower power levels and later at higher levels. The first usage, therefore, was as generator field regulators and later as d.c. motor armature power sources. The industry rapidly changed over. The thyristor control provides long life, high reliability, small flexible packages and some other advantages which have been discussed later in Chapter 3. About the future of d.c. machines supplied from thyristors Alexander Kusko¹ states "Motor drives using solid state power control elements are still in their early stages of commercial development. The next twenty-year period will see the electric automobile with thyristor speed control, the vast expansion of urban transportation using electric motor driven and thyristor controlled electric trains, heavy on and off highway vehicles of all types using gas turbines and electric drives, and new

generations of air conditioners, refrigerators, and other home appliances using solid-state controlled motors of all kinds ...".

Now the time has come when the users are pushing the development because they want better performance from a d.c. machine operating on rectified a.c. So the designers have to redesign the d.c. machine to improve the commutation performance of the machine supplied from thyristors. The problem associated with commutation for a d.c. machine operating on a smooth-voltage supply is already a difficult problem tackled by many scientists and engineers. The factors affecting the commutation performance of a d.c. machine supplied from smooth d.c. voltages have been listed below.

- (1) The voltage between adjacent commutator bars.
- (2) The reactance voltages induced in the coils undergoing commutation.
- (3) The compensating voltages induced in the commutating coils due to the compole flux which can be termed as speed induced voltages.
- (4) The design of the armature winding.
- (5) The mechanical and electrical characteristics of the brush commutator interface.
- (6) The geometric symmetry of the final motor assembly.

When the machine is operated from thyristor supply

these factors will play an equally important role and besides that the presence of a.c. components of armature/or field currents, which can be represented in the mathematical form $i = [I_{d.c.} + \sum_{n=1,2,\dots} I_n \sin(n\omega t)]$, will complicate an already difficult problem.

Generally the commutation problem with conventional d.c. motors operating on rectified power is quite severe and excessive brush sparking may cause rapid brush wear and commutator surface deterioration.

CHAPTER 1

SURVEY OF LITERATURE ON THE COMMUTATION PROBLEM IN D.C.
MACHINES OPERATING ON A SMOOTH VOLTAGE SUPPLY

1.1 INTRODUCTION

The d.c. machine is one of the earliest electrical machines brought into general use and it remains the most successful adjustable speed motor available.

The presence of a commutator makes it a mechanically complex piece of apparatus, and the challenging problems associated with commutation continue to be an embarrassment. A d.c. machine should operate under a specified load without excessive wear of the commutator and brushes. Commutation is good or bad depending on the degree of sparking, and as a general rule commutation in a successful d.c. machine should be black. The prediction of commutative performance is one of the most difficult tasks of a machine designer. For example, Thieler² states 'experience shows that many machines may show an excellent commutation for the first few hours or few days. Thereafter commutation may gradually get worse, the commutator showing signs of marking, with the result that real commutating trouble develops. Other machines on the contrary, may look a little doubtful on the test bed as regards commutation, but may run excellently in practice without appreciable wear of commutator or brushes'.

Engineers responsible for building and operating d.c. motors and generators have had to become more proficient in dealing with the problems of commutation in order to obtain more output from machines of a given size and cost

and to understand the duty imposed on carbon brushes. Langsdorf³ has stated, 'a rigorous treatment of the general case covering any type of winding is practically impossible because there is so many independent factors entering into the problem that the mathematical difficulties are insurmountable'.

Attempts were made as early as the beginning of 1900 by Lamme⁴, Dreyfuss⁵ and other to unfold the mystery of commutation process in the d.c. machines, and continued with some refinements and better assumptions by many scientists and engineers such as Thielers², Linville and Rosenberry, Jr.⁶, Alger and Bewley⁷, Tustin^{8,9}, Ward^{8,10}, Tarkanyi¹¹, Ewing and Patel¹², and others. But it still appears to be one of the unresolved areas of electrical machinery.

1.2 PRINCIPLE OF COMMUTATION

The time variation of emf induced in a full pitched coil of a d.c. machine at its running condition, is an exact replica of the *spatial* distribution of the flux density wave. The emf in the coil goes through zero at the instant when the active sides of the coil pass through the magnetic neutral position. To obtain direct current in the external circuit, it is therefore necessary to reverse periodically the connections of each armature coil with armature circuit. The commutator and brushes combine to form the reversing switch.

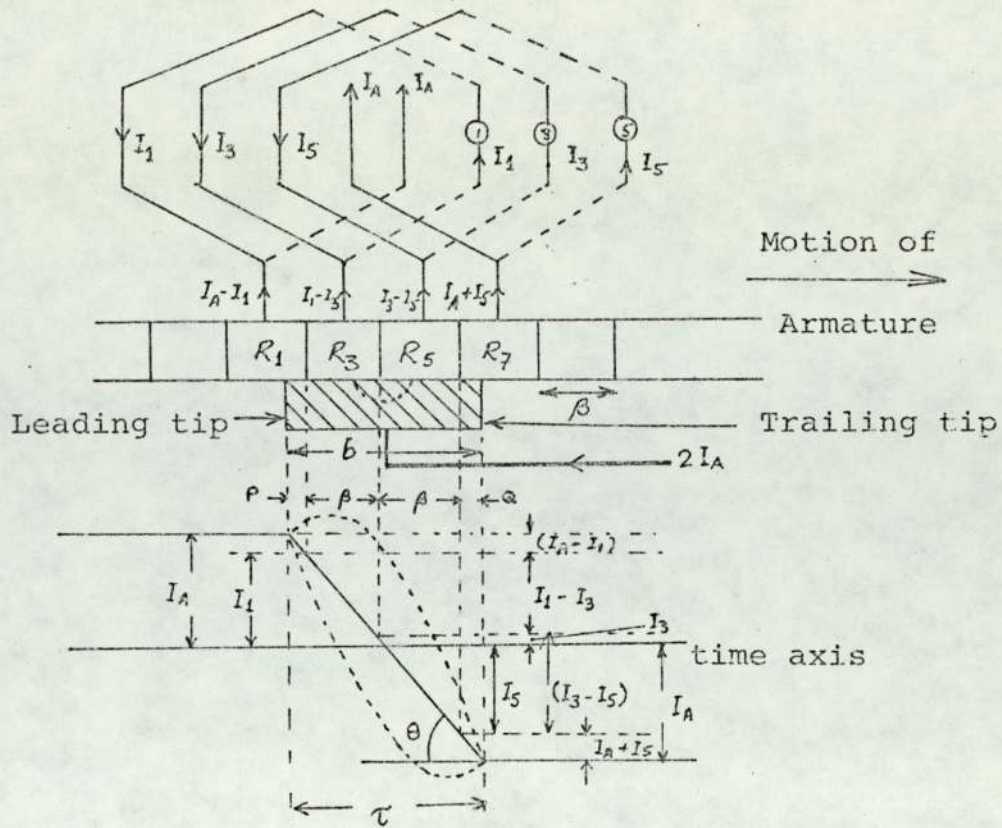


Fig. 1.1 Coil Currents, Linear Commutation.

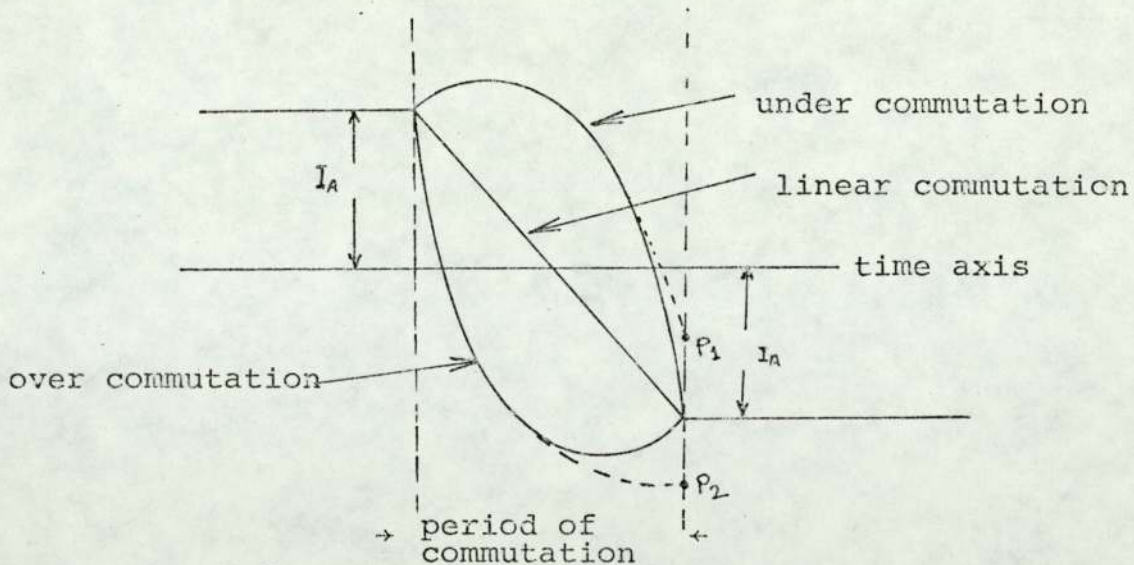


Fig. 1.2 Under-Commutation and Over-Commutation.

Fig.1.1 shows that the brush width is greater than the width β of a commutator segment, so that several coils are short circuited simultaneously. The time of commutation for a single coil is therefore -

$$\tau = \frac{b-b_m}{v_c}$$

where v_c = peripheral speed of the commutator

b_m = thickness of the mica separator between segments.

In the position indicated in the diagram, the currents I_1 , I_3 and I_5 in the short circuited coils are at different stages of the transition from $+I_A$ to $-I_A$, and on applying Kirchoff's first law to the junction points between coils, the current in the commutator risers (and through the segments R_1 , R_3 , R_5 and R_7) are respectively $I_A - I_1$, $I_1 - I_3$, $I_3 - I_5$, $I_5 - (-I_A)$. The lower part of Fig.1.1 shows that the current in each coil changes linearly from I_A to $-I_A$ in the time τ . The current densities at each brush contact are

$$\frac{I_A - I_1}{P} = \frac{I_1 - I_3}{\beta} = \frac{I_3 - I_5}{\beta} = \frac{I_5 - (-I_A)}{Q} = \tan \theta$$

which shows that the current density at each brush contact is uniform and hence the ohmic loss at the brush contact is least when commutation is linear. If the commutation is accelerated or retarded, as indicated by the dotted commutation curve in Fig.1.1, and also in Fig.1.2, it is seen that in the case of over commutation, the current density will be much increased at the leading tip of the brush, and much decreased or even reversed in sign, at the trailing tip. The reverse is the case when under commutation takes place. The fact that over commutation and under commutation may give rise

to abnormal current density at the brush contact indicates the possibility of excessive localized heating, which may bring about disintegration of the brush material as well as chemical changes in the copper of the commutator. Moreover, when the reversal current is either retarded or accelerated the current at the end of the period will tend to have a value, indicated by points such as P_1 or P_2 in Fig. 1.2, which differs from that of the circuit to which the commutated coil is to be connected and in that case the final equalisation may result in a destructive spark or arc at the trailing tip of the brush.

Langsdorf's³ approximate mathematical relations in commutating coil which give an idea about what is happening during the process of commutation, have the following assumptions:

- (1) The contact resistances between the brush and each of the segments which it touches remain constant during the process of commutation. These are Ω_{C1} , Ω_{C3} , Ω_{C5} , Ω_{C7} .
- (2) The resistances of the risers are negligible
- (3) The commutation is so nearly linear in all the coils simultaneously short-circuited that the time rate of change of current ($\frac{di}{dt}$) is the same in each of them.

Then, applying the Kirchoff's second law to the short circuited coil (3) under consideration which has been

shown in Fig.1.1, the instantaneous voltage-current equation becomes

$$E_r + L_c \frac{dI_3}{dt} + \sum M \frac{dI_3}{dt} + I_3 R_c + (I_3 - I_5) \Omega_{c5} - (I_1 - I_3) \Omega_{c3} = 0 \quad 1.1$$

where

I_3 = the instantaneous current in the short circuit coil (3)

R_c = resistance of coil (3)

L_c = self inductance of the coil

$\sum M$ = total mutual inductance between the coil (3) under consideration and neighbouring coils simultaneously short-circuited.

E_r = the speed induced voltages in the coil (3) by the rotation through the interpole region flux.

From Fig.1.1 the currents I_1 and I_5 are approximately equal in magnitude and opposite in sign, hence the term $I_5 \Omega_{c5}$ and $I_1 \Omega_{c3}$ in the equation 1.1 cancel out each other, assuming Ω_{c5} is approximately equal to Ω_{c3} . R_c has been neglected in comparison with the contact resistances. Thus the equation 1.1 can be written after some manipulation as:

$$E_r + i (\Omega_{c3} + \Omega_{c5}) = -(L + \sum M) \frac{di}{dt} \quad 1.2$$

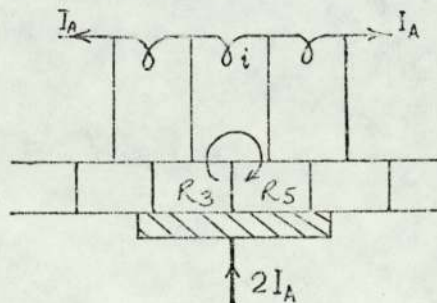


Fig. 1.3

The short circuit current i which will flow in the short-circuited coil through the brush as shown in Fig. 1.3 is governed by the equation 1.2. The direction of flow of i depends on the value of E_r .

The physical interpretation of the equation 1.2 is as follows:

$(L+M)$ is the total inductance of the coil undergoing commutation and the effect of total inductive emf (called the reactance emf) is always to oppose the change of current in the short-circuited coil from I_A to its final value $-I_A$. This total reactive emf must be balanced by the speed induced emf, E_r , and the ohmic drop at the brush contact, the former is known as voltage commutation, and the latter is resistance commutation.

Average value of E_r either may be greater or less than the reactance voltage. If E_r is large compared to reactance voltage, the current density will be large at the leading tip of the brush and the distribution of brush contact drop will be as shown by the curve A in Fig. 1.4, indicating the over commutation. On the other hand if E_r is small, the current density will be large at the trailing tip and the distribution of the brush contact drop will be the curve 'C' in the same figure, indicating the under commutation. Curve B in Fig. 1.4 shows a nearly uniform drop all along the brush contact which is the indication of nearly linear commutation. Gross estimation of density of flux under

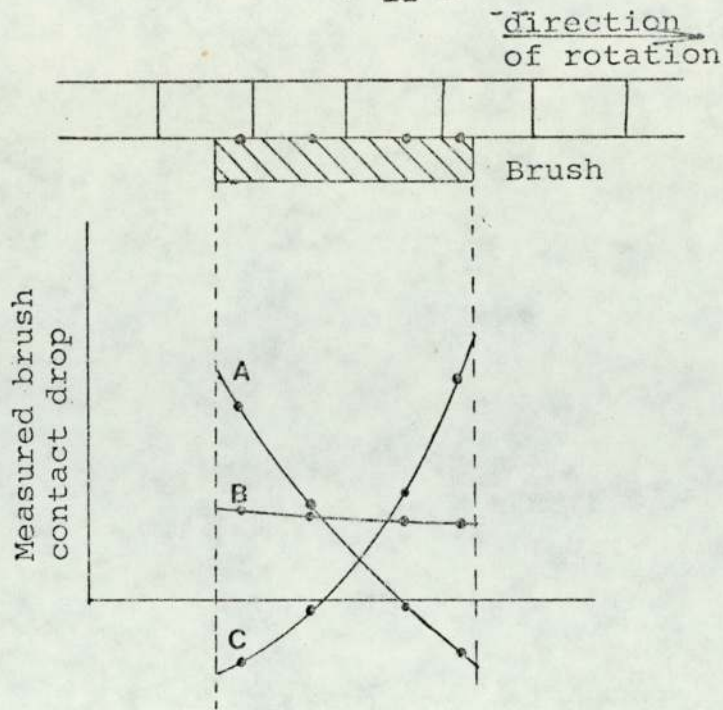


Fig. 1.4 Measurement of Brush Contact Drop

interpole can be made by simply equating the speed induced voltage to reactance voltage which does not include the contact voltage drop. Thus,

$$E_r = 2 B_{cp} L_{cp} V_a = 4 Z_s I_a \frac{\lambda L}{T_{cx}} \quad 1.3$$

$$B_{cp} = \frac{\lambda L}{L_{cp}} \cdot \frac{2 Z_s I_a}{\beta_{xA}} \quad 1.4$$

where

$\beta_{xA} = \beta_x \cdot \frac{D_A}{D_C}$ and is equal to the distance moved by the armature circumference during the time of commutation for the complete x coil sides in one layer of the winding. The simplifying assumptions which have been made to derive the equation 1.2 clearly indicate the deviations from the actual conditions. For example

- (1) $\frac{di}{dt}$ is not the same for all coils simultaneously short-circuited.
- (2) The speed induced voltage E_r and the brush contact resistance Ω_{C1}, Ω_{C3} etc., are complex functions of time and load current.

1.3 EVALUATION OF DIFFERENT ELEMENTS OF THE VOLTAGE

CURRENT MATRIX OF THE COMMUTATING COIL

The generalised voltage current matrix equation which takes into consideration the above mentioned facts, for the coils undergoing commutation, can be established with the help of well known commutation diagram that outlines the switching operation in relation to the actual geometry of the bars, poles, brushes and the position of the short-circuited coil. Such an equation for the commutation analysis takes the following form.

$$\begin{array}{c}
 \left| \begin{array}{c} E_1 \\ E_2 \\ E_3 \\ \vdots \\ E_r \end{array} \right| = \left| \begin{array}{cccc} L_{11} & L_{12} & \dots & L_{1n} \\ L_{21} & L_{22} & \dots & L_{2n} \\ L_{31} & L_{32} & \dots & L_{3n} \\ \vdots & \vdots & \vdots & \vdots \\ L_{r1} & L_{r2} & & L_{rn} \end{array} \right| \begin{array}{c} [-K(\sigma_1)^{1/n}] \\ [-K(\sigma_3)^{1/n}] \\ [-K(\sigma_5)^{1/n}] \\ \vdots \\ [K(\sigma_{2r-1})^{1/n}] \end{array} \begin{array}{c} [K(\sigma_2)^{1/n}] \\ [K(\sigma_4)^{1/n}] \\ [K(\sigma_6)^{1/n}] \\ \vdots \\ [K(\sigma_{2r})^{1/n}] \end{array} \left| \begin{array}{c} \frac{d}{dt}(I_1) \\ \frac{d}{dt}(I_2) \\ \frac{d}{dt}(I_3) \\ \vdots \\ \frac{d}{dt}(I_n) \\ 1 \\ 1 \end{array} \right|
 \end{array}$$

L_{11} , L_{22} -----, L_{12} , L_{13} ----- etc., are the self and mutual inductance of the commutating coils, associated with the fluxes in the regions (1), (3), (4) and (2) of Fig. 2.1 and $L_{11} \frac{di_1}{dt}$, $L_{12} \frac{di_2}{dt}$ ----- etc., are called the reactance voltages. $K(\sigma_1)^{\frac{1}{n}}$, $K(\sigma_2)^{\frac{1}{n}}$ ----- etc. are the nonlinear brush to bar contact voltage drops, K and n are constants obtained from the brush characteristics, E_1 , E_2 ----- etc., are the instantaneous values of speed induced voltages due to the interpolar region flux wave. Long investigations have already been made to calculate the reactance voltages of the commutating coils in terms of machine dimensions and winding configurations. The methods of calculating the reactance voltages due to the slot leakage flux, tooth top leakage flux, end winding fluxes by Dreyfuss⁵, Thielers², Ward^{8,10}, Tustin^{8,9}, Clayton and Hancock¹³ are sufficiently accurate to satisfy a d.c. machine designer for analysing the commutation process.

Carbon brush contact phenomena in electrical machinery is an extremely complicated subject, which has been studied theoretically and experimentally by Soper¹⁴ and others. Without going into the details of the complexity of brush contact phenomena, commutation analysis can be satisfactorily attacked by using the formula $V_b = K(\sigma)^{\frac{1}{n}}$ suggested by Ewing and Patel¹² and others to represent the nonlinear brush to bar contact voltage drop. The contact phenomena is much more complex than is suggested by $K(\sigma)^{\frac{1}{n}}$, although there is

nothing much one can do about it if the total phenomena is to be covered by the equation of the form (1.5).

For the estimation of speed induced voltages E_1, E_2 --- E_r in the commutating coils due to the interpolar region flux a few investigations have already been made. Linville and Rosenberry's⁶ analysis (1952) in this field can be summarised as follows:

Two fluxes have been considered to contribute towards the speed induced voltages E_r .

- (1) That due to compole and armature acting alone which is assumed to vary cosinusoidally with distance from compole centre line.
- (2) That due to mainfield acting alone, which is assumed to vary according to a sine hyperbolic law in the interpolar region.

The voltages induced in the coil undergoing commutation due to the fluxes (1) and (2) are e_{oq} and e_{od} respectively, which appear to be derived on 'Blv' basis. Thus for two coil sides

$$e_{oq} = \left[2A \cos \frac{\pi f \lambda}{2X} \cos \frac{\pi x}{2X} \right] \quad 1.6$$

and for each coil side

$$e_{od} = A_1 \sinh ax \quad 1.7$$

$\cos \frac{\pi f \lambda}{2X}$ has been introduced as a pitch factor for e_{oq} .

According to them, the airgap flux paths configuration under the compole has been shown in Fig.1.5.

f_λ is one half of difference between full coil pitch and actual coil pitch, A , X and x are shown in Fig. 1.6. M_{Oq} in Fig. 1.6 is the mutual inductance between coil group (O) and the line circuits of the quadrature axis. Assumed sine-hyperbolic distribution of the mainpole fringe flux has been shown in Fig. 1.7. Cosine and sine hyperbolic distributions are conveniently chosen mathematical form to represent the actual flux distribution in the interpolar region, and they rely on experimental measurements to evaluate the amplitudes A_1 and a .

In 1957 Alger and Bewley⁷ published a paper which is an extension of the work of Linville and Rosenberry adapted for use by the design engineer. Again cosinusoidal and hyperbolic relationships are used to represent the interpolar flux distribution due to compole and mainpole excitation, respectively. However the degree of accuracy of these expressions is not given, the authors merely stating that 'unfortunately no neat but nearly exact fit to the field of the commutating pole has been found. The functions e^{-x} and e^{-x^2} have been tried with the result that the analytical results fall between these two functional variations. The most accurate procedure would be to plot analytically determined field variation for the desired values of $\frac{S_t}{g_1}$ and then obtain the voltages graphically. However an easier

method was necessary to expedite the work and so a cosine distribution was chosen'.

Computer aided relaxation technique by Erdelyi and Fuchs¹⁵ for solving the field problem in the interpolar region of d.c. machine, seems to be extremely complicated for practical use.

One of the recent papers on commutation analysis is by Ewing and Patel¹² in 1972. They also obtained the speed-induced voltage by the 'Blv' method where l is the active length of the armature and v is the armature peripheral velocity. The flux density B is obtained by superimposing individual flux density distributions due to each of the current excited windings, assuming the rotor is smooth. The two dimensional field problem in the interpolar region is solved by them with the help of electrical analogs as used by Tozoni¹⁶, who transforms the irregular interpolar space into a hypothetical rectangular section having a known mathematical solution.

1.3.1 Concept of Tooth Pitch Flux Distribution in the Interpolar Region for the Estimation of Speed-Induced Voltages in the Commutating Coil and Scope for Further Work.

If an attempt is to be made to take slots into account when determining the speed-induced voltages the flux linkage concept suggested by Tustin⁸ and others, appears to be the more convenient. The region 5 of Fig.2.1 can be divided into

n number of equal submeshes of slot pitch length (P_s). If ϕ_i is the flux through one of these submeshes, a graph of ϕ_i as a function of angular displacement θ is referred to as the slot pitch flux distribution. The same slot pitch flux distribution is repeated for all the n number of meshes included within the coil span undergoing commutation.

The linkage at any instant is given by the sum of n ordinates of this slot pitch flux waveform. Hence, the compensating voltage due to the compole flux, pole fringe and armature reaction is

$$e = \sum_{i=1}^n \frac{d}{dt} \phi_i = \sum_{i=1}^n \frac{d\phi_i}{d\theta} \frac{d\theta}{dt} \quad 1.8$$

Neglecting possible variation of the core yoke mmf Tustin and Ward assumed parabolic arcs for the slot pitch flux distribution in order to evaluate the speed induced voltages.

From the literature survey it is evident that a need exists for a thorough investigation, both in theory and experiments, directed to achieve a relatively simple but accurate method for obtaining flux density or slot pitch flux distribution over the armature surface due to compole excitation, mainpole fringe flux and armature reaction in order to predetermine the compensating voltages for commutation analysis.

Schwarz Christoffel transformation has been used as a new approach for the interpolar region field analysis

in d.c. machines, and is discussed in detail in Chapter 2.

1.4 COIL CURRENT DURING THE PROCESS OF COMMUTATION

After obtaining the speed induced voltages E_r in the coil undergoing commutation from the field analysis given in Chapter 2, and knowing

- (1) All other coil currents except i_1 and i_2 .
- (2) The instantaneous values of contact voltage drops which can be described as an inverse function of geometric area of contact between brush and bar,
- (3) The values of self and mutual inductance coefficients L_{11} , L_{22} --- etc., from the design, the matrix equation (1.5) can be reduced to two equations

$$L_{11} \frac{dI_1}{dt} + L_{12} \frac{dI_2}{dt} = E_1 - \alpha_1 - \beta_1 \quad 1.9$$

and

$$L_{12} \frac{dI_1}{dt} + L_{22} \frac{dI_2}{dt} = E_2 - \alpha_2 - \beta_2 \quad 1.10$$

where α_i is instantaneous voltage drop due to mutual inductance, and β_i is net instantaneous contact voltage drop as an exponential function of current density in the brush. Starting with known initial values of coil currents, those equations 1.10 and 1.9 can be solved using the fourth order Runge-Kutta method, thus the coil currents can be obtained at every instant of time (as small as 10^{-6} seconds), during the process of commutation satisfying all the time the

condition of equality of both sides of the equations 1.8 and 1.9. The instantaneous values of E_1 , E_2 , α_1 , α_2 , β_1 , β_2 , are very important controlling factors so far as the commutation analysis is concerned. Knowing the currents in the commutating coil, the contact voltage drop between the brush and the bar can be calculated and the value of voltage drop at the instant where the last coil in the group leaves the brush is used as an index for the quantitative evaluation of commutation. The attainment of the best possible commutating conditions would in any case require the physical adjustments of the completed machine, for example, control of speed induced voltages E_r by appropriate setting of a shunt across the terminals of the interpole winding, or by altering the contact resistances by adjustment of the spring pressure, etc..

CHAPTER 2

SCHWARZ CHRISTOFFEL TRANSFORMATION AND THE FIELD PROBLEM
IN THE INTERPOLAR REGION OF A D.C. MACHINE

2.1 INTRODUCTION

For the analytical solution of Laplacian fields ($\nabla^2\phi = 0$) conformal transformation is the most powerful analytical method amongst all other methods, because it is capable of handling boundaries of much more complicated shape than the direct solution method, and the method of images. In general, the solution by conformal transformation takes very simple forms, and yields readily, expressions for flux density and permeance in magnetic fields. So the electromagnetic field problem in the interpolar region has been solved by Schwarz-Christoffel transformation.

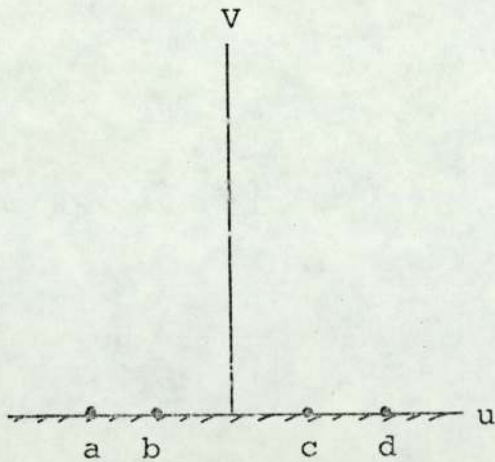


Fig. 2a w Plane

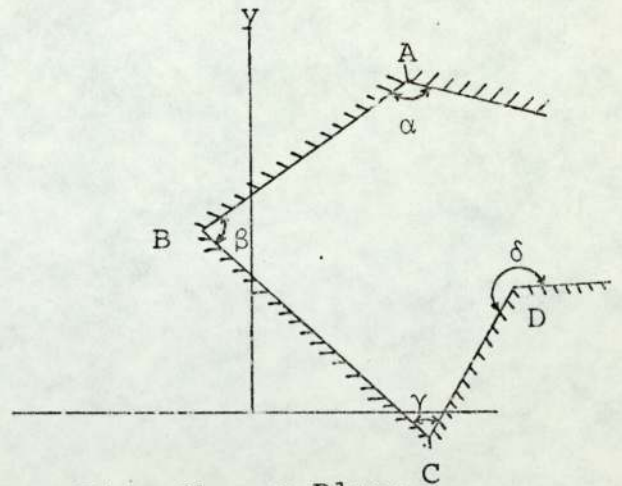


Fig. 2b z Plane

Consider the two planes shown in Fig. 2a and 2b; the regions to be transformed lie on the unshaded sides of the boundary lines and corresponding points are similarly

lettered. Then the conformal transformation from the real axis of w-plane to the polygonal boundary in the z-plane is obtained by integrating the equation (2.0)

$$\frac{dz}{dw} = A (w-a)^{\frac{\alpha}{\pi}-1} (w-b)^{\frac{\beta}{\pi}-1} (w-c)^{\frac{\gamma}{\pi}-1} \dots \dots \dots \quad (2.0)$$

which is known as Schwarz-Christoffel differential equation and a, b, c, d ----- are points on the real axis of the w-plane corresponding to the vertices of the polygon in the z-plane.

The complexity of the airgap boundaries in the inter-pole region shown in Fig.2.2, has been overcome by assuming that

- (a) some of the surfaces of the polygon extend to infinity.
- (b) flux lines as boundary.
- (c) and the armature being smooth (see Fig. 2.3, 2.8 and 2.11).

Then the Schwarz-Christoffel transformation (2.0) has been applied to those simplified polygonal boundaries to solve the interpolar region field problem without sacrificing much accuracy. Validity of those assumptions has been *verified*

- (a) When good agreement is found between theoretical and experimental flux distribution curves under the compole shown in Fig.2.20
- (b) When the theoretical flux density distributions obtained in this model exactly coincide with those

by Gibbs'¹⁷ and Binns'¹⁸ models in some special cases which have been discussed in detail in this chapter.

The field solutions obtained for these models can be computed with a small amount of memory storage, and it is more economic on computer time.

If the boundaries are tapered, curved and extremely complicated, finite element method can be used, which has some additional advantages over other methods of analysis. Erdelyi¹⁵ used the finite element method with computer aided relaxation technique to solve the field problem in the interpolar region, which seems to be extremely complicated for a design engineer.

2.2 FIRST MATHEMATICAL MODEL WITH MAINPOLE AND COMPOLE BOTH EXTENDED TO INFINITY AND SMOOTH ARMATURE

The following assumptions have been made to simplify the actual configuration shown in Fig.2.2.

- (a) The armature is smooth.
- (b) Compole and mainpole extended to infinity as shown in Fig. 2.3.

The compole is at potential v and the armature and mainpoles are at zero potential.

The given polygonal region in the z plane as shown in Fig. 2.3 has been mapped on auxiliary w plane with the help of conformal transformation shown in Fig. 2.4. The Schwarz-Christoffel transformation gives the relationship between z

plane and 'w' plane

$$\frac{dz}{dw} = A' \frac{\sqrt{(w-a)(w+b)}}{w(w+1)} \quad 2.1$$

Integrating 2.1 and using gaps at infinity, methods for finding the unknown constant A', and other constants, the following equation 2.2 has been obtained.

$$z = -\frac{g'}{\pi} \left(\frac{K_1}{K_4} \right) \left[\frac{A}{\sqrt{K_2}} \tan^{-1} \frac{\psi}{\sqrt{K_2}} + \frac{B}{\sqrt{K_3}} \tan^{-1} \frac{\psi}{\sqrt{K_3}} - \frac{C}{2} \log_e \left[\frac{1+\psi}{1-\psi} \right] \right] + jg \quad 2.2$$

where

$$A = \frac{K_2}{(K_3 - K_2)(K_2 + 1)}, \quad B = \frac{K_3}{(K_2 - K_3)(K_3 + 1)}, \quad C = \frac{1}{(K_2 + 1)(K_3 + 1)}$$

$$K_1 = -2(a+b)^2, \quad K_2 = \frac{b}{a}, \quad K_3 = \frac{(b-1)}{(a+1)}, \quad K_4 = a(a+1)$$

$$-\frac{A_L}{g'} = \sqrt{ab}, \quad \frac{g}{g'} = \sqrt{(1+a)(1-b)}, \quad \text{and } \psi^2 = \left\{ \frac{w+b}{w-a} \right\}$$

Details of mathematical steps in between equations 2.1 and 2.2 have been given in Appendix 5 .

The transformation from the 'w' plane to the ξ plane shown in Fig. 2.5 where the field is regular is given by

$$\xi = \frac{V}{\pi} \log w \quad 2.3$$

The magnitude of flux density at any point along the armature

surface is given by

$$B = \left| \frac{d\xi}{dz} \right| \mu_0 = \left| \frac{d\xi}{dw} \times \frac{dw}{dz} \right| \mu_0 \quad 2.4$$

$$B = \left| \frac{V}{g'} \mu_0 \frac{(1+w)}{\sqrt{(w-a)(w+b)}} \right| \quad 2.5$$

Now as $w \rightarrow \infty$, from the equation 2.5 the flux density tends to its uniform value in the middle of the compole core, given by $\frac{V}{g'} \mu_0$ which is also the maximum value. Taking the real part of the equation 2.2 one can find the values Z which correspond to the points within the range (-1.0) to $-\infty$ in the w plane. Calling the maximum value of the flux density B_{\max} unity the flux density curves on the armature surface for various values of $\left(\frac{A_L}{g'}\right)$ have been drawn and shown in Figs. 2.16 and 2.19

2.2.1 Discussion of the Theoretical Flux Density Distributions Obtained from the First Mathematical Model

The values of g' chosen are 2 mm, 4 mm and 6 mm while keeping the other dimensions A_L and g fixed at the same values, the flux density distribution curves over the smooth armature surface have been drawn and shown in Fig. 2.19, Fig. 2.16 and 2.18, using the equations 2.2 and 2.5, obtained from the theoretical analysis in section 2.1. These flux distribution curves have been compared with those obtained from Gibbs¹⁷ analysis where he solved the field problem to quantify the fringe flux at the main pole edges shown in

Fig. 2.6. The flux density distributions under the compole are the same for both cases when g' is small. The deviation between these two curves starts nearly at the edge of the compole and becomes more and more as one approaches towards the mainpole centre line. This is because the portion ABC shown in Fig. 2.3 was not included in the Gibbs' model given in Fig. 2.6. Gibbs obtained the following results

$$z = \frac{g}{2\pi} \left[2(w+1)^{\frac{1}{2}} - 2 \log \{(w+1)^{\frac{1}{2}} + 1\} + \log w \right] \quad 2.6$$

$$B = B_{\max} (w + 1)^{-\frac{1}{2}} \quad 2.7$$

where g is the dimension shown in Fig.2.6.

When the mainpole gap is made very large in the present analysis in 2.1, the flux density distribution on the smooth armature becomes the same as that obtained by Gibbs when the other dimensions are kept unaltered (see Fig.2.17 and 2.16) It is also interesting to note that the flux density distribution under the compole is not at all influenced when the mainpole air gap has been varied from $g = 10$ to 100 , shown in Fig. 2.17. Binns¹⁸ obtained the following mathematical expressions when he solved the field problem shown in Fig. 2.7.

$$z = \frac{2g}{\pi} \left\{ p \tan^{-1} \frac{pu}{g} + \frac{1}{2} \log \left(\frac{1+u}{1-u} \right) \right\} \quad 2.8$$

$$u^2 = \left[\frac{w - (g/p)^2}{w + 1} \right] \quad 2.9$$

and

$$B = B_{\max} \frac{w \sqrt{w-a}}{\sqrt{1-w}} \quad 2.10$$

For the same values of A_L and g , Binns' flux density distributions have been compared with those obtained from 2.2 and 2.5 with a very low value of g' and good agreement has been found. Thus the flux density curves obtained from the analysis in section 2.1, at a very low value of g' and high value of g' agree well with those obtained by Binns and Gibbs respectively, and this tends to confirm the theoretical analysis for the model considered in section 2.2.

2.2.2 Tooth Pitch Flux Distribution

The speed induced voltages in the commutating coils may be calculated either by BLV concept (speed voltage) or by flux linkage concept ($\frac{d\phi}{dt}$) which has been discussed in Chapter 1. To deal with BLV concept one has to be cautious about the flux density B at a point which should be taken for calculation. Since the armature is slotted the value of B will be the average of the flux densities with tooth in that position and then with the slot at the same position. The flux linkage concept suggested by Tustin⁸ and others appears to be easier. Space distribution of slot pitch

flux assuming smooth armature and given the compole mmf can be obtained in the following manner.

In the w plane shown in Fig. 2.4 the flux lines and equipotential lines are governed by the equation

$$\phi + j\psi = \frac{V}{\pi} \log_e w \quad 2.11$$

The flux between any two points w_1 and w_2 on the equipotential line where $\psi = 0$ is given by

$$\Delta_1 = (\phi_1 - \phi_2) = \frac{V}{\pi} \log_e \left(\frac{w_2}{w_1} \right) \quad 2.12$$

z_1 and z_2 corresponding to w_1 and w_2 in the w plane can be obtained from the equation 2.2 using the method of linear interpolation near the actual values of z_i which correspond to w_i in the w -plane. Taking the central line of the compole as the line of symmetry and using the equations 2.2 and 2.12, the theoretical plot of the tooth pitch flux distribution along the smooth surface of the armature with the compoles excited only, has been obtained and shown in Fig. 2.20. In this figure, the maximum value of the tooth pitch flux which occurs along the central line of the compole has been taken as the unity and $\frac{\tau}{g_r}$ is 4.0. This theoretical tooth pitch flux distribution has been compared with the experimentally measured curve and discussed in detail in Chapter 7. The centre line of the compole is taken as line of symmetry for the flux distribution.

2.3 NEWTON-RAPHSON METHOD

The Newton-Raphson method is one of the most common

numerical techniques for finding a root of an equation, and for introducing methods of checking out a program to remove its error, and to ensure accuracy.

Given a function of X , $F(X) = 0$, this method says that, subject to certain conditions, if X_i is an approximation to a root, a better approximation is given by

$$X_{i+1} = X_i - \frac{F(X_i)}{F'(X_i)} \quad 2.13$$

where $F'(X_i)$ is the derivative of $F(X)$ at the point X_i . This is called an iteration formula. Continuing in the same way, now substituting X_{i+1} into the same formula $F(X) = 0$, and so on, one gets a succession of approximation until $|X_{\text{new}} - X_{\text{old}}|$ is less than some specified value say 10^{-8} .

2.4 SECOND MODEL WITHOUT MAINPOLE

The mathematical problem adopted to solve the field problem in Section 2.2, introduces some error because the analysis shows that the flux density does not reach 100% at the centre of the compole, particularly when the compole is thin, the flux density reaches only 97% of its maximum value just at the centre line of the compole. In order to obtain the 100% of flux density at the centre line of the interpole another model has been considered in this section where the centre line of compole is the flux line.

From the results discussed in sub-section 2.2.1 it is

seen that the mainpole has very little effect on the interpolar region flux distribution, so the main pole has been omitted from the present configuration for the moment. The compole is at a potential V , the armature is smooth and at a potential 0 , the centre line AB of the compole is flux line as shown in Fig. 2.8. This is a problem with three corners. The conformal transformation from z -plane to the w -plane and then to the ξ plane have been shown in Fig.2.9 and 2.10. The Schwarz-Christoffel transformation gives the following relationships :

$$\frac{dz}{dw} = \frac{A (w - c)^{\frac{1}{2}}}{(w-b)^{\frac{1}{2}} (w-a)^{\frac{1}{2}}} \quad 2.15$$

$$\int dz = A \int \frac{(w-c)^{\frac{1}{2}} dw}{(w-b)^{\frac{1}{2}} (w-a)^{\frac{1}{2}}} + C \quad 2.16$$

The constant of integration C has been made zero by fixing the origin of X - Y co-ordinate system at the point $w=c$ in the z plane. A is constant, which will be evaluated in terms of known quantities, d_1 the distance from the edge of the compole to its centre line, and d_2 the compole airgap width. $w = c = 0$ and $w = a = 1$.

$$\int dz = d_1 = A \int_c^b \sqrt{\frac{w-c}{(w-a)(w-b)}} dw \quad 2.17$$

$$\int dz = jd_2 = A \int_b^a \sqrt{\frac{w-c}{(w-a)(w-b)}} dw \quad 2.18$$

From equations 2.17 and 2.18 the unknown constants A and b can be determined. The integrations of equations 2.17 and 2.18 can be evaluated either by Simpsons's or by Gaussian methods of numerical integration which have been used by Lawrenson^{18,19}, Binns^{18,20}, Gupta¹⁹ and Howe²¹. But in carrying out the numerical integration, the problem arises when the limits of integration are either 1 or b, because the function

$$f(w) = \left[\frac{(w-c)}{(w-1)(w-b)} \right]^{\frac{1}{2}}$$

has poles at $w = 1$ and $w=b$ and the function $f(w) \rightarrow \infty$ as $w \rightarrow 1$ or $w \rightarrow b$. For the numerical integration with Simpson's rule one can approach towards the poles within some limits (say 10^{-4} order) sacrificing some accuracy. It takes a long time in the digital computer to chose the limits within which one can approach towards the poles with reasonable accuracy, and to chose the step length for the numerical integration. The Gaussian integration technique used by Howe gives better results than Simpson's rule used by Gupta.

Howe estimated the error introduced due to the small excursion (δ_i) on both sides of limits of integration which are the poles of the function $f(w)$, the integration of which has to be computed with the help of Simpson's quadrature integral formula of variable step length.

$$\text{Thus the Error} = \int_{w_i}^{(1 \pm \delta_i)w_i} f(w) dw$$

when $f(w)$ in his mathematical model is of the form

$$f(w) = k \left[\frac{(w-w_1)^{\frac{\alpha_1}{\pi}-1} (w-w_2)^{\frac{\alpha_2}{\pi}-1} (w-100)^{\frac{1}{2}}}{w} \right]$$

and $f(w)$ is well behaved within the segment $(w_i, (1 \pm \delta_i)w_i)$. He presented a table 2.1 given below which summarizes the effect of δ_i in his model when used in conjunction with Simpson Quadrature integral formula of variable step length.

TABLE 2.1 (From Howe's work)

δ_1	I_1 (Gauss's method)	I_2 (Simpson's rule)
0.001	1.971189	4.530026
0.0005	1.971449	4.750699
0.0002	1.971587	5.042379
0.0001	1.971627	5.263022

Integrals computed for $w_1 = 3$, $w_2 = -90$. While dealing with the problem shown in Fig. 2.11 and discussed in section 2.5, the function $f(w)$ which is of the form $\frac{A_0}{w-p} \sqrt{\frac{(w-d)(w-a)}{(w-c)(w-b)}}$

has been integrated between any two limits which are the poles of function $f(w)$ using Simpson's quadrature integral formula of variable step length. It has been shown there in Table 2.2 how the values of integration change as the limits of integration approach towards the poles of the function $f(w)$. This problem of integration has been over-

come by using the elliptic integrals and functions. Within the limits $a > b \geq y > c$ the equation 2.18 becomes

$$\int dz = A \int_c^y \sqrt{\frac{(w-c)}{(b-w)(a-w)}} dw = A(b-c)g \int_0^{u_1} \text{sn}^2 u du$$

$$= A(b-c)g \cdot \left[\frac{1}{k^2} \{u - E(u)\} \right]_0^{u_1} \quad 2.19$$

$$\text{sn}^2 u = \frac{(w-c)}{(b-c)}, \quad k^2 = \frac{(b-c)}{(a-c)}, \quad g = \frac{2}{\sqrt{a-c}}$$

$$\psi = amu_1 = \text{Sin}^{-1} \sqrt{\frac{y-c}{b-c}}, \quad \text{sn } u_1 = \text{Sin } \psi$$

when $y = b$.

$$d_1 = A(b-c)g \left[\frac{1}{k^2} \{K - E\} \right] \quad 2.20$$

$U_1 = K =$ The complete elliptic integrals of 1st kind.

$$= \int_c^{\frac{\pi}{2}} \frac{d\xi}{\sqrt{1-k^2 \text{Sin}^2 \xi}}$$

and $E(u_1) = E(\pi/2, k) = E =$ Complete elliptic integral of 2nd kind.

Similarly, it can be shown that,

$$jd_2 = jA(b-c)g \left\{ \frac{E(\frac{\pi}{2}, k)}{k^2} \right\} \quad 2.21$$

$$\text{where } k^2 = \left(\frac{a-b}{a-c}\right), \quad g = \frac{2}{\sqrt{a-c}}, \quad \text{Sn}^2 n = \frac{(a-c)(w-b)}{(a-b)(w-c)}$$

$$\phi = \text{am } u_1 = \text{Sin}^{-1} \sqrt{\frac{(a-c)(y-b)}{(a-b)(y-c)}}, \quad \text{sn } u_1 = \text{Sin} \phi$$

The integration within the limit $y > a > b > c$

$$\int dz = A \int_a^y \sqrt{\frac{w-c}{(w-b)(w-a)}} \\ = A \cdot (a-c)g \{u_1 - E(u_1) + \text{dn } u_1 \text{ tn } u_1\} \quad 2.22$$

$$\text{sn}^2 u = \left[\frac{w-a}{w-b}\right], \quad k^2 = \frac{b-c}{a-c}, \quad g = \frac{2}{\sqrt{a-c}}$$

$$\phi = \text{am } u_1 = \text{Sin}^{-1} \sqrt{\frac{y-a}{y-b}}, \quad \text{sn } u_1 = \text{Sin} \phi.$$

From equations 2.20 and 2.21 the values of A and B can be determine . The second transformation from the w-plane to the ξ plane where the field is regular, gives

$$\frac{d\xi}{dw} = \frac{A_1}{\sqrt{(w-b)(w-a)}} \quad 2.23$$

$$\text{where } A_1 = \frac{1}{\pi}$$

$$\text{The flux density } B = \mu_0 \left| \frac{d\xi}{dw} \times \frac{dw}{dz} \right| = \mu_0 \left| \frac{1}{\pi A \sqrt{w-c}} \right|$$

2.24

The flux density reaches its maximum value at $w=a$, i.e. at the centre line of the compole which is obtained from 2.24.

$$B_{\max} = \mu_0 \left| \frac{1}{\pi A(a-c)^{\frac{1}{2}}} \right| = \left| \frac{\mu_0}{\pi A} \right| \quad 2.25$$

Calling the maximum flux density B_{\max} unity, the flux-density distribution on the armature surface can be obtained from equations 2.25 and 2.22. The flux density distribution curves [Figs.(2.16, 18, 19)] show a good agreement between the second model and Gibbs' model when the parameter $\frac{d_1}{d_2}$ is varied from 3.78 to 1.27. When $\left(\frac{B}{B_{\max}}\right)_t$ at the compole centre line is plotted against $\left(\frac{d_1}{d_2}\right)$ [Fig.(2.19a)], it shows that $\left(\frac{B}{B_{\max}}\right)_t$ becomes almost unity (0.995) when $\left(\frac{d_1}{d_2}\right) \geq 1.2$; below this Gibbs' model starts deviating from the second model. In Fig (2.19b) flux density curves p and r show the difference between second model and Gibbs' model when the chosen value of $\frac{d_1}{d_2}$ is 0.5.

Modified Gibbs' curves in the vicinity of the compole can be obtained by dividing each point of Gibbs' original curves by the factor $\left(\frac{B}{B_{\max}}\right)_t$ for the corresponding value of $\frac{d_1}{d_2}$. In Fig.(2.19b), Gibbs' original curve p is modified at each point to obtain the curve q . The Fig.(2.19b) also shows that the modified Gibbs' curve q is quite close to the curve r of the second model.

For the calculation of the flux density distribution in the vicinity of the compole when the value of $\frac{d_1}{d_2}$ is less than 1.2, the modified Gibbs' curve can be used rather than the complicated second model.

2.4.1. Tooth Pitch Flux Distribution for the Second Model

In the w -plane as shown in Fig. 2.9 the field is governed by the equation 2.26

$$\phi + j\psi = \frac{2}{\pi} \log_e \left(\sqrt{w-b} + \sqrt{w-a} \right) \quad 2.26$$

$$\Delta_2 = \left(\phi_1 - \phi_2 \right) = \frac{2}{\pi} \log_e \left\{ \frac{\sqrt{w_1-b} + \sqrt{w_1-a}}{\sqrt{w_2-b} + \sqrt{w_2-a}} \right\} \quad 2.27$$

using equations 2.27 and 2.22 slot pitch flux distribution

on the armature surface can be obtained.

Evaluation of complete and incomplete integrals of first and second kinds and elliptic functions have been discussed in detail in Appendix 1. The combination of models in Fig. 2.3 and 2.8 has been considered in section 2.5 and Fig. 2.11.

2.5 THIRD MATHEMATICAL MODEL

In the model shown in Fig. 2.11 the mainpole has been assumed to be infinitely long, which is true because the mainpole is quite large compared to the compole. The flux line is the centre line of the compole, so that the flux density reaches its maximum value at the middle of the compole. The armature has been assumed smooth because the slotted armature makes the problem extremely complicated. In Chapter 7 it has been discussed how one factor is obtained experimentally to take into account the effect of slots in the armature.

The compole only has potential V , the armature and the mainpole are at 0 potential, the Schwarz-Christoffel transformation from the z plane to the w plane gives the following equations

$$\frac{dz}{dw} = A_0 \frac{1}{(w-p)} \sqrt{\frac{(w-d)(w-a)}{(w-c)(w-b)}} \quad 2.28a$$

$$\int dz = \int \frac{A_0}{(w-p)} \sqrt{\frac{(w-d)(w-a)}{(w-c)(w-b)}} dw = \int f(w) dw \quad 2.28$$

The integral 2.28 can be evaluated within the limits of integration which may be the poles of the function $f(w)$, with the help of Simpson's quadrature integral formula of variable step length as suggested by Binns²⁰, Lawrenson and Gupta¹⁹.

The following table shows how the value of integration

$\int f(w) dw$ changes as the limits of integration approach towards the poles of the function $f(w)$. The numerical values of unknowns d, c, b, p, a , in the w plane have been chosen arbitrarily (see also Fig. 2.11).

$d_1 =$ Half of the compole width in the z plane

$$= \int_{d+\delta}^{c-\delta} f(w) dw \quad \text{where} \quad \delta \ll 1.0$$

TABLE 2.2

$d = 0.0, c = 0.99, b = 1.0, p = 10.0, a = 11.0$

δ	$c-\delta$	$d+\delta$	$d_1 = \int_{d+\delta}^{c-\delta} F(w) dw$
10^{-4}	.9899	0.0001	$.1315 \times 10^2$
10^{-5}	.98999	0.00001	$.1517 \times 10^2$

There is always a problem in choosing the right limits and step lengths of integration if numerical technique like

Simpson's rule is adopted to integrate the function $f(w)$ which has poles. Howe²¹ claimed that Gauss-Jacobi quadrature formula developed by Krylov²² is suitable for the problem he tackled.

Thus

$$\int_{-1}^1 (1-x)^\alpha (1+x)^\beta f(x) dx \approx \sum_{k=1}^M A_k f(x_k) \quad 2.28.1$$

and

$$Z_{i,i+1} = \left| K \sum_{k=1}^M A_k \prod_{J=1}^{i-1} \left[\frac{W_i + W_{i+1} + x_k (W_{i+1} - W_i)}{2.0} - W_j \right]^{\frac{\alpha_j}{\pi} - 1} X \right.$$

$$\times \prod_{J=i+2}^n \left[W_j - \frac{W_i + W_{i+1} + x_k (W_{i+1} - W_i)}{2.0} \right]^{\frac{\alpha_j}{\pi} - 1} X$$

$$\times \left(\frac{W_{i+1} - W_i}{2.0} \right)^{1 + \left(\frac{\alpha_i}{\pi} - 1\right) + \left(\frac{\alpha_{i+1}}{\pi} - 1\right)} \quad 2.28.2$$

The M nodes, x_k , and coefficients, A_k , of the polynomial have been derived

$$\rho_n^{(\alpha, \beta)}(x_k) = 0 \quad 2.28.3$$

and the useful weight functions are

$$-\frac{1}{2}\sqrt{(1-x)}, \quad \sqrt{1-x}, \quad \text{and} \quad \sqrt{(1-x)} (1+x)^{-\frac{1}{2}} \quad 2.28.4$$

However, the problem of uncertainty in the accuracy of integration due to the failure of proper choice of the limits and step length in the Simpson's quadrature formula as suggested by Binns,²⁰ Lawrenson and Gupta¹⁹, and difficulty in deriving the M nodes, and obtaining the right weight function and Jacobi polynomial for the Gauss-Jacobi quadrature formula used by Howe,²¹ has been overcome by the direct integration of the function $\int f(w)dw$ with the help of elliptic integrals and elliptic functions. Thus breaking 2.28 into partial fractions and then integrating, the following results have been obtained

$$\int dz = A_0 \left[\int \sqrt{\frac{(w-a)}{(w-b)(w-c)(w-d)}} dw + (p-d) \int \frac{dw}{\sqrt{(w-b)(w-c)(w-d)(w-a)}} \right. \\ \left. + \int \frac{(p-d)(p-a) dw}{(w-p)\sqrt{(w-b)(w-c)(w-d)(w-a)}} \right] \quad 2.29$$

The constant of integration has been made zero by fixing the origin at the point $w=d$, in the z plane.

Integrating 2.29 within the limit $a > b > c > y > d$ one gets

$$\int dz = jA_0 \left[\pm (a-c)g \cdot \frac{1}{\alpha^2} \left\{ k^2 u + (\alpha^2 - k^2) \Pi(\phi, \alpha^2, k) \right\} \right]_0^{u_1} \\ \pm (p-d)g \left[F(\phi, k) \right]_0^{u_1} \pm (p-d)(p-a) \frac{g}{(p-c)} \left[\frac{1}{\alpha^2} (\alpha_3^2 - \alpha^2) \right. \\ \left. \Pi(\phi, \alpha_3^2, k) + \alpha^2 u \right]_0^{u_1} \quad 2.30$$

Where y and c are the lower and upper limits of integration and,

$$\alpha_3^2 = \left[\frac{(c-d)(p-b)}{(b-d)(p-c)} \right]$$

$$g = \frac{2}{\sqrt{(a-c)(b-d)}}, \quad \text{sn}^2 u = \frac{(b-d)(c-w)}{(c-d)(b-w)}, \quad k^2 = \frac{(a-b)(c-d)}{(a-c)(b-d)}$$

$$k^2 < \alpha^2 = \left(\frac{c-d}{b-d} \right) < 1, \quad \phi = \text{amu}_1 = \text{Sin}^{-1} \sqrt{\frac{(b-d)(c-y)}{(c-d)(b-y)}}$$

When $y = d$

$$\begin{aligned} d_1 = j\Lambda_0 \left[\pm (a-c)g \cdot \frac{1}{\alpha^2} \{ k^2 K + (\alpha^2 - k^2) \Pi(\alpha^2, k) \} \pm (p-d)gK \right. \\ \left. \pm (p-d)(p-a) \frac{g}{(p-c)} \frac{1}{\alpha_3^2} \{ (\alpha_3^2 - \alpha^2) \Pi(\alpha_3^2, k) + \alpha^2 K \} \right] \end{aligned} \quad 2.31$$

$\Pi(\alpha^2, k)$ is the complete elliptic integral of third kind, and within the range $k^2 < \alpha^2 < 1$

$$\Pi(\alpha^2, k) = K + \frac{\pi\alpha \left[1 - \Lambda_0(v, k) \right]}{2 \sqrt{(\alpha^2 - k^2)(1 - \alpha^2)}} \quad 2.32$$

where

$$v = \text{Sin}^{-1} \sqrt{\frac{1 - \alpha^2}{k'^2}} \quad \text{and} \quad k'^2 = 1 - k^2 \quad 2.33$$

$$\Lambda_0(v, k) = \frac{2}{\pi} \left[\text{EF}(v, k') + \text{KE}(v, k') - \text{KF}(v, k') \right] \quad 2.34$$

$\Pi(\alpha_3^2, k)$ will be considered in two cases either $k^2 < \alpha_3^2 < 1$

or $0 < \alpha_3^2 < k^2$,

$$\Pi(\alpha_3^2, k) = K + \frac{\pi \alpha_3 [1 - \Lambda_0(v, k)]}{2 \sqrt{(\alpha_3^2 - k^2)(1 - \alpha_3^2)}} \quad (k^2 < \alpha_3^2 < 1) \quad 2.35$$

where

$$\Lambda_0(v, k) = \frac{2}{\pi} \left[E F(v, k') + KE(v, k') - KF(v, k') \right] \quad 2.36$$

$$\text{and } v = \text{Sin}^{-1} \sqrt{\frac{1 - \alpha_3^2}{k'^2}}$$

$$\Pi(\alpha_3^2, k) = K + \frac{\alpha_3 \text{KZ}(\beta, k)}{\sqrt{(1 - \alpha_3^2)(k^2 - \alpha_3^2)}} \quad (0 < \alpha_3^2 < k^2) \quad 2.37$$

where

$$\text{KZ}(\beta, k) = \text{KE}(\beta, k) - \text{EF}(\beta, k) \quad 2.38$$

and

$$\beta = \text{Sin}^{-1} \left(\frac{\alpha_3}{k} \right)$$

$Z(\beta, k)$ and $\Lambda_0(v, k)$ are known as Jacobian zeta functions and Heuman's Lambda functions. (See Appendix 2.)

Similarly, it can be shown by integrating (2.29) within the limit $a > b \geq y > c > d$

$$d_2 = \Lambda_0 \{ (a-c)g \frac{1}{\alpha_2} \left[k^2 K + (\alpha^2 - k^2) \Pi(\alpha^2, k) \right] + g(p-d)K$$

$$-(p-d)(p-a) \frac{g}{(p-c)} \frac{1}{\alpha^2} \left[(\alpha_3^2 - \alpha^2) \operatorname{II}(\alpha_3^2, k) + \alpha^2 k \right] \quad 2.39$$

where

$$\alpha_3^2 = \frac{(b-c)(p-d)}{(b-d)(p-c)}, \quad \operatorname{sn}^2 u = \frac{(b-d)(w-c)}{(b-d)(w-d)}, \quad k^2 = \frac{(b-c)(a-d)}{(a-c)(b-d)}$$

$$g = \frac{2}{\sqrt{(a-c)(b-d)}} \quad \text{and} \quad 0 < \alpha^2 = \frac{b-c}{b-d} < k^2$$

$$\phi = \operatorname{am} u_1 = \frac{\pi}{2} \quad \text{and} \quad \operatorname{sn} u_1 = 1$$

d_1 and d_2 are the two dimensions shown in the Fig. 2.11.

The value of A_0 can be found by using the method of gap at infinity in which the integration is done along a large semicircle. In the z plane Fig. 2.11, the distance between the surfaces as z approaches infinity is the constant value A_L . Substituting $w = Re^{j\theta}$ where $R \rightarrow \infty$, 2.28 becomes

$$\int dz = A_L = \int_{\pi}^0 \frac{A_0 j R e^{j\theta}}{R e^{j\theta}} d\theta = A_0 j \pi \quad 2.40$$

Hence

$$A_0 = -\frac{A_L}{j\pi} \quad 2.41$$

A similar investigation at the point $w=p$ gives another relation, where the values of both z and w are known. The value of Z changes abruptly at the point corresponding to $w=p$ by the amount fg . Hence from the equation 2.28

$$\int dz = jg = \lim_{\epsilon \rightarrow 0} \left[A \sqrt{\frac{(p-d)(p-a)}{(p-c)(p-b)}} \int \frac{dw}{(w-p)} \right]_{p-\epsilon}^{p+\epsilon} \quad 2.42$$

$$\frac{A_1}{g} = \sqrt{\frac{(p-c)(p-b)}{(p-d)(a-p)}} \quad 2.43$$

Out of five unknown constants a, b, c, d and p in the w plane, d and b have taken two suitable values.

$$d = 0 \text{ and } b = 1$$

The rest of the unknowns a, c, p and A_0 have been determined from four equations 2.31, 2.39, 2.41 and 2.43, and it is discussed in Appendix 3.

The second transformation from the w plane to the ξ plane where the field is uniform gives the following relation

$$\frac{d\xi}{dw} = \frac{A_2}{\sqrt{(w-c)(w-b)}} \quad 2.44$$

A_2 is constant given by

$$A_2 = \frac{1}{\pi}$$

The flux density on the armature surface is

$$\begin{aligned} B &= \mu_0 \left| \frac{d\xi}{dw} \cdot \frac{dw}{dz} \right| \\ &= \mu_0 \left| \frac{A_2}{A_0} \cdot \frac{(w-p)}{\sqrt{(w-d)(w-a)}} \right| \quad 2.45 \end{aligned}$$

When $w \rightarrow p$, that means well inside the mainpole flux density

goes to zero, which is true. Again the flux density reaches its maximum value at $w = b$, i.e. in the middle of the compole core, and the maximum flux density is given by

$$B_{\max} = \mu_0 \left[\frac{1}{A_L} \frac{(b-p)}{\sqrt{(b-d)(b-a)}} \right] \quad 2.46$$

The values of z on the armature surface corresponding to the points in the w plane within the limit $w = b$ to $w = p$, can be obtained by integrating 2.28. The integration of 2.28 within the limit $a > y > b > c > d$ is given by

$$\int dz = \frac{A_L}{\pi} \left\{ \pm (a-b)g \cdot \frac{1}{\alpha^2} \left[u + (\alpha^2 - 1) \Pi(\phi, \alpha^2, k) \right]_0^{u_1} \right. \\ \left. \pm (p-d)gF(\phi, k) \pm (p-d) \frac{g(p-a)}{(b-p)} \frac{1}{\alpha_3^2} \left[(\alpha_3^2 - \alpha^2) \Pi(\phi, \alpha_3^2, k) + \alpha^2 u \right]_0^{u_1} \right\} \quad 2.47$$

$$\text{where } \text{sn}^2 u = \frac{(a-c)(w-b)}{(a-b)(w-c)}, \quad k^2 = \frac{(a-b)(c-d)}{(a-c)(b-d)}$$

$$k^2 < \alpha^2 = \left(\frac{a-b}{a-c} \right) < 1, \quad g = \frac{2}{\sqrt{(a-c)(b-d)}} \quad \text{and} \quad \alpha_3^2 = \frac{(p-c)(a-b)}{(p-b)(a-c)}$$

$$\phi = \text{am } u_1 = \text{Sin}^{-1} \sqrt{\frac{(a-c)(y-c)}{(a-b)(y-c)}}, \quad \text{sn } u_1 = \text{Sin } \phi$$

The evaluation of third order complete and incomplete integrals have been discussed in Appendix 2. Calling the maximum flux density given by 2.46 unity the flux density

distributions along the armature surface have been obtained for various values of $\frac{A_L}{d_2}$, $\frac{\delta}{d_2}$, $\frac{d_1}{d_2}$ using the equations 2.47 and 2.45 as shown in Fig. 2.16 and 2.18. The flux density distribution along the armature surface under the mainpole obtained from equations 2.47 and 2.45 fall in between those from Gibbs' model and the model with compole and mainpole both extended to infinity in section 2.2. The Figs (2.16) and (2.18) show that the deviation between model 1 and model 3 occurs only in the vicinity of the mainpole, because they are plotted on the per unit basis. When the magnitudes of the flux densities are plotted in Fig (2.16a) they show that the flux densities estimated by model 3 are more than model 1 all over the curve. This is because the model 3 considers the centre line of the compole as a flux line and the constants in the w plane for model 3 are approximately evaluated by the optimisation technique.

2.5.1 Tooth Pitch Flux Distribution for the Third Model

The field in the w plane is obtained by integrating the equation 2.44 which is given by

$$\phi + j\psi = \frac{2}{\pi} \log_e \left(\sqrt{w-c} + \sqrt{w-b} \right) \quad 2.48$$

the quantity of flux within $w = w_1$ to $w = w_2$ which corresponds to the tooth pitch on the armature surface in the z plane is calculated from equation 2.49

$$\Delta\phi = \left(\phi_1 - \phi_2 \right) = \frac{2}{\pi} \log_e \left\{ \frac{\sqrt{w_1-c} + \sqrt{w_1-b}}{\sqrt{w_2-c} + \sqrt{w_2-b}} \right\} \quad 2.49$$

2.6 CONCLUSIONS

Flux Distribution under the Compole when Compole and Mainpole are both Excited

So far the expressions for tooth pitch flux and flux

density distributions in different configurations have been obtained on the assumptions that the compoles are at potential V and the mainpoles and armature are at zero potential. Now interchanging the position of compole and mainpole in the configurations shown in Fig.2.3 and 2.11 and changing the dimensions accordingly in the analysis given in sections 2.5 and 2.2, one can estimate tooth pitch flux and flux density distributions under the compole with the main pole at potential V_1 (say) and the interpole and armature at zero potential. Applying the method of superposition the tooth pitch flux or the flux density distributions thus obtained in two cases

- (1) When only the mainpoles are excited and
- (2) When only the interpoles are excited,

will be added at each point on the armature surface under the compole to get the resultant flux distributions due to the compole and mainpole both being excited at the same time; which brings us more towards the truth, but the problem of the commzone flux distribution or the flux density under the compole is not completed until the armature slots and armature reactions are taken into account. All the theoretical models so far considered, assume smooth armature which evaluate the flux or flux density more than it should with slotted armature. Theoretical investigation of the slotted armature surface needs to solve the field problems of the configurations shown in Fig. 2.14 and 2.15 which

becomes extremely complicated, and a practically impossible task to find the values of constants in the w plane.

An experiment was carried out with a tooth pitch search coil which is discussed in detail in section 7.2. Chapter 7, and factor $k_{\alpha} < 1.0$ has been found experimentally that should be multiplied at each point of the theoretical flux distribution curve in order to take the effect of slots into account. Carter's Coefficient takes into account the effect of having a deep slot opposite to a smooth magnetic face infinitely long at both ends and it is defined as

$$C = \frac{\text{The flux crossing the airgap for one slot pitch when one of the magnetic faces is smooth and the other surface has a slot and they are separated by an air gap.}}{\text{The flux crossing the air gap for one slot pitch when both the magnetic faces are smooth and separated by the same air gap.}}$$

The Carter's coefficient is applicable when the smooth surface is large in comparison with the slot and the tooth dimensions viz. mainpole in front of a slotted armature. The value of the Carter's coefficient is determined by the dimensions of the slot, tooth and air gap only and it does not change with the position of the slot with respect to the smooth surface so long as the air gap is fixed. While dealing with the slot pitch flux distribution in the interpolar region the Carter's coefficient can not be used excepting at the two extreme cases

- (1) When the slot is symmetrically placed along the compole centre line.
- (2) When the slot is far away from the compole.

because the slot pitch is comparable with compole dimension (the ratio is almost 1 for the experimental machine) and the slot pitch flux changes as the field pattern changes at each position of the slot with respect to the compole. The factor k_{α} in Fig (2.22) takes into account the effect of permeance variation on the slot pitch flux at each position of the slot.

From the Fig.(2.22) it is seen that the value of k_{α} at the compole centre line is 0.77 which is approximately equal to the Carter's coefficient 0.79. Also k_{α} tends to reach unity when the slot pitch search coil is far away from the compole which is similar to the case for a large air gap when the Carter's coefficient tends to 1.

From the experimental results in Fig.(2.22) Carter's coefficient can be related with the factor k_{α} by two equations, when the variation of k_{α} along the armature surface is approximately represented by two straight lines of different slopes.

Thus

- (1) from the compole centre line to the point p (see Fig 2.22)

$$k_{\alpha} = C_{\ell} + \left(\frac{\text{distance along the armature}}{\text{compole gap length}} \right) \times 0.032 \quad (2.50)$$

(2) from the point p and onwards

$$k_{\alpha} = k_{\alpha 1} + \left(\frac{\text{distance along the armature}}{\text{compole gap length}} \right) \times 0.0065 \quad (2.51)$$

where p is the point on the armature, twice the compole gap length away from the compole edge, C_{ℓ} is the Carter's coefficient at the compole centre line, and $k_{\alpha 1}$ is the value of k_{α} at the point p obtained from equation (2.50).

It may be suggested that the easier and quicker way to obtain the flux distribution ϕ_i under the compole with reasonable accuracy is to use the model 1 along with the factor k_{α} .

Whilst the above equations (2.50) and (2.51) describe the variation of k_{α} for the experimental machine, experience would have to be built up on other machines to obtain a general expression for k_{α} .

2.7 SUGGESTIONS FOR FUTURE WORK

The value of the factor k_{α} , which is multiplied to the theoretical flux distribution in the first model, considered in section 2.2, to take the effect of slots into account has been experimentally found from the test machine discussed in section 7.2. Chapter 7, but its value should be checked in other machines having different dimensions of tooth, slot, compole and mainpole for further confirmation.

The machine in its running condition has triangular armature mmf distributed along the armature surface, which has not been included in the analysis presented in this chapter. This makes the already difficult interpolar region field problem more complicated and calls for further investigation.

While dealing with the field problem in the interpolar region of the third model in section 2.5, only a limited value of $\frac{d_1}{A_1}$, $\frac{d_2}{A_1}$, and $\frac{g}{A_1}$ are chosen for the verification of the theoretical work which employs the nonlinear multi-variable optimisation technique for finding the values of constants in the w plane. With some mathematical refinements, the same method can be used to estimate the flux distribution under the compole for a model which includes slots in the armature. The theoretical limitations for those three ratios $\frac{d_1}{A_1}$, $\frac{d_2}{A_1}$, and $\frac{g}{A_1}$ have not been found out and this has been left for future work.

PART B

CHAPTER 3

3.1 SURVEY OF LITERATURE ON d.c. MACHINES OPERATING FROM RECTIFIED a.c. SUPPLY (WITH SPECIAL REFERENCE TO COMMUTATION)

3.1.1 Introduction

This chapter presents a survey of literature on the performance of d.c. machine supplied from controlled rectifier unit with particular reference to the commutation problem, in a chronological manner since 1930's. The theoretical investigation so far made by various authors for the analysis of d.c. machine supplied from various types of rectified source, including the newly developed SCR, with special interest on voltage and current wave-forms at the operating condition of the machine have been given in this chapter. The pulsating component of a.c. flux will produce eddy currents in the solid parts of the magnetic circuit. It has been discussed how different authors [redacted] have taken into account the effects of eddy currents induced in the solid shell towards the commutating flux.

3.1.2 Some Investigations at the Earlier Stage

Development of power tubes in the early 1930's brought the new approach to the problem of variable speed motors and it started replacing the motor generator sets which had been the normal source of power for large d.c. motors for many years. Power rectifiers were first used around 1940 in a steel rolling company in U.S.A. [redacted]

It is believed that a study of the effect of rectifier power supply on d.c. machine began in 1938 by Alexanderson and Edwards²³, who have mentioned in 'Electronic speed control of motors' about the new approach of speed control of d.c. machine by varying the armature voltage by phase control of the rectifier. It was also mentioned in that paper that when the phase controlled rectifier supplies d.c. motor, commutation will limit the magnitude of the ripple current permissible, and to smooth out the a.c. ripple an extra choke can be used in the armature circuit. The value of inductance will be

$$L = [E_r / (\frac{dI_{am}}{dt})]$$

where E_r is the maximum ripple voltage produced by the rectifier and $(\frac{dI_{am}}{dt})$ is the maximum change of armature current consistent with good commutation. They did not discuss the commutation problem with rectified d.c. supply deeply.

3.1.3 Theoretical Investigations on d.c. Machines Supplied from Rectified a.c.

It is believed that the first theoretical approach for the rectifier d.c. motor drive was made by Vedder and Puchlowski²⁴ in the year 1943, and it is worthwhile reviewing their theoretical work to understand its basic principles.

They considered a simplified circuit of a typical

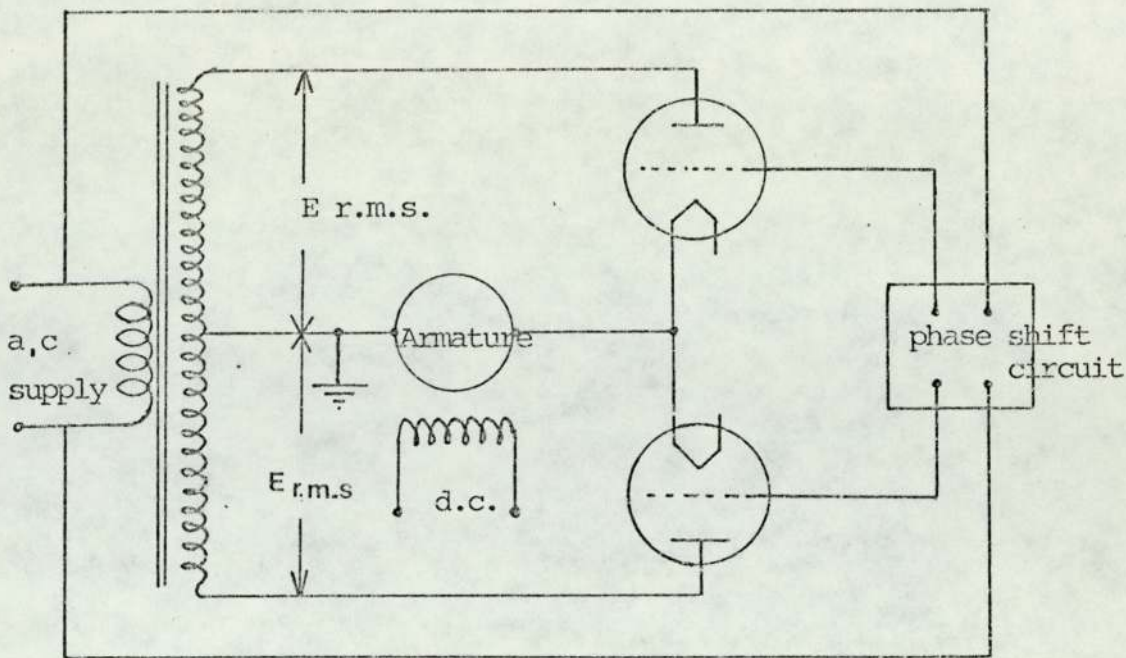


Fig. 3.1 The Elementary Diagram of a Single Phase Full Wave Rectifier d.c. Motor Drive (Vedder & Puchlowski²⁴)

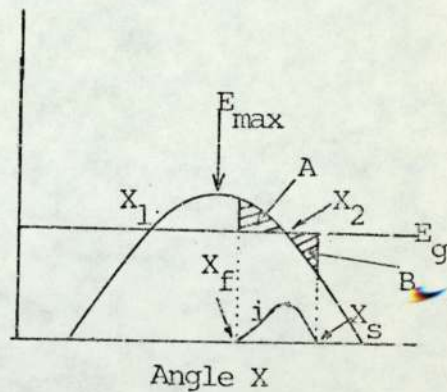
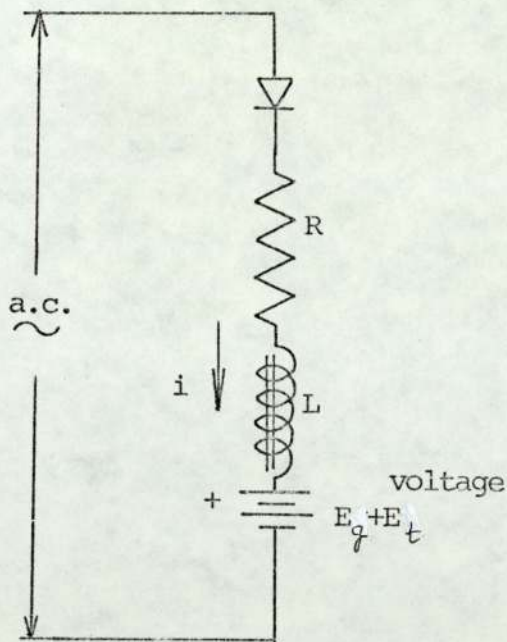


Fig. 3.2 An Elemental Half Wave Rectifier Circuit with Resistance, inductance and Counter electromotive force in the load

Fig. 3.3 A sine wave of voltage with counter electromotive force

single-phase full wave system, as shown in Fig. 3.1, in which the rectifier is composed of two thyatron tubes with their grids arranged for phase shift control to permit the tubes to start conducting at any chosen phase angle, with respect to the applied a.c. voltage, during each half cycle. The circuit in Fig. 3.1. was then converted into an equivalent circuit as shown in Fig.3.2. The assumptions they made for the analysis are as follows:

- (1) D.c. motor with separately excited field winding.
- (2) Constant armature inductance and the circuit inductances have been lumped in the inductance L .
- (3) The resistance of the armature and the external circuit have been lumped in the resistance R and are constant.
- (4) The counter electromotive force, E_g , is directly proportional to motor speed.
- (5) The transformer impedance is neglected.
- (6) The arc drop of the tube E_t is constant.
- (7) The effect of armature reaction is neglected.
- (8) The equivalent circuit shows only one half of the full wave rectifier.
- (9) The tube characteristics are such that the conduction can begin as soon as the instantaneous value of the transformer voltage is equal to or greater than $E_g + E_t$.

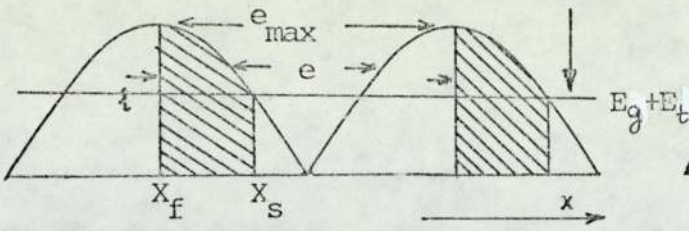


Fig. 3.4 The Waveform of Current and Voltage in a Full-wave Rectifier operating the d.c. Motor Which is Assumed to Have No Inductance.

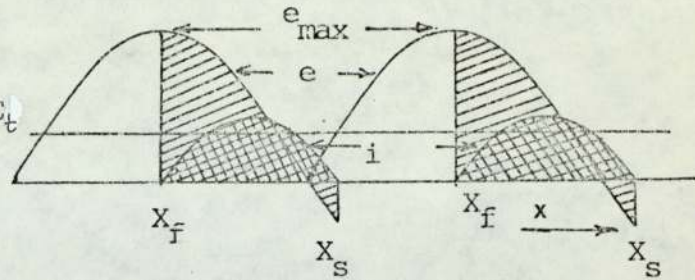


Fig. 3.5 The Waveform of Current and Voltage in a Full-wave Rectifier Operating the d.c. Motor which is Assumed to Have Inductance Present.

For the ideal case of zero armature inductance the current would flow until, in Fig. 3.4, e becomes less than $E_g + E_t$ at angle X_s which is called the 'stopping angle'. The current must stop flowing at the angle X_s , because the opposing voltages are equal and the rectifying property of thyatron does not permit reversal of current. The voltage e may be considered as applied to the armature during the interval X_f to X_s , and thus the hatched portion of Fig. 3.4 represents the voltage applied to the armature by the rectifier. The current pulse would have the same shape as the voltage wave from X_f to X_s . The general effect of inductance in the circuit is to reduce the peak of the current pulse and broaden its base by causing the current to continue flowing beyond the point where e equals $E_g + E_t$. The applied voltage during the interval X_f to X_s is shown by the single hatched line in Fig. 3.5, but the current does not follow the shape of the applied voltage and is

represented by the double-hatched curve i.

The voltage current equation for the equivalent circuit in Fig. 3.1 is

$$L \frac{di}{dt} + Ri + E_g + E_t = E_m \sin(X_f + \omega t) \quad (3.1)$$

Vedder and Puchlowski²⁴ obtained the complete solution of equation 3.1 given by

$$i = \frac{E_m}{R} \left\{ [\cos\theta \sin(x-\theta) - a] + [a - \cos\theta \sin(X_f - \theta)] \exp\left[-\frac{x - X_f}{\tan\theta}\right] \right\} \quad (3.2)$$

The equation 3.2 is the expression for the armature current pulse as a function of angle x.

'a' is called the speed factor given by

$$a = \frac{E_g + E_t}{E_m} \quad (3.3)$$

$$\theta = \cos^{-1}\left(\frac{R}{Z}\right) \quad (3.4)$$

Using the limits $X_f \leq x \leq X_s$

and $i \geq 0$

the expression 3.2 represents the equation for a single pulse of current.

Using the fact that $i = 0$, at $x = X_s$ a basic relationship between the firing and stopping angles has been obtained

$$\begin{aligned} & [a - \cos\theta \sin(X_s - \theta)] \exp\left(\frac{X_s}{\tan\theta}\right) \\ & = [a - \cos\theta \sin(X_f - \theta)] \exp\left(\frac{X_f}{\tan\theta}\right) \end{aligned} \quad (3.5)$$

Since it is not possible to represent the stopping angle X_s in the form of an explicit formula

$$X_s = F(X_f, \theta, a)$$

they calculated the value of X_s for each value of X_f and different values of parameter a and θ .

The maximum of the armature-current pulse occurs at an angle $x = X_p$ such that

$$\cos(X_p - \theta) \exp(X_p / \tan \theta) = \left[\frac{a}{\sin \theta} - \frac{\sin(X_f - \theta)}{\tan \theta} \right] \exp\left(\frac{X_f}{\tan \theta}\right) \quad 3.6$$

The equation 3.6 has been obtained by differentiating expression 3.2 with respect to x . One can get the expression for the peak value of the current pulse i_{\max} by putting the value of X_p from 3.6 into 3.2.

Another important result presented in this paper is the expression for the average value of the armature current I_{av} which is obtained by integrating the equation $e_a = E_m \sin x - (E_g + E_t)$ within the limit $x = X_f$ to $x = X_s$. Thus for a single phase full-wave rectification I_{av} which is proportional to torque of the motor is given by

$$I_{av} = \frac{1}{\pi} \frac{E_m}{R} [\cos X_f - \cos X_s - a(X_s - X_f)] \quad 3.7$$

In conclusion it should be pointed out that they considered the case where the current flows in discrete pulses, that is, two consecutive pulses of current corresponding to two consecutive half cycles of a single phase full wave

rectifier do not join with each other.

Schmidt and Smith²⁵ in the year 1948 published a paper in which they discussed the heating, commutation, and speed regulation of d.c. machines supplied from rectifier units. They considered both (1) continuous (2) discontinuous armature currents. Condition for continuous armature current is that the conducting period of one anode exceeds $\frac{360^\circ}{q}$ where q is the number of phases. Fig.3.6 shows the voltage and current of a typical 6 phase rectifier having counter electromotive force load with finite inductance. The voltage is made up of a d.c. component and an a.c. component whose frequency depends on the number of phases in the rectifier, and the supply frequency. At a moment when the voltage of the rectifier is at its average value and rising, the motor current will be at its minimum value. If this time be designated by t_0 and the next instant of equal rectifier voltage by t_1 , the motor current will vary over the interval by an amount

$$\Delta I = \int_{t_0}^{t_1} \frac{(E_d - e_d)}{L_d} dt \quad 3.8$$

where E_d = Motor counter electromotive force

e_d = Instantaneous d.c volts

L_d = d.c. circuit inductance which consists of the inductance of the load and the average inductance of the conducting windings of the rectifier transformer.

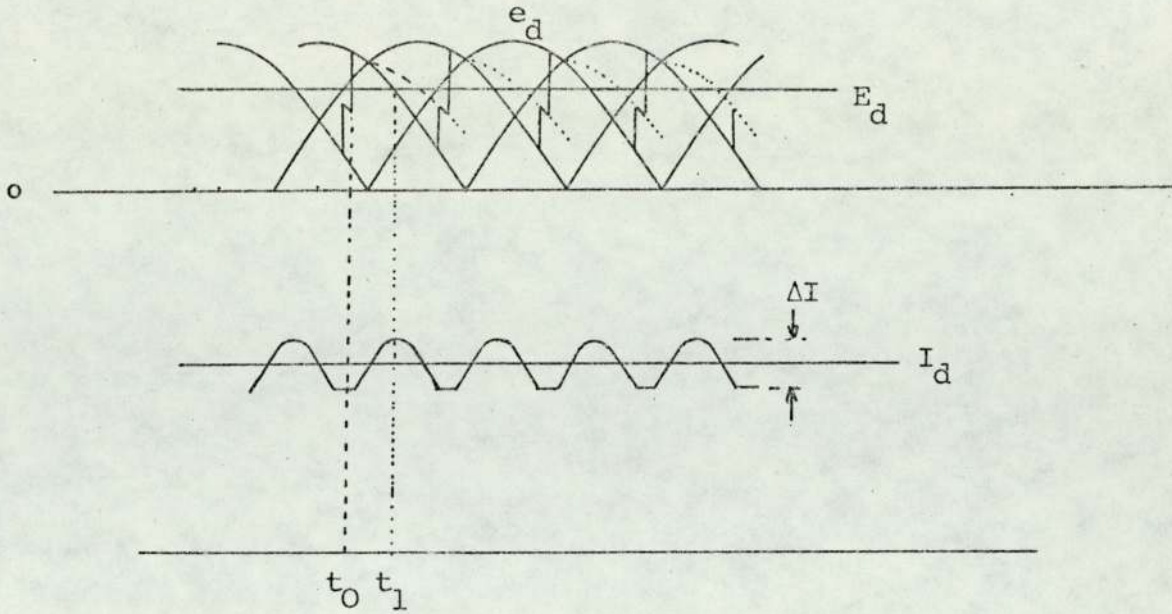


Fig. 3.6 Direct Voltage and Current of 6 Phase Rectifier with Moderate Value of Load Inductance

Now $\int_{t_0}^{t_1} (E_d - e_d) dt$ is proportional to the average value of the rectifier ripple voltage. The total current variation with q phases is

$$\Delta I = \frac{E_{av}}{2qfL_d} \quad 3.9$$

Thus, the current ripple can be determined if the number of rectifier phases, the amount of phase retard and the total d.c. circuit inductance are known.

For the discontinuous armature current shown in Fig. 3.7. they obtained the expression for the average value of rectified current given by

$$I_d = \frac{E_M}{2\pi X} [\sin \psi - \sin \theta + \frac{1}{2}(\theta - \psi)(\cos \psi + \cos \theta)] \quad 3.10$$

They did not take any resistance in the equivalent circuit which Vedder and Puchlowski considered in their analysis.

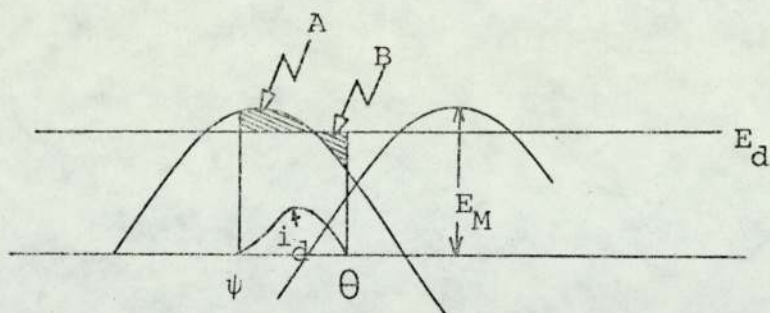


Fig. 3.7 Voltage and Current Relations in Controlled Rectifier with inductive Counter Electromotive Force Load.

If the rectifier has q anodes, the average current will be

$$I_{dq} = \frac{q E_M}{2\pi X} F(\psi, \theta) \quad 3.11$$

where $F(\psi, \theta) = [\sin\psi - \sin\theta + \frac{1}{2} (\psi - \theta) (\cos\psi + \cos\theta)]$

They mentioned in this paper that the extra losses in the current carrying and flux carrying parts of the machine depend on the magnitude and frequency of the ripple current present in the motor supply. About commutation they have stated ' The commutating performance of a d.c. motor operating from a rectifier power supply is adversely affected when the frequency of the ripple current is so high that the commutating pole flux is no longer proportional to and in phase with armature current. When this occurs the armature reaction is not properly compensated for and sparking may result. Non-proportionality may be caused by reduction of commutating pole flux by eddy current, phase displacement due to iron losses'. They did not give any rule or law which can quantify for the flux reduction

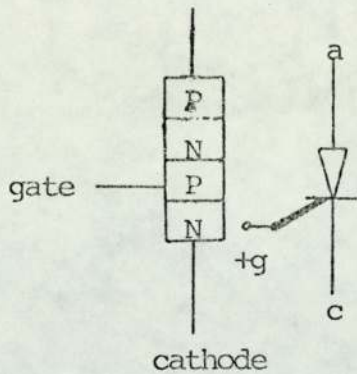
due to eddy current or estimation of phase displacement due to iron losses.

3.1.4 Development of SCR and Further Theoretical Investigations

After several years of development in the late 1950's and early 1960's the use of silicon controlled rectifiers came into being. These silicon controlled rectifiers were first available at lower power levels, and later at higher levels. As a result of their increased efficiency, reduction in maintenance requirements, ease of installation, convenience of control, and reduction in size, weight and cost, the thyristors became a useful element in the control circuit, and they replaced thyratrons, and mercury arc rectifiers which were previously used for field excitation control of all kinds of generators and motors, and armature voltage control of d.c. machines.

The silicon controlled rectifier is basically a four layer p-n-p-n semi-conductor device which stands in relation to the silicon power diode, as does the thyatron to the gas, or vapour-filled diode, or the grid controlled mercury-arc rectifier to its uncontrolled counterpart.

It may be regarded as a silicon diode to which has been added a third electrode, the gate, by means of which the initiation of forward conduction can be controlled. Fig. 3.8 shows a schematic representation of the device and Fig. 3.9



3.8 Schematic Representation of Controlled Rectifier and Graphical Symbol

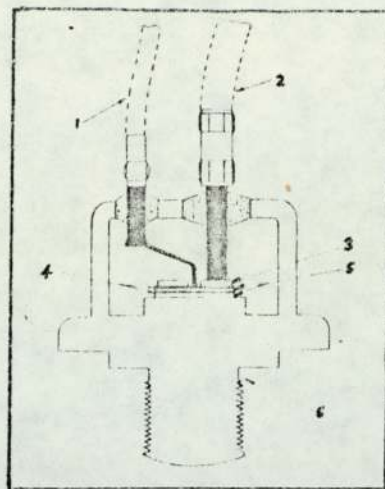


Fig. 3.9

Sectional View of Typical Silicon Controlled Rectifier

(Merrett²⁷)

1. Gate Connector
2. Cathode Connector
3. Current distributing ring
4. Silicon n-layers
5. Silicon p-layers
6. Anode Connector (mounting base).

is a sectioned drawing showing internal construction which follows generally the arrangements used for silicon diodes.

At this stage it will be worthwhile to discuss the common types of rectifier sources and the voltage and current waveforms. The following tabulation applies.

Rectifier type	Fundamental frequency in Hz.	Pulses per line cycle
1. Single phase half wave	50	1
2. Single phase full wave	100	2
3. Three phase, full wave, half controlled bridge	150	3
4. Three phase, full wave, full controlled bridge	300	6
5. Three phase, full wave, two phase shifted full controlled bridge	600	12

Table 3.1

The basic principle of the thyristor involves pulsing a thyristor on during the positive half cycle of the sine wave. The characteristic of a thyristor is such that it will remain in conduction until the polarity reverses or the sine wave goes to the negative half cycle. Therefore selecting the time during the positive half cycle to activate the thyristor will determine a specific power pulse duration. Single phase half wave and single phase full wave power sources are utilized primarily in the area of five kw, and less. The last three power sources listed in the table (3.4) are utilized in the larger h.p. motor.

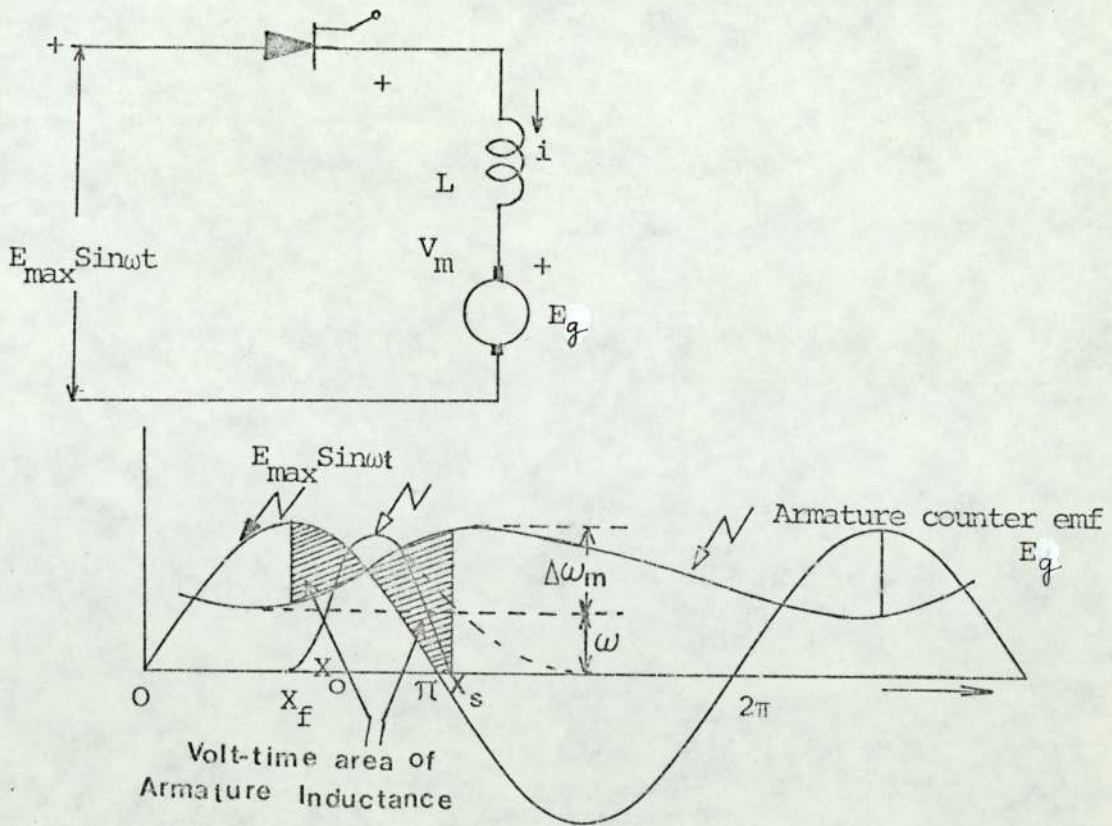


Fig. 3.10 Waveform for Half-wave Thyristor Drive

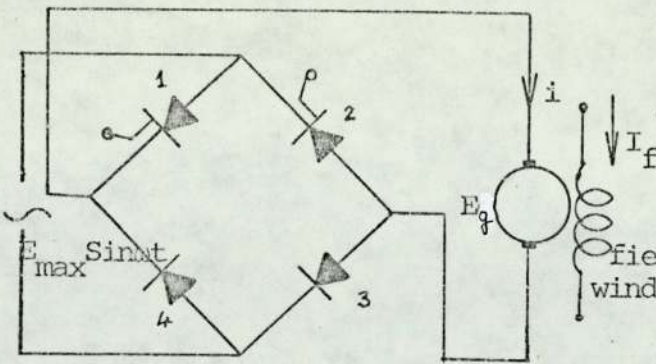


Fig. 3.11 Single Phase Full Wave Thyristor Drive Circuit

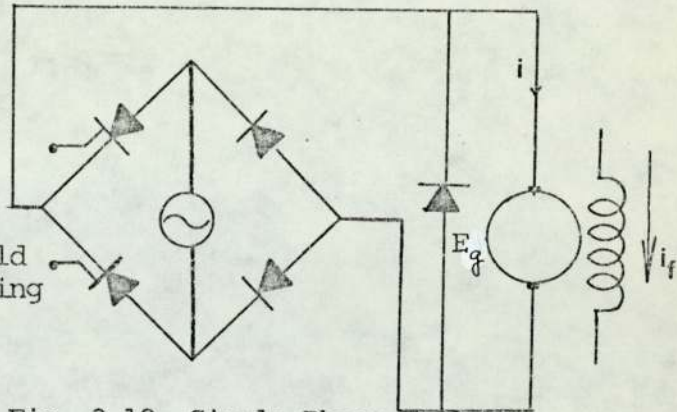


Fig. 3.12 Single Phase Full Wave Thyristor Drive Circuit With Freewheel Diode

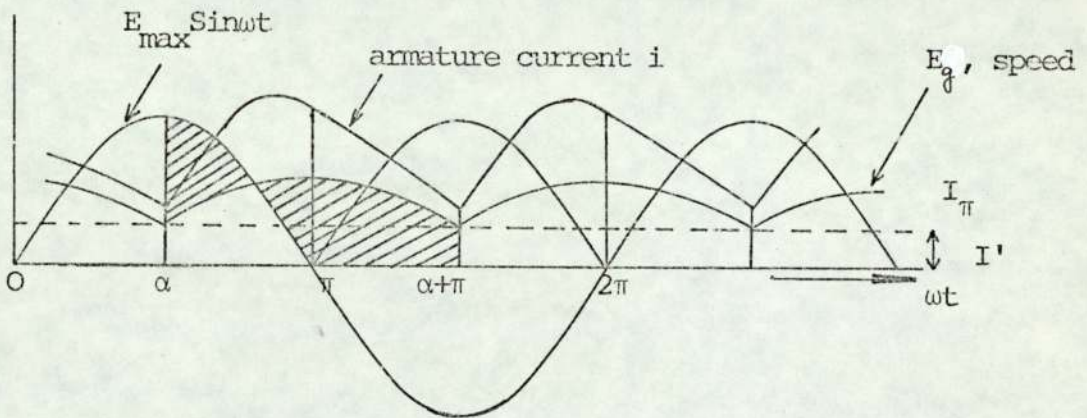


Fig. 3.13 Waveform for Full Wave Drive

The operation of single phase half wave thyristor system shown in Fig. 3.10 does not need any more explanation because it has already been discussed previously, when the power tube was considered in place of the thyristor. The expression for the discontinuous armature current obtained by Vedder and Puchlowski²⁴, discussed earlier in this section, is also applicable for the present case where the thyristor

has been used. Vedder et al. has assumed in their work that E_g is not a function of time which is acceptable only when the load is not heavy. Strictly speaking, the armature counter e.m.f. E_g which is directly proportional to the motor speed swings quite a lot if the load is heavy. This can be explained in the following manner.

During the armature-current conduction period within the interval $X_f \leq x \leq X_s$, electrical energy flows into the armature circuit, the interaction of current and field flux results in positive electromagnetic torque. The motor accelerates during the conduction period by the speed $\Delta\omega_m$ as shown in Fig. 3.10. From the end of the conduction period at $x = X_s$ of one cycle, and the start of the next conduction period at $x = 2\pi + X_f$, the motor coasts down by $\Delta\omega_m$. The motor supplies the load energy during the coasting period from its own kinetic energy. The armature inductance acts as a reservoir of electrical energy during the conduction period, the armature and load inertia act as a reservoir of mechanical energy during the coasting period. When the load is heavy, $\Delta\omega_m$ becomes large. To take into account this speed swing $\Delta\omega_m$ one ought to add half the value of $\Delta\omega_m$ with ω , which may be called as a base speed, so the E_g becomes $E_{g_{new}}$ which is proportional to $(\omega + \frac{\Delta\omega_m}{2})$.

Single phase full wave drive circuit is usually built as shown in Fig. 3.11, using two thyristors and two diodes. The diodes are placed so that they also serve to

provide free-wheeling current path across the armature terminals. The alternative circuit is shown in Fig. 3.12, in which the thyristors have a common cathode connection, but a separate free-wheeling diode must be used. In small motors, the armature ($\frac{L}{R}$) ratio may be so small that a free-wheeling diode will not contribute any assistance to increasing the conduction angle.

Merrett^{26,27} in the year 1966 presented his theoretical work for the single phase full-wave thyristor drive system. He adopted Veeder and Puchlowski's theoretical approach for the motor analysis which has been discussed previously.

When the motor is shunted by a flywheel diode the conducting thyristor will be turned off by the diode at approximately the supply voltage zero. He obtained the following expression for the average thyristor current by integrating (3.2) between the limits X_f and π .

$$I_{av} \Big|_{\text{Thyristor}} = \frac{E_m}{\pi R} \left[\cos^2 \theta + \cos X_f - a(\pi - X_f - \tan \theta) - (a \tan \theta - \sin \theta \sin(X_f - \theta)) \exp\left(\frac{-(\pi - X_f)}{\tan \theta}\right) \right] \quad 3.12$$

The starting value of diode current is obtained by substituting $x = \pi$ in equation (3.2) which gives

$$|i|_{\text{diode starting value}} = i_s = \frac{E_m}{R} \left[\cos \theta \sin \theta - a + \left[a - \cos \theta \sin(X_f - \theta) \right] \exp\left(\frac{-(\pi - X_f)}{\tan \theta}\right) \right] \quad 3.13$$

The diode current falls off exponentially from this value at a rate determined by motor back e.m.f. E_g and the armature resistance R such that

$$i_{\text{diode}} = \left(i_s + \frac{E_m}{R} \right) \text{Exp} \left(-t \frac{R}{L} \right) \quad 3.14$$

The diode becomes reverse biased and stops conducting when

$$i_{\text{diode}} = \frac{E_g}{R} \quad 3.15$$

From equations (3.14) and (3.15), the maximum conduction time of the diode is therefore

$$t_1 = \frac{L}{R} \text{Log}_e \left(1 + i_s \frac{R}{E_g} \right) \quad 3.16$$

Integration of equation (3.14) and substitution for t from (3.16) gives average value of diode

$$(I_{\text{av}})_{\text{diode}} = \frac{\tan \theta}{\pi} \frac{E_m}{R} D \left[1 - \frac{a}{D} \log_e \left(1 + \frac{D}{a} \right) \right] \quad 3.17$$

where

$$D = \left[\cos \theta \sin \theta - a + \{ a - \cos \theta \sin (X_f - \theta) \} \text{Exp} \left(\frac{-(\pi - X_f)}{\tan \theta} \right) \right] \quad 3.18$$

$$\text{and } \theta = \tan^{-1} \frac{\omega L}{R} .$$

The average value of armature current is

$$I_{\text{av}} = (I_{\text{av}})_{\text{Thyristor}} + (I_{\text{av}})_{\text{diode}} \quad 3.19$$

Once average armature current has been calculated, it can be substituted in the motor torque equation $T = C_2 I_a \phi$ to obtain the required speed-torque relationships.

When the armature current is continuous, i.e.

$\omega t_1 \geq X_f$ the starting condition for successive half cycles will be different. The final current waveform is shown in Fig. 3.13. For this case Merrett²⁶ used the general solution with some modification to obtain the expressions for I' and I_π shown in Fig. 3.13 in terms of R , L , E_m and θ . The basic differential equation (3.1), from which the discontinuous thyristor current equation was derived, has been modified. The new differential equation is

$$E_m \sin x - E_g = L \frac{di}{dt} + (i + I')R \quad 3.20$$

The instantaneous value of the thyristor current, i , has been obtained from (3.20) which is

$$i = I' + \frac{E_m}{R} \left\{ \cos \theta \sin(x - \theta) - \frac{E_g + I'R}{E_m} + \left[\frac{E_g + I'R}{E_m} - \cos \theta \right. \right. \\ \left. \left. \sin(X_f - \theta) \right] \exp\left(-\frac{R}{L} t\right) \right\} \quad 3.21$$

At supply angle π the thyristor turns off and diode starts conducting. The instantaneous thyristor current at angle π is

$$i_\pi = \frac{E_m}{R} \left[\frac{A}{\exp(-\beta)} - a \right] \quad 3.21a$$

I' which is diode current at angle X_f is

$$I' = \frac{E_m}{R} [A - a] \quad 3.22$$

Average value of thyristor current is

$$I_{av}(\text{Thyristor}) = \frac{1}{\pi} \int_{X_f}^{\pi} i \cdot dt$$

$$= \frac{E_m}{\pi R} \{ (\pi - X_f)(A - a) + \cos^2 \theta + \cos X_f - A(\pi - X_f - \tan \theta) \times \\ \chi \left[A \tan \theta - \sin \theta \sin(X_f - \theta) \right] \exp\left(\frac{-(\pi - X_f)}{\tan \theta} \right) \} \quad 3.23$$

and flywheel diode average current is given by the equation

$$(I_{av})_{diode} = \frac{E_m}{\pi R} \frac{X_f}{2} \left\{ A \left(1 + \frac{1}{\exp(-\beta)} \right) - 2a \right\} \quad 3.24$$

where $\beta = \frac{X_f}{\tan \theta}$

and

$$A = \frac{\cos \theta \exp(-\beta) \left[\sin \theta - \sin(X_f - \theta) \exp\left(\frac{-(\pi - X_f)}{\tan \theta} \right) \right]}{1 - \exp(-\beta) \exp\left(\frac{-(\pi - X_f)}{\tan \theta} \right)} \quad 3.25$$

The average armature current can be obtained by summing up the average thyristor and diode currents.

The solution is not exact as it assumes that the initial current I' is steady current, that is with zero rate of change. In practice there would be a small negative $\frac{di}{dt}$ component which should be taken into account.

Three phase full wave half controlled bridge and three phase full wave full controlled bridge.

The Voltage Current Waveform

Most of the integral horse-power solid state d.c. drive systems utilises three-phase thyristor rectifier circuits for providing the motor power. The three-phase incomplete bridge circuit as shown in Fig. 3.13a is most commonly used for d.c. motor drives because it requires only three thyristors to achieve the full range of control.

three
phase
line

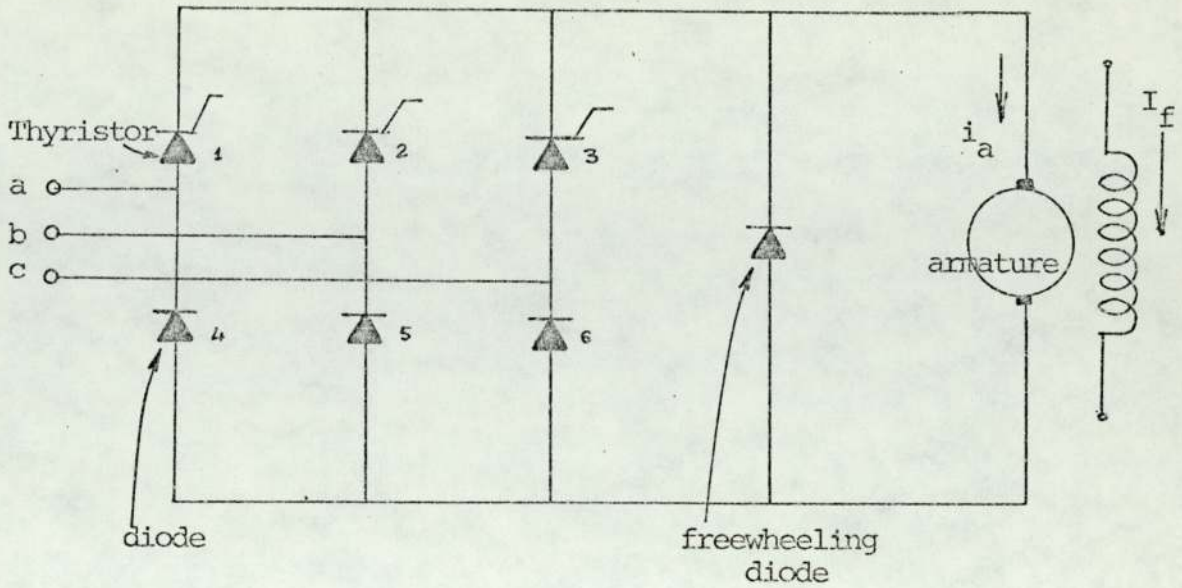


Fig. 3.13a Three Phase Incomplete Bridge Circuit

The remaining three elements of the bridge are diodes. The armature current has less ripple for small conduction angles. The incomplete bridge is usually operated with a free-wheeling diode to increase the conduction angle of the current for low speed, high torque operation. The difference between the instantaneous voltage V_m applied by the bridge to the motor and the armature voltage V_a is absorbed by the inductance and resistance of the armature circuit. The free-wheeling diode operates at the end of a current conduction period when the armature voltage attempts to reverse as the inductance discharges its energy. The operation of the circuit is shown in a sequence of waveforms for various firing angles in Fig. 3.13b.

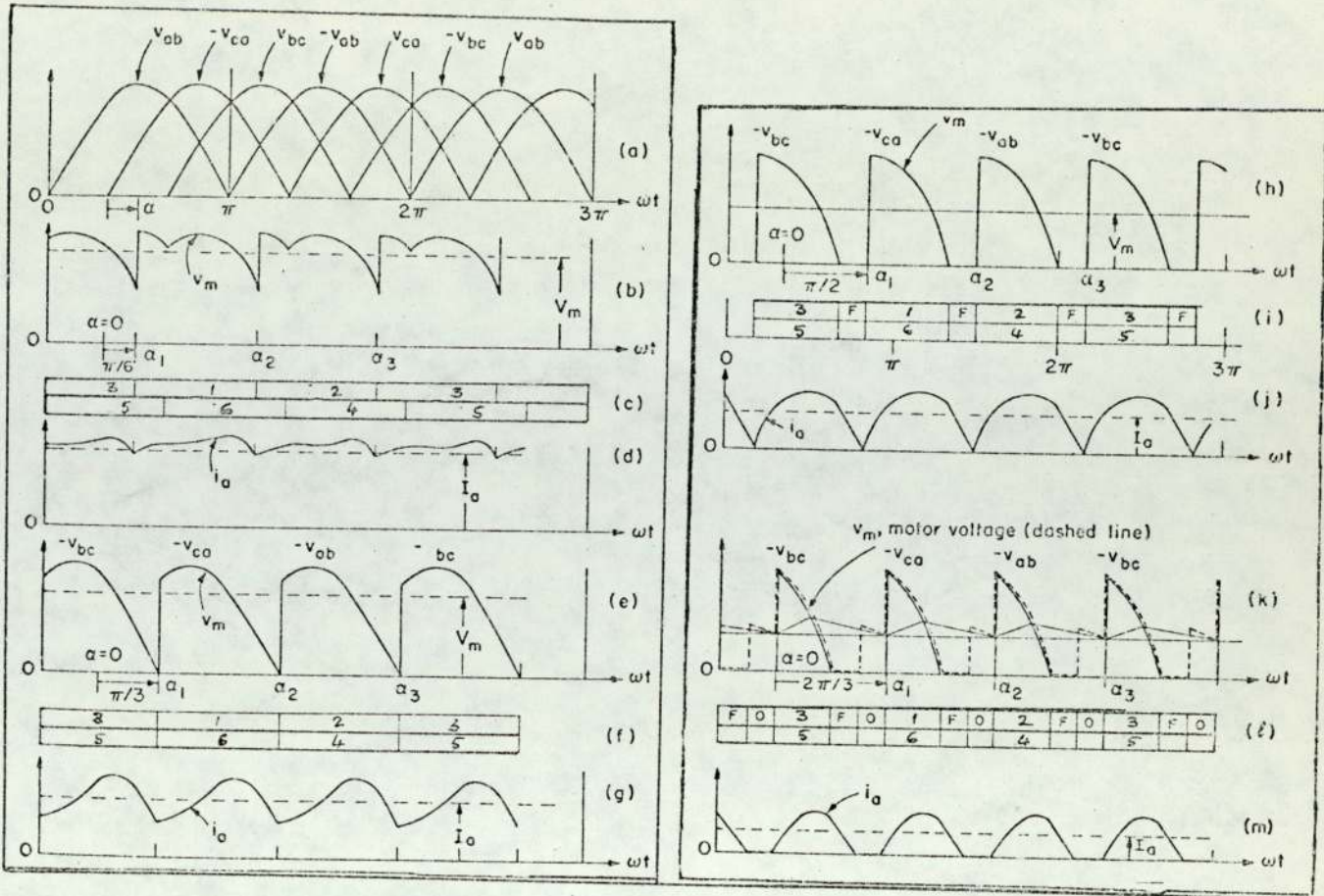


Fig. 3.13b Waveforms for the Incomplete Bridge Operation (Kusko¹)

The incomplete bridge requires a range of firing angle from $\alpha_1 = 0$ to $\alpha_1 = 180^\circ$ to obtain full control. The waveform up to about $\alpha_1 = 30^\circ$ is predominantly six pulse per cycle. From $\alpha_1 = 30^\circ$ to 180° , it is three pulse per cycle. The firing angles at which the current becomes discontinuous and the ripple amplitude depend upon the time constant $\frac{L}{R}$ of the armature circuit.

The complete bridge circuit is shown in Fig. 3.13c. It uses six thyristors and no diodes, except for free-wheeling operation. The thyristors are fired in sequence every 60° and the ripple is always six pulse per cycle. The complete bridge produces less ripple than the incomplete bridge, but

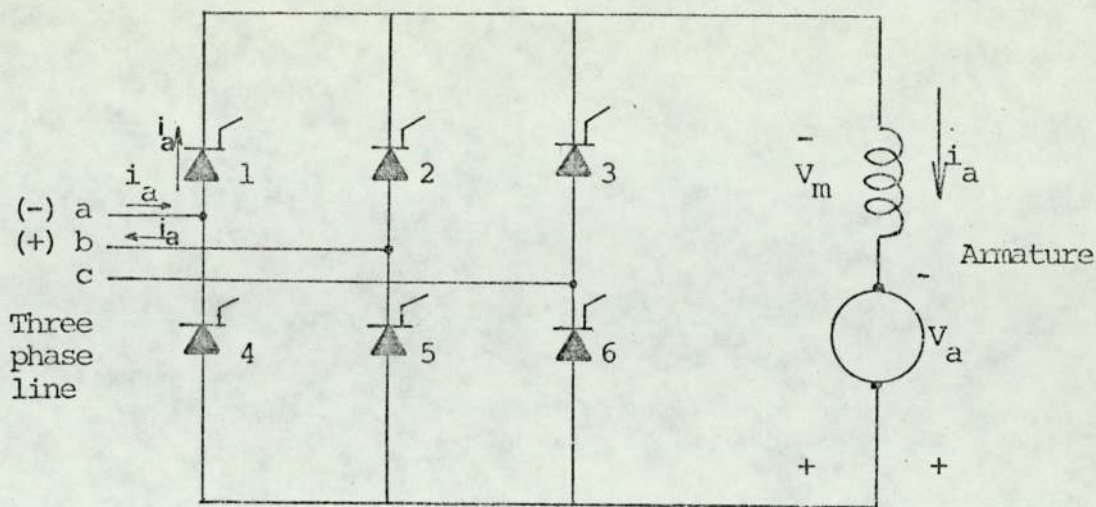


Fig. 3.13c Three Phase Complete Bridge

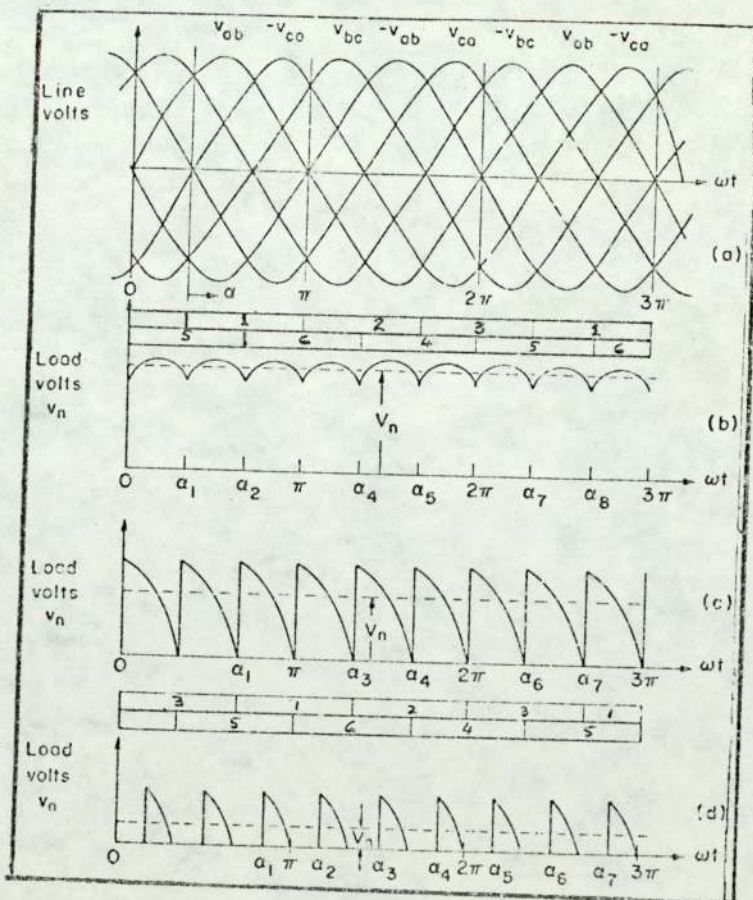


Fig. 3.13d Waveforms for Three Phase Bridge Rectifier with Resistance Load (Kusko.¹)

is primarily used where regeneration is required.

The operation of the complete bridge with a motor load and a freewheeling diode produces waveforms like those shown in Fig. 3.13d. For firing angles $\alpha_1 > 60^\circ$, the rectifier voltage becomes discontinuous and will be zero between pulses if the armature time constant keeps the current continuous through the freewheeling diode. If not, the armature voltage V_m will jump up to the generated voltage V_a when the freewheeling diode blocks as shown in Fig. 3.13b(k). The full range of control is obtained with a firing angle range of 120° . When the armature circuit has sufficient inductance to maintain continuous armature current, and no freewheeling diode is used, the armature voltage will go negative for $\alpha_1 > 60^\circ$ to balance the volt-time area of the inductance. The extreme case is shown in Fig. 3.13e(b) for $\alpha_1 = 90^\circ$. The average motor voltage V_m and the average current are zero. If the firing angle is retarded in the range $\alpha_1 = 90^\circ$ to 180° , the terminal voltage of the bridge will reverse and it will be capable of receiving power from a d.c. source of the same polarity. The extreme cases of rectifier operation at $\alpha_1 = 0$ and inverter operation at $\alpha_1 = 180^\circ$, are shown in Fig. 3.13e (a); the currents are shown in Fig. 3.13e(e) and (g). The direction of the current remains fixed but the voltages reverse.

So far the discussion has been directed towards the theoretical analysis of the armature current of

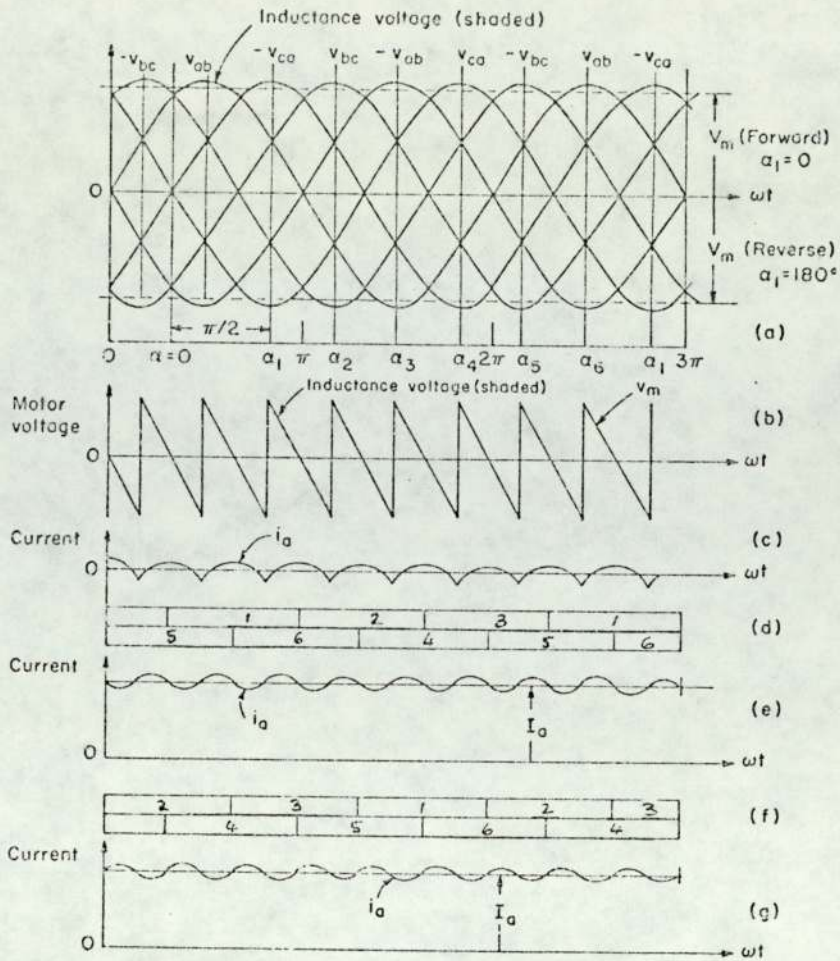


Fig. 3.13e Waveforms for Complete Bridge Operation (*Kusko¹*)

d.c. machines when supplied from various types of controlled rectifiers. It is seen that the armature current of a thyristor fed d.c. machine may be discrete pulses or a pulsating component, which is called 'ripple current', superimposed on the average d.c. level; this depends on the type of rectifier units used and the firing angle of the thyristor. The presence of harmonics in the armature current produces extra losses, eddy and hysteresis which increase heating, and not only that, the commutating ability of the motor becomes worse because the eddy currents produced by the a.c. component of the compole-circuit flux, particularly when the shell is

not laminated, damp the commutating flux and cause it to be phase displaced in time after the armature current. A survey of literature has to be continued to know the various ideas contributed by different investigators in tackling the eddy-current problem in d.c. machines carrying a.c. component of flux.

3.1.5 Lumped Circuit Impedance Representation for d.c. Machine

Ewing²⁸ has confirmed, from locked armature frequency response tests on a number of machines [redacted] that the frequency impedance locus corresponding to that of a simple series R-L circuit, does not hold good, [redacted] as [redacted] shown in Fig. 3.14. The deviation of the test result of the frequency impedance locus diagram from that of the simple RL circuit is due to the eddy currents generated in various parts of the windings and magnetic section of the motor. In fact, the equivalent circuit proposed by Ewing, shown in Fig. 3.15, is identical to that of a transformer with part of primary inductance shunted by a fictitious resistance representing the eddy current loss. R_a is the armature circuit d.c. resistance, and $(L_a + L_c)$ is the total armature circuit inductance. R_c is the fictitious shunt resistance which accounts for the eddy currents. The effect of the eddy current is to reduce the effective inductance and increase the apparent resistance. Analysis of the equivalent circuit shown in Fig. 3.15 and the test impedance measurements at a series of different

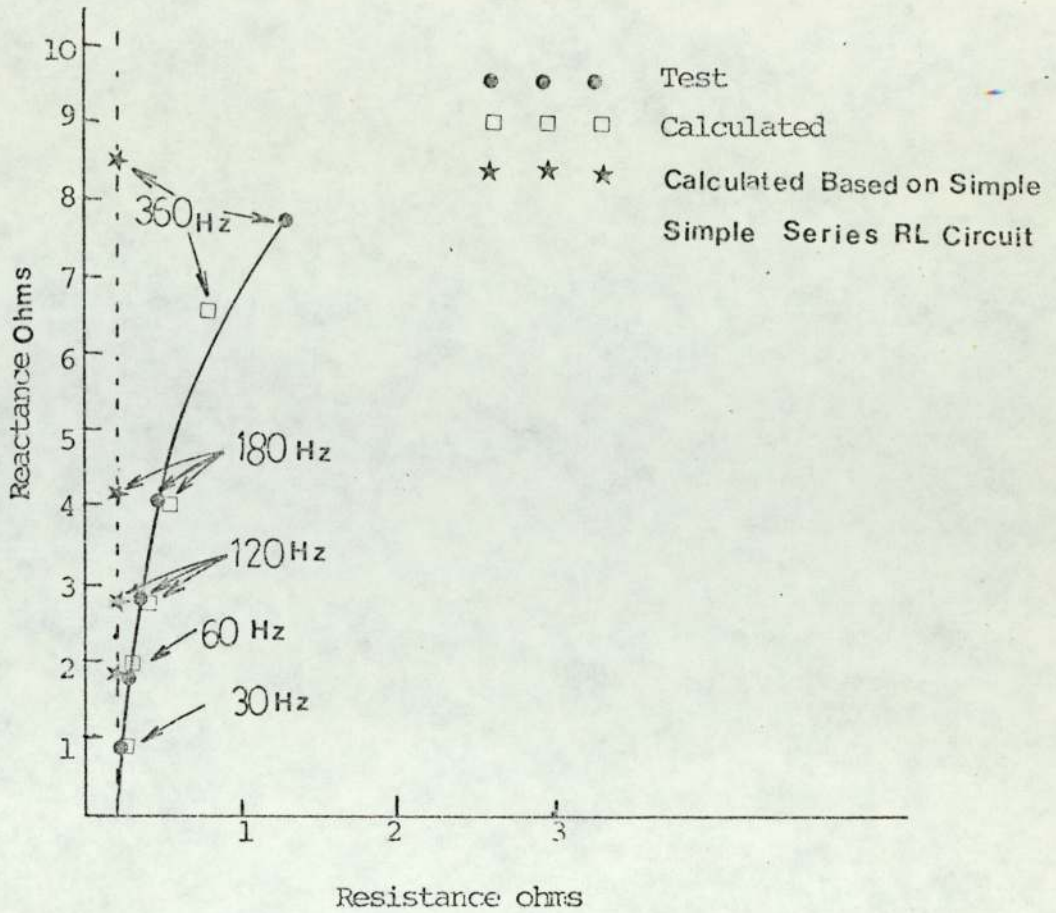


Fig. 3.14 Impedance Locus of d.c. Motor Using Locked Armature Test Data (Ewing.²⁸)

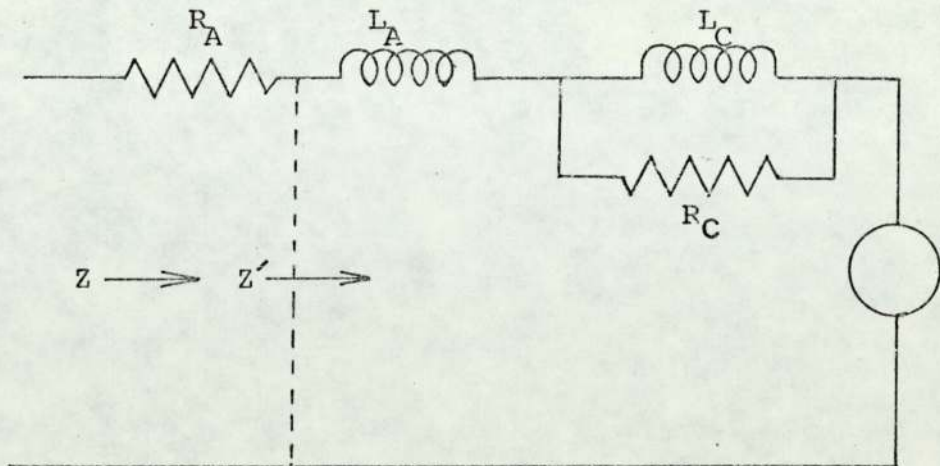


Fig. 3.15 Lumped Constant Equivalent Circuit (Ewing.²⁸)

frequencies for the test circuit, as shown in Fig. 3.16, with the shunt field excited at its rated ampere, enabled him to find out the values of

$$Z_c = \frac{R_c + jX_c}{R_c + j^2c}, R_c, (R_a + jX_a).$$

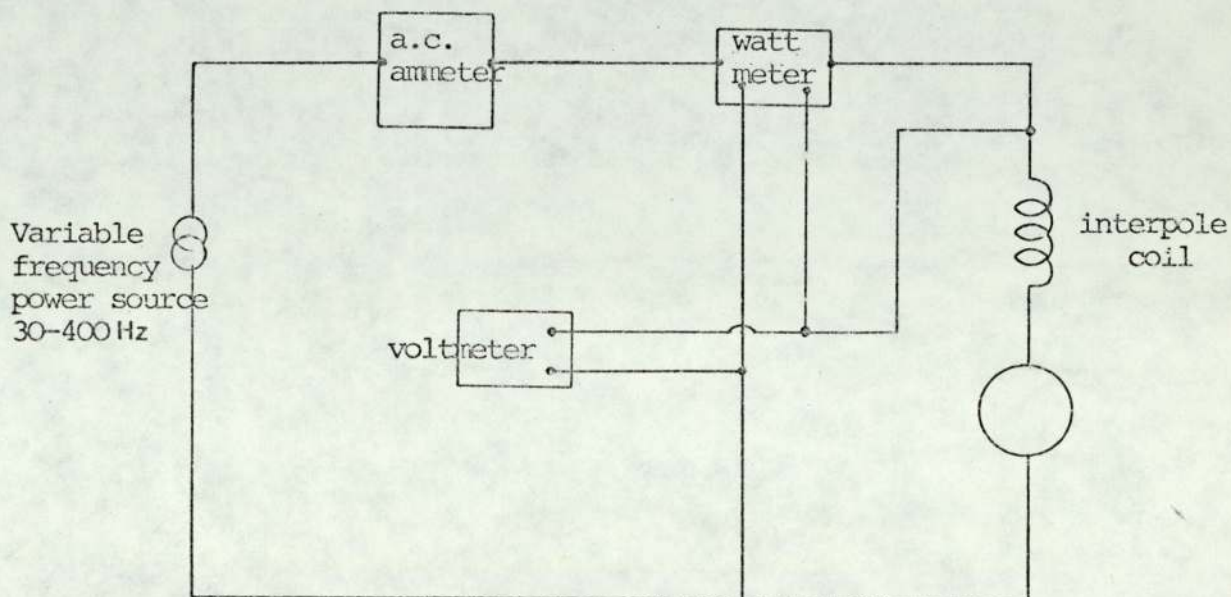


Fig. 3.16 Test Circuit (Ewing²⁸)

Calculated values of reactance and resistance have been plotted in Fig. 3.14 which show good agreement between theoretical and experimental results towards the lower frequency ranges (0 to 120 Hz). Ewing's method of lumped circuit representation of d.c. machine has been used by Tsivitse et al²⁹ for calculation of eddy current loss in d.c. machine operating on rectified a.c.

Conclusion and Discussion of Ewing's Work

The presence of eddy current in the solid shell and

other magnetic parts of the machine cause a change in the impedance of the energizing winding. Eddy currents also set up ohmic losses which must be drawn from the supply. An outside observer, with access only to the terminals of the winding thus sees an apparent increase in resistance. Secondly, the flux-carrying capacity of the magnetic parts of the machine is reduced by eddy currents and there is thus a reduction in the inductance of the winding. This change in the impedance of the winding is referred to as reflected impedance. The total complex impedance is given by

$$Z_o = R_o + j\omega \frac{\psi_o}{I_o} \quad 3.26$$

The flux linkage ψ_o is complex, with the result that the last term in equation 3.26 yields a real part which is reflected resistance (R'_o). This R'_o is R_c in Ewing's analysis. The value of Z_c which Ewing found out by semi-analytical and semi-experimental methods, depends on the machine dimensions and the winding configuration.

Hence, Z_c has to be calculated for each machine if the machine dimensions and windings are different. At the end of his paper, Ewing suggested that the improvement of simple R-L series lumped constant representation of the d.c. motor can be made by adding a shunting resistor around a portion of the circuit inductance. The value of shunting resistor has not been given in his paper, and nothing has been discussed about the calculation of reduction in a.c. flux and its phase

shift from the armature current due to eddy current, which seems to be more important from the commutation point of view. However, the lumped circuit parameters have first to be derived from the field theory, (i.e. distributed parameter) approach.

3.1.6 Magnetic Circuit of d.c. Machine and the a.c. Component of the Commutating Flux

Voltages produced in the commutating coil of a d.c. machine supplied from controlled rectifier units will be not only those which have already been discussed in the main introduction at the beginning of the thesis, for the d.c. machine operating on smooth voltage supply, but also some extra a.c. voltages originated from time varying component of current. These extra alternating emfs are -

- (1) \hat{E}_r , the alternating component of the reactive emf.
- (2) \hat{E}_t , the transformer emf due to the a.c. component of the mainpole flux.
- (3) \hat{E}_c , the a.c. emf due to the alternating component of commutating flux.

The resultant unbalanced extra a.c. emfs in the commutating coil will be the vector addition of three emfs mentioned above.

$$\Delta \hat{E} = \hat{E}_r + \hat{E}_c + \hat{E}_t \quad (3.27)$$

Estimation of these extra alternating emfs has been discussed in the details by Zolotariov³⁰ and Skobelev³¹.

According to Skobelev and others E_r is proportional to the amplitude of the armature ripple current and

$$E_t = jK_2 \phi_m e^{j\theta} \quad 3.28$$

$$E_c = K_3 \phi_c e^{j\phi} \quad 3.29$$

where

$$K_2 = 2\pi f N_t \quad 3.30$$

$$K_3 = \frac{2N_t V_a}{\tau_c} \quad 3.31$$

Skobelev obtained the reluctances in various parts of the magnetic circuit for the main field a.c. flux and the a.c. flux produced by the resultant effect of armature mmf and compole mmf, in terms of machine dimensions. Then the total reluctance Z_m of alternating components of the main field flux ϕ_m is calculated from its equivalent circuit, and

$$\phi_m = \frac{F_m}{Z_m} (\angle \psi), \text{ where } F_m \text{ is the a.c. component of}$$

mmf of the main field and Z_m is the equivalent reluctance of the equivalent circuit, Skobelev considered. The estimation of ϕ_c , the a.c. component of flux in the zone of commutation which is important from the commutation point of view, is rather complicated because it is resulted from ^{two} alternating mmfs, (armature F_a and the commutating pole F_{cr}). The a.c. flux in this case is comparatively weak.

The already known equivalent circuits for the steady

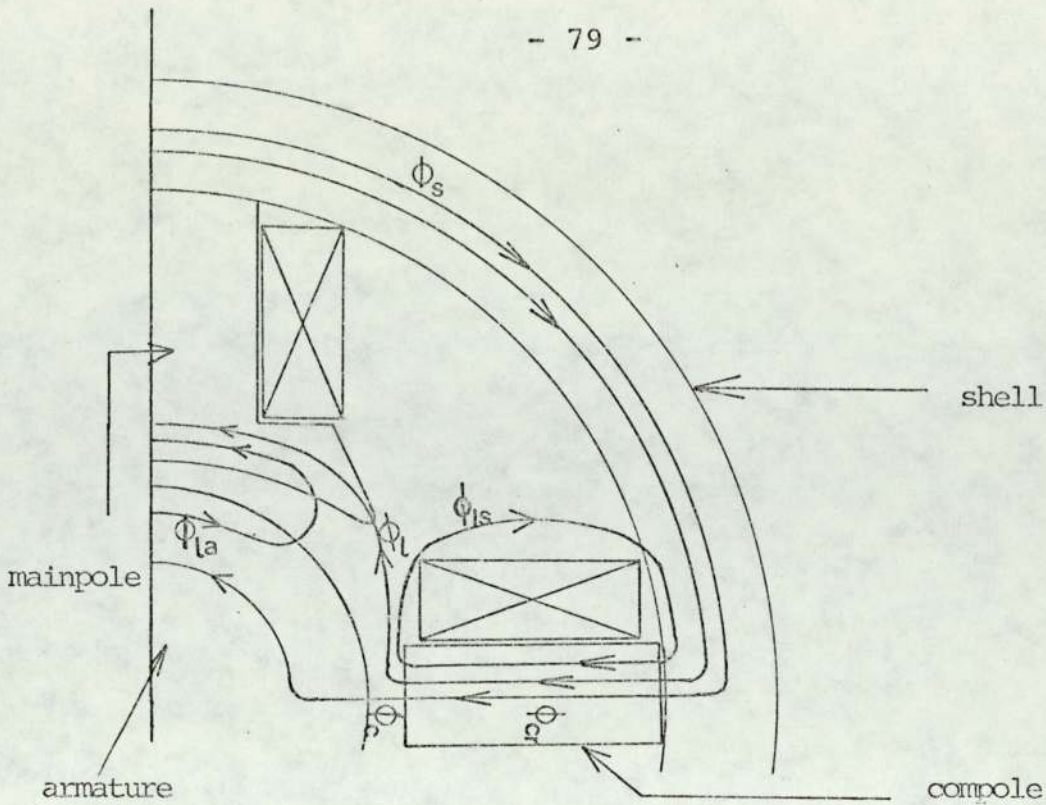


Fig. 3.17 The a.c. Component of the Fluxes which are made up of the Magnetizing Forces of the Armature and of the Compoles.

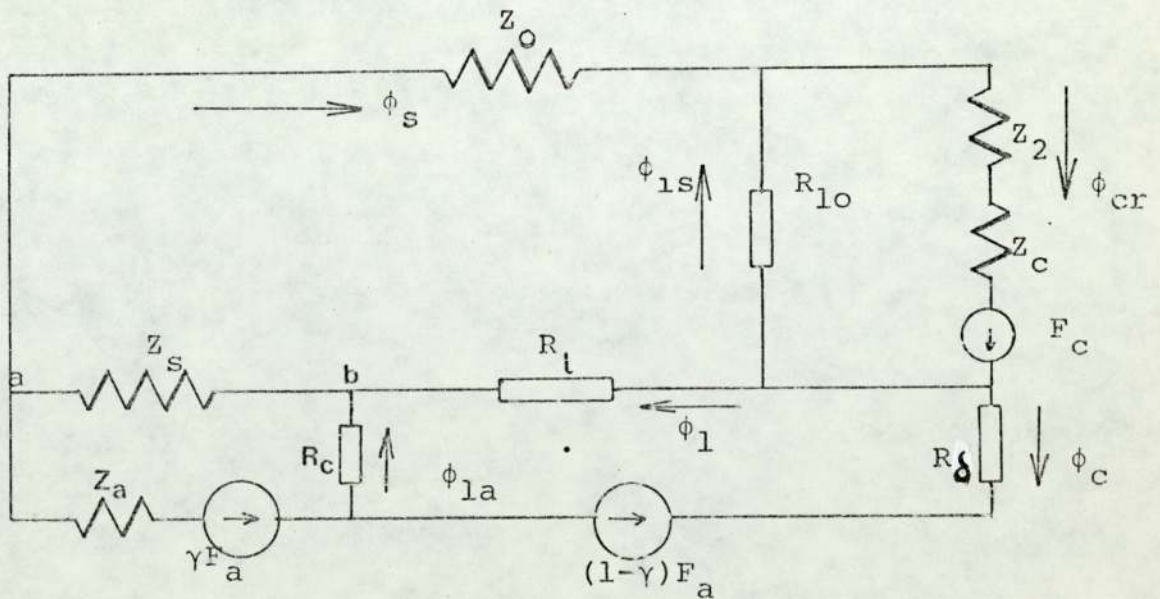


Fig. 3.18 Skobelev's Complete Equivalent Circuit for the a.c. Component of Comm-zone Flux

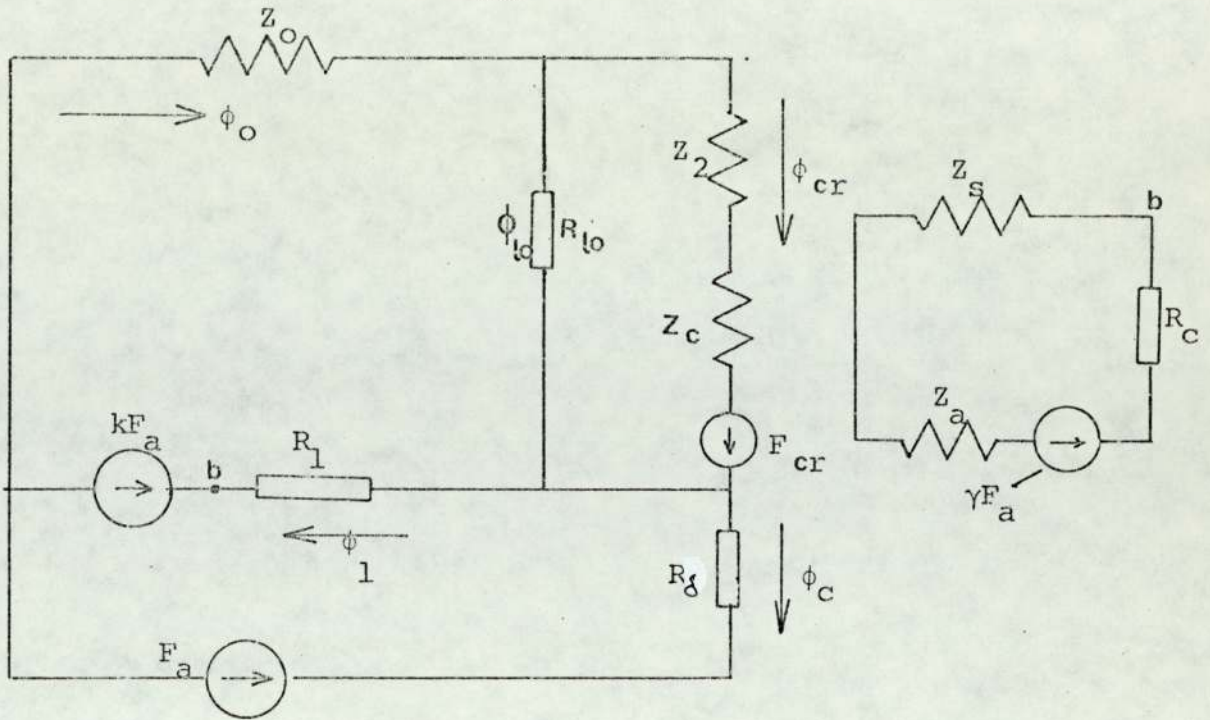


Fig. 3.19 Skobelev's Approximate Equivalent Circuit of Fig. 3.18 to Calculate Parameters

d.c. flux resulted from the compole and armature mmfs has been modified by Skobelev³¹ for the case when a.c. flux is considered and it has been shown in Fig. 3.18 and 3.19. The a.c. flux path in the machine for which the equivalent cct has been drawn, is shown in Fig. 3.17. Using the main and auxiliary equivalent ccts it can be shown that a.c. commutating flux due to the compole a.c. mmf alone will be

$$\phi_{c1} = \frac{F_{cr}}{A[R_{\delta} + Z_{OB}] + Z_{1B}} \quad 3.32$$

and that due to armature alone will be

$$\phi_{c2} = \frac{F_a \left\{ 1 + (1 - k) \frac{D}{R_l} \right\}}{BD + R_{\delta}} \quad 3.33$$

where

Z_o = the reluctance of the frame

Z_c = the reluctance of the core of the compole

Z_2 = the reluctance of the second airgap under the compole

R_δ = the reluctance of the main air gap under the compole

R_1 = the reluctance of the leakage at the shoes of the
mainpole

R_{1o} = the reluctance of the leakage at the frame

Z_a = the reluctance of the armature iron

Z_δ = the reluctance of the shoes of the main poles

R_c = the reluctance of the gap at the edge of the main
poles

$$Z_1 = Z_2 + Z_\delta$$

$$A = 1 + \frac{Z_1}{R_{1o}}$$

$$B = 1 + \frac{R_\delta}{R_1}$$

$$D = Z_o + \frac{Z_1}{A}$$

So the resultant a.c. flux in the interpolar region would be the sum of ϕ_{c1} and ϕ_{c2} by the principle of superposition. In his analysis reluctances in different parts of the magnetic circuits have been calculated in terms of machine dimensions. The net effect of eddy current induced in the solid parts of the magnetic circuit due to the pulsating component of a.c. flux, results in an a.c. reluctance which is complex in nature, greater in magnitude than the d.c. reluctance and causes the flux to lag behind the mmf.

It is believed that out of all the reluctances considered in the equivalent cct shown in Fig.3.18 for the a.c. component of flux, theoretical estimation of the value of Z_0 which is the reluctance offered by the shell is the most difficult task. From the survey of literature so far as the author's knowledge goes, it is evident that there is a dearth of published work dealing with the behaviour of eddy currents induced in the solid shell carrying a.c. component of flux, and the evaluation of complex a.c. reluctance offered by the shell. Skobelev's theoretical approach with constant permeability and assumed distribution of the eddy currents in the shell (see Fig. 3.20) seems to be the only work that has been done so far in tackling the shell eddy current problems.

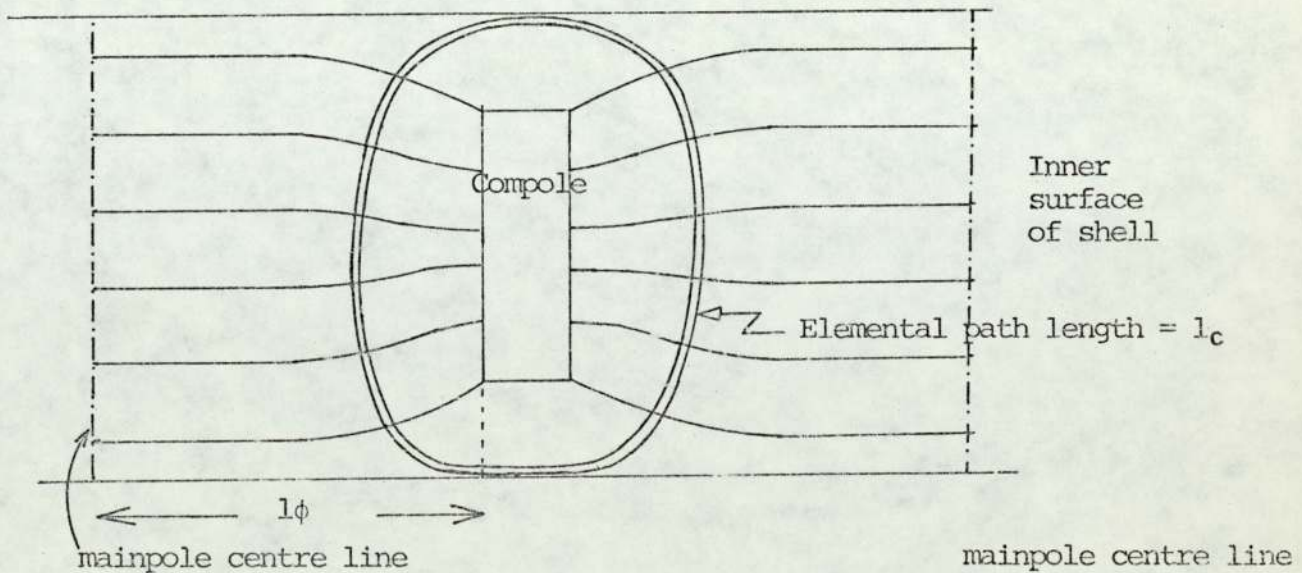


Fig. 3.20 A.c. Flux and Eddy Current Distribution on the Inner Surface of the Shell

(Skobelev³¹)

In this analysis the eddy currents and a.c. flux were assumed to be confined within the inner surface of the shell to a depth given by

$$\delta = \sqrt{\frac{2\rho}{\mu_r \mu_o \omega}}$$

He and others have shown shell permeance/pole =

$$\left[\sqrt{\frac{\omega}{2\rho\mu_r\mu_o}} \int_0^{l\phi} \frac{dx}{l_c} \right] (1 + j)$$

The eddy current path l_c was chosen to be

$$l_c = (\text{Compole perimeter} + 2\pi x)$$

SKobelev approximated the total length of the four circular corners of the eddy current paths by an equivalent length of $2\pi x$.

Since the shell flux density has a mean d.c. level the relative permeability must be given appropriate incremental value, taking into account the different flux levels in the two parallel paths of the shell. In connection with the effect of superposed steady field on the permeability in mild steel Ramsden's³² work on 'loss in solid poles of synchronous machines on load', should be mentioned. He discussed in detail various types of permeability particularly the incremental permeability and superposed a.c. d.c. flux density in the iron. Ramsden concluded that the loss in mild steel can be calculated accurately by a linear theory if the steady field strength is greater than the alternating field strength, otherwise a non-linear theory which allows for unsymmetrical

hysteresis loops is required for strong alternating fields. He developed a limiting non-linear theory but not tested.

From the survey of literature it has been gathered that a thorough investigation both experimental and theoretical has to be carried out.

- (1) to examine the validity of Skobelev's and others assumptions about a.c. flux and eddy current distribution in the shell.
- (2) to study the behaviour of the induced eddy currents towards the shell a.c. flux.
- (3) to study the variation of permeability of the shell material, which is mild steel, with the mean d.c. flux level.

A specially designed d.c. machine has been built and instrumented heavily to carry out the experimental work as suggested above. The experimental set up and test results have been discussed in detail in Chapter 4, 5 and 7. Chapter 6 has been devoted to the theoretical investigation of the shell eddy currents, based on the experimental evidence.

CHAPTER 4

DETAILS OF TEST MACHINE AND INSTRUMENTATION

4. INTRODUCTION

Detailed descriptions of the special test machine, experimental set-up, search coil installation and lay out of current density probes in different parts of the magnetic circuit of the test machine, and various measurement techniques have been given in this chapter. A few preliminary experiments such as magnetic balancing, brush setting and details of superimposed a.c. - d.c. supply to the compoles have also been discussed.

4.1 DESCRIPTION OF THE TEST MACHINE

The test machine is a 4-pole d.c. shunt motor with laminated interpoles and mainpoles. Rating of the test machine is 8 k.w., 420 volts, 20 Amps. line current, 20 Amps. armature current, speed 1750 rev/min.

Details of the Windings

Armature Winding


Two layer, wave winding.

Number of coils = 29

Number of Com segments = 87.

Number of sections per coil = 3.

Number of turns per coil = 6.

Gauge of wire - 1.5 x 1.0 mm²:  cross section of wire.

36 conductors per slot.

Total number of conductors = 36 x 29.

DETAILS OF DIFFERENT PARTS OF THE EXPERIMENTAL MACHINE

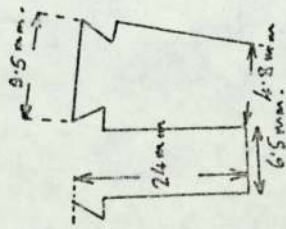
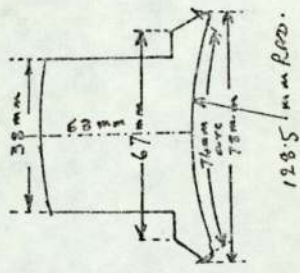
ARMATURE	MAINPOLE	COMMUTATOR	BRUSHES
<p>Diameter = 155 mm Core length = 135 mm Active core length = 122 mm Number of slots = 29 Tooth pitch = 16 mm</p> 	<p>Pole pitch = 122 mm Pole arc = 74 mm $\frac{\text{Pole arc}}{\text{Pole pitch}} = 60.7\%$ Mainpole air gap at its $\phi = 2.5$ mm Average mainpole air gap = 2.9 mm</p> 	<p>Diameter $D_k = 116$ mm Active length $L_k = 69$ mm Number of segments = 87</p>	<p>Number of brush arms = 4 Brushes per spindle = 2 Size of brush = 10×20 mm² Quality SA 45</p>

TABLE 4.1

Commutator pitch = 1-39.

Coil span - slot 1 to slot 8.

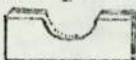
$$\frac{\text{Compole ampere turns}}{\text{Armature ampere turns}} = 1.44$$

Armature winding resistance = 1.1 Ω when cold and 1.45 Ω when hot.

	Mainpole winding	Compole winding
Number of turns/pole	2700	120
Length of mean turn	42.8 cm	37.5
Section of conductor	1964 mm ²	6.98 mm ²
Resistance cold/hot	407 Ω 533 Ω	.446 Ω .55 Ω

A specially designed frame which is a solid thick cylindrical shell as shown in Fig.4.1 has been used for the test machine. The dimensions of the shell are shown in Fig.4.1. The shell material is mild steel (BS 4360 Grade 43A, which is commercially known as EN3).

4.2 DETAILS OF THE TEST RIG

Armature, mainpoles, compoles and all other components were dismantled from the frame of the original machine supplied by Parsons and Peebles, Ltd. and they were fitted to a specially designed solid shell shown in Fig.4.1. The cylindrical solid shell with all the poles and interpoles after being fitted in the right position, was held tight in between two 20 mm thick  shaped bakelite

holders with the help of long bolts and spacers as shown in Fig. 4.2. Two adjustable steel keys were fitted up with screws at the base of the bakelite holder so that the solid shell with all the poles fixed on could slide along the key way of a steel bed. Two end brackets fitted with bearing boxes were used to hold the armature *parallel* to the bed plate.

It was checked carefully to make sure that the armature would run freely at its supporting ends. The brush holder was fixed to one of those end brackets. Special arrangement was made for alignment of the axis of the armature with that of the stator bore. The armature was placed symmetrically along the bore of the machine, and at that position the end brackets and the shell were clamped *to* the steel bed. The test rig and experimental set up are shown in Figs. 4.3 and 4.4a, 4.4b, 4.4c.

4.3 INSTRUMENTATION OF THE EXPERIMENTAL MACHINE

4.3.1 Shell Loop Search Coils

To measure the shell flux, 10 single turn search coils were installed around the shell surface, as shown in Fig. 4.5, so that the search coil planes were perpendicular to the direction of shell flux. 4C SWG lewmex wires were used for making these search coils. The search coils were stuck permanently on the shell surface with permabond. A thin piece of sponge was used to protect those search coils

sitting just under the root of the mainpole because they might get damaged due to the excessive pressure offered by the mainpole back surface when it was bolted with the shell. The possibility of damaging the insulation of the search coils at the sharp edge of the shell was overcome by making small 'V' notches at the edges with a triangular file. The search coil leads were carefully twisted together to avoid 'pick up' and soldered to the terminal board placed far away from the influence of the magnetic field of the machine.

4.3.2 Array of Search Coils in the Airgap at the Back of the Compole

These search coils were installed to measure the a.c. and d.c. flux density distribution in the second airgap at the back of the compole and the leakage flux distribution along the axial and peripheral directions at the edges of the compoles. Search coil arrangement shown in Fig.4.6 was suggested because of the symmetrical flux distributions about X and Y axes on the compoles (see Fig. 4.6). The difficulty in laying a dense array of search wires on the inner surface of the cylindrical shell gave rise to an idea of installing them on a thin plastic plate of thickness 0.8 mm.

First of all about 0.05 mm deep straight line scratches, as shown in Fig.4.6 were made by a scriber on the thin plastic plate, and then 42 SWG wire pushed into those straight

grooves and stuck with permabond. All search wires were shorted by a copper path at one end and the other ends were closely twisted together one after another and then taken out and soldered at the terminal boards. The two plastic plates on which the search coils were installed as shown in Fig.4.5, were then fixed to roots of the interpoles with the help of double-sided sellotape.

4.3.3 Tooth Pitch Search Coil

Tooth pitch d.c. flux distribution along the armature surface due to the interpoles excited only which has been discussed in Chapter 2, was experimentally obtained by the search coil shown in Fig. 4.7. The search coil comprised of rectangular single turn coil glued on the armature surface with permabond. The length of the search coil is equal to that of the armature core and its width is equal to the tooth pitch. The search coil leads were carefully twisted and brought out to the terminal board.

4.3.4 Search Coils Around the Core of Interpole and on the Sideface of the Compole

These search coils were installed to measure the total flux through the compole and side leakage flux. They are shown in Fig. 4.8a and 4.8b.

4.3.5 Current Density Probes on the Surface of the Shell

The magnitude of the eddy current density in the surface of the solid shell was estimated by measuring the voltage difference between two points 5 mm apart on the surface. The probes used to measure the voltage were formed by welding constantan wires at those two points. The two leads of the current density probes were then closely twisted together to avoid pick up. A 'Sipican' welding machine was used for welding the probe wires on the surface of the shell. The welds between constantan wires and the shell surface were obtained by passing a pulse of energy from a capacitor discharge unit through the relatively high contact resistance between them. Both the amplitude and time of the pulse could be controlled. Successful welds were obtained by trial and error as the contact resistance is dependent on the pressure applied and the cleanliness of the surface. The current density probes used were all of 5 mm pitch; this was considered to be the minimum allowable distance for reasons of accuracy, both in defining the length of a probe and in obtaining a voltage signal greater than the pick up voltage and noise level of the amplifiers used. Bearing in mind that the nature of the shell flux is symmetrical about its central plane, AA_1 in Fig. 4.9a, a number of current density probes have been welded on the shell surfaces (inner, side, and outer) over a peripheral distance $(\lambda/2)$, the $\frac{1}{2}$ of the interpole to that of the main-pole. The location of the current density probes are shown in Fig. 4.9 and Fig. 4.9a.

4.3.5.1 Calculation of Surface Current Density from the Probe Readings

If the amplitude of the fundamental component of the voltage signal obtained from the J-probe terminals is V volts then the fundamental component of the mean value of the current density over a distance, l , is

$$J = \frac{V}{\rho l} \quad 4.1$$

where ρ is the resistivity of the shell material and $l = 5\text{mm}$. Current density J at any point can be split up into two mutually perpendicular component vectors J_x and J_y such that magnitude of the current density

$$|J| = \sqrt{J_x^2 + J_y^2} \quad 4.2$$

and the vector J makes an angle θ with J_x , as shown in Fig. 4.10, given by

$$\theta = \tan^{-1} \left(\frac{J_y}{J_x} \right) \quad 4.3$$

Equations 4.2 and 4.3 are applicable when J_x and J_y have been measured in x and y directions by current density probes of small pitch.

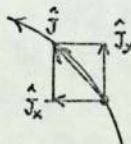


Fig. 4.10 Resolution of J Vector in X and Y Direction

4.4.1 MEASUREMENT TECHNIQUES

4.4.1.1 Flux Meter

Non-varying steady flux was measured by the method of reversals using a 'Norma' ballistic flux meter. The instrument was critically damped through a precision decade resistance in series with the input terminals. According to the instruction manual the input terminal resistance should be always 30 ohms. The calibration of the fluxmeter was checked against a 'Hibbert' magnetic standard and found to be within 1% of the standard over the entire range.

4.4.1.2 Measurement of a.c. Flux

The average, r.m.s. and peak value of the emf induced in the search coils were measured using a Bruel and Kjaer valve voltmeter (Model No.2409). The instrument inverts every other half cycle, integrates over a period of time and displays the average value on a scale. The internal calibration of the instrument was used. The instrument should be warmed up for at least 30 minutes before taking any reading. When the measured value of peak to r.m.s. ratio of the voltage signal from the search coils was within the limit $1.414 \pm .02$, the average fundamental a.c. flux embraced by the search coil was calculated by simply dividing the average value of the induced voltage by angular frequency.

In the case of distorted voltage signal from the search coil, integrator circuit of type 'O' plug in unit of a C.R.O. model (533A) was used to integrate the $\frac{d\phi}{dt}$ signal in order to

obtain the flux wave. Then the amplitude of the fundamental and other harmonics of the flux wave were measured with a harmonic analyser. The integrator circuit which was used for experimental measurements have been described below.

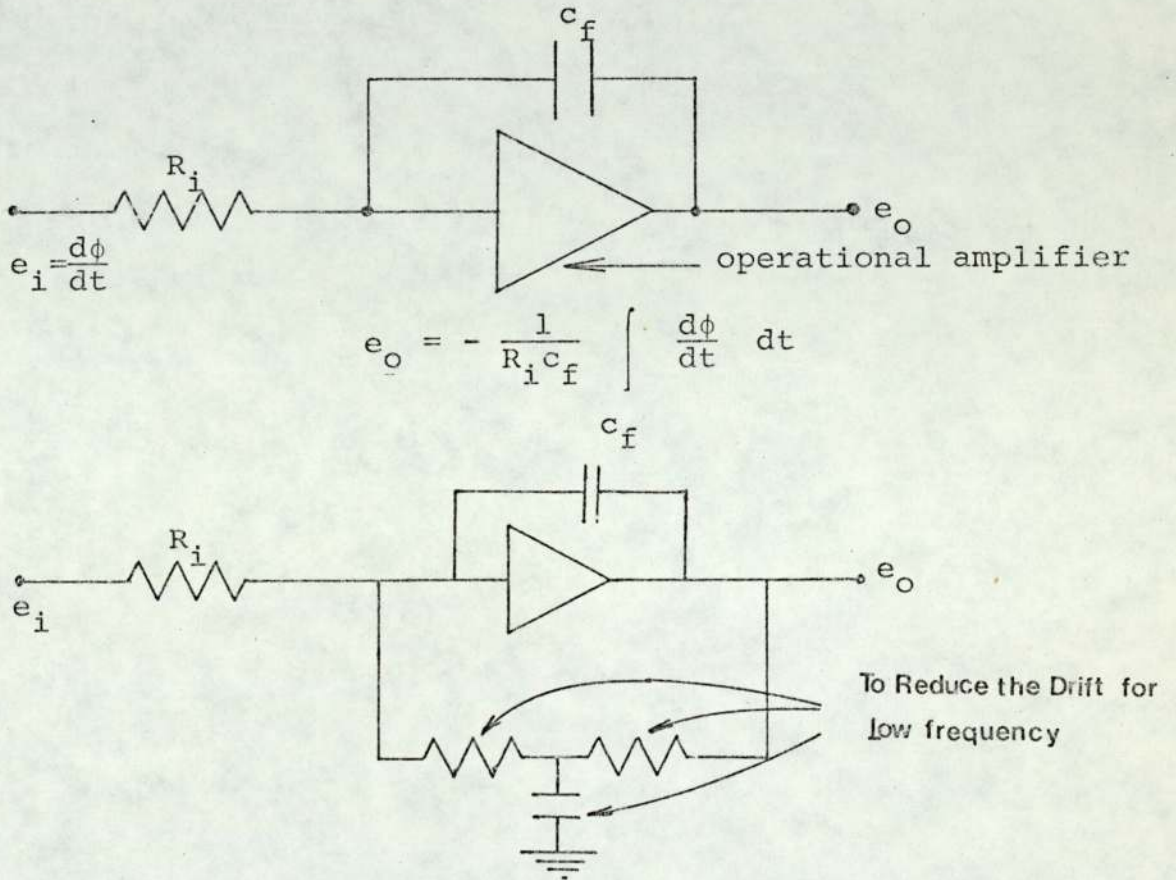


Fig. 4.11 Integrator Circuit

The output voltage from the integrator is inversely proportional to the time constant of the feedback network, and directly proportional to the integral of the input voltage. A good starting point in any integration application is to make the $R_i C_f$ time constant approximately equal to the period of the signal to be integrated. The basic circuit integrates not only a.c. component of signals but the d.c. components and drift as well. To prevent this condition when

integrating repetitive signals an integration low frequency rejection circuit is incorporated, with the operational amplifier. The integrator circuit was checked in the following manner. A purely sine wave from a precision signal generator was applied as an input signal and the output signal was 90° out of phase with respect to input one.

When the voltage signals $(\frac{d\phi}{dt})$ from the search coils or the signal from the current density probes were too low to be measured, a Burr Brown operational amplifier together with a filter circuit which minimises the noise, was used to amplify the signal. The amplified signal was then integrated or measured directly by Bruel and Kjaer or Solartron digital voltmeter. The maximum magnification factor of the Burr Brown amplifier was 10^3 . Thus the flux measured

$$\phi_{av} = \frac{R_i C_f}{A} e_{o_{av}} \quad 4.4$$

Where A is the amplification factor of the amplifier. Amplified signals were always checked on the oscilloscope screen to confirm that the amplified signal was not corrupted with noise.

4.5.1 HARMONIC ANALYSIS

The oscillograms of the voltages from the current density probes and of the flux wave and $(\frac{d\phi}{dt})$ wave were analysed when the peak to r.m.s. ratio was not close to 1.414. Standard

Library programme in Fortran IV language was used for the harmonic analysis. The ordinates of the waves were fed to the Digital PDP9 computer as input data. The computer programme has been given in the appendix(4.COM.PRO.5).The average values of the fundamental and higher harmonics obtained from the computer results were compared with the corresponding measured ones from the harmonic analyser as a cross check.

4.6 PRELIMINARY EXPERIMENTS

4.6.1 Experiments to Check the Magnetic Balancing in the Test Machine

Magnetic unbalancing in the machine might cause the major upset in the experimental results in the later stage. Magnetic unbalancing in the machine might arise due to the following reasons:

- (1) If the armature axis does not coincide with the axis of the stator bore.
- (2) If all the second airgaps under the compoles are not equal.
- (3) If the distances between one pole tip to the next pole tip are not equal.
- (4) If the central planes of the poles do not coincide with the shell axis, etc.

The following tests were carried out to confirm that this test machine was magnetically balanced. All the brushes were taken off and a.c. excitation (50 ω) was applied to

the compole windings connected in series. There should not be any flux going through the core of the main pole in radial direction, if the machine was magnetically balanced.

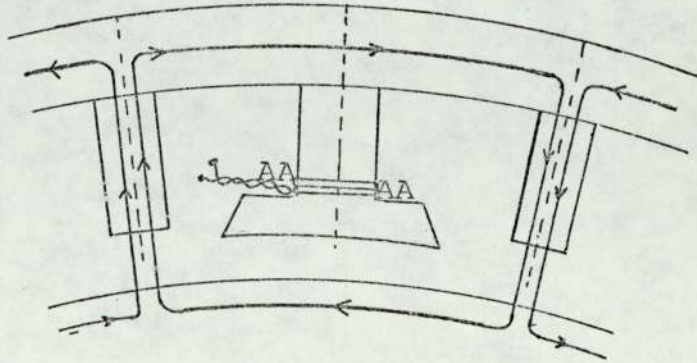


Fig. 4.12 Flux Path when the Machine is Magnetically Balanced

Some voltage was produced indeed in the search coil AA, proving the magnetic unbalancing within the machine. All possible sources for unbalancing were checked and rechecked until there was no voltage in the search coil with compoles excited from the a.c. supply. Thus the machine was magnetically balanced. At this condition it was decided to dowel the mainpoles because it would be necessary to take the main poles off from the shell to do some experiments at the later stages.

4.6.2 Brush Setting in the Magnetic Neutral Axis

The following test was performed to obtain the magnetic neutral axis. The armature was excited through the brushes from a.c. 50 \sim cycles supply. The voltage induced in one of the interpole windings was fed to the oscilloscope. The brush gear was slowly turned until the

peak of the voltage wave reached its maximum value, and this was the magnetic neutral position which was marked on the end bracket.

4.7 MEASUREMENT OF ELECTRICAL CONDUCTIVITY OF THE STEEL USED FOR SHELL

Electrical conductivity of the mild steel (BS 4360 Grade 43A or EN3) was not available in any engineering material handbook so a test was performed on a solid cylindrical EN3 material, 1" in diameter and 10" in length. The electrical conductivity σ was found to be

$$\sigma = 0.085 \times 10^8 (\Omega.m)^{-1}$$

or $\rho = 11.81 \times 10^{-8} \Omega.m$ at $40^\circ C$

4.8 SUPERIMPOSED a.c.-d.c. SUPPLY

4.8.1 Background to the Superposed a.c.-d.c. Supply

At this stage it is worthwhile to discuss advantages and disadvantages of several different circuit arrangements which have already been used for the superposition of a periodic field on steady d.c. field. The exciting winding can be supplied from d.c. and a.c. supplies which are connected either in series or in parallel. The circuits for both the cases have been shown in Fig. 4.13.

Both a.c. and d.c. supplies can be controlled independently. The capacitor C which is in series with a.c. supply blocks the d.c. current which otherwise flows through the a.c.

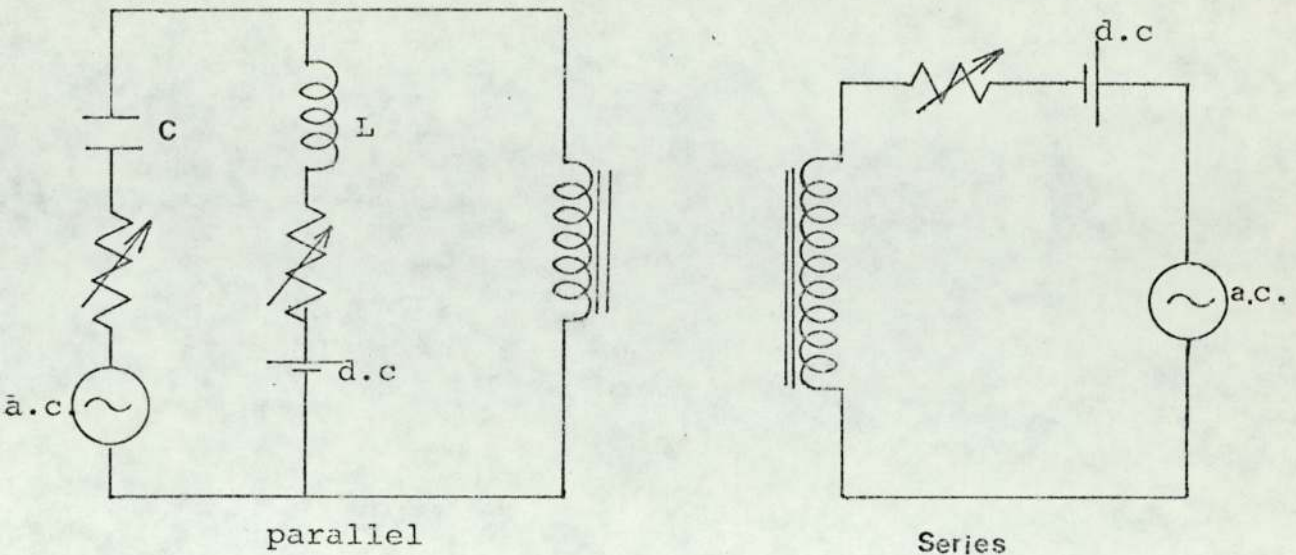


Fig. 4.13

supply. Similarly, a.c. is restricted from flowing through d.c. supply by large inductance 'L'. The impedance of the series blocking capacitor (C) may cause distortion of the a.c. voltage if the sinusoidal flux is required. If sinusoidal current is required extra series impedance may be added in addition to C. To choose the value of the blocking inductance L is critical because if a.c. current goes through the d.c. supply it may cause harmonic losses in the d.c. supply and consequent distortion of the winding current. The parallel circuit is recommended by B.S.933:³³
and was used by Carter and Richards³⁴, Mondal et al.³⁵, and Choudhury et al.³⁶

For sinusoidal current, the series circuit is more suitable, as shown in Fig. 4.13. A large air cored reactor

is used according to the level of a.c. voltage available. The air cored reactor should be used to avoid a decrease of inductance by the d.c. current and extra iron losses. The main trouble with this circuit is that there is always some interaction between the a.c. and d.c. supplies, and both d.c. and a.c. must flow through the current and power measuring instruments. The series circuit with modifications to reduce the series impedance and interdependence of a.c. and d.c., was first used by Chubb and Spooner³⁷. Charlton and Jackson³⁸, Edgar³⁹, Sims and Clay⁴⁰ and others, also used the same circuit with some modifications in their experiments.

Independent control and measurement of the a.c. and d.c. is possible by two windings circuit as shown in Fig. 4.14.

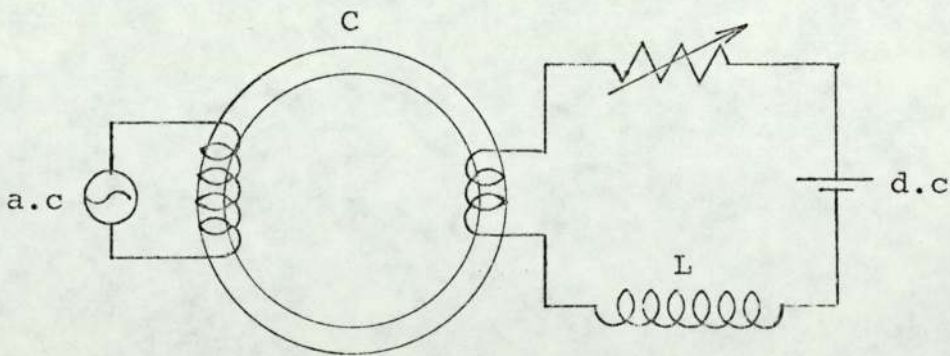


Fig. 4.14

A.c. winding pushes the a.c. flux while the d.c. flux is also produced in the same core by the d.c. winding; thus the coexistence of a.c. and d.c. flux is possible. A

resistor or air cored reactor can be inserted in a.c. circuit for the sinusoidal current. The main disadvantage is that a large air-cored reactor 'L' is required in the d.c. circuit to limit the induced alternating current which would cause additional losses and contribute to the periodic field. This circuit was first used by Rosenbaum⁴¹ in 1912 and then by Niwa and Asami⁴².

The circuit arrangement using two cores, shown in Fig. 4.15 is another method for superposing steady and periodic fields. Two core circuits are mostly used in d.c. controllable reactors including transductor and magnetic amplifiers.

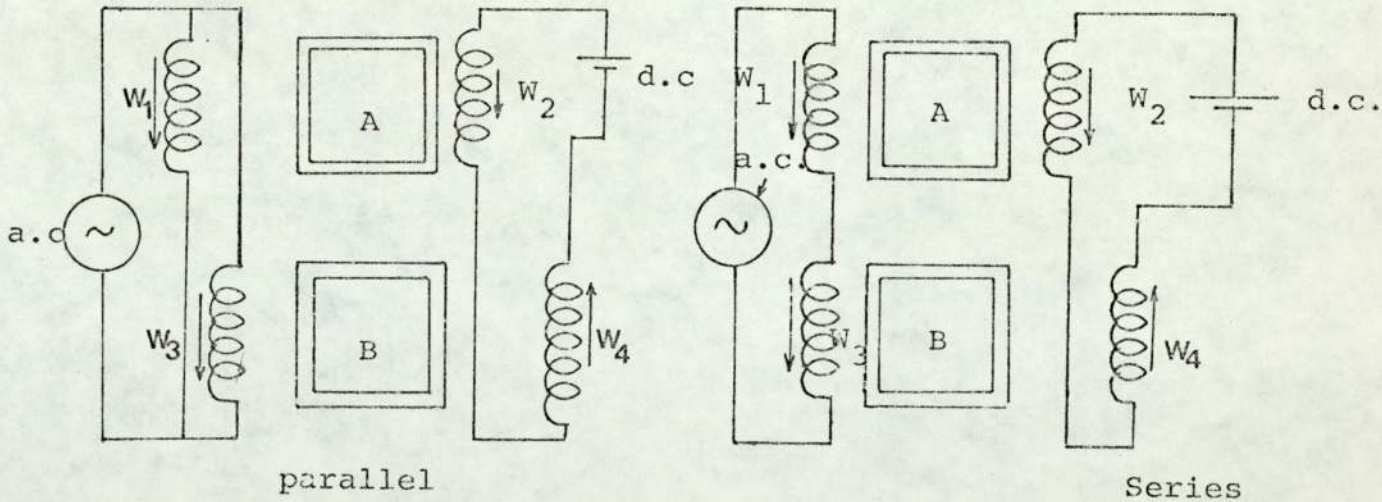


Fig. 4.15

Two core circuit employs two identical cores A and B, each having two windings. The alternating current in the d.c. winding is eliminated because these windings being

connected in series in such a sense that the induced alternating voltages oppose one another. Parallel and series arrangements have been shown in Fig. 4.15. Neither of the circuits could be used with complete satisfaction if sinusoidal current is desired. The series circuit would be suitable, apart from the even harmonic currents in the d.c. circuit. This was confirmed by Charlton and Jackson³⁸ who observed a substantially constant a.c. current in the d.c. circuit as the d.c. circuit resistance was varied. These circuits were investigated by Coales⁴³ and others like Boyajian⁴⁴, Johnson et al⁴⁵ and Vallauri⁴⁶.

All the methods so far discussed have the main disadvantage of producing either sinusoidal flux or sinusoidal current. These disadvantages have been largely overcome by using a feedback circuit which has been discussed in detail by Ramsden³².

4.9 ONE WINDING PARALLEL CIRCUITS FOR PRODUCING SUPERPOSED STEADY AND PERIODIC FIELDS IN THE TEST MACHINE AND THE SIMULATION OF THYRISTOR FED d.c. MACHINE

It has already been discussed in detail in Chapter 3 that the shell of a d.c. machine supplied from thyristor has steady d.c. flux distribution, shown in Fig. 4.16, but it is not the complete picture - besides this steady field distribution the shell also carries pulsating a.c. flux, which has also been shown in Fig. 3.17, chapter 3.

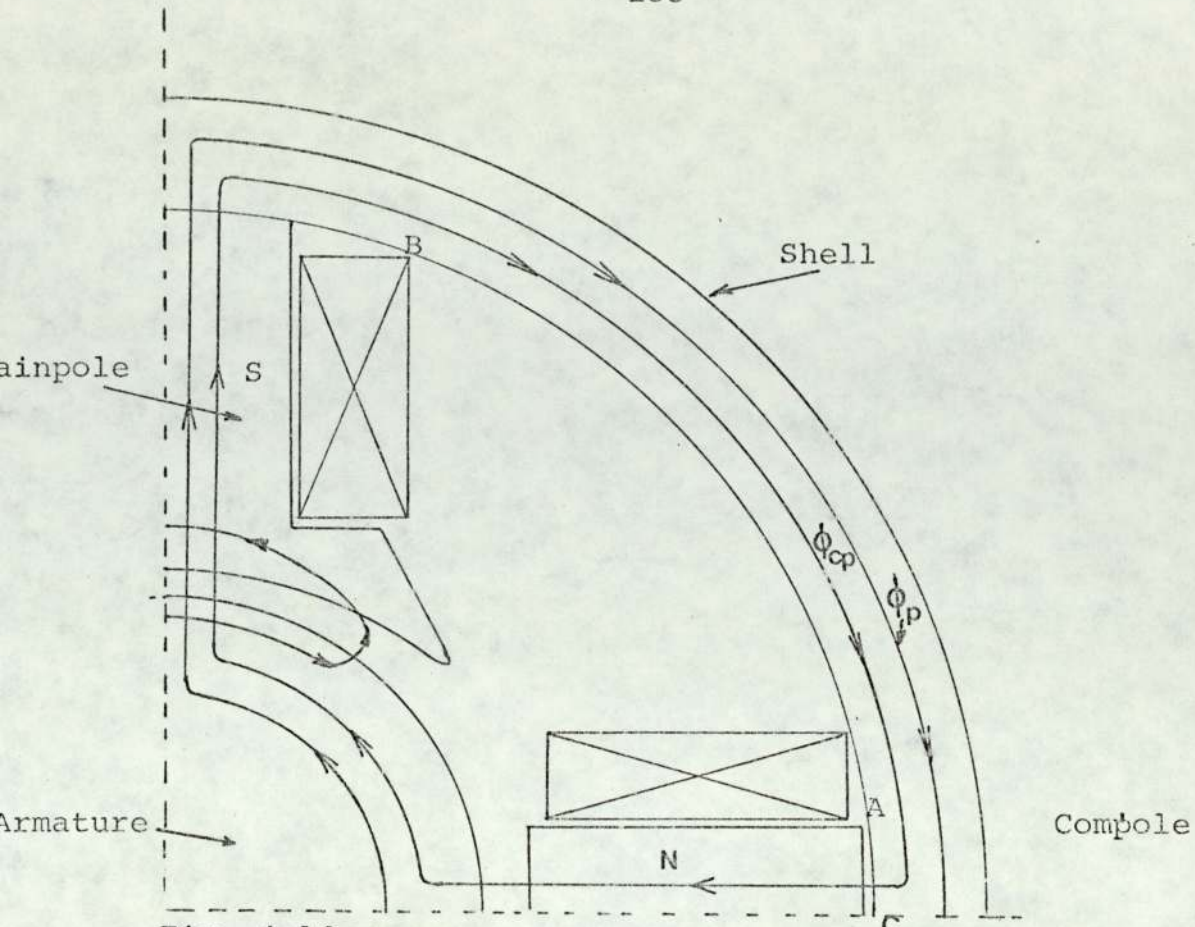


Fig. 4.16 D.c. Flux Distribution in the Shell

Considering the d.c. flux paths in the machine, it is seen from Fig. 4.16 that the steady flux levels in the two wings of the shell about the centre line of the interpole are different, $\frac{1}{2}(\phi_{cp} + \phi_p)$ in one side and $\frac{1}{2}(\phi_p - \phi_{cp})$ in the other side. It was thought from every angle to choose the right circuit arrangement which out of all those circuits already discussed in Section 4.8, can produce the same fluxing condition (both steady and time varying) in the shell as exactly what it should be if the machine was fed from thyristor supply.

One winding parallel circuit a.c. - d.c. power supply as described in Section 4.8.1 was found to be the most

suitable one to solve the problem of producing the superposed steady and time varying field in the shell of the machine. The schematic diagram of a.c. - d.c. superposed supply for the experimental machine has been shown in Fig. 4.17.

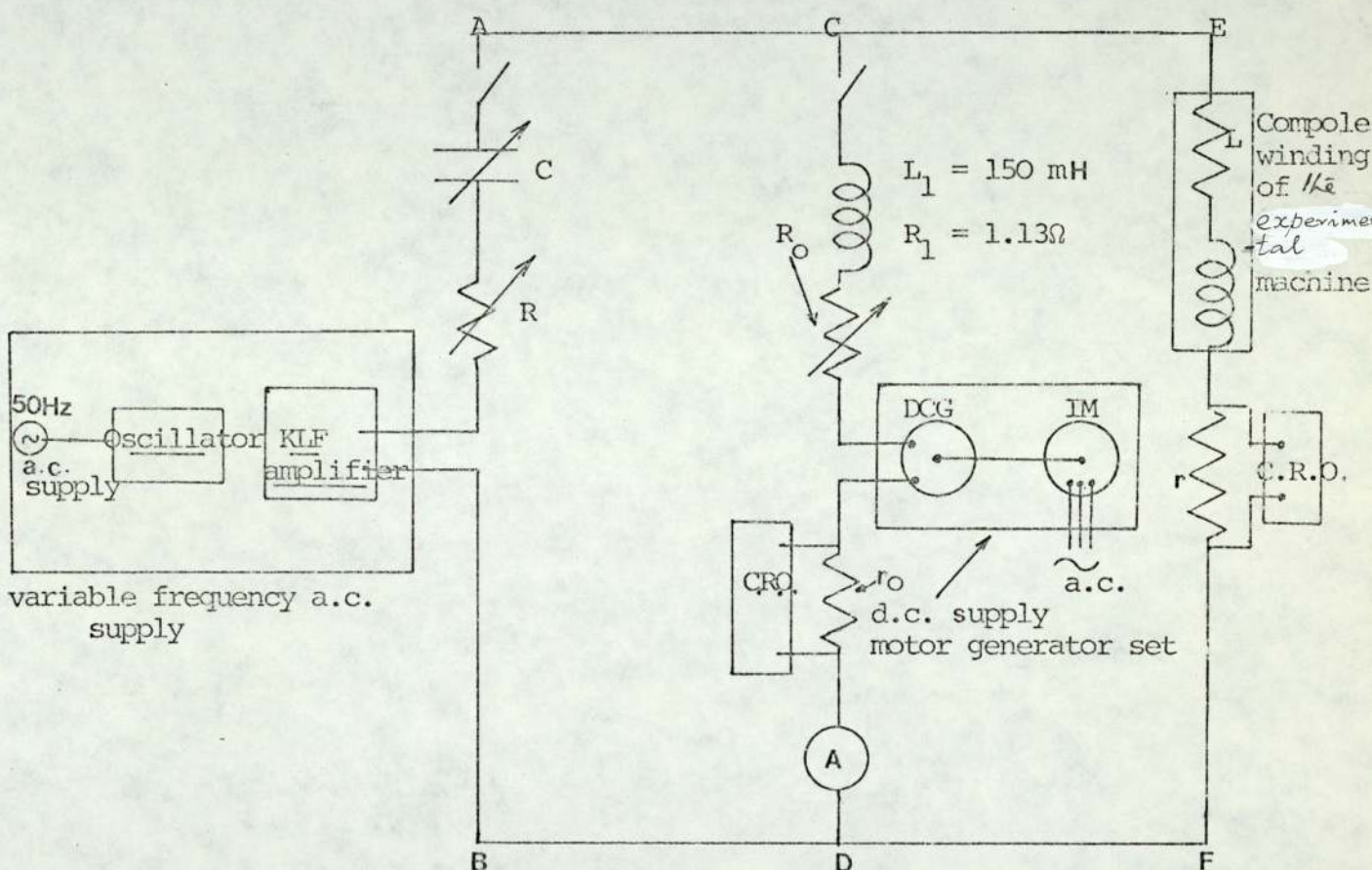


Fig. 4.17 Schematic Circuit Diagram for the a.c. - d.c. Superposed Supply to the Experimental Machine

A variable frequency source consisting of oscillator and KLF amplifier has been described in detail in section 4.10. D.c. supply was obtained from a motor generator set.

D.c. level of excitation to the compole winding was changed by varying the resistance R_0 . The value of L_1 was so chosen that it was able to smooth out the a.c. ripple in the line CD for various amplitudes of a.c. ripple used (from 8A to 20A peak to peak), throughout all the frequency range (5~ to 600~) and for various d.c. levels of excitation chosen. The value of L_1 chosen was approximately ten times that of L , where L is the inductance of the interpole winding. The peak to peak values of a.c. ripple in the line EF were measured by C.R.O. across 'r' shown in Fig. 4.17. 'C' is a variable capacitor bank, used for two reasons -

(1) it blocks the d.c. current from flowing through the amplifier circuit

and

(2) corrects the power factor of the amplifier at a given frequency f .

The rough guide line to estimate the value of C is :

$$\omega = \frac{1}{\sqrt{LC}} \quad 4.5$$

where $\omega = 2\pi f$ and $L \approx L_1$. Various values of C at a given frequency and for a particular value of a.c. and d.c. load current were tried, starting from the rough estimation given by equation 4.5, until the best result was obtained. The minimum limit of frequency for the a.c. supply chosen, was 5 Hz, because that was the lowest limit of frequency one could use with satisfactory performance of the a.c. supply

which has been discussed in section 4.10. The upper limit of frequency was decided to be 600 Hz because that is the fundamental ripple frequency present in the line current for the commonly used rectified power supply available in the market. This has been discussed in Chapter 3.

4.10 DETAILS OF THE VARIABLE FREQUENCY a.c. POWER SUPPLY

The output of the Farnell oscillator was fed to the input of the Savage KLF power amplifier (O.P. value type V1505 S/N) as shown in Fig. 4.17. With the help of the oscillator, the frequency of the input a.c. signal can be changed from 5 Hz to 1000 Hz. The operation of the amplifier has been briefly described.

Input The signal input to the amplifier is at 600 ohms. The input voltage should not be greater than 0.25 volts or less than 0.06 volts r.m.s.

Output Four primary/secondary ratios are provided on the output transformer and selection is made by inserting the appropriate plug into the socket on the top of the output transformer. The following chart is given for the output voltage with load.

Plug No.	Output volts at full drive	load in ohms
A	50V	2.5 Ω
B	75V	5.6 Ω
C	100V	10.0 Ω
D	200V	40.0 Ω

The output voltage can be varied by controlling the gain of the amplifier or the input voltage from the oscillator.

Frequency Range

The amplifier can be used quite satisfactorily within the frequency range 4 Hz to 2000 Hz. Within this band it will deliver power with good waveform.

Waveform distortion	Frequency
1.4%	50~
1%	400~
1%	1000~
less than 2%	below 50~

The schematic electrical circuit diagram for the experimental work has been shown in Fig. 4.18.

CHAPTER 5

MEASURED EDDY CURRENT DISTRIBUTION ON SHELL SURFACE

5.1 INTRODUCTION

It is believed from the literature survey in Chapter 3, that the theoretical investigation made by Skobelev³¹ about the shell eddy currents is based on the following assumptions to simplify the problem.

- (1) Only the compoles are present in the magnetic circuit
- (2) Circular eddy current distribution around the compole
- (3) Constant permeability of the shell material.

In real life, the laminated mainpoles in the magnetic circuit, the mean level of d.c. component of shell flux, and the reaction mmf produced by the armature winding, which are all present in thyristor fed d.c. machine at its running condition, makes the shell eddy current problem more complicated.

To study the behaviour of shell eddy currents, the following experiments were carried out.

- (1) The interpoles alone were excited from an a.c. supply. The armature was placed in its position with no brushes touching the commutator surface. The mainpoles were removed.
- (2) The mainpoles were put back to their original position with the help of dowels, section 4.2, with all the other conditions as in (1).

- (3) The mainpoles were excited from a separate d.c. supply and the interpoles were excited from the a.c. - d.c. superposed supply discussed in sections 4.9 and 4.10, with the armature in place.
- (4) The armature was excited from a separate d.c. source with the other conditions as in (3).

The procedure and results of the experiments which were carried out using the current density probes on the surface of the shell, shell loop search coils and the search coils in the air gap at the back of the compole with conditions (1) and (2) are discussed in this chapter; those with the conditions (3) and (4) are given in Chapter 7.

Hammond's⁴⁷ theoretical work on a δ function coil carrying a.c. current in front of a semi-infinite slab is mentioned and his results compared with the measured shell eddy current distribution underneath the compole.

5.2 EDDY CURRENT DISTRIBUTION ON THE SURFACE OF THE SHELL FROM THE EXPERIMENTAL EVIDENCE

5.2.1 Experimental Results from the Current Density Probes

The interpole windings were supplied from 50 Hz a.c. supply with the armature in position, but without the mainpoles. The location of the current density probes on the outer inner and side surfaces of the shell are shown in Fig.4.9 and 4.9a. The voltage signals from the current density probes were magnified 50 times with the Burr Brown amplifier

discussed in sub-section 4.4.1.2. The peak r.m.s. ratios of voltage signals from all the current density probes were very nearly equal to 1.414 (within $\pm 0.1\%$), which permits the use of measured average values from the Bruel and Kjaer V.T.V.M. as the average values of the fundamental component of the voltage signal. This was checked with a harmonic analyser.

The average values of the fundamental components of the current densities were obtained from

$$J = (V/\rho l)$$

Average values of fundamental J_X and J_Y components measured at different points along 0° , 9° , 18° , 27° , 36° , and 45° (mechanical) lines on the shell surface (see Figs. 4.9 and 4.9a) are shown in Figs. 5.1 to 5.6. AA_1 , BB_1 , CC_1 , DD_1 , EE_1 , FF_1 are the lines on the surface of the shell shown in Fig. 4.9a. The value of ρ for the steel used for shell was measured experimentally as $11.81 \times 10^{-8} \Omega m$ (section 4.7). The resultant \hat{J} distributions were obtained from $\sqrt{J_X^2 + J_Y^2}$ (sub-section 4.3.5.1) and these have been plotted in Figs. 5.1 to 5.6 and 5.7. Good agreement was found when the areas under E_Y distribution curves were compared with the measured average voltages from the shell loop search coils at the same frequency and excitation. The reason is given below.

According to Faraday's law

$$\oint \hat{E}_y \cdot d\hat{l} = \frac{d\phi}{dt}$$

Now $\oint \hat{E}_y \cdot d\hat{l} = \rho \oint \hat{J}_y \cdot d\hat{l}$ 5.1

$\oint \hat{J}_y \cdot d\hat{l}$ along any closed loop around the shell at 0° or 9° or anywhere on the shell shown in Fig.4.9 is twice the area under the corresponding J_y distribution curves. The symmetry of flux distribution about the central plane of the shell gives the multiplying factor 2. The measured areas under the $E_y (= \rho J_y)$ distribution curves should be divided by the units used along the co-ordinate axes. The average values of voltages equal to $\frac{d\phi}{dt}$ were measured by the shell loop search coils at the same excitation and frequency of the interpole winding. $(\frac{d\phi}{dt})$ measured from the shell loop search coils and $(2 \int \hat{E}_y \cdot d\hat{l})/u$ have been compared in Fig. 5.8. This is a cross check for the measured current density distribution. The experiments were performed at constant temperature so that ρ was reasonably constant. Current density distributions along AA_1, BB_1, CC_1 on the inner surface of the shell are shown in Fig. 5.9. The direction of flow of eddy currents along the central lines of the inner and outer surfaces of the shell are completely axial, there is no eddy current at the point O shown in Fig.4.9a, the eddy currents are completely axial along the 45° line around the shell shown in the same figure. Only the tangential component of eddy current exists along the 0° line around the shell and there is no eddy current at the point I'_1 (see Fig.4.9).

With the help of the experimentally-obtained current-density distributions, various limits of integration were tried along different lines on the surface of the shell by trial and error method, until a satisfactory pattern of eddy current paths on the side and upper surface of the shell was achieved. The end path pattern is shown in Fig. 5.10, which can be explained in the following way. 3.5 units of current, which is obtained by integrating the current density distribution curve along UV, with the limit UU_1 , flows through the tube 1. The width of the tube is narrow at one end, and becomes broader as it goes towards YZ, which is the central line of the outer surface of the shell. Thus the current density at UU_1 is greater than that in the opposite side of the tube. Similarly, all other current tubes have been drawn such that the total current emanating from the edge UV is equal to the sum total of currents along the lines YZ and ZV, which satisfies the Amperes Circuital law. Integration of current density distribution within a certain limit which is total current, was obtained by measuring the area under the curve. The direction of current flow changes at the point P and there is no eddy current in the region PQZR because the eddy current flows around the shell such that they offer minimum resistance loss (see Fig.5.10).

The theoretical approach for predicting the distribution of the current density on the side and back surface of the shell is given in Chapter 8.

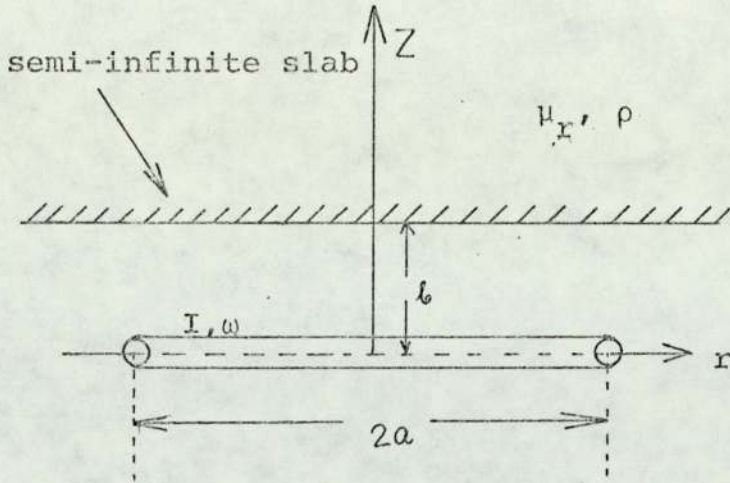


Fig. 5.11 Circular Coil in Front of a Semi-infinite Slab.
(Hammond⁴⁷)

5.2.2 Present Problem and Theoretical Investigation of Eddy Currents Induced in a Semi-infinite Slab by a δ Function Coil Carrying a.c. Current

The eddy current distribution on the shell, underneath the interpole seems to be similar to a problem investigated by Hammond⁴⁷. He analysed the eddy currents induced in a semi-infinite slab by a circular current loop carrying a.c. current shown in Fig. 5.11, with the help of vector potential \hat{A} .

The vector potential \hat{A} is defined by

$$\text{Curl } \hat{A} = \hat{B} \quad 5.2$$

$$\text{div } \hat{A} = 0 \quad 5.3$$

The permeability of the slab was assumed constant. Using the boundary conditions he found the solutions for \hat{A}_θ which satisfied the equations in cylindrical co-ordinate system

$$\frac{\partial^2 \hat{A}_{\theta 1}}{\partial r^2} + \frac{1}{r} \cdot \frac{\partial \hat{A}_{\theta 1}}{\partial r} - \frac{\hat{A}_{\theta 1}}{r^2} + \frac{\partial^2 \hat{A}_{\theta 1}}{\partial z^2} = 0 \quad 5.4$$

outside the slab

and inside the slab

$$\frac{\partial^2 \hat{A}_{\theta 2}}{\partial r^2} + \frac{1}{r} \frac{\partial \hat{A}_{\theta 2}}{\partial r} - \frac{\hat{A}_{\theta 2}}{r^2} + \frac{\partial^2 \hat{A}_{\theta 2}}{\partial z^2} = \mu \sigma \frac{\partial \hat{A}_{\theta 2}}{\partial t} \quad 5.5$$

Thus the vector potential A within the slab is

$$\hat{A}_{\theta 2} = I \mu_0 \mu_r \int_0^\infty \exp\left(-\frac{kb}{a}\right) J_1(k) J_1\left(\frac{kr}{a}\right) \frac{k}{k\mu_r + \sqrt{k^2 + jp^2}} \exp\left(-\sqrt{(k^2 + jp^2)}(z-b)/a\right) dk \quad 5.6$$

(when $z \leq b$)

using the equation

$$\hat{J}_\theta = \sigma \frac{\partial}{\partial t} \hat{A}_{\theta 2} \quad 5.7$$

the expression for current density becomes

$$\hat{J}_\theta = \frac{-jp^2 I}{a^2} \int_0^\infty \exp\left(-\frac{kb}{a}\right) J_1(k) J_1\left(\frac{kr}{a}\right) \frac{k \exp\left(-\sqrt{(k^2 + jp^2)}(z-b)/a\right)}{\mu_r k + \sqrt{k^2 + jp^2}} dk \quad 5.8$$

J_0 and J_1 are the Bessel functions of the first kind and order zero and unity. In order to find out the total eddy current per unit radius which is $\int_b^\infty J_\theta dz$, one has to evaluate the integral in equation 5.8. Moullin⁴⁸, Poritsky and Jerrard⁴⁹ paid considerable attention to the numerical evaluation of this type of integral. In the case of inductance limited eddy current, i.e. $p \geq k\mu_r$, the line density of eddy current

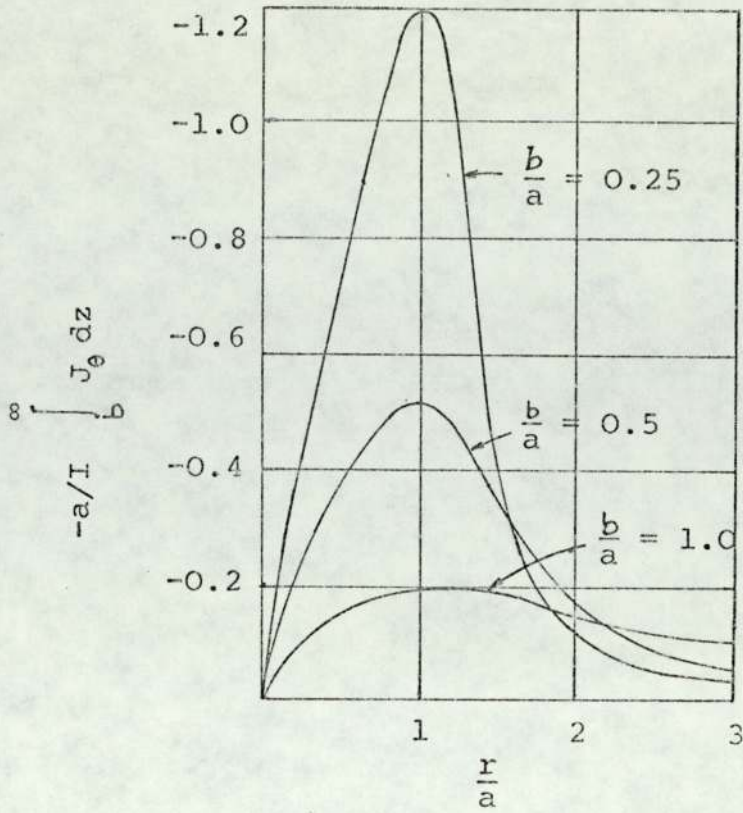


Fig.5.12 Eddy Current Flow per Unit Radius
(Hammond⁴⁷)

per unit radius becomes

$$\int_b^{\infty} J_e dz = - \frac{I}{a} \int_0^{\infty} \exp\left(-\frac{kb}{a}\right) J_1(k) J_1\left(\frac{kr}{a}\right) k dk \quad 5.9$$

The plot of eddy current flow per unit radius is shown in Fig. 5.12. Whether the coil is circular or rectangular the eddy currents induced in the slab, which is the shell in the experimental machine, are similar in nature. Fig. 5.12 shows that there is no eddy current at the centre and it reaches its maximum value at the edge of the δ function coil - this sort of eddy current pattern underneath the compole is found experimentally (see Fig. 5.9). A theoretical approach for explaining the behaviour of shell eddy currents in the experimental machine is made in Chapter 6, where the problem is attacked in a different way.

5.2.3 A.c. Flux Tests in the Airgap at the Back of the Compole Using the Array of Search Coils

The frequency of interpole supply was varied from 100 Hz to 600 Hz with the help of oscillator and KLF amplifier, discussed in section 4.10. The excitation to the compoles was kept constant throughout the experiment, the mainpoles were removed and the armature was in position without the brushes on the commutator surface. The output voltages from the search coils (section 4.3.2) were amplified and measured. These $\left(\frac{d\phi}{dt}\right)$ voltages were almost pure sinusoid for the whole range of frequencies; this was checked on the

oscilloscope and the measured peak to r.m.s. ratio was very nearly 1.414. The amplified average values of the search coil voltage waves measured with Bruel and Kjaer V.T.V.M. were then divided by the corresponding angular frequency to get the average values of the a.c. flux embraced by the search coil. The sinusoidal nature of $(\frac{d\phi}{dt})$ waves were also checked with a harmonic analyser. Average values of the (fundamental) flux waves were then divided by the actual areas of search coils to obtain the flux densities. The areas of the search coils were enlarged 100 times with the help of the 'Nikon' magnifying machine and were then measured with a planimeter. The actual positions of the search coils with respect to the centre line and edges of the compoles were also obtained from the enlarged view of the interpole face along with the search coils fixed on a transparent plastic plate, which was fixed to the interpole back face with double sided sellotape. The flux densities were plotted at the centres of the search coils, and the peripheral and axial variation of flux densities at the back of the compole are shown in Figs. 5.13 and 5.14 respectively. These tests are discussed in section 5.2.5.

5.2.4 D.c. Flux Test in the Airgap at the Back of the Compole Using the Same Array of Search Coils

The interpoles were excited from a d.c. supply, all other conditions remaining the same as those in Section 5.2.3. The d.c. fluxes linking the search coils were measured with the 'Norma' ballistic fluxmeter (see sub-section 4.4.1.1) by the reversal of the compole d.c. excitation.

Dividing the measured fluxes by the corresponding true search coil areas the average flux density along the width of search coil were obtained and plotted at their centres. The d.c. flux density distributions thus obtained under the compole and beyond the compole edge in the peripheral direction of the shell has been shown in Fig.5.15. This experimental flux density distribution has been compared with that obtained from Gibbs'¹⁷ analysis where he solved the field problem to quantify the fringe flux from the mainpole's edge, given by the equations 2.6 and 2.7., and good agreement has been found. (See Fig.5.15). The experimental flux density curve in the airgap at the back of the compole has also shown good agreement with that theoretically obtained from equations 2.20, 2.21, 2.22 and 2.24, derived in section 2.4.

5.2.5 Discussion of the Experimental Results Obtained from the Search Coils and Current Density Probes

From Figs. 5.13 and 5.14 it is observed that as the frequency increases at a given compole excitation the a.c. flux density curves are depressed further down under the compole; this depression may be explained in the following way. For a given d.c. compole excitation, there exists a flux in the machine which is dictated by the magnetic circuit, and the flux pattern inside the airgap at the back of the compole is a good indication of the total mmf patterns acting on that gap which is rectangular in shape provided that the iron on both sides of the airgap is unsaturated and that the fringe flux is

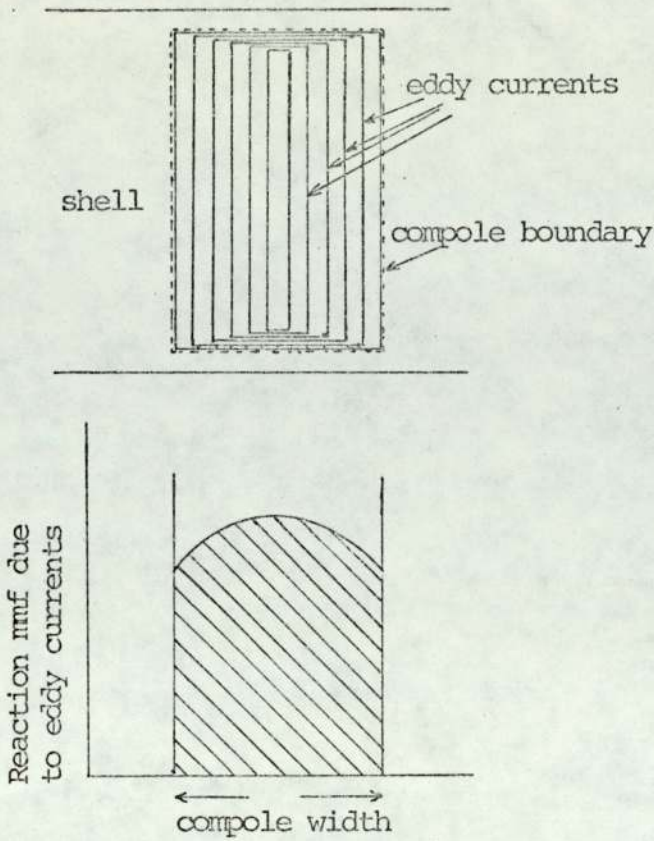


Fig. 5.17 Eddy Current Distribution in the Shell under the Compole

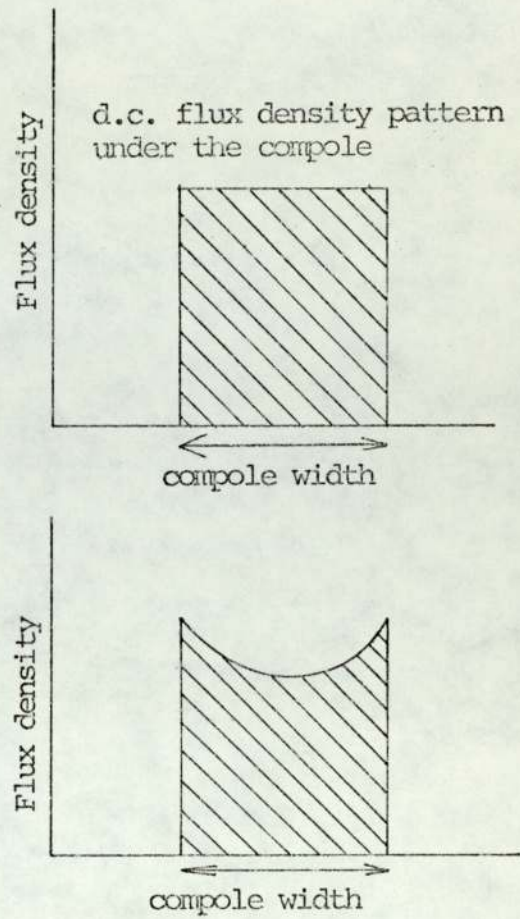


Fig. 5.16 The Resultant Flux Density Distribution

neglected. The idealized d.c. flux density pattern under the compole is shown in Fig. 5.16, which agrees well with that obtained experimentally in Fig. 5.15 if the fringe flux is neglected. Now, if the compole winding carries a.c. current, the pulsating flux produces eddy currents on the shell underneath the compole. The pattern of these eddy current paths on the shell has been suggested as shown in Fig. 5.17. These eddy currents behave like the concentric winding and the distribution is such that line density is zero at the compole centre line and goes to a maximum value, which has been confirmed both from the experimental evidence shown in Fig. 5.9 and from the

theoretical deductions given in sub-sections 5.2.2 based on delta function coil carrying current in front of a semi-infinite slab (see also Fig. 5.12). These eddy currents underneath the compole, the length of which is much greater than its width, in turn produces a reaction mmf drawn in Fig. 5.17. The combined effects of eddy current reaction mmf and the field mmf produces the flux density distribution pattern as shown in Fig. 5.16, which is also experimentally confirmed (see Fig. 5.13). As the supply frequency to the compole rises, keeping the excitation constant, the eddy current density increases, the eddy current reaction mmf rises, and the flux will fall. This increased reaction mmf depresses flux density distribution curves (under the compole) further down, as shown in Fig. 5.13. As the frequency increases the a.c. flux in the shell under the compole will be concentrated more near the boundary of the compole which has been mentioned by Dodd and Deeds⁵⁰, in their paper dealing with the eddy current problem of a circular coil driven by a constant amplitude alternating current, and is found true from the experimental evidence (see Fig. 5.13). The distribution of the eddy currents outside the boundary PQRS as shown in Fig. 5.18, may be explained in the following way. The pulsating flux emanating from the compole as soon as it reaches the shell surface becomes mainly tangential to the surface and travels towards the next pole. The a.c. components of shell flux cannot go deep into the shell and

will be confined within the skin depth, which is governed by the supply frequency and the shell material. The eddy currents close their circuits on the surface of the shell with minimum resistance loss and they behave like a short circuited secondary of the transformer (see also Fig. 5.18). In Fig. 5.18 the shell surface is cut along $X_1X_7Y_1Y_7$ and developed, and PQRS is the boundary of the compole_A. ^(see also Fig. 5.19) It is also found from the experimental current density distribution curves that the total eddy current along AB is equal to the sum of those along CU_2 and U_2U_1 . The reaction mmf produced by those shell eddy currents has been theoretically calculated in section 6.4.3, in terms of the physical parameters of the machine and excitation to the compole and the supply frequency.

5.2.6 Change in the Eddy Current Distribution in the Shell due to the Presence of Mainpoles in the Magnetic Circuit of d.c. Machine

The mainpoles were now replaced and only the compoles were excited from the variable frequency supply as described in section 4.10. The average values of the fundamental component of current densities along the central line X_4Y_4 of the inner surface of the shell (see Fig. 5.18) were measured at various frequencies ranging from 50 Hz to 600 Hz with constant compole a.c. excitation. The eddy currents are completely axial and the distributions along that line are shown in Fig. 5.20 and compared with those measured at the same frequencies and excitations when the mainpoles were

not on. From Fig. 5.20 the current distributions with the mainpoles and without the mainpoles are everywhere the same, except in the region near and under the mainpoles. There is a sudden fall of eddy current distribution under the mainpole, because the shell loses some of its pulsating a.c. flux which has low^{a.c.} reluctance shunt path through the root of the laminated mainpole. As the frequency increases the shell^{a.c.} reluctance rises and consequently more a.c. flux leaves the shell and flows through the low^{a.c.} reluctance laminated iron core of the mainpole. This is shown in Fig.5.21. The average values of the shell a.c. fluxes with and without the mainpole were also measured from the shell loop search coils, discussed in section 4.3.1. (See also Fig. 4.5).

The distribution of these fluxes in the peripheral direction from the edge of the compole to the central line of the mainpole are shown in Fig. 5.22, which confirms the loss of a.c. flux from the shell to the core of the mainpole. This fall of eddy currents under the mainpoles can be taken into account by choosing the right limit of integration in the X direction for the calculation of reaction mmf due to shell currents, discussed in Chapter 6.

CHAPTER 6

THEORETICAL WORK ON EDDY CURRENTS INDUCED IN THE SOLID SHELL DUE TO A.C. EXCITATION TO THE COMPOLES

6.1 INTRODUCTION

From the experimental results in Chapter 5, the eddy current distribution on the surface of the shell has been obtained. From the experimental facts and assuming

- (1) the shell to be infinitely long in the axial direction
- (2) constant μ_r of the shell material for the moment
- (3) mainpoles not being considered into the magnetic circuit

the two dimensional Poissonian field equation has been solved for the problem, where the solid shell of finite thickness is subjected to a pulsating mmf wave rectangular in space. Solutions of Maxwell's field equation for \underline{H} and \underline{E} are found which satisfy the interface boundary conditions. The distribution of current induced in shell due to all the space harmonics of the pulsating primary rectangular mmf is theoretically obtained and consequently an analytical formula for the reaction mmf due to those induced eddy currents are obtained in terms of physical parameters of the machine, electrical conductivity and permeability of the shell material, frequency and magnitude of a.c. excitation to the compole.

The variation of μ with H is taken into account in

the later stage of the theoretical work by introducing Davies' ^{51, 52} formula $(\mu_0 \mu_r)^{\frac{1}{4}} H = kH^m$ which represents the B-H curve above the knee, into the calculations. Thus the variation of reaction mmf with frequency has been found theoretically, including the variable permeability into the calculation.

μ_r varies with the position in the shell as the magnetic field strength H varies from point to point. A new approach has been made to solve the equation connecting the magnetic field strength and other field quantities, after H on the surface of the shell being replaced by $(\mu_0 \mu_r)$ from Davies' formula, at every point on the shell for each harmonic of the rectangular mmf wave, in order to examine the space variation of μ_r all over the surface.

Considering the space variation of permeability, current density distribution on the surface of the shell has also been theoretically calculated.

6.2 THE MATHEMATICAL MODEL

The model chosen for analysis is the machine without mainpoles, unrolled to fit a rectangular co-ordinate system shown in Figs. 6.1 and 6.2, the solid shell becoming a flat plate of thickness d_0 . Y is measured in the radial direction from a distance b_0 below the solid shell.

X is measured along the peripheral direction and Z is measured in the direction of the axis of the machine. Wood

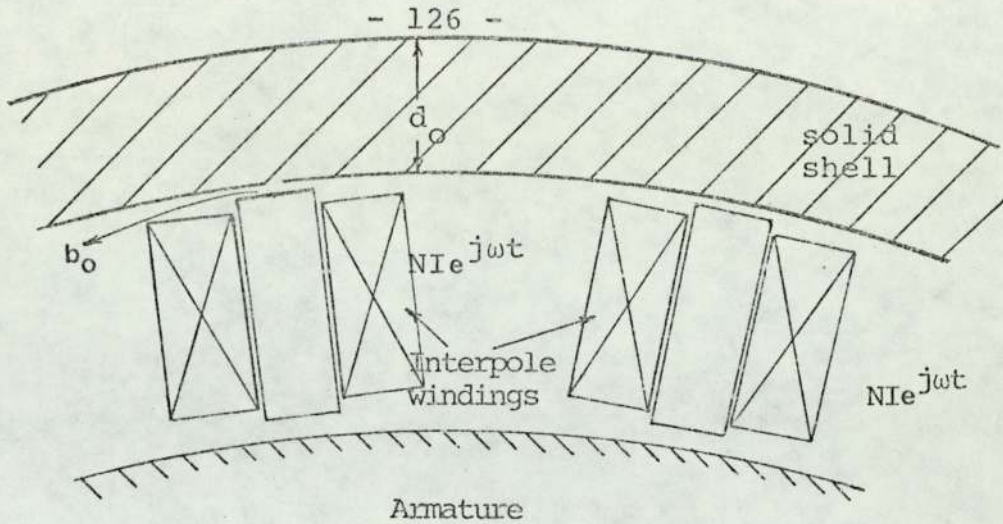


Fig. 6.1 Machine Without Main Pole

and Concordia⁵³ have shown that a very little error is involved if the rectilinear model is used instead of cylindrical, provided that the fundamental pole pitch \gg depth of penetration and fundamental pole pitch to air gap length $\gg 1.0$. The rectilinear co-ordinate system presents hyperbolic functions in the analytic solutions for the field distribution rather than the complicated Bessel function if the cylindrical geometry is used.

6.3 ASSUMPTIONS OF THE THEORETICAL MODEL,

- (1) The shell is subject to a mmf wave produced by the interpole windings, as shown in Fig. 6.2 which has rectangular distributions in space and pulsates with a frequency ω in time.
- (2) Current density vector J has been assumed to be purely axial and does not vary along z axis, which is very nearly true from the experimentally obtained current density distributions on the inner surface of the shell given in Chapter 5.

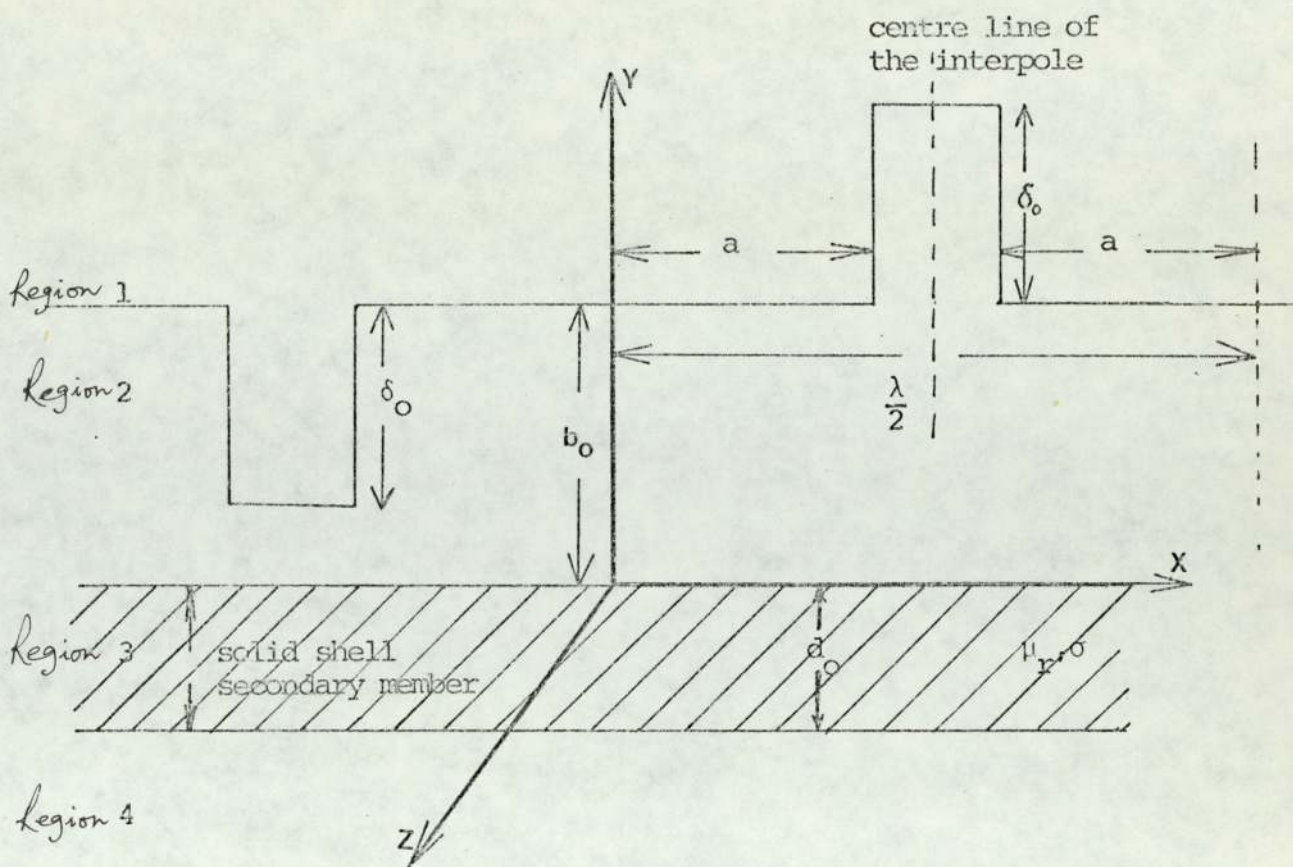


Fig. 6.2 Linear Model of the Machine.

- (3) The shell is infinite in z - direction and end region problem has been ignored
- (4) The excitation to the compole windings is purely sinusoidal with angular frequency ω .
- (5) The shell is composed of homogeneous magnetic material. The relative permeability μ_r of the shell material is constant in time and space for the derivation of the fundamental equations only. In the later stage of the theoretical work the relative permeability has been allowed to vary.
- (6) The thin core of the interpole is neglected, which is a dubious assumption.
- (7) Hysteresis has been neglected.
- (8) The electrical conductivity σ in region (3) of Fig. 6.2 is finite and constant.

6.4 THEORETICAL DEDUCTIONS

6.4.1 Eddy Current Distribution

The pulsating rectangular mmf wave can be represented by a Fourier series given by

$$F = \text{Re} \left[\frac{4\delta_0}{\pi} \sum_{n=1,3,5}^{\infty} \frac{1}{n} \cos \frac{n2\pi a}{\lambda} \sin n \frac{2\pi x}{\lambda} \right] \exp(j\omega t) \quad 6.1$$

$\exp(j\omega t)$ takes into account the time variation of all the harmonics of the rectangular wave. Each space harmonic of the mmf wave can be considered as being produced by their corresponding finely divided sinusoidally distributed current sheet placed at a distance b_0 from the surface of the shell. Fig. 6.3 shows space fundamental component of the mmf wave and current sheet. The fundamental component of the current sheet can be described by

$$A_{z1} = \text{Re} A_1 \cos \frac{2\pi x}{\lambda} \exp(j\omega t) \quad 6.2$$

and the corresponding fundamental mmf is

$$F_1 = \text{Re} \frac{4\delta_0}{\pi} \cos \frac{2\pi a}{\lambda} \sin \frac{2\pi x}{\lambda} \exp(j\omega t) \quad 6.3$$

where A_z is the line density of current in amperes per metre, ω is the angular frequency of pulsation in radians per second, and λ is the wavelength of the spatial current variation in the X direction. For the ease of solution

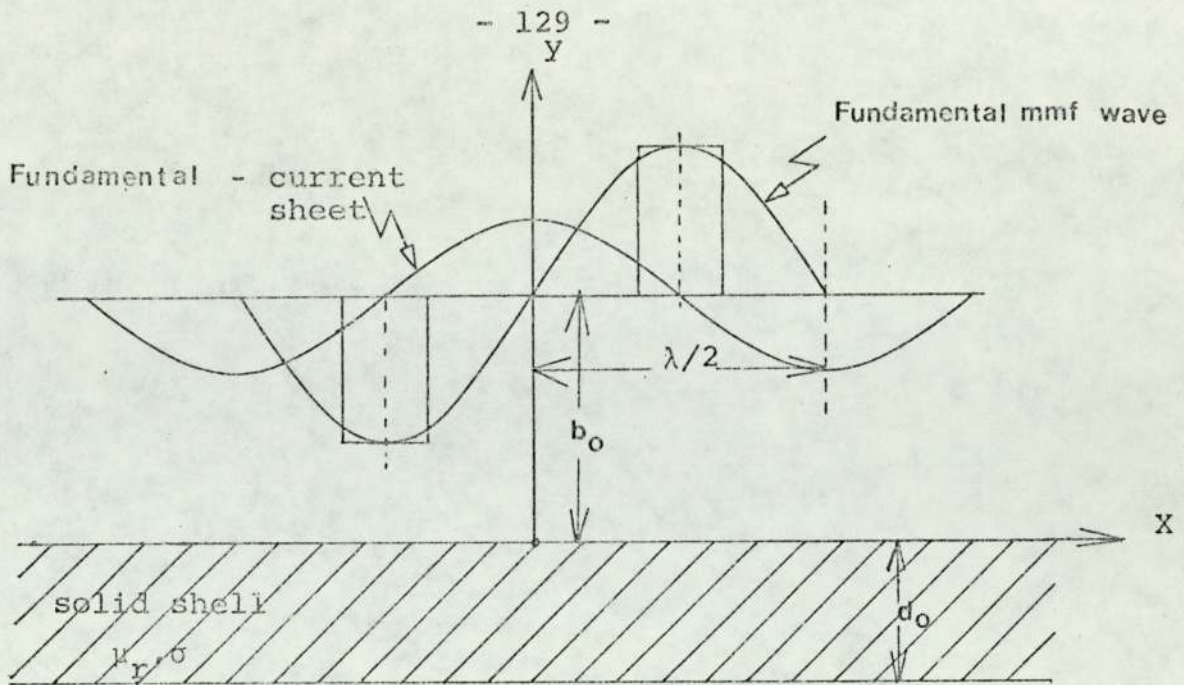


Fig. 6.3

'Re' may be omitted. Maxwell's equations for electromagnetic fields in linear conducting media are:

$$\text{Curl } \hat{H} = \hat{J} \quad 6.4$$

$$\text{Curl } \hat{E} = - \frac{\partial B}{\partial t} \quad 6.5$$

together with

$$\text{div } \hat{B} = 0 \quad 6.6$$

$$\hat{B} = \mu_0 \mu_r \hat{H} \quad 6.7$$

$$\hat{J} = \sigma \hat{E} \quad 6.8$$

$$\text{div } \hat{J} = 0 \quad 6.9$$

From these equations and assumptions (5) and (8) in section 6.3, it can be shown that for the shell (region 3 of Fig. 6.2)

$$\nabla^2 \hat{H} = \mu_0 \mu_r \sigma \frac{\partial \hat{H}}{\partial t} \quad 6.10$$

$$\nabla^2 \hat{E} = \mu_0 \mu_r \sigma \frac{\partial \hat{E}}{\partial t} \quad 6.11$$

and elsewhere

$$\nabla^2 \hat{H} = 0 \quad 6.12$$

$$\nabla^2 \hat{E} = 0 \quad 6.13$$

Field quantities \hat{H} and \hat{E} vary sinusoidally and may be described by

$$\hat{H} = \text{Re } \underline{H} \exp(j\omega t) \quad 6.14$$

$$\text{and } \hat{E} = \text{Re } \underline{E} \exp(j\omega t) \quad 6.15$$

where \underline{H} and \underline{E} are complex vectors. Using 6.14 and 6.15 the equations 6.12 and 6.13 can be written as

$$\nabla^2 \underline{H} - \frac{1}{\delta^2} (1+j)^2 \underline{H} = 0 \quad 6.16$$

$$\nabla^2 \underline{E} - \frac{1}{\delta^2} (1+j)^2 \underline{E} = 0 \quad 6.17$$

and equations 6.12 and 6.13 become

$$\nabla^2 \underline{H} = 0 \quad 6.18$$

$$\nabla^2 \underline{E} = 0 \quad 6.19$$

The general solution of the equations 6.16, 6.17, 6.18 and 6.19 is of the form

$$\dot{R}_i = \{S_i \exp(-j\gamma y) + T_i \exp(+j\gamma y)\} \exp(-jqx) \quad 6.20$$

where \dot{R} stands for any one of the field quantities \underline{H}_X , \underline{H}_Y , or \underline{E}_Z and i for any one of those four regions (see Fig. 6.2).

$$\gamma = (q^2 + \frac{2j}{\delta^2}) \quad 6.21$$

δ is known as skin depth given by

$$\delta = \sqrt{\frac{2}{\omega \sigma \mu_0 \mu_r}} \quad 6.22$$

$$\text{and } q = \frac{2\pi}{\lambda} \quad 6.23$$

γ can be written as

$$\gamma = P + jQ$$

$$\text{where } P = \left(q^4 + \frac{4}{\delta^4}\right)^{\frac{1}{4}} \cos\left(\frac{\theta}{2}\right) \quad 6.24$$

$$Q = \left(q^4 + \frac{4}{\delta^4}\right)^{\frac{1}{4}} \sin\left(\frac{\theta}{2}\right) \quad 6.25$$

$$\text{and } \theta = \tan^{-1}\left(\frac{2}{\delta^2 q^2}\right) \quad 6.26$$

By applying the following boundary conditions

- (1) \underline{B}_Y is continuous at the interface of two adjacent regions which means

$$(\underline{B}_Y)_{i+1} = (\underline{B}_Y)_i \quad 6.27$$

$$(2) \quad (\underline{H}_X)_{i+1} - (\underline{H}_X)_i = A_{Z1} \text{ or } 0 \quad 6.28$$

$$(3) \quad \underline{B} \rightarrow 0 \text{ as } Y \rightarrow \pm \infty \quad 6.29$$

The coefficients S_i and T_i can be obtained in terms of known quantities like A_1 , μ_o , μ_r , γ , q , b_o and d_o .

Thus in region (3) \underline{E}_{Z3} is given by

$$\underline{E}_{Z3} = \frac{-j\omega(2\mu_o\mu_r\hat{A}_1) [q\mu_r \sinh\gamma(y+d_o) + \gamma \cosh\gamma(y+d_o)]}{\{(q\mu_r + \gamma)^2 \exp(\gamma d_o) - (q\mu_r - \gamma)^2 \exp(-\gamma d_o)\}} \times$$

$$\times \{\exp j(\omega t - qx) \cdot \exp(-qb_o)\} \quad 6.30$$

The eddy current density induced within the shell i.e. the region (3), due to the fundamental current sheet is given by

$$\underline{J}_{z3} = \frac{-j\omega\sigma(2\mu_o\mu_r\hat{A}_1)[q\mu_r\text{Sinh}\gamma(y+d_o)+\gamma\text{Cosh}\gamma(y+d_o)]}{\{(q\mu_r+\gamma)^2\exp(\gamma d_o)-(q\mu_r-\gamma)^2\exp(-\gamma d_o)\}} \times \left\{ \exp j(\omega t - \gamma x) \exp(-\gamma b_o) \right\}$$

6.31

For the 3rd, 5th and 7th harmonic current sheet the corresponding eddy currents induced in the shell will be

$$\underline{J}_{z3n} = \frac{(-2j\omega\sigma\mu_o\mu_r)\hat{A}_{zn}[q_n\mu_r\text{Sinh}\gamma_n(y+d_o)+\gamma_n\text{Cosh}\gamma_n(y+d_o)]}{\{(q_n\mu_r+\mu_n)^2\exp(\gamma_n d_o)-(q_n\mu_r-\mu_n)^2\exp(-\gamma_n d_o)\}} \times \left\{ \exp j(\omega t - q_n x) \exp(-q_n b_o) \right\}$$

6.32

where

(n odd)

$$q_n = \frac{2\pi n}{\lambda}, \quad \gamma_n = (q_n^2 + \frac{2j}{\delta^2})^{\frac{1}{2}}$$

and
$$A_{zn} = \frac{4}{\pi} \frac{A_o}{n} \text{Cos } n \frac{2\pi a}{\lambda}$$
 6.33


At a distance x and at any instant of time t the eddy current within the shell due to the rectangular pulsating primary mmf is the sum of all the odd harmonics of \underline{J}_{z3n} . Thus

$$\underline{J}_{z3r} = -2 j\omega\sigma\mu_0\mu_r \sum_{n=1,3,5,\dots}^{\infty} \frac{\hat{A}_{zn} [q_n\mu_r \sinh\gamma_n(y+d_0) + \gamma_n \cosh\gamma_n(y+d_0)]}{\{(q_n\mu_r + \gamma_n)^2 \exp(\gamma_n d_0) - (q_n\mu_r - \gamma_n)^2 \exp(\gamma_n d_0)\}} \times$$

$$\times \{\exp j(\omega t - q_n x) \exp(-q_n b_0)\} \quad 6.34$$

When the width of the shell d_0 is very much greater than the depth of penetration δ , the current distribution within shell can be obtained by making $d_0 \rightarrow \infty$ in the equation 6.34 and this becomes

$$\underline{J}_{z3r} = \sum_{n=1,3,5,\dots}^{\infty} -j\omega\sigma\mu_0\mu_r \hat{A}_{zn} \exp j(\omega t - q_n x) \exp(-q_n b_0) \cdot \left[\frac{\exp(\gamma_n y)}{q_n\mu_r + \gamma_n} \right]$$



6.35

On the surface of a thick shell the current density distribution is given by

$$\underline{J}_{z3r} = \text{Re} \sum_{n=1,3,5}^{\infty} \frac{-j\omega\sigma\mu_0\mu_r \hat{A}_{zn} \exp j(\omega t - q_n x - \psi_n) \exp(-q_n b_0)}{[(q_n\mu_r + P_n)^2 + Q_n^2]^{\frac{1}{2}}} \quad 6.36$$

where $\gamma_n = P_n + jQ_n$ 6.37

$$\psi_n = \tan^{-1} \left(\frac{Q_n}{q_n\mu_r + P_n} \right) \quad 6.38$$

$$P_n = (q_n^4 + \frac{4}{\delta^4})^{\frac{1}{4}} \cos \frac{\theta_n}{2} \quad 6.39$$

$$Q_n = (q_n^4 + \frac{4}{\delta^4}) \sin \frac{\theta_n}{2} \quad 6.40$$

$$\theta_n = \tan^{-1} \frac{2}{\delta^2 q_n^2} \quad 6.41$$

6.4.2 Magnetic Field Strength Within the Shell

The solution of equations 6.16 and 6.18 gives the magnetic field strength within the shell. Considering all the odd harmonics the expression for \underline{H}_{x3r} becomes

$$\underline{H}_{x3r} = \sum_{n=1,3,5}^{\infty} \frac{2\hat{A}_{zn} [q_n \mu_r \gamma_n \text{Cosh} \gamma_n (y+d_o) + \gamma_n^2 \text{Sinh} \gamma_n (y+d_o)]}{\{(q_n \mu_r + \gamma_n)^2 \exp(\gamma_n d_o) - (q_n \mu_r - \gamma_n)^2 \exp(-\gamma_n d_o)\}} \times \\ \times \{\exp j(\omega t - q_n x) \exp(-q_n b_o)\} \quad 6.42$$

and

$$\underline{H}_{y3r} = \sum_{n=1,3}^{\infty} \frac{2j q_n \hat{A}_{zn} [q_n \mu_r \text{Sinh} \gamma_n (y+d_o) + \gamma_n \text{Cosh} \gamma_n (y+d_o)]}{\{(q_n \mu_r + \gamma_n)^2 \exp(\gamma_n d_o) - (q_n \mu_r - \gamma_n)^2 \exp(-\gamma_n d_o)\}} \times \\ \times \{\exp j(\omega t - q_n x) \exp(-q_n b_o)\} \quad 6.43$$

Comparing $|\underline{H}_{x3r}|$ with $|\underline{H}_{y3r}|$

$$\left| \frac{\underline{H}_{x3r}}{\underline{H}_{y3r}} \right| = \left| \frac{\gamma_n}{q_n} \right| \quad 6.44$$

When $\frac{1}{\delta}$ is very large $\gamma_n \gg q_n$ and \underline{H}_{x3r} predominates \underline{H}_{y3r} within the shell. Physical interpretation of the predominance of

H_{x3r} over H_{y3r} is given by Davies⁵¹ in his paper, where he has stated 'when the flux passing from pole to pole is confined to a small section, so it has to be a very high flux density. To drive the flux, a high mmf in the x direction must exist'. When $\frac{\gamma_n}{q_n} \gg 1$ the resultant field strength H_{x3r} becomes in terms of J_{z3r}

$$H_{x3r} = - \frac{1}{2\sigma\mu_0\mu_r j\omega} \sum_{n=1,3,5}^{\infty} \frac{J_{z3r} [q_n \mu_r + \gamma_n \tanh \gamma_n (y+d_0)]}{[q_n \mu_r \tanh \gamma_n (y+d_0) + \gamma_n]} \quad 6.45$$

For a thick shell when $d_0 \gg \delta$, d_0 can be made $d_0 \rightarrow \infty$ and H_{x3r} becomes

$$\left| H_{x3r} \right| \rightarrow \left| \frac{J_{z3r}}{2\alpha^2} \right| \quad \text{when } d_0 \rightarrow \infty, \tanh \gamma_n (y+d_0) \rightarrow 1. \quad 6.46$$

6.4.3 Reaction mmf due to the Eddy Currents Induced in the Shell

The eddy currents induced in the shell due to the pulsating rectangular mmf wave, flow in the axial direction only, and their variations in the peripheral direction and along the depth have been discussed in sub-section (6.4.1). Fig.6.4 shows a section through the shell and the contour ABCD, chosen to calculate the mmf. The nett mmf acting on the countour ABCDA is given by the integral of \underline{H} around ABCDA and also by the total current flowing through it.

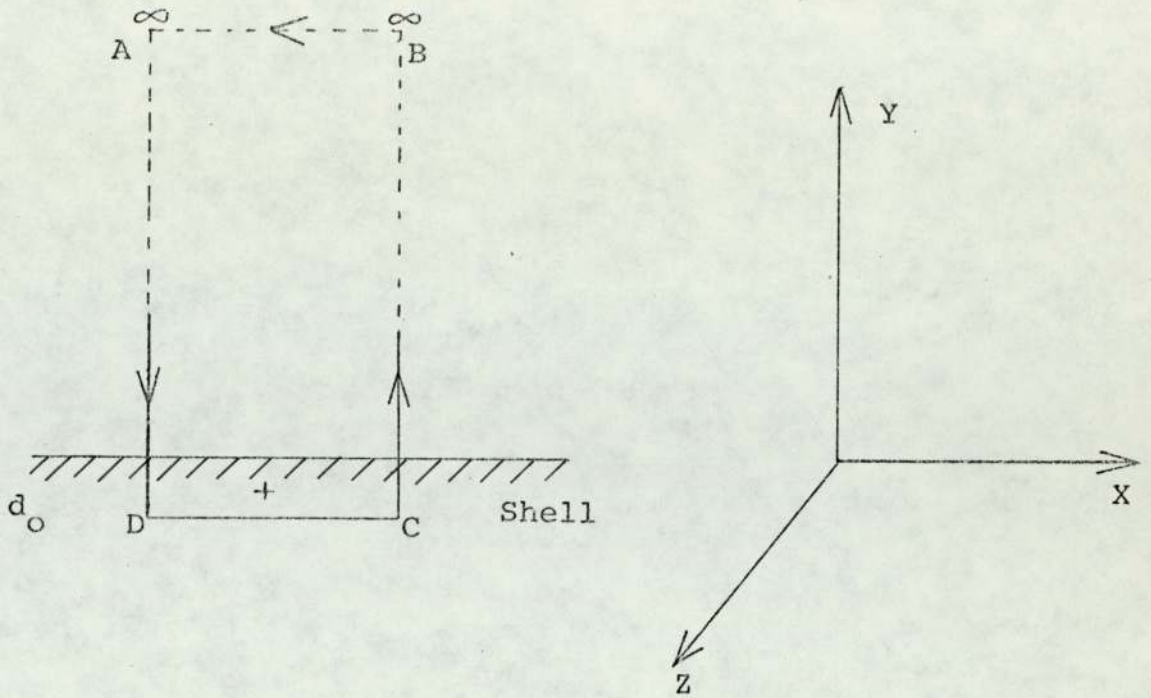


Fig. 6.4 Contour used to Calculate Eddy Current Reaction mmf

Consider now the integral of \underline{H} around the contour ABCDA

$$F_e = \oint \underline{H} \cdot d\underline{l} = \int_D^C \underline{H} \cdot d\underline{l} + \int_C^B \underline{H} \cdot d\underline{l} + \int_B^A \underline{H} \cdot d\underline{l} + \int_A^D \underline{H} \cdot d\underline{l} \quad 6.47$$

\underline{H} must tend to zero as $y \rightarrow \infty$ and since A and B are taken to be at $y \rightarrow \infty$, $\int_B^A \underline{H} \cdot d\underline{l} = 0$ and $\int_C^B \underline{H} \cdot d\underline{l}$ cancels out with $\int_D^A \underline{H} \cdot d\underline{l}$ because they are equal and opposite. Hence the only integral which exists is $\int_D^C \underline{H} \cdot d\underline{l}$ in 6.47. Applying Ampere's circuital law

$$F_e = \int \underline{H} \cdot d\underline{l} = \int_D^C \underline{H} \cdot d\underline{l} = \text{total eddy currents embraced}$$

(line integral, along ABCDA)

$$\text{within ABCDA} = \int \int \underline{J}_{z3r} \, dy \, dx = \quad 6.48$$

surface
integral

This mmf F_e produced by the eddy currents tends to oppose the main flux. With proper limits of integration in equations 6.48 and using the equation 6.34 the mmf F_e can be calculated. Thus considering all the harmonics of \underline{J}_{z3r} , F_e becomes

$$F_e = \int_0^{-d_0} \int \underline{J}_{z3r} dx dy$$

$$F_e = -2j\omega\mu_0\mu_r \int_0^{-d_0} \int \sum_{n=1,3,5}^{\infty} \frac{\hat{A}_{zn} [q_n \mu_r \text{Sinh} \gamma_n (y+d_0) + \gamma_n \text{Cosh} \gamma_n (y+d_0)]}{\{(q_n \mu_r + \gamma_n)^2 \exp(\gamma_n d_0) - (q_n \mu_r - \gamma_n)^2 \exp(-\gamma_n d_0)\}} \times$$

$$\times [\exp\{-q_n (jx+b)\} \exp(j\omega t)] dy dx \quad 6.49$$

Mathematically it is allowed to take out the \sum sign before $\int \int$ hence

$$F_e = -2j\omega\mu_0\mu_r \sum_{n=1,3,5}^{\infty} \int \int \frac{\hat{A}_{zn} [q_n \mu_r \text{Sinh} \gamma_n (y+d_0) + \gamma_n \text{Cosh} \gamma_n (y+d_0)]}{\{(q_n \mu_r + \gamma_n)^2 \exp(\gamma_n d_0) - (q_n \mu_r - \gamma_n)^2 \exp(-\gamma_n d_0)\}} \times$$

$$\times [\exp\{-q_n (jx+b)\} \exp(j\omega t)] dy dx \quad 6.50$$

$$F_e = \sum_{n=1,3,5}^{\infty} \omega \beta_n \int_0^{-d_0} \int [q_n \mu_r \text{Sinh} \gamma_n (y+d_0) + \gamma_n \text{Cosh} \gamma_n (y+d_0)] \exp(-jqx) dy dx$$

6.51

$$\text{where } \beta_n = \frac{-2j\sigma\mu_o\mu_r\hat{A}_{zn}\exp(j\omega t)\exp(-q_n b_o)}{\{(q_n\mu_r + \gamma_n)^2 \exp(\gamma_n d_o) - (q_n\mu_r - \gamma_n)^2 \exp(-\gamma_n d_o)\}}$$

6.52

After integrating 6.51 first with respect to y and then to x , F_e becomes

$$F_e = \sum_{n=1,3,5}^{\infty} \frac{\omega\beta_n}{jq_n} \left[\frac{q_n\mu_r}{\gamma_n} \{1 - \text{Cosh}\gamma_n d_o\} - \text{Sinh}\gamma_n d_o \right] \cdot \exp(-jq_n x)$$

6.53

If the thickness of the shell $d_o \gg \delta$, the depth of penetration, which is true for all practical purposes, in the limit d_o tends to ∞ so that $\exp(-\gamma_n d_o) \rightarrow 0$ and the equation for F_e becomes

$$\text{Lim}_{d_o \rightarrow \infty} F_e = \sum_{n=1,3,5}^{\infty} \left[\frac{\omega\sigma\mu_o\mu_r\hat{A}_{zn}\exp j(\omega t - q_n x)\exp(-q_n b_o)}{\gamma_n q_n \{(q_n\mu_r + \gamma_n)\}} \right] \quad 6.54$$

6.4A Variable Permeability and Electromagnetic Field Quantities

So far the field quantities like eddy current densities J_{z3r} , field strength H_{x3r} and mmf F_e due to eddy currents have been derived from the Maxwell's field equations in sections (6.4.1, 6.4.2 and 6.4.3) in terms of the primary excitation, supply frequency, the physical parameters of the machine like b_o , λ , d_o , and the permeability $\mu_o\mu_r$ and conductivity σ of the shell material, with the assumption that the

permeability of the iron is constant everywhere in the shell and the hysteresis has been neglected. In the reality the permeability at every point in the shell is different because the field is different. So one has to take the variable permeability into account for the derivation of field quantities in the shell.

There are quite a few analytic functions which can represent the normal B-H curve. They are inserted into the Maxwell's equations and rigorous solutions of the electromagnetic field distributions may be obtained. The analytic functions which are applicable to the region above the knee of the curve and into saturation have been listed below.

$$B = aH^b \quad 6.55$$

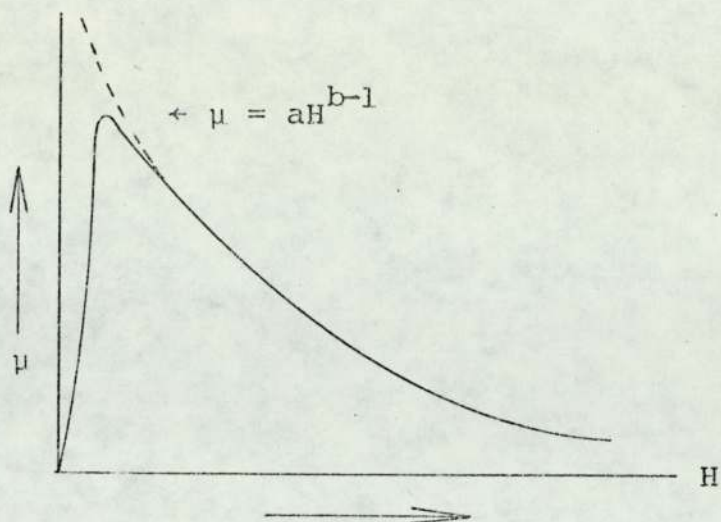
$$B = \exp(H/a + bH) \quad 6.56$$

$$B = (H/a + bH) \quad 6.57$$

$$B = (a - b/H) \quad 6.58$$

$$H = cB + dB^3 \quad 6.59$$

The equation 6.57 is known as Fröhlich equation used by Lim⁵⁴ et al in obtaining a finite different solution for the loss in solid iron. When the value of H is within 100 - 5000 AT/m for the mild steel, the equation 6.58 is the most suitable for representing the region around the knee of the B-H curve. Poritsky and Butler⁵⁵ used the cubic equation 6.59 for the B-H curve. The parabolic equation given by 6.55 is most suitable for representing the saturated region of the B-H curve (typically 1500 - 30,000 AT/m for mild steel), and it



μ vs H for the normal B - H curve and for the analytic representation of $B = aH^b$.

Fig. 6.5

can be used with fair accuracy to represent the whole of the B - H curve except at low values of H . Davies⁵¹ used the equation $(\mu_r \mu_o)^{\frac{1}{4}} H = kH^m$, which can be obtained from the parabolic representation of B - H curve given by 6.55 for the analysis of eddy current couplings and brakes. From the equation $B = aH^b$ it can be shown that $\frac{B}{H} = (\mu_o \mu_r) = aH^{b-1}$ which has been plotted against H and compared with that obtained from the normal B - H curve; in Fig. 6.5. It is interesting to note that when the constant b in equation 6.55 is made 1.0, the relationship between B and H becomes linear and the value of $\mu_r \mu_o$ is simply given by a . The B - H curve for the mild steel (BS4360 Grade 43A, EN3) which is the shell material has been shown in Fig. 6.6. A straight line was obtained when $(\mu_o \mu_r)^{\frac{1}{4}} H$ was plotted against H on a log-log graph paper for the same material, thus proving the Davies' formula $(\mu_o \mu_r)^{\frac{1}{4}} H = kH^m$.

From Fig. 6.7 the values of k , m , a and b have been found out. The steel used for the shell of the experimental machine has the following magnetic properties

$$(\mu_o \mu_r)^{\frac{1}{4}} H = 0.676H^{0.81} \quad 6.60$$

$$\text{and } B = 0.1441H^{0.24} \quad 6.61$$

6.4.4.1 Space Variation of μ_r in the Shell and the Surface Current Density

From the equation 6.42 in sub-section 6.4.2 the field strength on the surface of the shell due to the n th space harmonic current sheet can be derived which varies sinusoidally with time, and given by

$$\underline{H}_{xsn} = \text{Re} \left[\frac{\hat{A}_{zn} \gamma_n \exp\{-q_n(jx + b_o)\}}{q_n \mu_r + \gamma_n} \right] \quad 6.62$$

where \underline{H}_{xsn} is the time average of the field strength. The real part of 6.62 is

$$\underline{H}_{xsn} = \hat{A}_{zn} \left[\frac{P_n^2 + Q_n^2}{(q_n \mu_r + P_n)^2 + Q_n^2} \right]^{\frac{1}{2}} \cos\{\tan^{-1} \left(\frac{Q_n}{P_n} \right) - \tan^{-1} \left(\frac{Q_n}{(q_n \mu_r + P_n)} \right)\} \cos q_n x \exp(-q_n b_o) \quad 6.63$$

P_n and Q_n are functions of $(\mu_o \mu_r)$ given in sub-section 6.4.1. From Davies' analytical relationship between

$(\mu_o \mu_r)^{\frac{1}{4}}$ and H

$$H_{xsn} = [(\mu_o \mu_r)^{1/4(m-1)}] \left(\frac{1}{k}\right)^{1/(m-1)} \quad 6.64$$

and

$$(\mu_o \mu_r) = k^4 (H_{xsn})^{4(m-1)} \quad 6.65$$

Now substituting the values of H_{xsn} in terms of $(\mu_o \mu_r)$ from equation 6.64 into 6.63 one gets

$$\hat{A}_{zn} \left\{ \frac{\left[q_n^4 + \frac{4\mu^2}{c^2} \right]^{\frac{1}{2}}}{\left(\frac{q_n}{\mu_o} \right)^2 \mu^2 + \left(q_n^4 + \frac{4\mu^2}{c^2} \right)^{\frac{1}{2}} + \frac{2P_n q_n \mu}{\mu_o}} \right\}^{\frac{1}{2}} \times$$

$$\times \cos \left\{ \frac{1}{2} \tan^{-1} \frac{2\mu}{q_n^2 c} - \tan^{-1} \left[\frac{Q_n}{\frac{q_n \mu}{\mu_o} + P_n} \right] \right\} \cos q_n x \exp(-q_n b_o) \dots$$

$$- \{ (\mu)^{\frac{1}{4}(m-1)} \left(\frac{1}{k}\right)^{1/(m-1)} \} = 0 \quad 6.66$$

where $\mu_o \mu_r = \mu$ and $c = \frac{2}{\omega \sigma}$

For a particular value of \hat{A}_{zn} , x and n , there is one and only one value for μ which can be found out by solving the equation 6.66. The equation 6.66 is a transcendental equation from which the value μ cannot be found without the help of computer. Newton Raphson's method, which is an iterative method discussed in section 2.3, has been applied to solve the equation. If the left hand side of the equation 6.66 is called as $F(\mu)$ then the first derivative of $F(\mu)$ is

$$\begin{aligned}
 F'(\mu) = & \hat{A}_{zn} \cos q_n \times \exp(-q_n b) \left[\frac{1}{2} \cos\left(\frac{1}{2} \tan^{-1} \frac{2\mu}{q_n c} - \tan^{-1} \frac{Q_n}{c_n}\right) \right] \cdot (U_1)^{-\frac{1}{2}} \times \\
 & \times \left[\frac{4(c_n + Q_n^2)(V_1^{-\frac{1}{2}}) \frac{\mu}{2c} - (V_1^{\frac{1}{2}}) \left[2\mu \left(\frac{q_n}{\mu_0}\right)^2 + 4(V_1^{-\frac{1}{2}}) \frac{\mu}{2c} + \frac{2P\sigma}{\mu_0 n} \right]}{(c_n^2 + Q_n^2)} \right] + \left(\frac{2q_n \mu}{\mu_0} \frac{dP}{d\mu} \right) \\
 & \times \left[-U_1^{\frac{1}{2}} \left(\sin\left(\frac{1}{2} \tan^{-1} \frac{2\mu}{q_n c} - \tan^{-1} \frac{Q_n}{c_n}\right) \right) \left\{ \frac{1}{2} \left(\frac{q_n^2 c}{\mu^2 + \frac{q_n^2 c^2}{4}} \right) - \left(\frac{1}{\left(\frac{Q_n}{c_n}\right)^2 + 1} \right) \right\} \right] \times \\
 & \times \left[\frac{c_n \left[\left(\sin\left(\frac{1}{2} \tan^{-1} \left(\frac{2\mu}{q_n c}\right) \right) \cdot \left(\frac{2\mu}{c}\right) (V_1)^{-3/4} + \frac{1}{2} (V_1)^{\frac{1}{2}} \cdot \left(\cos\left(\frac{1}{2} \tan^{-1} \frac{2\mu}{q_n c}\right) \right) \cdot \left(\frac{q_n^2 c/2}{\mu^2 + \frac{q_n^2 c^2}{4}}\right) \right) \right]}{Q_n \mu_0 + \left(\cos\left(\frac{1}{2} \tan^{-1} \left(\frac{2\mu}{q_n c}\right) \right) \cdot \left(\frac{2\mu}{c}\right) (V_1)^{-3/4} - \frac{1}{2} (V_1)^{\frac{1}{2}} \cdot \left(\sin\left(\frac{1}{2} \tan^{-1} \frac{2\mu}{q_n c}\right) \right) \cdot \left(\frac{q_n^2 c/2}{\mu^2 + \frac{q_n^2 c^2}{4}}\right) \right)} \right] \\
 & \times \left[\left(\frac{1}{k}\right)^{\frac{1}{m-1}} \cdot \frac{1}{4(m-1)} \cdot (\mu)^{\frac{-4m+5}{4(m-1)}} \right]
 \end{aligned}$$

TABLE 6.1

PHYSICAL PARAMETERS OF THE EXPERIMENTAL MACHINE

$\lambda = 452$ mm, $b_0 = 0.64$ mm, $a = 91.25$ mm, $\sigma = 0.085 \times 10^8$

Compole excitation = 10Amps, $f = 50$ Hz, $k = 0.676$

$m = 0.81$, at the point $x = 0$ on the surface of the shell.

FUNDAMENTAL	3rd harmonic	5th harmonic	7th harmonic	9th harmonic
A_{zn}	5515.96	4194.36	2565.46	952.88
q_n	41.70	69.5	97.3	125.1
Initial guess value	0.008	0.009	0.024	.06
1st iteration $(\mu_0 \mu_r)_n$	0.008 902 13	0.013 565 95	0.036 498 09	.097 613 55
2nd iteration $(\mu_0 \mu_r)_n$	0.009 067 44	0.018 663 18	0.050 894 58	0.151 407 06
3rd iteration $(\mu_0 \mu_r)_n$	0.009 071 87	0.022 600 23	0.062 704 13	0.217 685 38
4th iteration $(\mu_0 \mu_r)_n$	0.009 071 87	0.024 097 52	0.067 742 97	0.279 511 30
5th iteration $(\mu_0 \mu_r)_n$		0.024 249 94	0.068 376 09	0.313 284 66
6th iteration $(\mu_0 \mu_r)_n$		0.024 251 32	0.068 384 5	0.319 977 93
		0.024 251 31	0.068 384 5	0.320 185 41
				0.320 185 46

$$\text{where } u_1 = \left[\frac{P_n^2 + Q_n^2}{C_n^2 + Q_n^2} \right] \quad 6.68$$

and

$$V_1 = \left[q_n^4 + \frac{4\mu^2}{c^2} \right] \quad 6.69$$

$$C_n = \left(\frac{q_n \mu}{\mu_0} + P_n \right) \quad 6.70$$

and

$$\begin{aligned} \frac{d}{d\mu} P_n &= \cos \frac{1}{2} \tan^{-1} \left(\frac{2\mu}{q_n \frac{2}{c}} \right) \left[\frac{1}{4} \left(q_n^4 + \frac{4\mu^2}{c^2} \right)^{-3/4} \cdot \frac{8\mu}{c^2} \right] - \\ &- \frac{1}{2} \left[q_n^4 + \frac{4}{c^2} \right]^{1/4} \left(\sin \frac{1}{2} \left(\tan^{-1} \frac{2\mu}{q_n \frac{2}{c}} \right) \right) \left\{ \frac{q_n^2 c/2}{\mu^2 + \frac{q_n^4 c^2}{4}} \right\} \end{aligned} \quad 6.70a$$

Computer programme of iterative method of calculating μ has been given in the appendix (4.Com.Pro.4). The Table 6.1 shows how μ at a particular point on the surface of the shell has been evaluated with the help of iterative Newton Raphson process from its initial guess values for various values of \hat{A}_{zn} and n with other parameters remaining the same.

Table 6.1 shows how the values of $(\mu)_n$ converge to the actual values which satisfy the equation 6.66 with the help of iterative method.

The parabolic fit of the original B-H curve given by equation 6.61 presents some error when $\hat{A}_{zn} \rightarrow 0$ because the

value of μ_r goes very high according to the formula $B = aH^b$ at lower values of H which has been shown in Fig. 6.5. Using a mean value around $\hat{A}_{zn} \rightarrow 0$ the values of $(\mu_o \mu_r)$ were obtained at a particular point on the surface of the shell satisfying the equation 6.66 for various harmonic current sheets (up to 13th) and then substituted into the current density equation 6.35. All the current densities at a point x on the surface of the shell thus obtained for various harmonic current sheets are then added up to get the mean value of J_{-z3r} . The mean value of current densities at various points over the surface of the shell along the line X_4Y_4 for a particular frequency and excitation were measured experimentally, which has been discussed in Section 5.2, and are plotted and compared with those theoretically computed J_{-z3r} (see Fig.6.8). Good agreement is found between measured and calculated values of J_{-z3r} .

6.4.4.2 Relationship Between Supply Frequency and mmf Due to Eddy Currents with Constant Value of a.c. Excitation

The higher the supply frequency, the more is the eddy current induced in the shell, consequently the reaction mmf will be more if the excitation to the compoles remains the same. The relationship between ω and F_e becomes complicated if the variable permeability is introduced into the calculations. Considering only the fundamental component of the pulsating current sheet and space average distribution of \hat{A}_{z1} , it can be shown from equation 6.62 that

$$\underline{H}_{xsl} = \frac{\sqrt{\frac{\omega\sigma}{2}} \mu_0 \hat{A}_{z1} \exp(-q_n b_0)}{q_1 (\mu_0 \mu_r)^{1/2} + \sqrt{\frac{\omega\sigma}{2}} \mu_0} \quad 6.71$$

provided $\frac{1}{\delta} \gg q_1$

Now substituting the value of $\mu_0 \mu_r$ in terms of \underline{H}_{xsl} from the equation 6.65 into 6.71

$$\underline{H}_{xsl} = \frac{c_1 c_3 \sqrt{\omega}}{q_1 k^2 (\underline{H}_{xsl})^{2(m-1)} + c_3 \sqrt{\omega}} \quad 6.72$$

$$\text{where } c_1 = A_{z1} \exp(-q_n b_0) \quad 6.73$$

$$\text{and } c_3 = \sqrt{\frac{\sigma}{2}} \mu_0 \quad 6.74$$

Thus using Davies' formula 6.65 the space fundamental of field strength on the surface of the shell has been related with angular frequency ω , given by

$$q_1 k^2 (\underline{H}_{xsl})^{2m-1} + c_3 \sqrt{\omega} \underline{H}_{xsl} - c_1 c_3 \sqrt{\omega} = 0 \quad 6.75$$

$$\text{or } F(\underline{H}_{xsl}) = 0 \quad 6.76$$

Equation 6.75 has been solved to obtain the value of \underline{H}_{xsl} for a particular value of ω with the help of Newton Raphson's method, discussed in Section 2.3. It is necessary to find out the first derivative of $F(\underline{H}_{xsl})$ which must exist

for this iterative method.

Differentiating $F(H_{xs1})$ with respect to H_{xs1}

$$\frac{\partial}{\partial H_{xs1}} \left[F(H_{xs1}) \right]$$

$$= (2m-1)q_1 k^2 (H_{xs1})^{2m-2} + c_3 \sqrt{\omega} \quad 6.77$$

for low values of ω q_1 becomes $\gg \frac{1}{\delta}$ and the factor $\frac{q_1 \mu_r}{\gamma} \gg 1.0$ hence H_{xs1} becomes

$$H_{xs1} = c_0 \frac{\sqrt{\omega}}{\sqrt{\mu_o \mu_r}} \quad 6.78$$

where $c_0 = \left[\frac{\exp(-q_1 b_o \hat{A}_{z1} \mu_o / q_1)}{q_1} \right]$ 6.79

using 6.65 the relationship between H_{xs1} and ω becomes

$$H_{xs1} = \left(\frac{c_0}{k^2} \right)^{\frac{1}{2m-1}} \cdot (\omega)^{\frac{1}{2(2m-1)}} \quad 6.80$$

From equations 6.54 and 6.62 it can be shown that the mmf (F_{el}) in terms of H_{xs1} is given by

$$F_{el} = \left[\frac{H_{xs1}}{2q_1} \right] \quad 6.81$$

now by solving the general equation 6.75 the values of H_{xs1} can be found out for the range of frequencies from 5 Hz to 600 Hz, while keeping the other parameters unchanged. All

equations in subsection 6.4.4.2 hold good for other harmonics also. Thus theoretically obtained F_{e1} from the equations 6.75 and 6.80 has been plotted against ω in the Fig.7.12 for various values of m (0.81 to 0.70). These curves have been compared with the measured ones in Fig.7.11 and 7.17, and discussed in Chapter 7.

CHAPTER 7

FURTHER EXPERIMENTS AND THE VERIFICATION OF THE THEORETICAL RESULTS

7.1 INTRODUCTION

Measurements of d.c. flux distribution from a search coil of width equal to the tooth pitch, stuck on the armature surface, with the compoles excited only and verifications of the theoretical results of Chapter 2, are given in this chapter.

Measurements of a.c. component of shell flux at various frequencies with the conditions (3) and (4) given in 5.1, were obtained from a shell loop search coil. The relationships between the supply frequency and the a.c. shell flux under various conditions with different levels of steady and pulsating fluxes in the shell are discussed in this chapter.

7.2 MEASUREMENTS OF TOOTH PITCH FLUX DISTRIBUTION

The interpoles of the test machine were excited from a d.c. supply, the main poles were fitted on to the shell and the armature was in position. The output terminals of the tooth pitch search coil in sub-section 4.3.3 were connected across the 'Norma' fluxmeter. The position of the search coil with respect to a compole centre line was obtained with the help of a semi-circular scale fixed on the base plate, and a pointer attached to the shaft of the machine. The flux from the tooth pitch search coil, measured by the compole field reversal method, was maximum when the centre

line of the compole coincided with that of the search coil. Fluxes at other positions of the tooth pitch search coil with respect to the centre line of that particular compole were also measured and are shown in Fig.2.20 and 2.21. In Fig.2.20 a good agreement is found between theoretical p.u. flux distribution using the equations 2.12 and 2.2, and experimental measurements, but the curves drawn on p.u. basis suppress many truths in the actual distribution. So the magnitudes of the tooth pitch fluxes are calculated from the theoretically derived equations 2.12 and 2.2 and plotted along the armature surface and compared with the measured values. (See Fig.2.21.)

7.2.1 Discussion and Conclusions

From Fig. 2.21 the theoretical flux distribution is greater than the measured values all along the armature surface and the maximum deviation between those two curves is found to be about 30%, which occurs at the centre line of the compole. This over-estimation of the tooth pitch flux is because the theoretical model considered in Chapter 2 excludes the slots in the armature. The ratio of theoretical and experimental tooth pitch flux at each point on the armature surface are plotted in Fig. 2.22 as multiplying factor k_{α} versus the distance from the centre line of the compole. The value of k_{α} varies from 0.77 at the centre of the compole to 0.91 near the mainpole. To take the effect of slots into account the theoretical curve should be multiplied at each point by the corresponding values of k_{α} .

Solutions with elliptic functions and integrations and the nonlinear multi-variable optimisation techniques discussed in section 2.5 for the field problem in the interpolar region having five corners in the z plane, give almost the same tooth pitch flux distribution as obtained from equations 2.12 and 2.2. Hence it can be suggested that from the physical parameters of the machine and the excitation to the compole, one can estimate the tooth pitch flux distribution over the armature surface with reasonable accuracy, using the much simpler mathematical solutions of the field problem having compole and mainpole both extended to infinity. The multiplying factor k_{α} should be used to take the slots into account.

7.3 MEASUREMENTS OF D.C. FLUX DENSITY IN THE SHELL

The mainpoles of the test machine were excited from a d.c. supply to its rated value in steps with the armature in position. Mainpole ampere turns versus flux density in the shell are shown in Fig. 7.1. This was obtained by measuring the shell flux with the help of a shell loop search coil nearest to the compole shown in Fig. 4.5. by the method of field reversal. Fluxes were measured with 'Norma' flux-meter. Fig. 7.1 shows that 0.51 T is the flux density in the shell due to the mainpole excited to the rated value of ampere turns 1825 AT/per pole. The compoles and mainpoles were then both excited from d.c. sources. The chosen values of d.c. compole excitation were 4.5A, 9A, 11.25A and 13.5A, and the excitation to the mainpole was kept fixed at 0.68A

(1825AT/mainpole). The d.c. flux densities in the shell were measured with mainpole and compole both excited, using the same shell loop search coil nearest the compole and are given in the Table 7.1. These are generally the values of d.c. flux levels in the shell of the machine at its working condition when supplied from various types of rectified sources, discussed in Chapter 3. The values of these d.c. flux densities are used in Section 7.4. It should be mentioned here that the shell flux density at the other side of the compole decreases as the compole excitation increases.

MAINPOLE EXCITATION	COMPOLE EXCITATION	SHELL FLUX DENSITY
0.68A (d.c)	4.5A (d.c)	0.65T
0.68A (d.c)	9A	0.69T
0.68A (d.c)	11.25A	0.71T
0.68A (d.c)	13.5A	0.73T

TABLE 7.1

7.4 EXPERIMENTS WITH SUPERPOSED A.C. - D.C. SUPPLY AND THE RELATIONSHIP BETWEEN THE SUPPLY FREQUENCY AND THE A.C. SHELL FLUX WITH DIFFERENT LEVELS OF STEADY AND PULSATING FLUXES IN THE SHELL

On top of the d.c. excitation, purely sinusoidal a.c. excitations of various frequencies ranging from 5 Hz to 600 Hz

were superimposed and fed to the compole. Superposition of a.c. and d.c. supply is discussed in detail in Section 4.9 and is shown in schematic circuit diagram (see Fig.4.17). The peak to peak value of the d.c. current from the rectified power sources can be obtained by integrating the fundamental voltage equation

$$e = I_{dc} R_A + E + L \frac{di}{dt} \quad 7.1$$

for the rectifier and motor armature circuit in Chapter 3, within the time interval t_1 and t_2 . Thus the peak to peak current

$$\Delta I = \frac{1}{L} \int_{t_1}^{t_2} (e - E_{dc}) dt \quad 7.2$$

where t_1 is the time at which the current is minimum and t_2 the time at which the current is maximum. L is the armature circuit inductance E_{dc} is the average value of d.c. voltage which is equal to $(I_{dc} R_A + E)$. I_{dc} is the average value of d.c. current and E is the armature counter emf. E_{dc} can be calculated from the a.c. line voltage and firing angle with the help of formula given by Tsivitse and Schiff²⁹. The time integral $\int_{t_1}^{t_2} (e - E_{dc}) dt$ can be determined by calculating the area between the voltage curve e and the voltage line E_{dc} . This integral has been evaluated for various types of thyristor supply and plotted in terms of $\frac{E_{dc}}{E_{do}}$ in Tsivitse and Schiff's paper. E_{do} is the maximum value of average d.c. voltage. Measuring the value of L and using the equation

7.2, the magnitudes of peak to peak current from various rectifier sources were calculated, considering the ratio of compole mmf to armature reaction mmf which is equal to 1.44 given in Chapter 4.

20A, 14A, and 8A p-p values of a.c. excitation were chosen as suitable and were used throughout the experiments. An oscilloscope was accurately calibrated to measure the a.c. and d.c. currents in the compole circuits. The magnitude of a.c. excitation for a particular frequency could be altered by varying the values of capacitance and resistance, the gain of the amplifier, and the input voltage of the oscillator. A wave analyser and a C.R.O. were used to make sure that the a.c. excitation was purely sinusoidal throughout the experiments.

The $(\frac{d\phi}{dt})$ signal from a shell loop search coil nearest to the compole was integrated and the mean values of the fundamental of the flux wave were measured with the help of a wave analyser for a set value of a.c. excitations to the compole, with the d.c. excitations to the compole being varied from 4.5A to 13.5A in steps. The mainpole excitation was kept fixed at 0.68 A. Oscillograms of $(\frac{d\phi}{dt})$ wave from a shell loop search coil under various a.c. and d.c. fluxing conditions in the shell and at different supply frequencies, are shown in Fig. OS7.1 to OS7.10. Oscillograms show that the distortion of voltage waveforms is not much even when the frequency is increased to 600 Hz. Considering the

distortion in the a.c. excitation from the oscillator and KLF amplifier, 5 Hz was the minimum permissible limit of frequency. Families of fundamental flux versus frequency (ranging from 5 Hz to 600 Hz) curves are shown in Fig. 7.2 to 7.4, for various values of d.c. excitations to the compole with constant excitation to the mainpole. It is to be noted that the flux frequency curves with constant a.c. excitation are similar to those obtained by plotting fundamental flux against slip with constant excitation mmf of eddy current couplings (see Fig. 7.5 taken from Wright's⁵⁶ thesis)

The curves in Fig. 7.2 to 7.4 are extrapolated to meet the Y axis in order to obtain the fluxes in the shell at zero frequency which has been called ϕ_0 . For particular values of a.c. and d.c. excitations the reduction of fundamental shell flux, which is the difference between ϕ_0 and ϕ due to the eddy currents induced in the shell, is plotted in a log-log paper. It is discovered that a straight line runs from 25 Hz to 600 Hz which shows that there exists a power relationship between $\Delta\phi = \phi_0 - \phi$ and frequency f when $f > 25\text{Hz}$. A family of curves of $\Delta\phi$ versus f on log-log paper having almost the same slope within the frequency range 25 Hz to 600 Hz, was obtained for various values of a.c. excitations and is shown in Fig. 7.6. Families of these log-log plots of $\Delta\phi$ VS. f are shown in Fig. 7.6 to 7.9 for various values of d.c. excitations to the compoles with other conditions remaining the same. It is found that the slope changes with

the change in d.c. excitation to the compole (see Fig. 7.6 to 7.9). Fig. 7.10 also shows how the experimentally obtained fundamental flux reduction curves are changed in an orderly manner when the magnitude of steady d.c. flux level in the shell varies from 0.65 T to 0.73 T, given in Table 7.1. The curve OB in Fig. 7.11 is the plot of calculated reaction mmf due to eddy current against frequency by solving the equation 6.75 with $m = 0.758$. The curve OA in Fig. 7.11, is obtained experimentally by plotting the reductions of fundamental flux against frequency when the resultant d.c. flux density in that half of the shell where the shell loop search coil 1 (see Fig.4.5) is sitting, is 0.69T. The shape is similar, as can be seen from Fig. 7.11, if they are plotted in p.u. basis.

The values of fundamental flux reduction and the reaction mmf at 600 Hz for the curves OA and OB respectively, are taken as maximum and equal to unit, in Fig. 7.11. Good agreement is found between OA and OB within the frequency limit 30 Hz to 600 Hz, because the shell which is already crowded with d.c. flux becomes saturated with pulsating a.c. flux produced by the a.c. excitation of the compoles. The deviation between OA and OB is quite high (about 25%) below 25 Hz, because the analytical relationship between ω and F_{e1} is based on the assumption that $\frac{1}{\delta} \gg q$ which means the equation 6.71 only holds good when frequency is high.

The close similarity of two families of curves in

Fig. 7.10 and 7.12 suggest that the index m changes with d.c. level of flux in the shell. How the theoretical curves in Fig. 7.12 are drawn have been explained in section 6.4.4.2. As m changes the fundamental reaction mmf changes, which is governed by equation 6.75, and consequently the slopes of the curves relating the reduction of fundamental flux with frequency at a constant value of a.c. excitation are altered with the help of analytical relationships between F_{el} , ω and m in Chapter 6, the variation of fundamental reaction mmfs with index m at a constant a.c. excitation to the compole are tabulated for various frequencies (see Table 7.2).

The whole method which has been discussed earlier in this section, for the estimation of fundamental reaction mmf due to eddy currents in the shell from the experimental $\Delta\phi$ VS. f curves and equations in Chapter 6 considering the physical parameters of the machine with various steady flux density levels in the shell and a constant a.c. excitation to the compole can be summarised in the following steps.

Step 1

Get the value of m for which best match is obtained between the theoretical reaction mmf curve and the experimental curve for a particular value of d.c. flux level in the shell. Use the formula 6.80 and 6.81 of Chapter 6 for calculating F_{el} . The computer programme for iterative solution of equation 6.80 is given in Appendix (4.Com.Pro.3). The values of physical parameters of the machine, a.c. excitation to the

TABLE 7.2

VARIATION OF FUNDAMENTAL REACTION MMF F_{el} WITH INDEX m

Dimensions of experimental machine used for calculations

$b_o = 0.64 \text{ mm}, \quad \lambda = 452 \text{ mm}, \quad a = 91.3 \text{ mm}$

$\sigma = 0.085 \times 10^8 (\Omega\text{m})^{-1} \quad k = 0.676$

Compole a.c AT/Pole (peak value)	Frequency in Hz	Values of index m used	Fundamental reaction mmf (AT)
1200	50	0.81 0.78 0.76 0.74 0.72	35.6 64.2 94.8 135 181
1200	100	0.81 0.78 0.76 0.74 0.72	56.5 98.2 137 182 228
1200	300	0.81 0.78 0.76 0.74 0.72	106 165 209 251 288
1200	600	0.81 0.78 0.76 0.74 0.72	145 209 250 286 316

compole, and initial guessed value of surface H are supplied as the input data for the computer programme.

Step 2

After knowing the proper value of m which satisfies all the conditions, one can find F_{e1} theoretically using the same equations of Chapter 6.

7.4.1 Discussion and Conclusions

- (1) m for the mild steel grade BS 4360, Grade 43A used for the shell is 0.81, but when the d.c. flux level in the shell is 0.73T at which the d.c. machine operates, the value of m goes down to about 0.75 consequently the reaction mmf due to eddy current changes for a particular value of a.c. excitation to the compole and the supply frequency, given in table 7.2.
- (2) Only the fundamental reaction mmf has been considered in Section 7.4 and the higher order harmonics are neglected because of the following two reasons which reduce harmonics by the factor $\frac{1}{n^2}$.
 - (a) The magnitudes of the primary mmf distribution in space are reduced by the factor $\frac{1}{n}$, and
 - (b) for any harmonic q, which is equal to $\frac{2\pi n}{\lambda}$, comes into the denominator of the equation 6.81, so that F_{en} is again reduced by the factor $\frac{1}{n}$.

- (3) The experiments so far carried out in section 7.4 does not include the reaction mmf produced by the armature winding. So the next step would be to include armature reaction mmf in the experiments.

7.4.2 Experiments Including Armature Reaction

The experimental set-up described in Section 7.4 was kept unaltered, except that the armature was excited from a separate d.c. source. Brushes were placed at the correct position on the commutator surface so that the peak of the static triangular armature mmf lies opposite the compole centre line. The method adopted for brush setting has already been discussed in sub-section 4.6.2. Arrangements were made to block the rotor, and the armature temperature was kept low by cooling. Thus a reasonable simulation of a thyristor fed d.c. machine at its running condition was achieved and the experiments were carried out as discussed in 7.4. A family of curves were obtained by plotting the fundamental shell flux against frequency with compole a.c. excitations 20A, 14A and 8A p-p. D.c. excitations to the compole, mainpole and armature were 20A, .68A and 20A respectively (see Fig. 7.13).

From the curves in Fig.7.13, $\Delta\phi$ against frequency is plotted on log-log paper (see Fig. 7.14) showing the power relationship between $\Delta\phi$ and f above 30 Hz. The average slope of these curves in Fig. 7.14 is 0.355 within the frequency range 30 to 600 Hz. The families of curves in Fig. 7.14 and 7.8 are compared and found to be almost the same, because the

mean level of d.c. shell fluxes which govern the slope of $\Delta\phi$ VS. f curves are almost equal in both the cases which were verified theoretically and from the experimental measurements. The resultant flux density in the shell due to the combined action of two opposite mmfs (compole and armature reaction) and the flux density due to the compole mmf acting along in the magnetic circuit were evaluated theoretically by using the Skobelev's³⁴ equivalent circuits for the magnetic paths in d.c. machine, which has already been discussed in detail at the end of Chapter 3. The elements of the equivalent circuit were calculated from the machine dimensions with the help of the formula given in Chapter 3. To confirm that the index m varies with the d.c. level of the shell flux the experiments were continued with the value of excitation to the mainpole reduced from .68A to .39A, keeping other conditions unaltered and the flux frequency curves are shown in Figs. 7.15 and 7.16. They also show that as the d.c. flux level in the shell goes down the value of the slope increases even with the presence of armature reaction mmf in the magnetic circuit. Good agreement is found between the theoretical and experimental results shown in Fig. 7.17 where 0.77 is used for the value of m .

7.5 DISCUSSION AND CONCLUSIONS

From the experimental results discussed in Section 7.4.2 it can be concluded that in a d.c. machine carrying

pulsating component of a.c.flux at its running condition a power law exists between the frequency and the amount of a.c. flux reduction due to the eddy currents induced in the shell and the power depends on the d.c. flux level in the shell. The mmf drop due to the eddy currents reaction mmf in the analysis tending to oppose the main flux can be estimated if the calculations are done in steps which are given at the end of Section 7.4. Even if the extra ampere turns are applied from the compole the resultant commutating flux thus obtained may not reach the required value for satisfactory commutation, hence the whole process is to be repeated and compole ampere turn has to be altered each time until a balance is reached when compole mmf can push the right amount of a.c. flux through the comm-zone. This sort of ampere turn adjustment has to be carried out after the machine being completed.



51

Davies' μ -H relationship which he applied for his eddy current coupling to take into account the variable μ , is also applicable in the shell eddy current problem; thus the generality of his formula is proved.

Experiments with superposed a.c. - d.c. supply discussed in Section 7.4 show that the index m is a function of d.c. flux density in the shell, which is not found in the literature.

CHAPTER 8

SUGGESTIONS FOR FURTHER WORK

- (1) The eddy current distribution in the shell has been obtained only for one supply frequency 50 Hz, and one excitation. The experiments should be continued with higher frequencies and higher compole excitation.
- (2) No experiments have been performed to measure the phase angle between the a.c. component of compole flux and the corresponding current. This has been left for future work.
- (3) The experiments in Chapter 7 have been performed with an understanding that the main field is excited from a smooth d.c. source. Experiments should be continued in future with superposed a.c. - d.c. supply in the main field also, which is the case when the main field of a d.c. motor is not separately excited.
- (4) Experiments with superposed a.c. - d.c supply discussed in Section 7.4, should be carried out with higher values of d.c. flux level in the shell to find out the relationship between the index m and d.c. flux density.
- (5) Expression for the phase angle of the reaction mmf or current density or field strength has not been derived in Chapter 6, but one can easily find out by mathematical manipulation of hyperbolic terms which are functions of depth and of Y_n in equations 6.42, 6.43, 6.34 and of only complex γ_n term in the equation 6.54 of

Chapter 6.

- (6) The complex shell impedance of the shell can be obtained with the help of equation $\frac{E_{z3}}{H} = Z_{y3}$. Equations describing the magnetic field strength and electric field strength in the shell which will be substituted in the impedance equation have already been given in Chapter 6.

The power loss in the shell due to eddy currents can be obtained theoretically by integrating $(\underline{J}_z)^2/\sigma$ through the shell volume and over a period of time

$$w = \int \int \int \frac{\underline{J}_z^2}{\sigma} dt dx dy dz$$

The expression \underline{J}_z can be obtained from Chapter 6.

- (7) Experimentally obtained eddy current distribution on the side and top surfaces of the shell as shown in Fig. 5.10 of Chapter 5 might be explained by considering the case where the flow of current from the electrodes shown in Fig. 8a, is similar to that in Fig. 5.10. The top and side surfaces of the shell can be developed on the z-plane and the electrodes of potentials V and zero have been placed as shown in Fig. 8a.

The distribution of flow of current can be obtained by solving the field problem with the help of Schwarz-Christoffel transformation. It can be shown that the

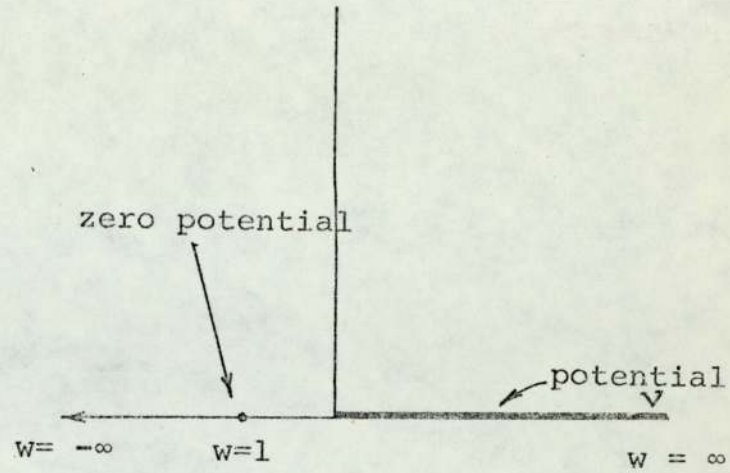
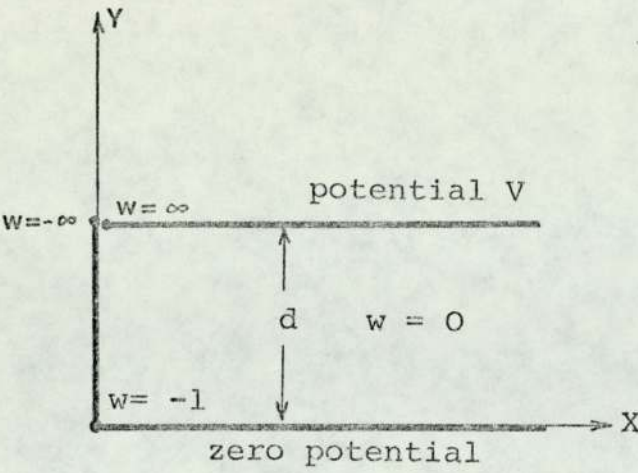


FIG. 8a Z PLANE

FIG. 8b W PLANE

equation connecting z and w plane is

$$z = -\frac{d}{\pi} \text{Log} \left[\frac{(1+w)^{\frac{1}{2}} - 1}{(1+w)^{\frac{1}{2}} + 1} \right] + j d \quad (8.1)$$

Using the ξ plane where the field is regular the current density J becomes

$$J = \frac{\sqrt{w+1}}{d} \quad (8.2)$$

$$J = \frac{\left[1 - \exp\left(\frac{-z\pi}{d}\right) \right]}{d \left[1 + \exp\left(\frac{-z\pi}{d}\right) \right]} \quad (8.3)$$

Along the x-axis in Fig. 8a the current density has only one component which is J_X given by

$$J_X = \frac{1}{d} \tanh \left(\frac{\pi x}{2d} \right) \quad (8.4)$$

From the experimental evidence it is seen that the current

density distribution along U_1 U_2 U_3 in Fig. 5.18 is tan hyperbolic in nature which is also proved from the analytical expression 8.4

REFERENCES

REFERENCES

1. Kusko, A. : 'Solid-State d.c. motor drives',
The MIT Press, 1969.
2. Thielers, G. : 'A new aspect of commutation',
ASEA, March, 1946.
3. Langsdorf, A.S.: 'Principles of d.c. Machines',
Mc Graw-Hill, N.Y., 1940.
4. Lamme, B.G. : 'A theory of commutation and its
application to interpole machines',
AIEE Transactions, vol.30, part 3,
1911, pp.2359-2404.
5. Dreyfuss, A. : 'Die stromwendung grosser
Gleichstrommaschinene', Julius
Springer, Berlin, 1929, in German.
6. Linville, T.M. 'Commutation of large d.c. motors
and Rosenberry, G.M. Jr.: and generators', AIEE, Jan.1952,
pp. 326-36.
7. Alger, J.R.M. 'Analysis of d.c. machine commutation',
and Bewley, D.T. : Trans. AIEE, Vol.76, 1957, pp.399-413.
8. Tustin, A. and 'The emf induced in the armature
Ward, H. : coils of d.c. machines during
commutation', Proc. IEE, Vol.109,
part C, pp.456-74.
9. Tustin, A. : 'Direct current machines for control
systems', Spon, 1952.

10. Ward, H. : 'Emf induced in the end turns of armature coils during commutation', Proc. IEE, Vol.109, part C, April 1962, pp. 475-87.
11. Tarkanyi, M.,
Ward, H. and
Tustin, A. : 'Electronic computers applied to commutation analysis', Proc. IEE, vol.109, part C, April 1962, pp.488-507.
12. Ewing, J.S.
and Patel, B.L. : 'Contribution to commutation analysis', Trans. IEEE, PAS, 1972, pp.1663-68.
13. Clayton, A.E.
and Hancock, N.N. : 'Performance and design of direct current machines', Pitman, 1959.
14. Soper, P.F. : 'Carbon brush contact phenomena in electrical machinery', Proc. IEE, Vol.96, part II, 1949, pp.645-655.
15. Erdelyi, E.A.
and Fuchs, E.F. : 'Commutating region fields of non-linear d.c. machines', Electrical Machines in the Seventies, Dundee Conference.
16. Tozoni, O.V. : 'Mathematical models for the evaluation of electric and magnetic field', Iliffe Books. Ltd., 1968, London.
17. Gibbs, W.J. : 'Conformal Transformations in Electrical Engineering', Chapman and Hall, 1958.
18. Binns, K.J. and
Lawrenson, P.J. : 'An analysis and computation of electric and magnetic field problems', Pergamon Press, 1963.

19. Lawrenson, P. and Gupta, S.K. : 'Conformal transformation employing direct search techniques of minimisation', Proc. IEE, Vol.115, March, 1968, pp. 427-31.
20. Binns, K.J. : 'The magnetic field and centering force of displaced ventilating ducts in machine cores', Proc. IEE, Vol. 108, Part C, 1964.
21. Howe, D. : 'The applications of numerical methods to the conformal transformation', J. Inst. Maths. Applics., Vol.12, 1973, pp. 125-36.
22. Krylov, V.I. : 'Approximate calculation of integrals', Mc Millan, London, New York, 1962.
23. Alexanderson, E.F.W., Edwards, M.A. and Willis, C.H. : 'Electronic speed control of motors', Trans. AIEE, Vol.57, June, 1938, pp.343-52.
24. Vedder, E.H. and Puchlowski, K.P. : 'Theory of rectifier d.c. motor drive', Trans. AIEE, Vol.62, 1943, pp.863-69.
25. Schmidt, A., Jr. and Smith, W.P. : 'Operation of large d.c. motors from controlled rectifiers', Trans. AIEE, Vol. 67, part 1, 1948, pp.679-83.
26. Merrett, J. : 'Thyristor speed control of d.c. shunt motors from a single phase supply', Mullard Technical Communications, Vol.8, No.80, March, 1966, pp.298-313.

27. Merrett, J. : 'Thyristor speed control circuit design for d.c. shunt motors supplied from a.c. mains', Mullard Technical Communications, Vol.9, No.84, November, 1966.
28. Ewing, J.S. : 'Lumped circuit impedance representation for d.c. machines', Trans. IEEE, PAS, Vol.87, No.4, April, 1968, pp.1106-10.
29. Tsivitse, P.J. and Schiff, A.N. : 'Static power sources for d.c. motors', Iron and Steel Engineer, February, 1969, pp.67-76.
30. Zolotariov, P.A. : 'The prediction of commutation in rectifier supplied traction motors', Bulletin of the Inst. of Higher Education - Electro-mechanics (NL0078.030) Russia, No.12, 1958, pp.35.
31. Skobelev, V.E. : 'A method of calculating the emf's produced in the commutating coils of an armature by the a.c. components of the pulsating currents and fluxes', Electromechanics (NLL 0078.030), No.6, 1959, pp.41 (Russia).
32. Ramsden, V.S. : 'The loss in solid poles of synchronous machines on load', Ph.D. thesis, University of Aston in Birmingham, 1972.

33. B.S.933 'Magnetic Materials for use under combined d.c. and a.c. magnetisation', 1941.
34. Carter, R.O. and Richards, D.L. : 'The incremental magnetic properties of silicon-iron alloys', Proc. IEE, Vol.97, part II, 1950, pp.199-214.
35. Mondal, R.K., Bhattacharya, S.N. and Choudhury, J.K. : 'Measurement of incremental magnetic loss by bridge and wattmeter methods', J. Inst. Engrs. (India), Elect. Engg. Div., Vol. 46, EL6, 1966, pp.464-477.
36. Choudhury, J.K., Mondal, R.K. and Bhattacharya, S.N. : 'A current feed back method for correction of flux wave distortion in incremental magnetic testing', J.Inst. Engrs. (India), Elect. Engg. Div., Vol.47, EL3, 1967, pp.81-94.
37. Chubb, L.W. and Spooner, T. : 'The effect of displaced magnetic pulsations on the hysteresis loss of sheet steel', Proc. AIEE, Vol.34, part 2, 1915, pp.2321-42.
38. Charlton, O.E. and Jackson, J.E. : 'Losses in iron under the action of superposed alternating and direct current excitations', Trans. AIEE, Vol. 44, 1925, pp. 824-31.
39. Edgar, R.F. : 'Loss characteristics of silicon steel at 60 cycles with d.c. excitation', Trans. AIEE, Vol.52, 1933, pp.721-26.

- 40.Sims, L.G.A. and
Clay, D.L. : 'Incremental magnetisation',
Wireless Engineer, Vol.12, 1935,
pp.238-45 and 312-320.
- 41.Rosenbaum, M. : 'Hysteresis loss in iron taken
through unsymmetrical cycles of
constant amplitude', JIEE, Vol.48,
1912, pp.534-45.
- 42.Niwa, Y. and
Asami, Y. : 'Magnetic properties of sheet steel
under superposed alternating field
and unsymmetrical hysteresis losses',
Researches of the Electrochemical
Laboratory, Tokyo, No.124, 1923.
- 43.Coales, J.D. 'On a method of using transformers
as choking coils and its application
to the testing of alternators',
JIEE, Vol.42, 1908, pp.412-54.
- 44.Boyajian, A. : 'Theory of d.c. excited iron-core
reactors and regulators', Trans.
AIEE, Vol.43, 1924, pp.919-36.
- 45.Johnson, W.C.,
Merrell, B.C. and
Alley, R.E. : 'Universal curves for d.c.
controllable reactors', Trans.
AIEE., Vol.68, 1949, pp.31-40.
- 46.Vallauri, A. : 'Hysteresis in iron for
asymmetric cycle of magnetisation',
Assoc. Elect., Ital., Vol.15,
1911, 79-92.

47. Hammond, P. : 'The calculation of the magnetic field of rotating machines', Proc. IEE, part C, 1962, pp.508-15.
48. Moullin, E.B. : 'The principles of electromagnetism', Clarendon Press, 1955, pp.238.
49. Poritsky, H. and Jerrard, R.P. : 'Eddy current losses in a semi-infinite solid due to nearby alternating current', AIEE Transactions 1954, Vol.73, pp.97-106.
50. Dodd, C.V. and Deeds, W.E. : 'Analytical solutions to eddy current probe-coil problem', J. App. Phy., Vol.39, No.6, May, 1968, pp.2829-38.
51. Davies, E.J. : 'Experimental and theoretical study of eddy-current couplings and brakes', IEEE, August, 1963, pp.401-17.
52. Davies, E.J. : 'General theory of eddy-current couplings and brakes', Proc. IEE, Vol. 113, No.5, May 1966, 825-37.
53. Wood, A.J. and Concordia, C. : 'An analysis of solid rotor machines, pt. II, Effect of Curvature', Trans. IEEE, 1960, 78, (III), pp.1666.

54. Lim, K.K. and
Hammond, P. : 'Universal loss chart for the calculation of eddy-current losses in thick steel plates', Proc. IEE, 197, (4), pp.857.
55. Poritsky, H. and
Butler, J.M. : 'A.c. flux penetration into magnetic materials and saturations', IEEE Trans. Communications and Electronics, 1964, 83, pp.99.
56. Wright, M.T. : 'Steady-state and transient performance of eddy-current coupling', Ph.D. Thesis. The University of Aston in Birmingham, November, 1972.
57. Freeman, E.M. : 'The calculation of harmonics due to slotting in the flux density waveform of a dynamo electric machine', Proc. IEE, Vol.109, part C, No.16, June 1962, pp.578-88.
58. Byrd, P.F. and
Friedman, M.D. : 'Handbook of elliptic integrals for engineers and scientists'. Springer-Verlang, N.Y. 1971.
59. Dwight, H.B. : 'Tables of integrals and other mathematical data', Mc Millan, N.Y. 1966.

BIBLIOGRAPHY

- (I) Abramowitz, M. and Segun, I.A. : 'Handbook of Mathematical Functions', Dover, 1972.
- (II) Agarwal, P.D. : 'Eddy current losses in solid and laminated iron', Trans. IEEE, 1969, 78, (1), pp.169.
- (III) Bewley, L.V. : 'Two dimensional fields in electrical engineering', Dover, 1963.
- (IV) Bowden, A.L. : 'A study of magnetic non-linearity and finite length effects in solid iron subjected to a travelling mmf wave', Ph.D. Thesis, University of Aston in Birmingham, 1973.
- (V) Boz orth, R.M. : 'Ferromagnetism', Van Nostrand, 1951.
- (VI) Carter, F.W. : 'Magnetic field of dynamo electric machine', Journal IEE, pp.1115-38, 1926.
- (VII) Das, S. : 'An experimental study of the face plate eddy current coupling', M.Sc. dissertation. The University of Aston in Birmingham, 1973.
- (VIII) Davies, E.J. : 'Two experimental studies in dynamoelectric machinery', Part one, Ph.D. Thesis, University of Bristol, 1961.

- (IX) Dunaiski, R.M. : 'The effect of rectifier power supply on large d.c. motors', IEEE, June 1960, pp.253-58.
- (X) Fischer, J. and Moser, H. : 'The representation of the magnetisation curve by simple algebraic and transcendental functions', Archiv Electrotechnik, 1956, 42, pp.286. In German.
- (XI) Grimshaw, K.P. : 'Electromagnetic principles of commutation in d.c. machines', International Journal Electrical Engineering Education, Vol.2, Sept. 1964, pp.59-69.
- (XII) King, K.G. : 'The application of silicon controlled rectifiers to the control of electrical machines', Proc. IEEE, Vol. 110, No.1, January 1963, pp.197.
- (XIII) Lammeraner, J. and Stafl, M. : 'Eddy currents', Iliffe, 1966.
- (XIV) Mc Connell, H.M. : 'Eddy current phenomena in ferro-magnetic materials', AIEE, Trans. 1954, 73, (I), pp.226.
- (XV) Morse, P.M. and Feshbach, H. : 'Methods of theoretical physics', Mc Graw-Hill, 1953.
- (XVI) Mukherjee, K.C. and Neville, A. : 'Magnetic performance of identical double slotting', Proc. IEE, Vol.118, No.9, 1971.

- (XVII) Pillai, K.P.P. : 'Predetermination of generated voltage in heteropolar inductor alternators', Proc. IEE, Vol. 122, No.11, Nov. 1975.
- (XVIII) Pohl, R. : 'Electromagnetic and mechanical effects in solid iron due to alternating or rotating magnetic fields', Proc. IEE, 1944, 91, pp.239.
- (XIX) Puchlowski, K.P. : 'Electronic control of d.c. motors', Trans. AIEE, Vol.62, 1943, pp.870.
- (XX) Robinson, C.E. : 'Redesign of d.c. motors for applications with thyristor power supplies', Trans. IEEE, Vol.I, GA-4, No.5, 1968, pp.508.
- (XXI) Say, M.G. : 'Performance and design of alternating current machines', Pitman, 1936.
- (XXII) Shobert, E.I. : 'Carbon Brushes', Chemical Publishing, 1965.
- (XXIII) Stoll, R.L. : 'The Analysis of Eddy Currents', Clarendon Press, Oxford, 1974.

APPENDIX 1

EVALUATION OF ELLIPTIC INTEGRALS OF FIRST AND SECOND KINDS

The integral
$$\int_0^w \frac{dw}{\sqrt{(1-w^2)(1-k^2w^2)}} = \int_0^\phi \frac{\theta}{\sqrt{1-k^2\text{Sin}^2\theta}} \equiv F(\phi, k) = \text{sn}^{-1}(w, k)$$

$$w = \text{Sin}\theta \qquad \text{A.1.1}$$

is known as incomplete elliptic integral of first kind when $\phi = \pi/2$ the integral becomes complete elliptic integral of first kind denoted by 'K'.

The integral
$$\int_0^w \frac{\sqrt{1-k^2w^2}}{\sqrt{1-w^2}} dw = \int_0^\phi \sqrt{1-k^2\text{Sin}^2\theta} d\theta \equiv E(\phi, k)$$

A.1.2

is known as incomplete elliptic integral of second kind and denoted by E. The number k is called modulus. The value of k lies within $0 < k < 1$. k' is known as complementary modulus and is related to k by

$$k' = \sqrt{1-k^2} \qquad \text{A.1.3}$$

Flow diagram of computer programme to evaluate $K(\alpha)$, $E(\alpha)$, $F(\phi, \alpha)$, and $E(\phi, k)$ using Arithmetic - Geometric mean method discussed by Freeman⁵⁷ is given

$$\alpha = \text{Sin}^{-1}k \qquad \text{A.1.4}$$

APPENDIX 2

EVALUATION OF ELLIPTIC INTEGRALS OF THIRD KIND

$$\text{The integral } \Pi(\phi, \alpha_3^2, k) = \int_0^y \frac{dw}{(1-\alpha_3^2 w^2) \sqrt{(1-w^2)(1-k^2 w^2)}} = \int_0^\phi \frac{d\theta}{(1-\alpha^2 \sin^2 \theta) \sqrt{1-k^2 \sin^2 \theta}}$$

A.2.1

$$|y = \sin \phi = \text{sn } u_1, w = \sin \theta = \text{snu}, \alpha_3^2 \neq 1 \text{ or } k^2|$$

is known as incomplete elliptic integral of the third kind in Legendre's canonical form. When ϕ becomes $\frac{\pi}{2}$, $y = 1$, $u_1 = k$, the integral is said to be complete.

The incomplete elliptic integral A.2.1 can be evaluated in the following way,

when $0 < k < \alpha_3^2 < 1$

$$\Pi(\phi, \alpha_3^2, k) = u_1 + \frac{\pi \alpha_3}{2} \frac{[\Omega_2 - u_1 \Lambda_0(v, k)]}{\sqrt{(\alpha_3^2 - k^2)(1 - \alpha_3^2)} \times K} \tag{A.2.2}$$

where $\Lambda_0(v, k) = \frac{2}{\pi} [EF(v, k') + KE(v, k') - KF(v, k')]$

$$v = \sin^{-1} \sqrt{\frac{1 - \alpha_3^2}{k'^2}}$$

$$\Omega_2 = u_1 - \frac{2K}{\pi} \tan^{-1} \left[\frac{2 \sum_1^\infty q^{m^2} \sin 2mV \sinh |2m(p-w)|}{1 + 2 \sum_1^\infty q^{m^2} \cos 2mV \cosh |2m(p-w)|} \right]$$

$$V = \frac{\pi u_1}{2K}, w = |\pi F(v, k')| / 2K, p = \frac{\pi K'}{2K}, q = e^{-2P}$$

when $0 < k^2 < \alpha_3^2 < k$

$$\Pi(\phi, \alpha_3^2, k) = \frac{\alpha_3 \pi [u_1 \Lambda_0(\xi, k) - \Omega_6]}{2 \sqrt{(\alpha_3^2 - k^2)(1 - \alpha_3^2)}} K \quad \text{A.2.3}$$

$$\Lambda_0(\xi, k) = \frac{2}{\pi} [EF(\xi, k') + KE(\xi, k') - KF(\xi, k')]$$

$$\xi = \sin^{-1} \frac{\sqrt{\alpha_3^2 - k^2}}{\alpha_3^2 k'^2}$$

$$\Omega_6 = \frac{2K}{\pi} \tan^{-1} \left[\frac{2 \sum_{m=1}^{\infty} q^{m^2} \sin(2mV) \sinh(2mw)}{1 + 2 \sum_{m=1}^{\infty} q^{m^2} \cos(2mV) \cosh(2mw)} \right]$$

$$V = \frac{\pi u_1}{2K}, w = [F(\xi, k')] / 2K, q = e^{-2P}, p = \frac{\pi K'}{2K}$$

when $0 < \alpha_3^2 < k^2$

$$\Pi(\phi, \alpha_3^2, k) = u_1 + \frac{\alpha_3 [u_1 Z(\beta, k) - \Omega_3]}{\sqrt{(1 - \alpha_3^2)(k^2 - \alpha_3^2)}} \quad \text{A.2.4}$$

$$Z(\beta, k) = [E(\beta, k) - \frac{E}{K} F(\beta, k)] , \beta = \sin^{-1} \left(\frac{\alpha_3}{k} \right)$$

$$\Omega_3 = \sum_{m=1}^{\infty} \frac{\sin(2mw) \sin(2mv)}{m \sinh(2mp)}$$

$$v = \frac{\pi u_1}{2K}, w = [\pi F(\beta, k)] / 2K, p = \frac{\pi K'}{2K}, q = e^{-2p}$$

$$\infty > \alpha_3^2 > 1$$

$$Z(A, k) = E(A, k) - \frac{E}{K} F(A, k), A = \sin^{-1} \left(\frac{1}{\alpha_3} \right), v = (\pi u_1) / 2K$$

$$w = [\pi F(A, k)] / 2K, p = \frac{\pi K'}{2K}, q = e^{-2p}$$

$$\Omega_4 = \frac{1}{2} \operatorname{Ln} \frac{\sin(w+v)}{\sin(w-v)} + \sum_{m=1}^{\infty} \frac{q^m \sin(2mw) \sin(2mv)}{m \sinh(2mp)}$$

$$\Pi(\phi, \alpha_3^2, k) = \frac{-\alpha_3 [u_1 Z(A, k) - \Omega_4]}{\sqrt{(\alpha_3^2 - 1)(\alpha_3^2 - k^2)}}$$

Elliptic integrals of third kind are discussed in detail in Byrd and Friedman's Handbook ⁵⁸ of Elliptic Integrals (see pages 223-239).

APPENDIX 3

A.3.1 COMPARISON BETWEEN ELLIPTIC INTEGRAL AND SIMPSON'S QUADRATURE FORMULA

From equation 2.31 in Section 2.5 it is seen that d_1 which is the distance between $w=c$ to $w=b$ in the z plane (see Fig. 2.11) can take any one of these four values written below.

Within the limit $a > b > c > y \geq d$

$$d_1 = jA_0 \left| + (a-c)g \frac{1}{\alpha^2} \{k^2K + (\alpha^2 - k^2)\Pi(\alpha^2, k)\} + (p-d)gK \right. \\ \left. + (p-d)(p-a) \frac{g}{(p-c)} \frac{1}{\alpha_3^2} \{(\alpha_3^2 - \alpha^2)\Pi(\alpha_3^2, k) + \alpha^2K\} \right| \quad \text{A.3.1}$$

or

$$= jA_0 \left| + (a-c)g \frac{1}{\alpha^2} \{k^2K + (\alpha^2 - k^2)\Pi(\alpha^2, k)\} + (p-d)gK \right. \\ \left. - (p-d)(p-a) \frac{g}{(p-c)} \frac{1}{\alpha_3^2} \{(\alpha_3^2 - \alpha^2)\Pi(\alpha_3^2, k) + \alpha^2K\} \right| \quad \text{A.3.2}$$

or

$$= jA_0 \left| + (a-c)g \frac{1}{\alpha^2} \{k^2K + (\alpha^2 - k^2)\Pi(\alpha^2, k)\} - (p-d)gK \right. \\ \left. + (p-d)(p-a) \frac{g}{(p-c)} \frac{1}{\alpha_3^2} \{(\alpha_3^2 - \alpha^2)\Pi(\alpha_3^2, k) + \alpha^2K\} \right| \quad \text{A.3.3}$$

or

$$= jA_0 \left| - (a-c)g \frac{1}{\alpha^2} \{k^2K + (\alpha^2 - k^2)\Pi(\alpha^2, k)\} + (p-d)gK \right. \\ \left. + (p-d)(p-a) \frac{g}{(p-c)} \frac{1}{\alpha_3^2} \{(\alpha_3^2 - \alpha^2)\Pi(\alpha_3^2, k) + \alpha^2K\} \right| \quad \text{A.3.4}$$

For a given set of values of d, c, b, p and a in the w plane there will be one and only one value for d_1 . The right value of d_1 has been selected out of four values given by the equation A.3.1, A.3.2, A.3.3, A.3.4, by comparing those four equations with that which has been obtained by evaluating the integral

$$\int_{w=d+\xi}^{w=c+\xi} dz = \int_{w=d+\xi}^{w=c+\xi} A_0 \times \frac{1}{w-p} \sqrt{\frac{(w-d)(w-a)}{(w-c)(w-b)}} \quad \text{A.3.5}$$

with the help of Simpson's rule. Simpson's quadratures arranged to operate with a variable step length has been employed to evaluate the integral A.3.5, which has been discussed in detail by Lawrenson and Gupta¹⁹. Since the function

$$f(w) = \left| \frac{1}{w-p} \sqrt{\frac{(w-d)(w-a)}{(w-c)(w-b)}} \right|$$

has poles and zeros at various points, the accuracy of integration depends on how closely one can approach towards the poles and zeros of the function. The values of ξ which will be zero in the limiting condition are changed continuously until the difference between the two consecutive results of integration of A.3.5 falls within the prescribed accuracy. It is found that the suitable values of ξ lie between 10^{-3} to 10^{-5} for the function $f(w)$. However for a given set of values of d, c, b, p, a , using Simpson's rule with variable step length and variable ξ the integral A.3.5 is evaluated as accurately as possible and compared with

those (A.3.1, 2, 3, 4,) obtained by direct integration employing elliptic functions and it is found that they are very nearly equal if the equation A.3.3 is chosen. Similarly, it has been proved that d_2 which is the length bc in the z plane shown in Fig.2.11 is given by

within the limit $a > b \geq y > c > d$

$$d_2 = A_0 \left\{ \frac{(a-c)g}{\alpha^2} [k^2K + (\alpha^2 - k^2)\Pi(\alpha^2, k)] - g(p-d)K \right. \\ \left. + (p-d)(p-a) \frac{g}{p-c} \frac{1}{\alpha_3^2} [(\alpha_3^2 - \alpha^2)\Pi(\alpha_3^2, k) + \alpha^2K] \right\} \quad A.3.6$$

Computer programme for evaluating d_1 and d_2 by direct integration of the function $f(w)$ which involves the elliptic functions is given in Appendix (4.Com.Pr.1).

A.3.2 EVALUATION OF UNKNOWNNS c,p,a, IN THE w PLANE USING NONLINEAR MULTIVARIABLE OPTIMIZATION TECHNIQUE

Out of five unknowns in the w plane any two constants say d and b have been given convenient numerical values. $d = 0$ and $b = 1$. Given the initial approximate values for other unknowns and using the equations 2.31, 2.39, which are in terms of elliptic functions and 2.43, algebraic function, one can write the error function E as the sume of the squares of the differences between specified and computed z plane dimensions which can be written as

$$E = \sum_{k=1}^3 [f_k(\hat{X})]^2 \quad A.3.2.1$$

Each function $f_k(\hat{X})$ represents a component of the total error.

Thus

$$\begin{aligned}
 f_1(\hat{X}) &= (d_1)_{\text{specified}} - (d_1)_{\text{Computed with initial approximate values of } c,p,a} \\
 f_2(\hat{X}) &= (d_2)_{\text{specified}} - (d_2)_{\text{Computed with initial approximate values of } c,p,a} \\
 f_3(\hat{X}) &= (g)_{\text{specified}} - (g)_{\text{Computed with initial approximate values of } c,p,a}
 \end{aligned}
 \quad \left. \vphantom{\begin{aligned} f_1(\hat{X}) \\ f_2(\hat{X}) \\ f_3(\hat{X}) \end{aligned}} \right\} \text{A.3.2.2}$$

where several parameters of the function f_k can be considered to be elements of a vector. In order to minimise the function E the following mathematical technique which is known as the Gauss Newton method, has been adopted.

A vector values function \hat{f} is defined by

$$\hat{f}^T = [f_1(\hat{x}) \quad f_2(\hat{x}) \quad f_3(\hat{x})] \quad \text{A.3.2.3}$$

such that

$$E = \hat{f}^T \hat{f} \quad \text{A.3.2.4}$$

The contribution to the value of E due to changes in the parameters c,p,a , defined the Jacobian gradient vector. It is clear that the change in any of of these parameters will affect all the elements of f in equation A.3.2.3, and that each of these will contribute to the total error in equation A.3.2.4. A new matrix has been defined which gives the variation of each function $f_1(X) \dots f_3(X)$ due to variation

of each parameter c, p, a , viz:

$$A = \begin{bmatrix} \frac{\partial f_1}{\partial c} & \frac{\partial f_1}{\partial p} & \frac{\partial f_1}{\partial a} \\ \frac{\partial f_2}{\partial c} & \frac{\partial f_2}{\partial p} & \frac{\partial f_2}{\partial a} \\ \frac{\partial f_3}{\partial c} & \frac{\partial f_3}{\partial p} & \frac{\partial f_3}{\partial a} \end{bmatrix} \quad \text{A.3.2.5}$$

The elements of Jacobian 'g' can be derived by partial differentiation of A.3.2.1 with respect to each parameter in turn as

$$\frac{\partial E}{\partial x_i} = \sum_{k=1}^m 2 |f_k(X)| \frac{\partial f_k(X)}{\partial x_i} \quad \text{A.3.2.6}$$

where x_i stands for anyone of c, p, a .

Hence,

$$\begin{bmatrix} \frac{\partial E}{\partial c} \\ \frac{\partial E}{\partial p} \\ \frac{\partial E}{\partial a} \end{bmatrix} = 2 \begin{bmatrix} \frac{\partial f_1}{\partial c} & \frac{\partial f_2}{\partial c} & \frac{\partial f_3}{\partial c} \\ \frac{\partial f_1}{\partial p} & \frac{\partial f_2}{\partial p} & \frac{\partial f_3}{\partial p} \\ \frac{\partial f_1}{\partial a} & \frac{\partial f_2}{\partial a} & \frac{\partial f_3}{\partial a} \end{bmatrix} \begin{bmatrix} f_1(X) \\ f_2(X) \\ f_3(X) \end{bmatrix} \quad \text{A.3.2.7}$$

Or in matrix form

$$g = 2 A^T f \quad \text{A.3.2.8}$$

A second partial differentiation of equation A.3.2.3, assuming that the second partial derivatives of f_k exists, gives

$$\frac{\partial^2 E}{\partial x_i \partial x_j} = 2 \sum_{k=1}^m \frac{\partial [f_k(X)]}{\partial x_i} \frac{\partial [f_k(X)]}{\partial x_j} + 2 \sum_{k=1}^m f_k(X) \frac{\partial^2 [f_k(X)]}{\partial x_i \partial x_j} \quad \text{A.3.2.9}$$

The usual least squares procedure assumes that the second term can be neglected. Therefore

$$\frac{\partial^2 E}{\partial x_i \partial x_j} \approx 2 \sum_{k=1}^m \frac{\partial [f_k(X)]}{\partial x_i} \frac{\partial [f_k(X)]}{\partial x_j} \quad \text{A.3.2.10}$$

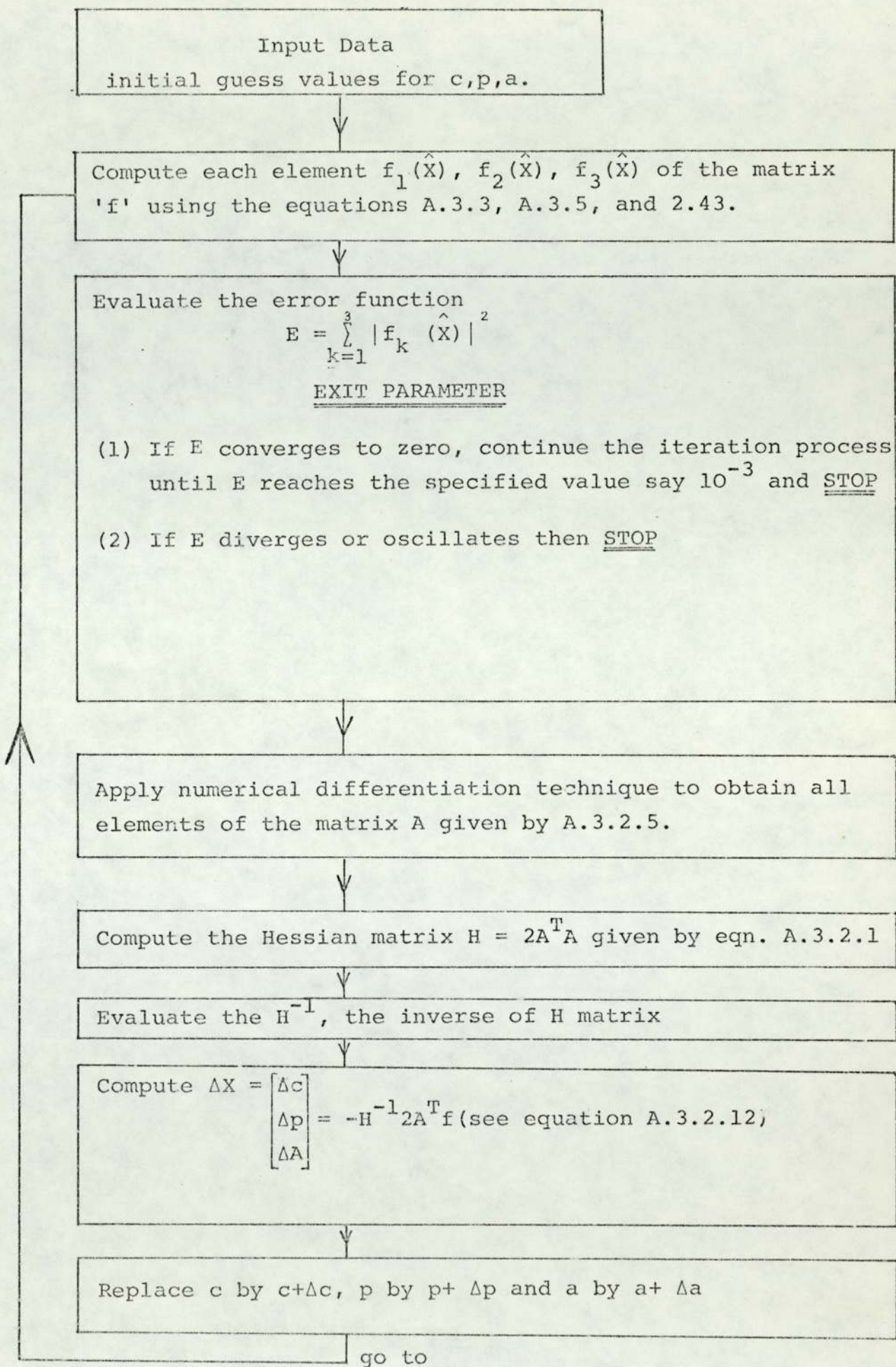
This equation for all i and $j = 1, \dots, n=3$ gives an approximation to the elements of the Hessian matrix as

$$H \approx 2A^T A \quad \text{A.3.2.11}$$

With the help of the Hessian matrix and the Jacobian vector it can be shown that the increment ΔX is given by

$$\Delta X = - [A^T A]^{-1} A^T f \quad \text{A.3.2.12}$$

In summary, the above equation A.3.2.12 gives the least squares increment for the minimisation of the sum of the squares of the functions $f_1(X)$, $f_2(X)$, $f_3(X)$ of three parameters c , p , a . The least squares optimization procedure is the Newton-Raphson method utilizing this increment. Termination is effected by recognizing that the value of E remains almost constant over a number of successive iteration. Numerical differentiation technique has been employed to obtain the elements of the matrix A . From the equation A.3.2.12 each parameter will be replaced by their present value plus ΔX to start with for the next iteration. The least squares minimisation can now be put into step by step form as given overleaf.



On combining the procedures discussed in section A.3.2 the computer programme for finding the values of c , p , a , which when inserted into the equations A.3.3, A.3.5, and 2.43 satisfy the specified dimension, d_1 , d_2 , g , A_1 in the z plane, using the nonlinear multivariable optimisation technique has been prepared and given in Appendix (4.Com.pr.2). Table A.3.1 is an example to demonstrate the application of this method to a typical polygonal boundary in the z plane discussed in section 2.5 (see also Fig.2.11), where the specified dimensions in the model are

$$\frac{d_1}{A_1} = .3858, \quad \frac{d_2}{A_1} = .3086, \quad \text{and} \quad \frac{g}{A_1} = .1286$$

CONCLUSION

The efficiency of the method can be improved by limiting the step size so that a solution is not predicted for outside the range of a valid first order approximation to Hessian matrix H . In this case a fraction λ of the predicted change ΔX can be used and the process becomes

$$X_{k+1} = X_k + \lambda \Delta X_k$$

where $\lambda < 1.0$ can either be fixed in advance or found by a linear search.

Computation time is influenced by the initial estimates of the variable. It is often difficult to make a good initial estimate of the w plane constants since single changes in polygon dimensions can alter the order of magnitudes of the w plane constants very much. It is not possible to give general

TABLE A.3.1

CONVERGENCE OF THE TRANSFORMATION FOR THE BOUNDARY SHOWN IN FIG. 2.11

Ultimate aim is to obtain the values of c, b, a, which corresponds to

$$\frac{d_1}{A_1} = .3858, \frac{d_2}{A_1} = .3086, \frac{g}{A_1} = .1286.$$

Number of Iteration	Initial guess values for			Percentage error in dimensional ratios (in z plane)			Error function E
	c	p	a	$\frac{d_1}{A_1}$	$\frac{d_2}{A_1}$	$\frac{g}{A_1}$	
0	.99	14.0	14.5	24.3479%	-4.2005%	58.1968%	5.51500
	values of c p a at end of each iteration						
1	.976 216	12.657 561	12.738 560	-4.7059%	7.7284%	-32.5279%	1.077 387
2	.963 290	11.862 529	12.015 696	- .7823%	.5462%	-3.6688%	.012 370
3	.961 511	11.639 416	11.801 060	.3231%	.3655%	.0698%	.001 096
4	.961 089	11.689 473	11.852 023	.0684%	-.1590%	.0085%	.000 154
5	.961 102	11.660 566	11.822 324	.2045%	-.0160%	-.0046%	.000 132
6	.961 416	11.713 222	11.875 867	-.0274%	-.0398%	.0038%	.000 016

guidance with regard to the initial guess values of the variables and sometimes serious difficulty is encountered in the convergence of the error function E if the initial estimates of the w plane constants are not of the right order of magnitude.

APPENDIX (4. COM. PRO.1)

Computer programme to evaluate g , A_1 , d_1 and d_2 , which involve elliptic integrals and functions (equations A.3.1 to A.3.4 and A.3.6) when the constants c , p , a , b and d in the w plane are given.

```
DIMENSION AK1(50),Q(50),E(50),F(50),EE(50)

PI=4.0*ATAN(1.0)
D=0.0
B=1.0
10  PAUSE 1
    READ (1, )C,P,A,AL,ZZ
700  G=2.0/(SQRT((A-C)*(B-D)))
    AA=SQRT((A-B)/(A-C))
    AAA=AA*AA
12  A1=SQRT(((C-D)*(A-B))/((A-C)*(B-D)))
    AA1=A1*A1
    N=1
    U=SQRT(((A-C)*(ZZ-B))/((A-B)*(ZZ-C)))
15  W=U/(SQRT(1.0-(U*U)))
40  Y=ATAN(W)
    AO=1.0
    BO=(1.0-(A1*A1))**.5
    CO=A1
    SUM=CO*CO
    Z=0.0
    AN=1.0
20  A2=(AO+BO)/2.0
    B2=SQRT(AO*BO)
    C2=(AO-BO)/2.0
    P1=(C2*C2)*((2.0)**(AN))
    Y2=ATAN((BO/AO)*(SIN(Y)/COS(Y)))-(ATAN(SIN(Y)/COS(Y)))+(2.0*Y)
    TERM=(C2)*SIN(Y2)
    Z=Z+TERM
    SUM=SUM+P1
    IF(ABS(C2) .LT. 1.0E-08) GO TO 21
    AN=AN+1.0
    AO=A2
    BO=B2
    Y=Y2
    GO TO 20
21  AK1(N)=PI/(2.0*A2)
    Q(N)=SUM/2.0
    E(N)=(1.0-Q(N))*AK1(N)
    F(N)=Y2/((A2)*(2.0**AN))
    EE(N)=Z+((F(N)/AK1(N))*E(N))
    IF(N .EQ. 3) GO TO 70
    IF(N .EQ. 4) GO TO 71
    IF(N .EQ. 6) GO TO 110
    IF(A1 .LT. AAA) GO TO 30
    IF(AA1 .LT. AAA) GO TO 31
30  N=N+2
    LL=3
    U1=SQRT((1.0-AAA)/(1.0-AA1))
    W=U1/(SQRT(1.0-(U1*U1)))
```

```
A1=SQRT(1.0-AA1)
GO TO 40
31  N=N+3
    LL=4
    U2=SQRT((AAA-AA1)/(AAA*(1.0-AA1)))
    W=U2/(SQRT(1.0-(U2*U2)))
    A1=SQRT(1.0-AA1)
    GO TO 40
70  V1=(2.0/PI)*((E(1)*F(3))+(AK1(1)*EE(3))
1- (AK1(1)*F(3)))
    VO=(PI*F(1))/(2.0*AK1(1))
    WO=(PI*F(3))/(2.0*AK1(1))
    PO=(PI*AK1(3))/(2.0*AK1(1))
    QO=EXP(-2.0*PO)
    M=1
    GG1=0.0
    HH1=0.0
100  PP=FLOAT(M)
    BB=(2.0*PP)*(PO-WO)
    CC=EXP(BB)
    DD=EXP(-BB)
    EF=(CC-DD)/2.0
    FF=(CC+DD)/2.0
    PPP=PP*PP
    GG1=GG1+((QO**PPP)*(SIN(2.0*PP*VO))*(EF))
    HH1=HH1+((QO**PPP)*(COS(2.0*PP*VO))*(FF))
    IF(M.EQ.11) GO TO 102
    M=M+1
    GO TO 100
102  GG=2.0*GG1
    HH=1.0+(2.0*HH1)
    GGO=(GG/HH)
    HHO=F(1)-(((2.0*AK1(1))/PI)*(ATAN(GGO)))
    WRITE(2,101)HHO
101  FORMAT(F14.7)
    S=2.0*(SQRT((AAA-AA1)*(1.0-AAA))*AK1(1))
    T=F(1)+(((PI*AA)*(HHO-(F(1)*V1)))/S)
    XA=SQRT(((P-C)*(A-B))/((P-B)*(A-C)))
    XXA=XA*XA
    IF(XXA.GT.1.0) GO TO 106
    GO TO 10
106  N=6
    U3=1.0/XA
    W=U3/(SQRT(1.0-(U3*U3)))
    A1=SQRT(((C-D)*(A-B))/((A-C)*(B-D)))
    GO TO 40
71  V1=(2.0/PI)*((E(1)*F(4))+(AK1(1)*EE(4))
1- (AK1(1)*F(4)))
    VO=(PI*F(1))/(2.0*AK1(1))
    WO=(PI*F(4))/(2.0*AK1(1))
    PO=(PI*AK1(3))/(2.0*AK1(1))
    QO=EXP(-2.0*PO)
    I=1
    GG1=0.0
    HH1=0.0
200  PP=FLOAT(I)
    BB=(2.0*PP)*WO
    CC=EXP(BB)
    DD=EXP(-BB)
    EF=(CC-DD)/2.0
    FF=(CC+DD)/2.0
    PPP=PP*PP
    GG1=GG1+((QO**PPP)*(SIN(2.0*PP*VO))*(EF))
    HH1=HH1+((QO**PPP)*(COS(2.0*PP*VO))*(FF))
    IF(I.EQ.11) GO TO 202
    I=I+1
```



```
202 GO TO 200
GG=2.0*GG1
HH=1.0+(2.0*HH1)
GGO=(GG/HH)
HHO=((2.0*AK1(1))/PI)*(ATAN(GGO))
WRITE(2,201)HHO
201   FORMAT(F14.7)
S=2.0*(SQRT((AAA-AA1)*(1.0-AAA)))*AK1(1)
T=((PI*AA)*((F(1)*V1)-(HHO)))/(S)
XA=SQRT(((P-C)*(A-B))/((P-B)*(A-C)))
XXA=XA*XA
IF(XXA.GT.1.0)GO TO 206
GO TO 10
206   N=6
U3=1.0/XA
W=U3/(SQRT(1.0-(U3*U3)))
A1=SQRT(((C-D)*(A-B))/((A-C)*(B-D)))
GO TO 40
110   SV1=EE(6)-((E(1)*F(6))/(AK1(1)))
SWO=(PI*F(6))/(2.0*AK1(1))
SVO=(PI*F(1))/(2.0*AK1(1))
IF(LL.EQ.3)SPO=(PI*AK1(3))/(2.0*AK1(1))
IF(LL.EQ.4)SPO=(PI*AK1(4))/(2.0*AK1(1))
S00=EXP(-2.0*SPO)
K=1
SGG=0.0
300   SPP=FLOAT(K)
SBB=(2.0*SPP*SPO)
SCC=EXP(SBB)
SDD=EXP(-SBB)
SEF=(SCC-SDD)/2.0
SGG=SGG+(((S00**SPP)*(SIN(2.0*SPP*SWO))*
1(SIN(2.0*SPP*SVO)))/(SPP*SEF))
IF(K.EQ.10)GO TO 301
K=K+1
GO TO 300
301   SHH=((ALOG((SIN(SWO+SVO))/(SIN(SWO-SVO))))*0.5)+SGG
SS=SQRT(XXA-1.0)*(XXA-AA1)
ST=(-XA)*((F(1)*SV1)-SHH)/SS
R1=((A-B)*G*(F(1)+((AAA-1.0)*T))/AAA
R2=(P-D)*G*F(1)
R3=((P-D)*(P-A)*G*(((XXA-AAA)*ST)+(AAA*F(1)))/((B-P)*XXA)
DDD=AL/PI
DZ1=(R1+R2+R3)*DDD
DZ2=(R1+R2-R3)*DDD
DZ3=(R1-R2+R3)*DDD
DZ4=(-R1+R2+R3)*DDD
BM=(P-1.0)/(SQRT(A-1.0))
BM1=(P-ZZ)/(SQRT((A-ZZ)*(ZZ)))
BMO=(BM1/BM)*100.0
WRITE(2,403)DZ4,ZZ,BMO
403   FORMAT(3F12.6)
ZZ=ZZ+0.05
GO TO 700
```

APPENDIX (4.COM.PRO.2)

Computer Programme to find the unknowns c, p, a , in the w plane using the nonlinear multivariable optimisation technique when the values of d_1, d_2, g, A_1 in the z plane are given. Elliptic functions and integrals involved in the equations relating z plane and w plane are also evaluated in this computer programme.

```
COMMON AK(90),Q(90),E(90),SAK1(90),SQ(90),SE(90),SF(90),SEE
1(90),AR(9,9),DR(9,9),ZH(9,9),TDR(9,9),TB(50,50)
1,V2(90),DINV(9,9),ZHA(9,9),HAF(9,9)
D=0.0
B=1.0
NT=1
10 PAUSE 1
READ (1,11)C,P,A,AL
11 FORMAT(F12.6)
5 G=(2.0)/(SQRT((A-C)*(B-D)))
AA=SQRT((C-D)/(B-D))
R3=(SQRT(((P-D)*(A-P))/((P-C)*(P-B))))*AL
WRITE(2,55)R3
55 FORMAT(F12.6)
N=1
12 A1=SQRT(((C-D)*(A-B))/((A-C)*(B-D)))
13 A0=1.0
BO=(1.0-(A1*A1))*0.5
CO=A1
SUM=CO*CO
AN=1.0
14 A2=(A0+BO)/2.0
B2=SQRT(A0*BO)
C2=(A0-BO)/2.0
P1=(C2*C2)*((2.0)**(AN))
SUM=SUM+P1
IF(ABS(C2) .LT. 1.0E-08) GO TO 15
A0=A2
BO=B2
AN=AN+1.0
GO TO 14
15 AK(N)=3.141592/(2.0*A2)
Q(N)=(SUM)/2.0
E(N)=(1.0-(Q(N)))*AK(N)
IF(N .EQ. 10) GO TO 80
N=N+1
U=SQRT((1.0-(AA*AA))/(1.0-(A1*A1)))
40 W=U/(SQRT(1.0-(U*U)))
Y=ATAN(W)
SA1=SQRT(1.0-(A1*A1))
42 SA0=1.0
SBO=SQRT(1.0-(SA1*SA1))
SCO=SA1
SSUM=SCO*SCO
```


SZ=0.0

SAN=1.0

20 SA2=(SA0+SB0)/2.0

SB2=SQRT(SA0*SB0)

SC2=(SA0-SB0)/2.0

SP1=(SC2*SC2)*((2.0)**(SAN))

SY2=ATAN((SB0/SA0)*(SIN(Y)/COS(Y)))-(ATAN(SIN(Y)/COS(Y)

1))+(2.0*Y)

TERM=(SC2)*(SIN(SY2))

SZ=SZ+TERM

SSUM=SSUM+SP1

IF(ABS(SC2) .LT. 1.0E-08) GO TO 21

SAN=SAN+1.0

SA0=SA2

SB0=SB2

Y=SY2

GO TO 20

21 SAK1(N)=3.141592/(2.0*SA2)

SQ(N)=(SSUM/2.0)

SE(N)=(1.0-SQ(N))*SAK1(N)

SF(N)=SY2/((SA2)*(2.0**SAN))

SEE(N)=SZ+((SF(N)/SAK1(N))*SE(N))

IF(N .EQ. 12) GO TO 90

IF(N .EQ. 13) GO TO 91

IF(N .EQ. 11) GO TO 85

IF(N .EQ. 3) GO TO 35

IF(N .EQ. 4) GO TO 36

V1=(2.0/3.141592)*((E(1)*SF(2))+(AK(1)*SEE(2))-(AK(1)*SF(2)))

V3=SQRT(((AA*AA)-(A1*A1))*(1.0-(AA*AA)))

V2(N)=AK(1)+(((3.141592*AA)*(1.0-V1))/(2.0*V3))

AA1=SQRT(((C-D)*(P-B))/((B-D)*(P-C)))

AA2=AA1*AA1

A2=A1*A1

IF(A2 .LT. AA2) GO TO 30

IF(AA2 .LT. A2) GO TO 31

30 N=N+1

U=SQRT((1.0-AA2)/(1.0-(A1*A1)))

GO TO 40

31 N=N+2

U=AA1/A1

W=U/(SQRT(1.0-(U*U)))

Y=ATAN(W)

SA1=A1

GO TO 42

35 AV1=(2.0/3.141592)*((E(1)*SF(3))+(AK(1)*SEE(3))-(AK(1)*SF(3)))

AV3=SQRT(((AA2)-(A2))*(1.0-(AA2)))

V2(3)=AK(1)+(((3.141592*AA1)*(1.0-AV1))/(2.0*AV3))

GO TO 70

36 BV=(AK(1)*SEE(4))-(E(1)*SF(4))

BV3=SQRT((1.0-AA2)*(A2-AA2))

V2(4)=AK(1)+((AA1*BV)/(BV3))

GO TO 71

70 RR1=((A-C)*(G)*((A1*A1*AK(1))+(((AA*AA)-(A1*A1))*V2(2))))/(AA*AA)

RR2=(P-D)*(G)*(AK(1))

RR3=((P-D)*(P-A)*(G))/(P-C)

RR4=((((AA2)-(AA*AA))*(V2(3)))+(AA*AA*AK(1)))/(AA2)

GO TO 72

71 RR1=((A-C)*(G)*((A1*A1*AK(1))+(((AA*AA)-(A1*A1))*V2(2))))/(AA*AA)

RR2=(P-D)*(G)*(AK(1))

```
RR3=((P-D)*(P-A)*(G))/(P-C)
RR4=((AA2-(AA*AA))*(V2(4)))+(AA*AA*AK(1))/(AA2)
GO TO 72
72 RR5=RR3*RR4
RR6=AL/3.141592
R1=(-RR1+RR2-RR5)*RR6
WRITE(2,78)R1
78 FORMAT(F12.6)
AA=SQRT((B-C)/(B-D))
A1=SQRT(((B-C)*(A-D))/((A-C)*(B-D)))
N=10
GO TO 13
80 N=11
U=AA/A1
W=U/(SQRT(1.0-(U*U)))
Y=ATAN(W)
SA1=A1
GO TO 42
85 BV=(AK(10)*SEE(11))-(E(10)*SF(11))
BV3=SQRT((1.0-(AA*AA))*((A1*A1)-(AA*AA)))
V2(11)=AK(10)+((AA*BV)/(BV3))
AA1=SQRT(((B-C)*(P-D))/((B-D)*(P-C)))
AA2=AA1*AA1
A2=A1*A1
IF(A2 .LT. AA2) GO TO 88
PAUSE 2
IF(AA2 .LT. A2) GO TO 89
89 N=12
U=AA1/A1
W=U/(SQRT(1.0-(U*U)))
Y=ATAN(W)
SA1=A1
GO TO 42
90 BV=(AK(10)*SEE(12))-(E(10)*SF(12))
BV3=SQRT((1.0-AA2)*(A2-AA2))
V2(12)=AK(10)+((AA1*BV)/(BV3))
GO TO 95
88 N=13
U=SQRT((1.0-AA2)/(1.0-A2))
GO TO 40
PAUSE 3
91 AV1=(2.0/3.141592)*((E(10)*SF(13))+(AK(10)*SEE(13))
1-(AK(10)*SF(13)))
AV3=SQRT(((AA2)-(A2))*(1.0-(AA2)))
V2(13)=AK(10)+(((3.141592*AA1)*(1.0-AV1))/(2.0*AV3))
GO TO 96
95 RR1=((A-C)*G*((A1*A1*AK(10))+((AA*AA)-(A1*A1))
1*V2(11)))/(AA*AA)
RR2=(P-D)*(G)*(AK(10))
RR3=((P-D)*(P-A)*(G))/(P-C)
RR4=((AA2-(AA*AA))*(V2(12)))+(AA*AA*AK(10))/(AA2)
GO TO 100
PAUSE 4
96 RR1=((A-C)*(G))*((A1*A1*AK(10))+((AA*AA)-(A1*A1))*
1V2(11)))/(AA*AA)
RR2=(P-D)*(G)*(AK(10))
RR3=((P-D)*(P-A)*(G))/(P-C)
RR4=((AA2-(AA*AA))*(V2(13)))+(AA*AA*AK(10))/(AA2)
GO TO 100
```



```
100  RR5=RR3*RR4
      RR6=AL/3.141592
      R2=(-RR1+RR2-RR5)*RR6
      WRITE(2,915)R2
915  FORMAT(F12.6)
      IF (NT .EQ. 20) GO TO 111
      IF(NT .EQ. 21) GO TO 112
      IF(NT .EQ. 22) GO TO 113
      AR(1,1)=R1-7.50
      AR(2,1)=R2-2.0
      AR(3,1)=R3-2.50
      ER=(AR(1,1)*AR(1,1))+(AR(2,1)*AR(2,1))+(AR(3,1)*AR(3,1))
      WRITE(2,110)ER
110  FORMAT(F12.8)
      NT=20
      DEL=0.00001
      C=C+DEL
      GO TO 5
111  DR1=R1-(AR(1,1)+7.50)
      DR(1,1)=DR1/DEL
      DR2=R2-(AR(2,1)+2.0)
      DR(2,1)=DR2/DEL
      DR3=R3-(AR(3,1)+2.50)
      DR(3,1)=DR3/DEL
      NT=21
      C=C-DEL
      P=P+DEL
      GO TO 5
112  DR4=R1-(AR(1,1)+7.50)
      DR(1,2)=DR4/DEL
      DR5=R2-(AR(2,1)+2.0)
      DR(2,2)=DR5/DEL
      DR6=R3-(AR(3,1)+2.50)
      DR(3,2)=DR6/DEL
      NT=22
      P=P-DEL
      A=A+DEL
      GO TO 5
113  DR7=R1-(AR(1,1)+7.50)
      DR(1,3)=DR7/DEL
      DR8=R2-(AR(2,1)+2.0)
      DR(2,3)=DR8/DEL
      DR9=R3-(AR(3,1)+2.50)
      DR(3,3)=DR9/DEL
      DO 114 I=1,3
      DO 114 J=1,3
114  TDR(J,I)=(DR(I,J))*2.0
      DO 115 II=1,3
      DO 115 KK=1,3
      ZH(II,KK)=0.0
      DO 115 JJ=1,3
115  ZH(II,KK)=ZH(II,KK)+TDR(II,JJ)*DR(JJ,KK)
      GO TO 116
      DET1=ZH(1,1)*((ZH(2,2)*ZH(3,3))-(ZH(2,3)*ZH(3,2)))
      DET2=ZH(1,2)*((ZH(2,3)*ZH(3,1))-(ZH(2,1)*ZH(3,3)))
      DET3=ZH(1,3)*((ZH(2,1)*ZH(3,2))-(ZH(2,2)*ZH(3,1)))
      DET=DET1+DET2+DET3
      DINV(1,1)=((ZH(2,2)*ZH(3,3))-(ZH(2,3)*ZH(3,2)))/DET
      DINV(1,2)=((ZH(1,3)*ZH(3,2))-(ZH(1,2)*ZH(3,3)))/DET
```

```
DINV(1,3)=((ZH(1,2)*ZH(2,3))-(ZH(1,3)*ZH(2,2)))/DET
DINV(2,1)=((ZH(2,3)*ZH(3,1))-(ZH(2,1)*ZH(3,3)))/DET
DINV(2,2)=((ZH(1,1)*ZH(3,3))-(ZH(1,3)*ZH(3,1)))/DET
DINV(2,3)=((ZH(1,3)*ZH(2,1))-(ZH(1,1)*ZH(2,3)))/DET
DINV(3,1)=((ZH(2,1)*ZH(3,2))-(ZH(2,2)*ZH(3,1)))/DET
DINV(3,2)=((ZH(1,2)*ZH(3,1))-(ZH(1,1)*ZH(3,2)))/DET
DINV(3,3)=((ZH(1,1)*ZH(2,2))-(ZH(1,2)*ZH(2,1)))/DET
GO TO 702
116 DO 211 III=1,3
DO 210 JJJ=1,3
TB(III, JJJ)=ZH(III, JJJ)
210 CONTINUE
211 CONTINUE
JJ1=4
JJ2=6
DO 202 III=1,3
DO 202 JJJ=JJ1, JJ2
202 TB(III, JJJ)=0.0
DO 203 III=1,3
JJJ=III+3
203 TB(III, JJJ)=1.0
DO 610 KKK=1,3
KPI=KKK+1
IF(KKK .EQ. 3) GO TO 500
LLL=KKK
DO 400 III=KPI,3
400 IF(ABS(TB(III, KKK)) .GT. ABS(TB(LLL, KKK))) LLL=1
IF(LLL .EQ. KKK) GO TO 500
DO 410 JJJ=KKK, JJ2
TEMP=TB(KKK, JJJ)
TB(KKK, JJJ)=TB(LLL, JJJ)
410 TB(LLL, JJJ)=TEMP
500 DO 501 JJJ=KPI, JJ2
501 TB(KKK, JJJ)=TB(KKK, JJJ)/TB(KKK, KKK)
IF(KKK .EQ. 1) GO TO 600
KMI=KKK-1
DO 510 III=1, KMI
DO 510 JJJ=KPI, JJ2
510 TB(III, JJJ)=TB(III, JJJ)-TB(III, KKK)*TB(KKK, JJJ)
IF(KKK .EQ. 3) GO TO 700
600 DO 610 III=KPI,3
DO 610 JJJ=KPI, JJ2
610 TB(III, JJJ)=TB(III, JJJ)-TB(III, KKK)*TB(KKK, JJJ)
700 DO 701 III=1,3
DO 701 JJJ=1,3
KKK=JJJ+3
701 DINV(III, JJJ)=TB(III, KKK)
702 DO 303 IJJ=1,3
DO 303 KKJ=1,3
ZHA(IJJ, KKJ)=0.0
DO 303 JJJ=1,3
303 ZHA(IJJ, KKJ)=ZHA(IJJ, KKJ)+DINV(IJJ, JJJ)*TDR(JJJ, KKJ)
DO 803 IIM=1,3
DO 803 KKM=1,1
HAF(IIM, KKM)=0.0
DO 803 JJJ=1,3
803 HAF(IIM, KKM)=HAF(IIM, KKM)+ZHA(IIM, JJJ)*AR(JJJ, KKM)
C=C-HAF(1,1)
P=P-HAF(2,1)
A=A-DEL-HAF(3,1)
WRITE(2,49)C,P,A
49 FORMAT(3F12.6)
NT=25
GO TO 5
```


APPENDIX (4.COM. PRO.3)

Computer programme for solving the equation 6.80 of Chapter 6 in order to obtain fundamental H on the surface of shell when the physical parameters of the machine, a^c excitation to the compole, and conductivity of the shell material are given.

F4P9 V36A
>R,L-1AS25

END PASS1

```
      PAUSE 1
      READ(1,5)AO,H,FF
5      FORMAT(F12.6)
      A2=0.09125
      F1=33000.0*(AO/4.0)
      B1=0.0847F+68
      D=0.452
      F=(2.0*3.141592*A2)/D
      B0=0.000635
      Z1=((COS(F))*(4.0*F1))/3.141592
      Z=ABS((Z1)*0.5)
      C=(2.0*3.141592)/D
      C1=4.0*3.141592*1.0F-C7
      C0=B0*C
      C2=Z*(EXP(-C0))
      C3=(SORT(B1/2.0))*C1
      F0=50.0
40      V=2.0*3.141592*F0
      W1=SORT(V)
30      FH=((0*0.457)*((H)**(0.4)))+(H*C3*W1)-(C2*C3*W1)
      FH1=((0*0.1823)*((H)**(-0.6)))+(C3*W1)
      H1=H-(FH/FH1)
      H2=H1-H
      WRITE(2,50)H2
50      FORMAT(F12.6)
      IF(ABS(H2) .LT. 1.0E-03) GO TO 35
      H=H1
      GO TO 30
35      FH2=((0*0.457)*((H1)**(0.62)))+(H1*C3*W1)-(C2*C3*W1)
34      WRITE(2,10)H1,F0,FH2
10      FORMAT(F12.5,3X,F12.5,3X,F12.5)
      F0=F0+FF
      GO TO 40
```

APPENDIX (4.COM. PRO.4)

Computer programme of iterative method of calculating variable μ on the surface of the shell for various odd harmonic current sheets (1,3,5...) when the physical parameters of the machine and a.c. excitation to the compole are given as input data.

```
30  DO 40 N=1,21,2
    X=0.0001
    AN=N
    B0=0.000635
    X1=0.0
    F1=33000.0
    AK=0.676
    AM=0.81
    C1=4.0*3.141592*1.0E-07
    A1=2.0*3.141592*300.0
    A2=0.09125
    B1=0.0847E+08
    D=0.452
    C=2.0/(A1*B1)
    F=((2.0*3.141592*A2)/D)*AN
    Z1=((COS(F))/AN)*((4.0*F1)/(3.141592))
    Z=ABS((Z1)*0.5)
    WRITE(2,56)Z
56  FORMAT(F12.6)
    Q=(2.0*3.141592*AN)/D
    WRITE(2,4)Q
4   FORMAT(F13.7)
    Q1=(Q*Q*Q*Q)
    Q2=(Q*Q)
35  B2=(C*C)/(X*X)
    B3=(B2)**0.5
    G=ATAN((2.0)/(B3*Q2))
    A4=((Q1+(4.0/B2))**0.25)*(COS(G/2.0))
    B4=((Q1+(4.0/B2))**0.25)*(SIN(G/2.0))
    C4=((Q*X)/(C1))+A4
    P1=((Q2*C)/2.0)/((X*X)+((Q1*C*C)/4.0))
    P2=(Q1)+(4.0/B2)
    P3=((((2.0*X)/(C*C))*((P2)**(-(0.75)))*(COS(G/2.0)))-
1   1*(0.5*((P2)**0.25)*(SIN(G/2.0))*(P1)))+(Q/C1)
    P0=(P3)-(Q/C1)
    P4=((((2.0*X)/(C*C))*((P2)**(-(0.75)))*(SIN(G/2.0)))-
1   1*(0.5*((P2)**0.25)*(COS(G/2.0))*(P1)))
    P5=((C4*(P4))-(B4*(P3)))/(C4*C4)
    P6=(B4)/(C4)
    P7=(0.5*(P1))-(((1.0)/(1.0+(P6*P6)))*(P5))
    P8=((A4*A4)+(B4*B4))/((C4*C4)+(B4*B4))
    P9=((P8)**0.5)*(SIN((G)/2.0)-(ATAN(P6)))*(P7))
    P10=((2.0)*(X)*((Q)/(C1))*((Q)/(C1)))+(4.0)*((P2)**(-(0.5)))
```



```
1*((X)/(C*C)))+((2.0*A4*Q)/(C1))
P11=((2.0*Q*X)/(C1))*(P0)
P12=P11+P10
P13=(P12)*((P2)**(0.5))
P14=((4.0*X)/(C*C))*((C4*C4)+(B4*B4))*((P2)**(-(0.5)))
P15=(P14-P13)/(((C4*C4)+(B4*B4))*((C4*C4)+(B4*B4)))
P16=((P8)**(-(0.5)))*(P15)
P17=(0.5)*(COS((0.5*G)-(ATAN((B4)/(C4))))))
P18=P16*P17
P19=(AM-1.0)
P20=((1.0/AK)**((1.0)/(P19)))
P21=(X)**((((-(4.0))*AM)+(5.0))/(4.0*P19))
P22=(P20*P21*0.25)/(P19)
DFX=((Z*(COS(Q*X1))*(EXP(-(Q*B0))))*(P18-P9))-(P22)
P23=((Z*(COS(Q*X1))*(EXP(-(Q*B0))))*((P8)**0.5)
P24=COS((ATAN((B4)/(A4)))-(ATAN(P6)))
FX=(P24*P23)-(((X)**((0.25)/(P19)))*(P20))
X4=X-((FX)/(DFX))
WRITE(2,23) X4
23  FORMAT(F12.8)
X5=X4-X
IF(ABS(X5) .LT. 1.0E-06) GO TO 32
X=X4
GO TO 35
32  WRITE (2,10) X4
10  FORMAT(F12.9)
40  CONTINUE
STOP
END
```

PIP V13A

>T PP-DT2 DAS12 SRC

>

APPENDIX (4. COM. PRO.5)

Computer programme for Harmonic Analysis

```

0001 LIST (LP)
0002 PROGRAM (FXX)
0003 INPUT 1 = CR0
0004 INPUT 3 = TR0
0005 INPUT 5 = CR1
0006 OUTPUT 2 = LD0
0007 OUTPUT 6 = LP1
0008 COMPRESS INTEGER AND LOGICAL
0009 COMPACT
0010 TRACE 2
0011 END

```

```

0012 TRACE 1
0013 READ FROM (CR)
0014 MASTER
0015 INTEGER X, XEND, N, NEND, KEND, N2, POINTS
0016 REAL NREAL, KREAL, F(100), A(51), B(49)
0017 REAL PERCENT(49)
0018 DO 60 READ(1,82) RADIUS
0019 82 FORMAT(F7.2)
0020 WRITE(2,83)
0021 83 FORMAT('1',10X,'FOURIER ANALYSIS OF THE
0022 *FOR MILD STEEL SHELL',/,10X,90(' '),/)
0023 READ(1,82) N
0024 62 FORMAT (I2)
0025 WRITE(2,84) RADIUS
0026 84 FORMAT(10X,'RADIUS=',F7.2,/,10X,15(' '),/)
0027 POINTS=2*N-1
0028 READ(1,100) FO,(F(L),L=1,POINTS)
0029 100 FORMAT(6F10.3)
0030 AU=FO
0031 DO 63 I=1,POINTS
0032 65 AU=AO+F(I)
0033 NREAL=N
0034 AC=AO/NREAL
0035 KEND=N-1
0036 DO 64 K=1,KEND
0037 A(K)=FO
0038 B(K)=0.0

```

CURRENT DENSITY


```

0026 KREAL=X
0027 DO 65 X=1,POINTS
0028 XREAL=X
0029 ARG=3.14159265*KREAL*XREAL/NREAL
0030 A(K)=A(K)+F(X)*COS(ARG)
0031 B(K)=B(K)+F(X)*SIN(ARG)
0032 A(K)=A(K)/NREAL
0033 B(K)=B(K)/NREAL
0034 AMP=SQRT(A(1)**2+B(1)**2)
0035 GA=ATAN2(B(1),A(1))
0036 GAMMA=GA*(180./3.14159265)
0037 PERCENT(K)=SQRT((A(K)**2+B(K)**2)/(A(1)**2+B(1)**2))*100.0
0038 A(N)=FO
0039 DO 66 X=1,POINTS
0040 XREAL=X
0041 ARG=3.14159265*XREAL
0042 A(N)=A(N)+F(X)*COS(ARG)
0043 A(N)=A(N)/NREAL
0044 WRITE(2,41) N,POINTS
0045 FORMAT(1H0,10X,3HN =, I4, 5X, 8HPPOINTS =, I4)
0046 WRITE(2,42) A0
0047 FORMAT(10X,'A0=',F10.5)
0048 WRITE(2,101)
0049 * I AMPLITUDE
0050 * B I,12X,'%',9X,'MAG',11X,'GAMMA',/,10X,90('°'),/
0051 * H I,10X,'ANGLE',/,10X,'H I',10X,'A I',10X,'
0052 * HARMONIC',10X,'TERM',10X,'TERM',10X,'TERM',10X,
0053 WRITE(2,43) A(1),B(1),AMP,GAMMA
0054 FORMAT(10X,' I',4X,F10.3,4X,F10.3,6X,' 100.000',3X,F7.3,7
0055 *X,F7.2)
0056 NEND=N-1
0057 DO 74 I=2,NFND
0058 WRITE(2,44) I,A(I),B(I),PERCENT(I)
0059 FORMAT(13X,I2,8X,F10.3,4X,F10.3,6X,F10.3)
0060 GO TO 60
0061 STOP
0062 END

```

APPENDIX 5

A.5.1 THE CONSTANTS A', a, AND b IN TERMS OF KNOWN QUANTITIES IN THE z PLANE

The value of A' can be found by integrating round a semicircle when the corner of the polygon is at $z = \pm \infty$. When this happens, as the path from one side to the other in the z plane approaches the corner at infinity, so the radius of the semicircle in the w plane gets larger and larger and in the limit become infinite.

Then $R \rightarrow \infty, W = Re^{j\theta}$ A.5.1

$$dw = jR e^{j\theta} d\theta$$
 A.5.2

$$\int dz = A'Rj \int_{\pi}^0 \frac{e^{j\theta}}{Re^{j\theta}} d\theta$$
 A.5.3

$$\int dz = -A'j\pi$$
 A.5.4

In the z plane $\int dz = jg'$

hence $A' = -g'/\pi$ A.5.5

A similar investigation at the other end of the configuration in the z plane where $w = 0$ gives the relation between a and b. Here the path of integration is a small semicircle centred on the origin and of radius 'r' where $r \rightarrow 0$. Then as before

$$w = re^{j\theta}$$

$$\int dz = \frac{A j\sqrt{ab}}{r.e^{j\theta}} \cdot r.j.e^{j\theta} \int_{\pi}^0 d\theta$$
 A.5.6

$$A_1 = -g' \sqrt{ab} \quad \text{A.5.7}$$

Referring to Fig. 2.4 it is seen that the value of w as one moves along the positive real axis from the origin passes through the point $w = -1$. Fig. 2.3 shows that the corresponding value of z changes abruptly at the point corresponding to $w = -1$ by the amount jjg . Hence from equation 2.1

$$\int dz = jjg = \frac{\pi j A' \sqrt{(-1-a)(-1+b)}}{-1} \quad \text{A.5.8}$$

From equation A.5.8 and substituting the value of A' from A.5.5

$$\frac{g}{g'} = \sqrt{(1+a)(1-b)} \quad \text{A.5.9}$$

A.5.2 THE INTEGRATION $A' \int \frac{\sqrt{(w-a)(w+b)}}{w(w+1)} dw$

The integrand is not in a form in which Dwight's Table can be applied and some preliminary treatment is necessary.

Put

$$\psi^2 = \frac{w+b}{w-a} \quad \text{A.5.10}$$

$$w = \frac{b+\psi^2 a}{\psi^2-1} \quad \text{A.5.11}$$

and $dw = - \frac{2\psi(a+b)}{(\psi^2-1)^2} d\psi \quad \text{A.5.12}$

Substituting the values of w and dw in terms of ψ

$$\int dz = A' \int \frac{\sqrt{(w-a)(w+b)}}{w(w+1)} dw + c$$

$$= - A' \int \frac{2\psi^2 (a+b)^2 d\psi}{(b+\psi^2 a) \{b+\psi^2 (a+1)-1\} (\psi^2-1)} + c \quad \text{A.5.13}$$

$$= \frac{K_1}{K_4} A' \int \frac{\psi^2 d\psi}{(K_2+\psi^2) (K_3+\psi^2) (\psi^2-1)} + c \quad \text{A.5.14}$$

where the values of K_1, K_2, K_3, K_4 in terms of a and b are given in section 2.2.

Breaking up the integrand in A.5.14 into partial fractions, it becomes

$$\left[\frac{A}{(K_2+\psi^2)} + \frac{B}{(K_3+\psi^2)} + \frac{C}{(\psi^2-1)} \right] d\psi \quad \text{A.5.15}$$

The values of A, B and C are given in section 2.2 in Chapter 2.

Using Dwight's Table ⁵⁹ A.5.15 can be integrated and the final form is given by equation 2.2 of Chapter 2.

FIGURES FOR CHAPTER 1

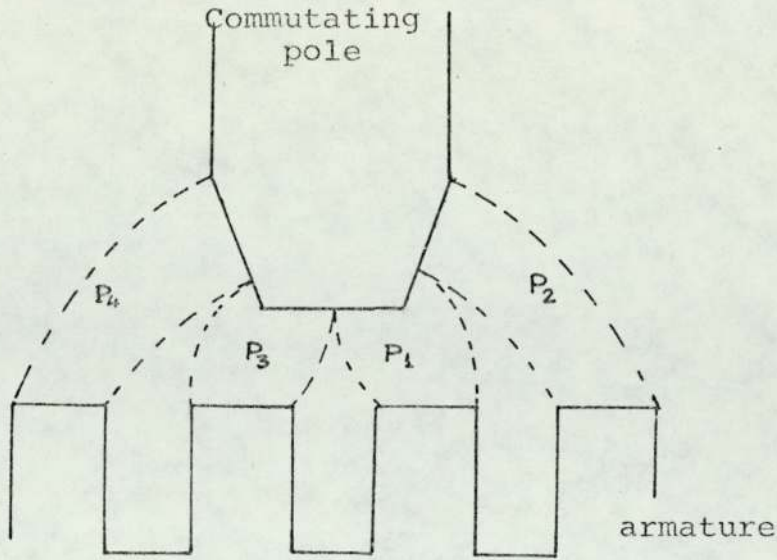


Fig. 1.5 Airgap Flux Path

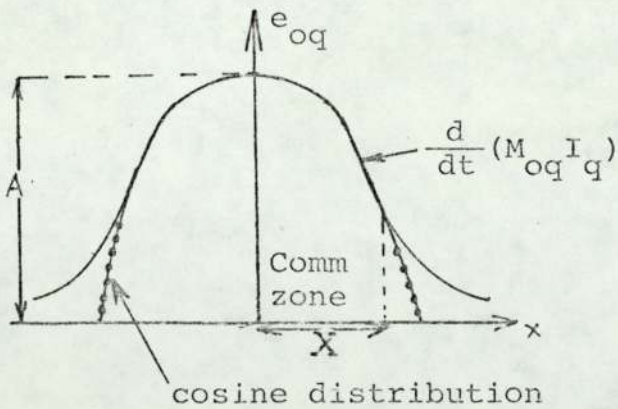


Fig. 1.6 Flux Distribution Curve resulting from Line Current.

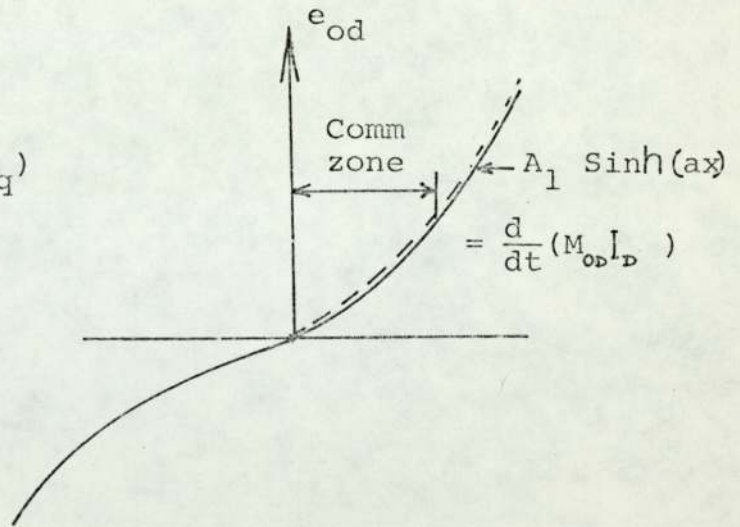


Fig. 1.7 Flux Distribution Curve resulting from Field Current. x is the Distance along the armature surface from centre of the comm zone.

FIGURES FOR CHAPTER 2

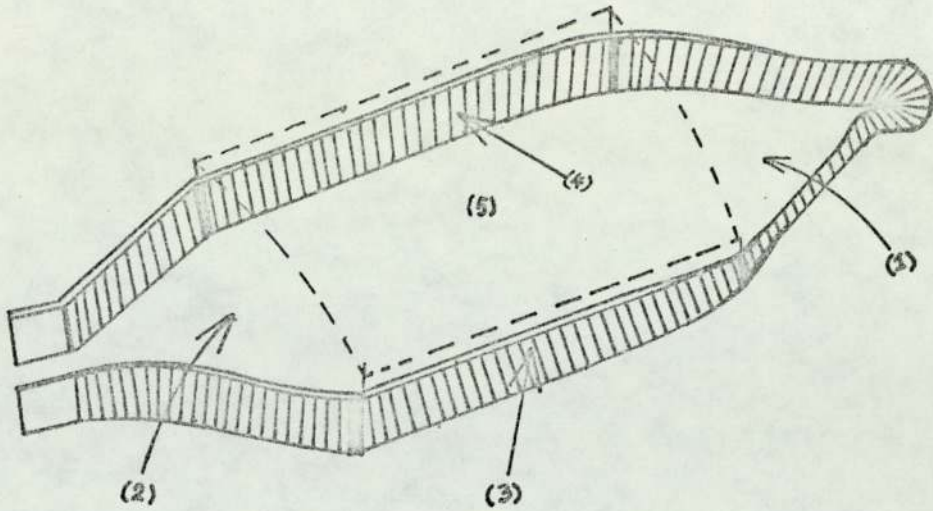


Fig. 2.1 Division of Area Enclosed by a Coil into Five Meshes for Definition of Components of emf.

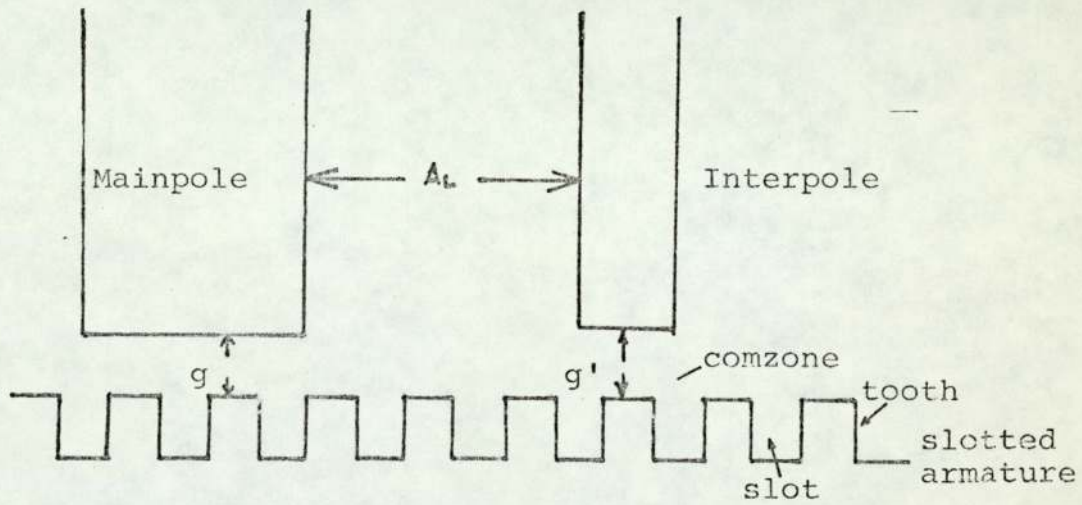


Fig. 2.2

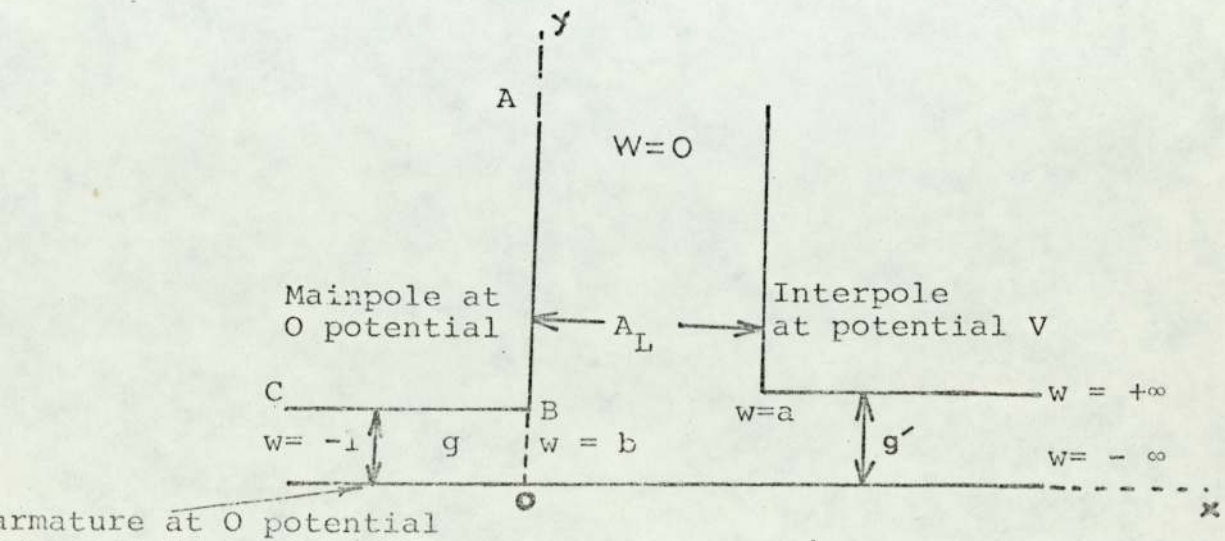


Fig. 2.3 Configuration for First Model. (Z plane.)

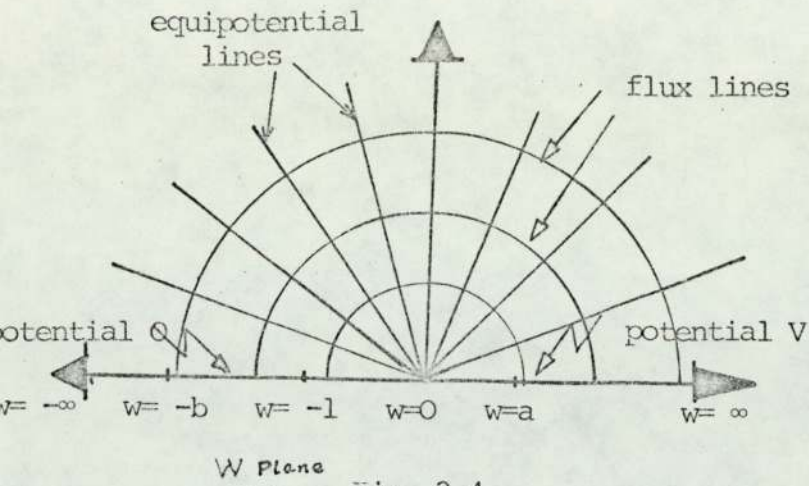


Fig. 2.4

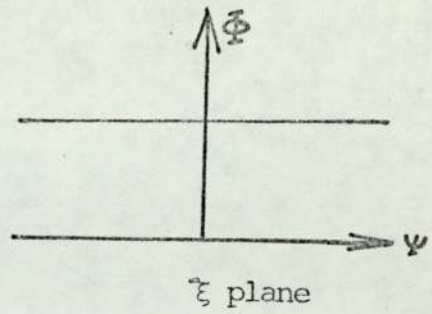


Fig. 2.5

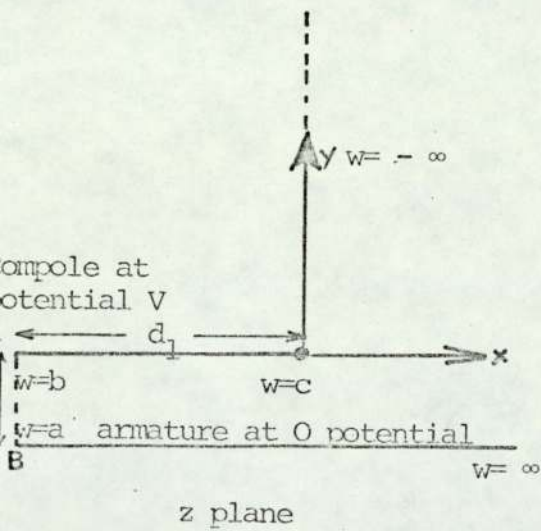


Fig. 2.8 Configuration for Second Model.

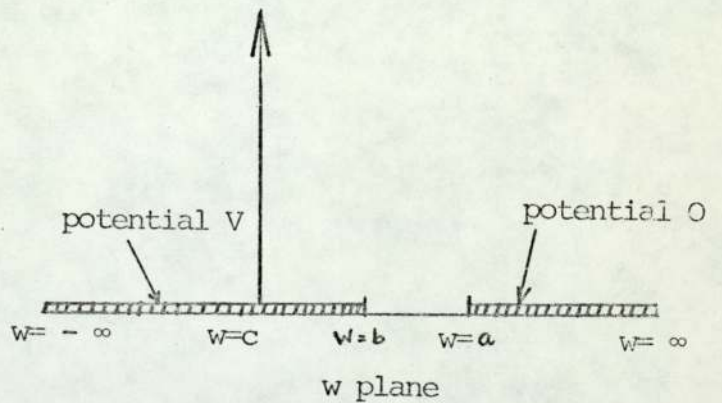


Fig. 2.9

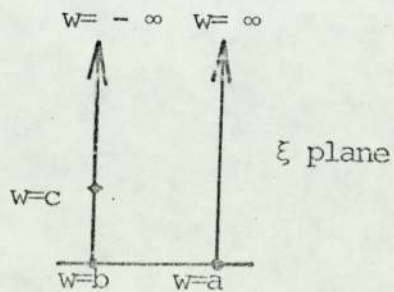


Fig. 2.10

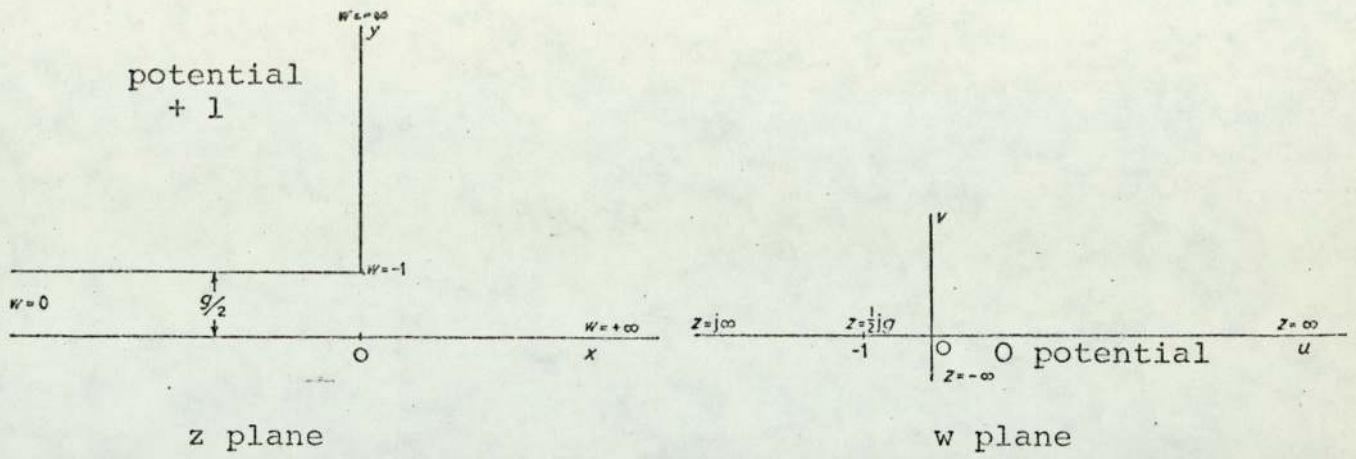


Fig. 2.6. Field Problem with One Right Angle and One Smooth-surface Solved by Gibbs

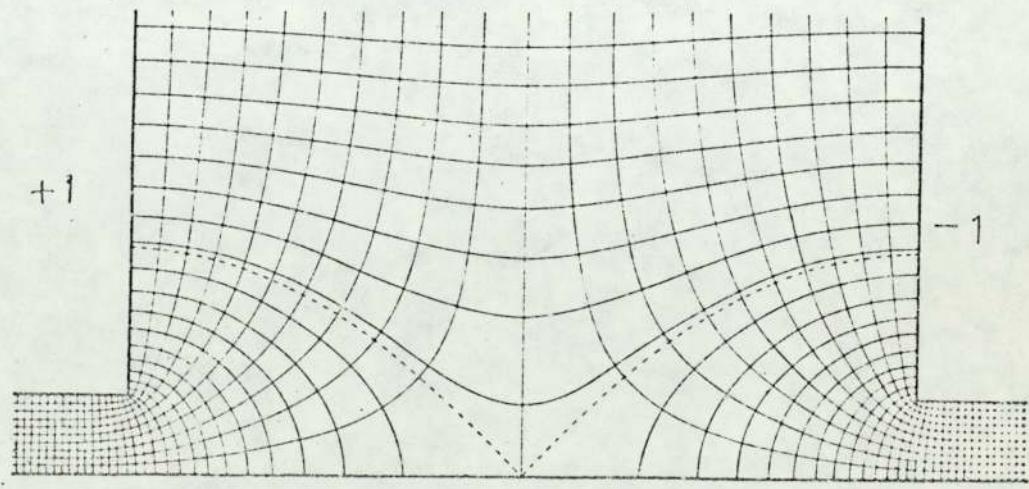
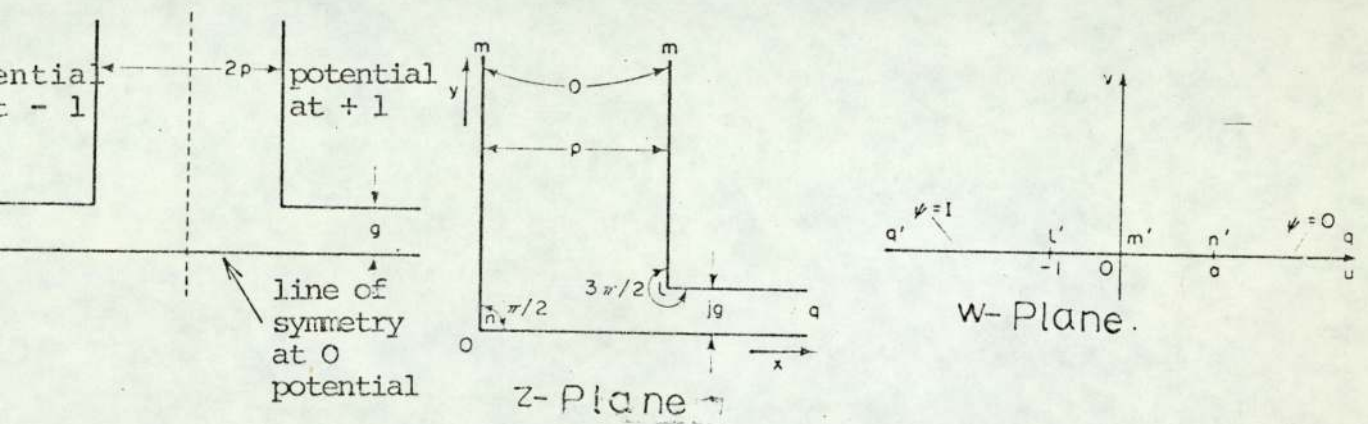


Fig. 2.7 Field Problem with Two Right Angles at Different Potentials and a Line of Symmetry Solved by Binns.

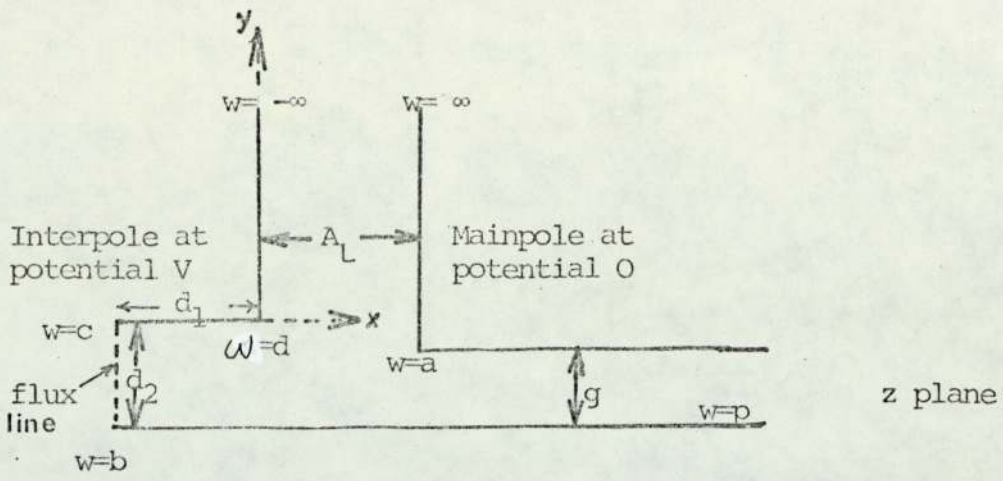


Fig. 2.11 Configuration for Third Model

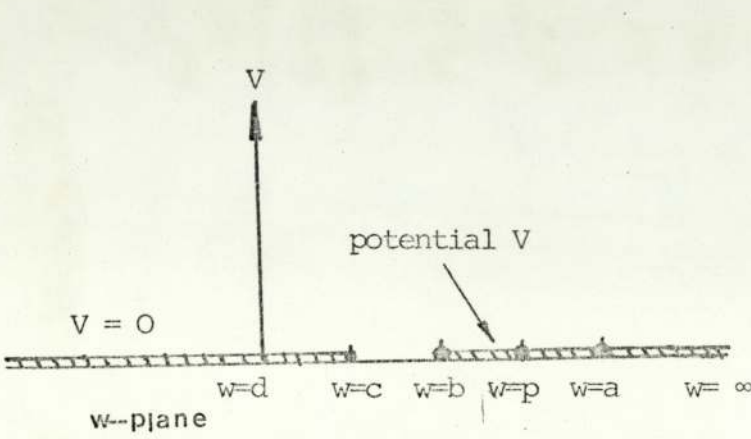


Fig. 2.12

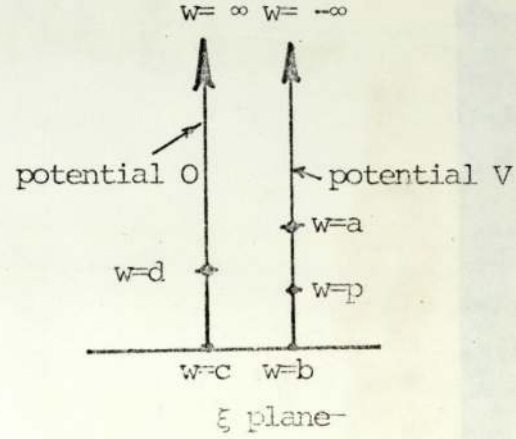


Fig. 2.13

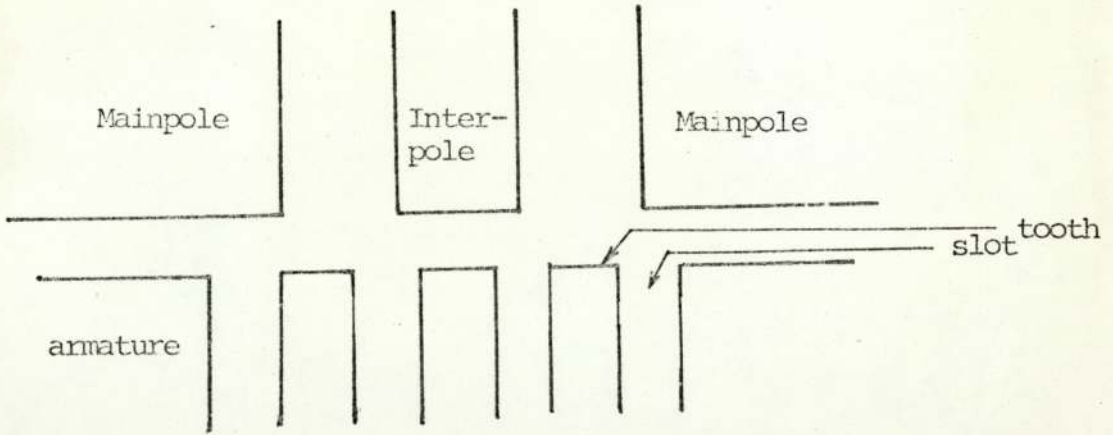


Fig. 2.14

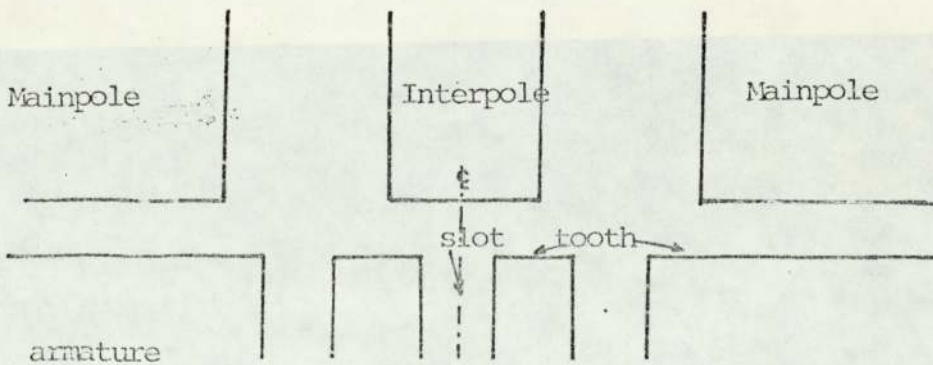
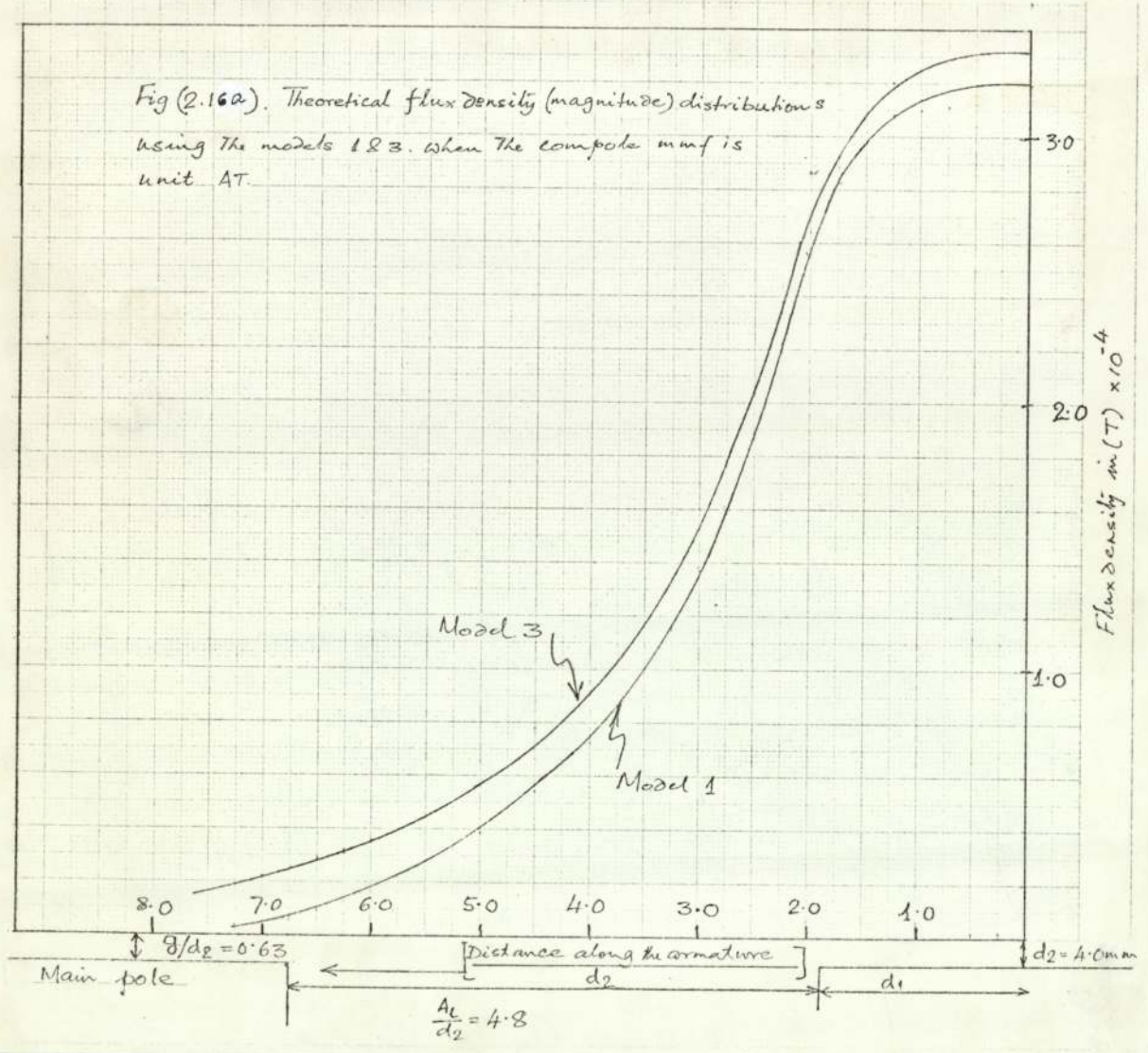


Fig. 2.15

Fig (2.16a). Theoretical flux density (magnitude) distributions using the models 1 & 3. When the complete mmf is unit AT.



1st Model, 1 p.u. = $\beta_{max} = \frac{V}{g} \mu_0$, see page 25.
 2nd Model, see page 35 eqn. 2.25.
 3rd Model, see page 44 eqn. 2.46.
 Gibbs' Model, 1 p.u. = $\beta_{max} = \frac{V}{g} \mu_0$, see Ref. 17

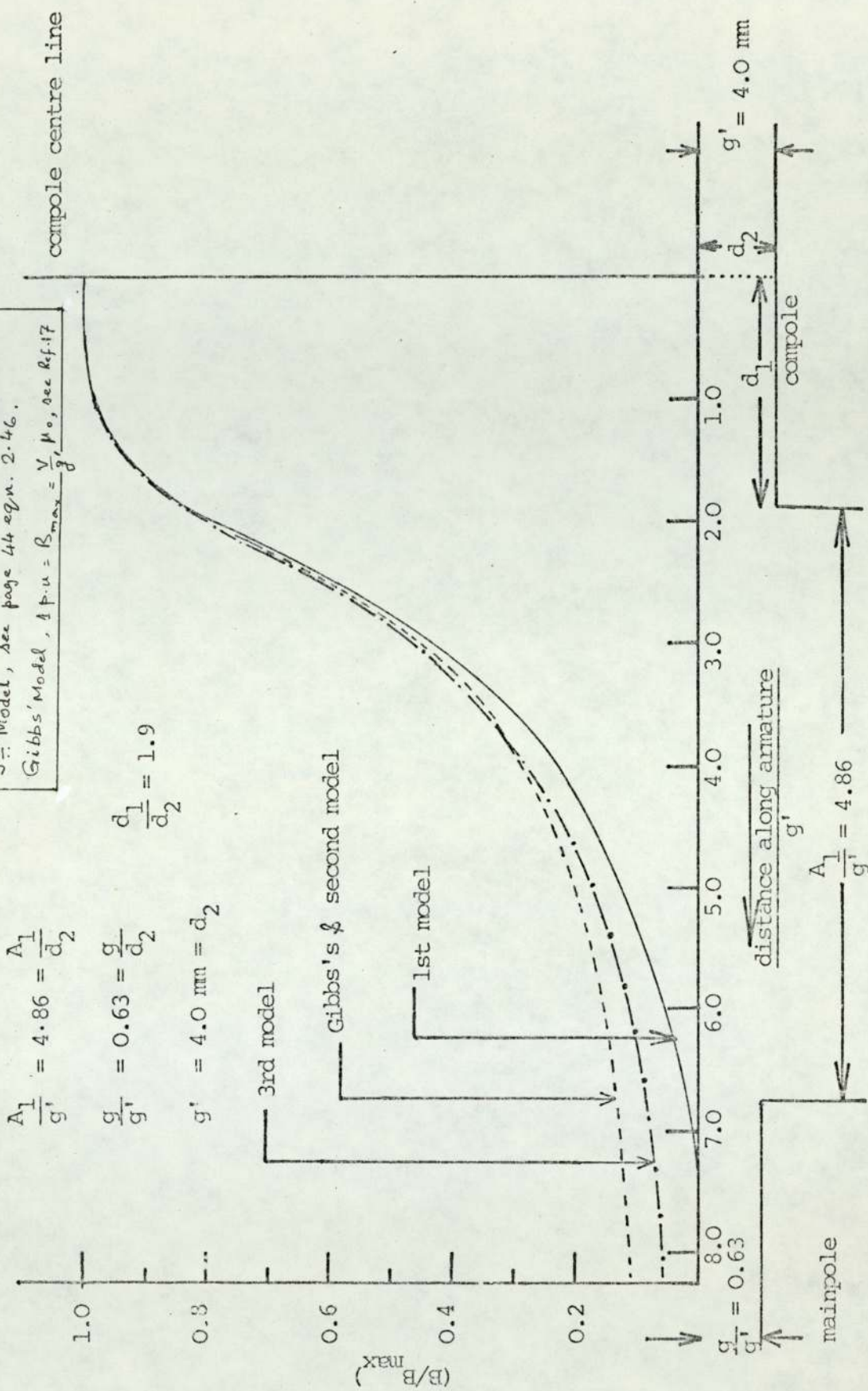


FIG. 2.16 THEORETICAL FLUX DENSITY DISTRIBUTION.

For p.u. bases, See Fig. 2.16.

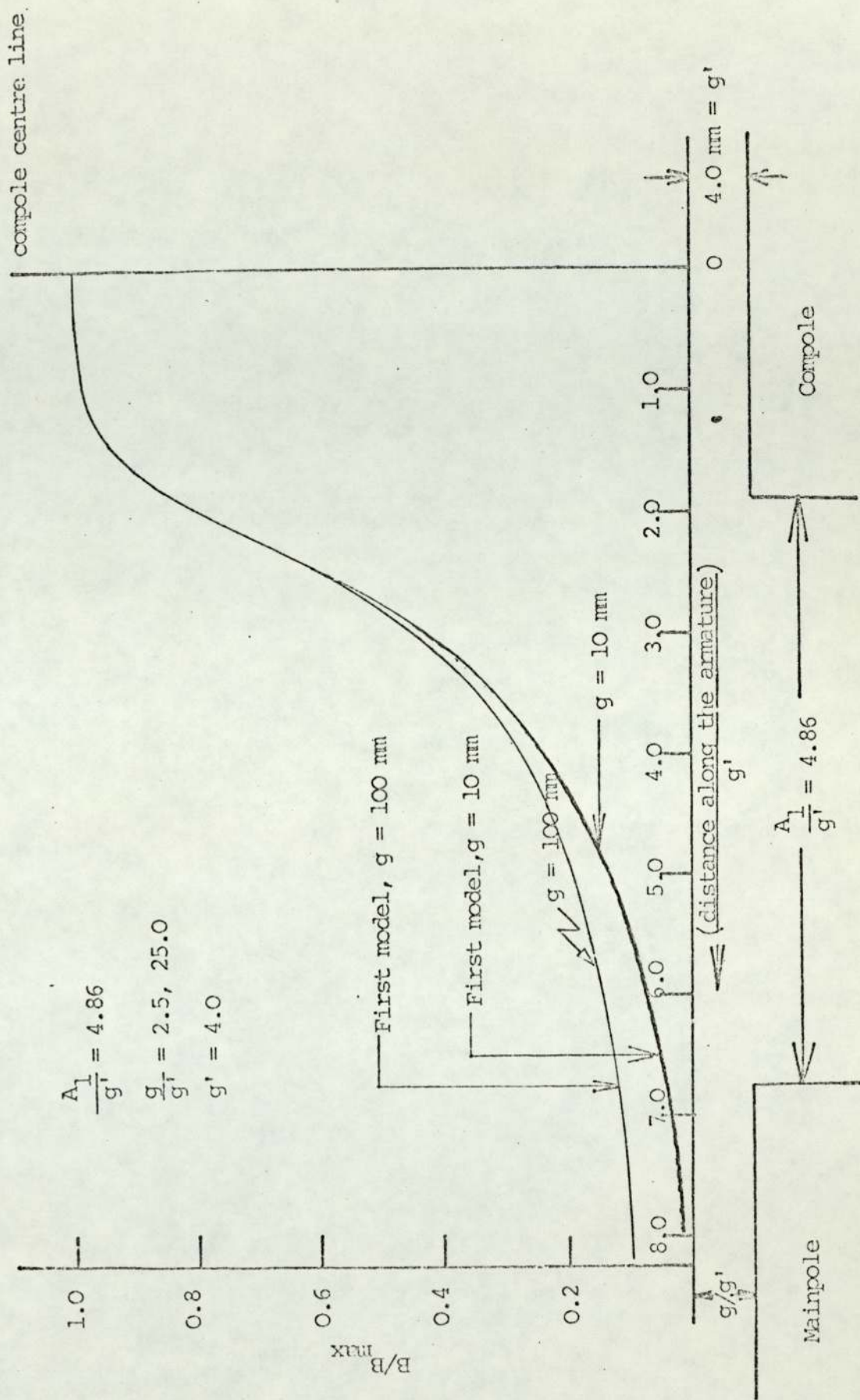


FIG. 2.17 THEORETICAL FLUX DENSITY DISTRIBUTION.

For p.u. bases see Fig. 2.16

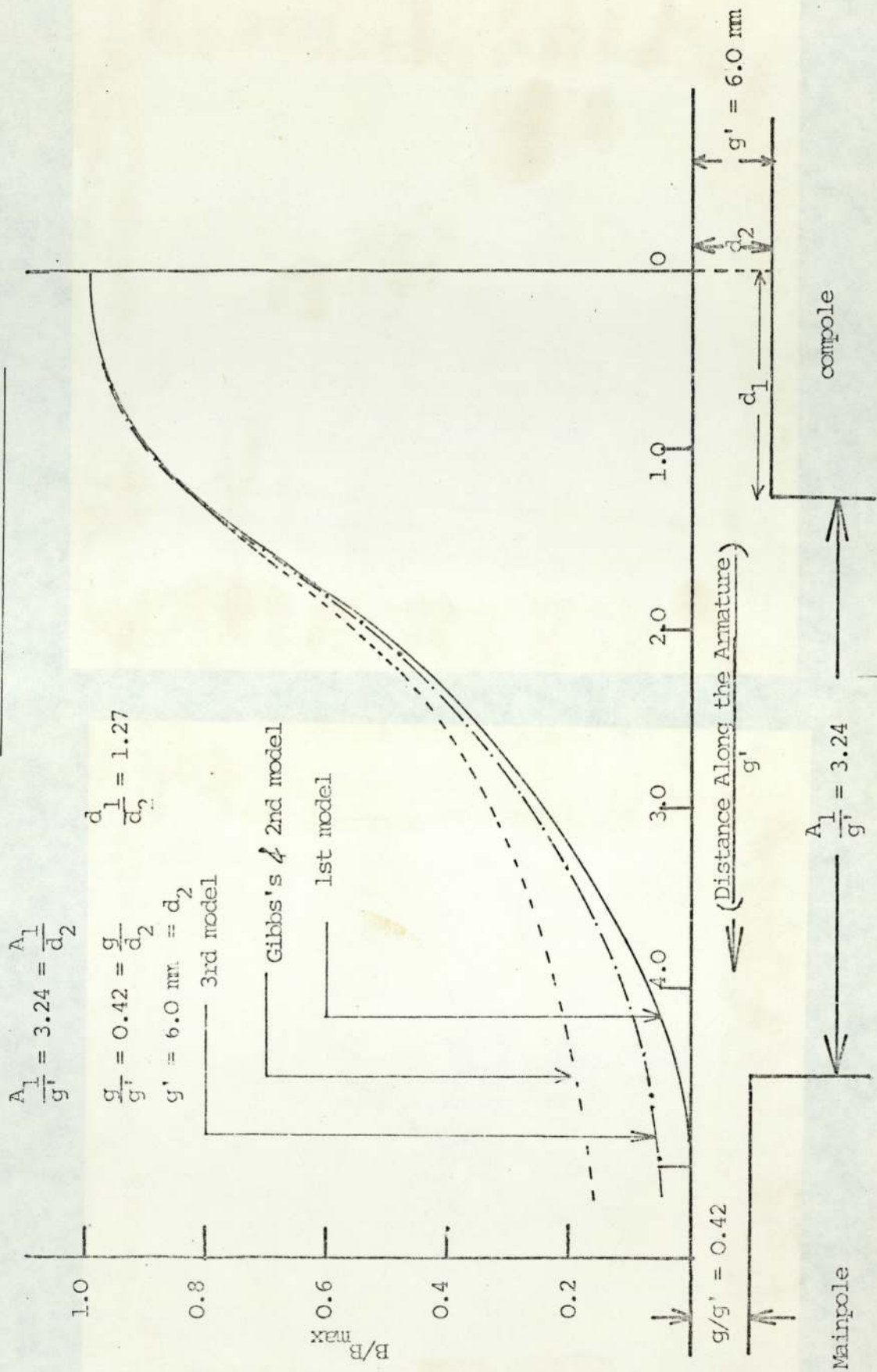


FIG. 2.18 THEORETICAL FLUX DENSITY DISTRIBUTION.

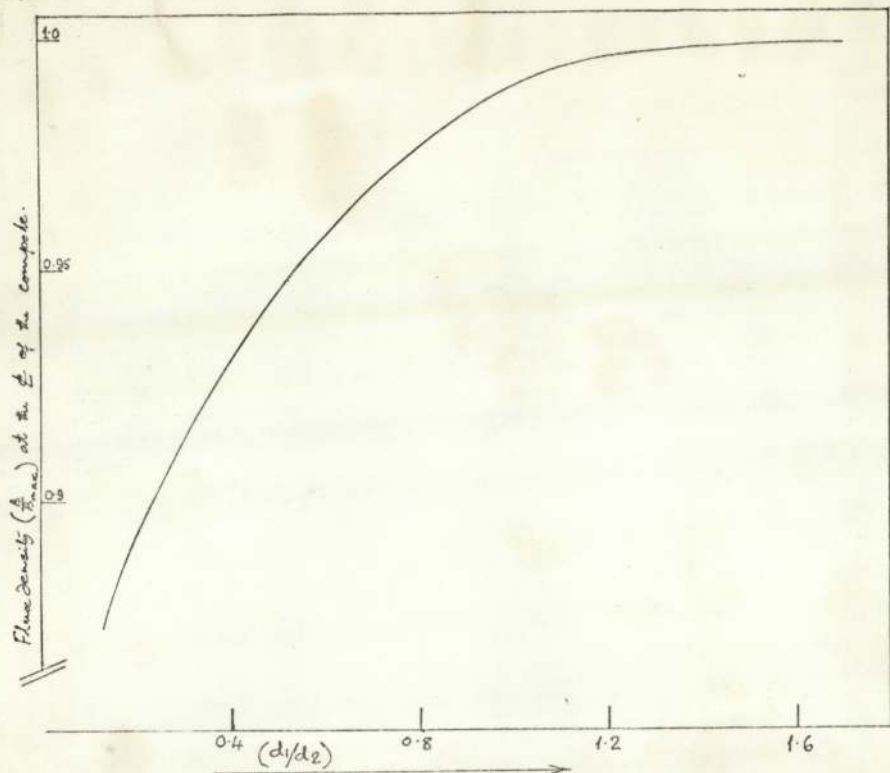


Fig. (2.19A). Variation of $(\frac{B}{B_{max}})_E$ with the parameter (d_1/d_2) using Gibbs' model.

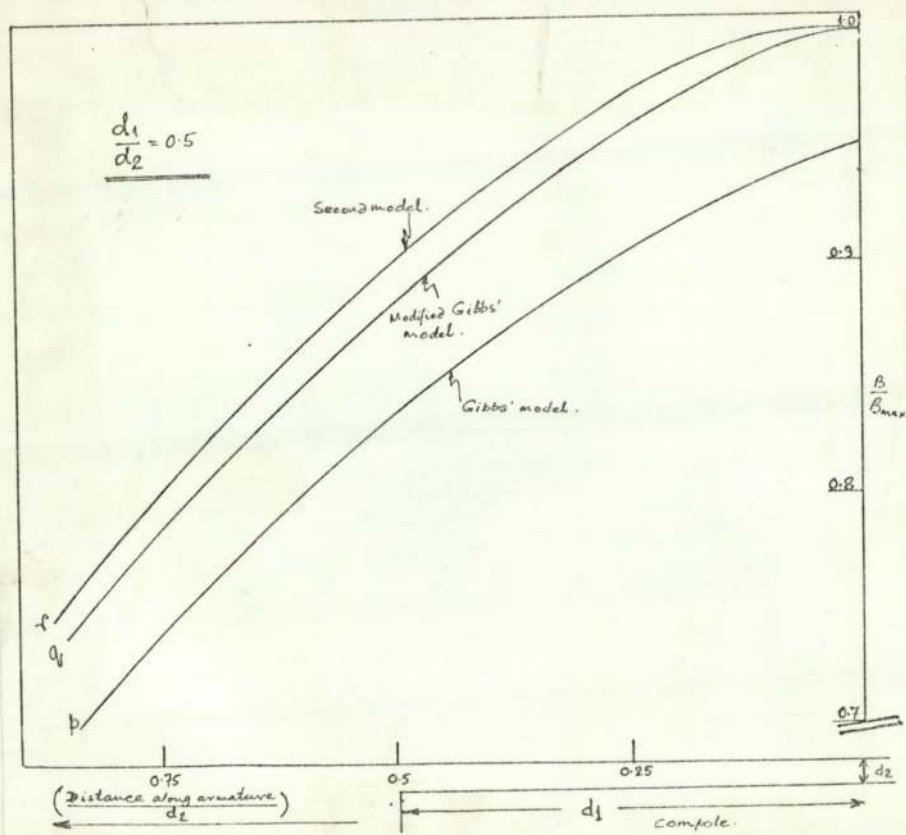


Fig (2.19B) Theoretical Flux Density Distributions.

For p.u. bases see Fig. 2.16

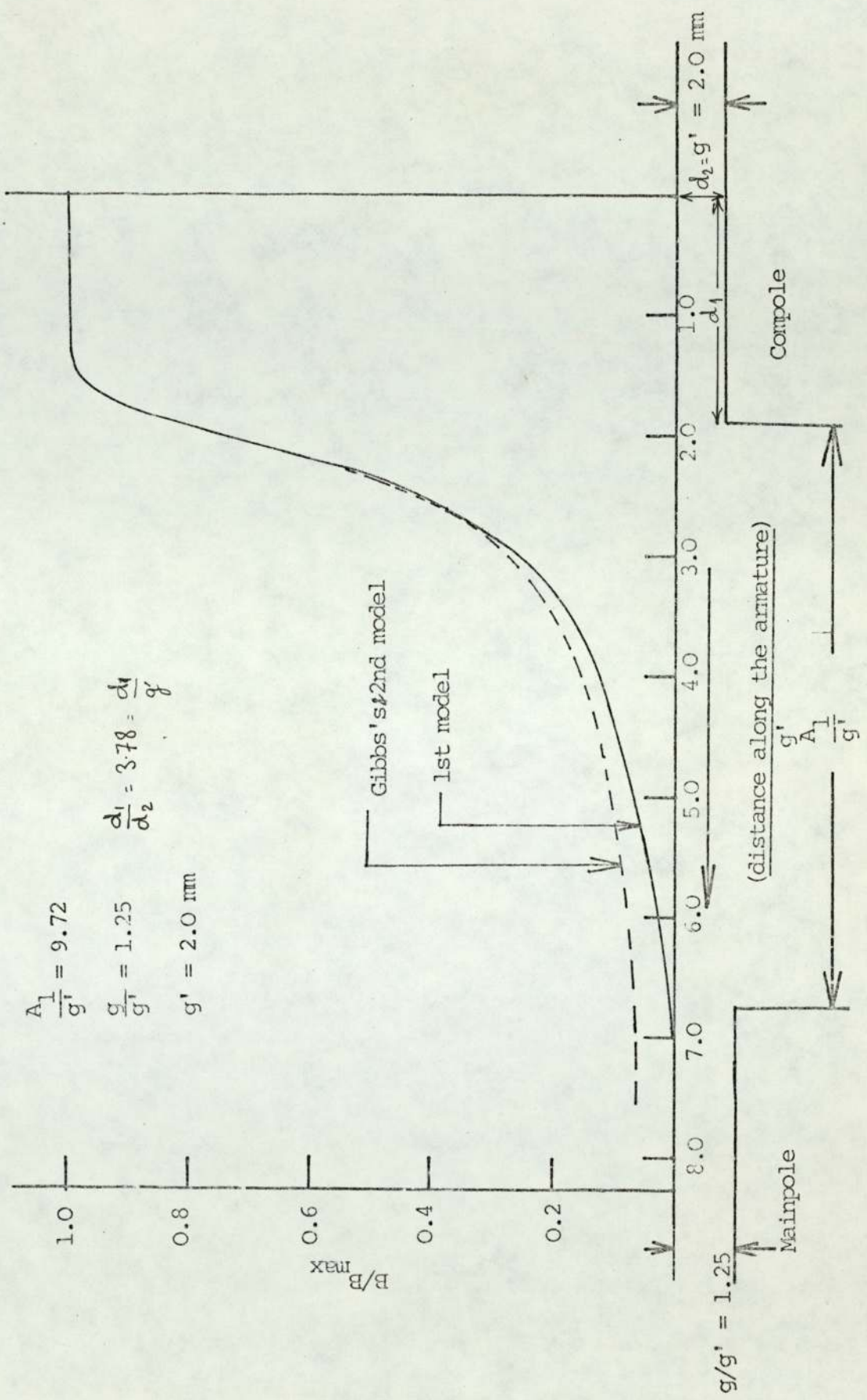


FIG. 2.19 THEORETICAL FLUX DENSITY DISTRIBUTION

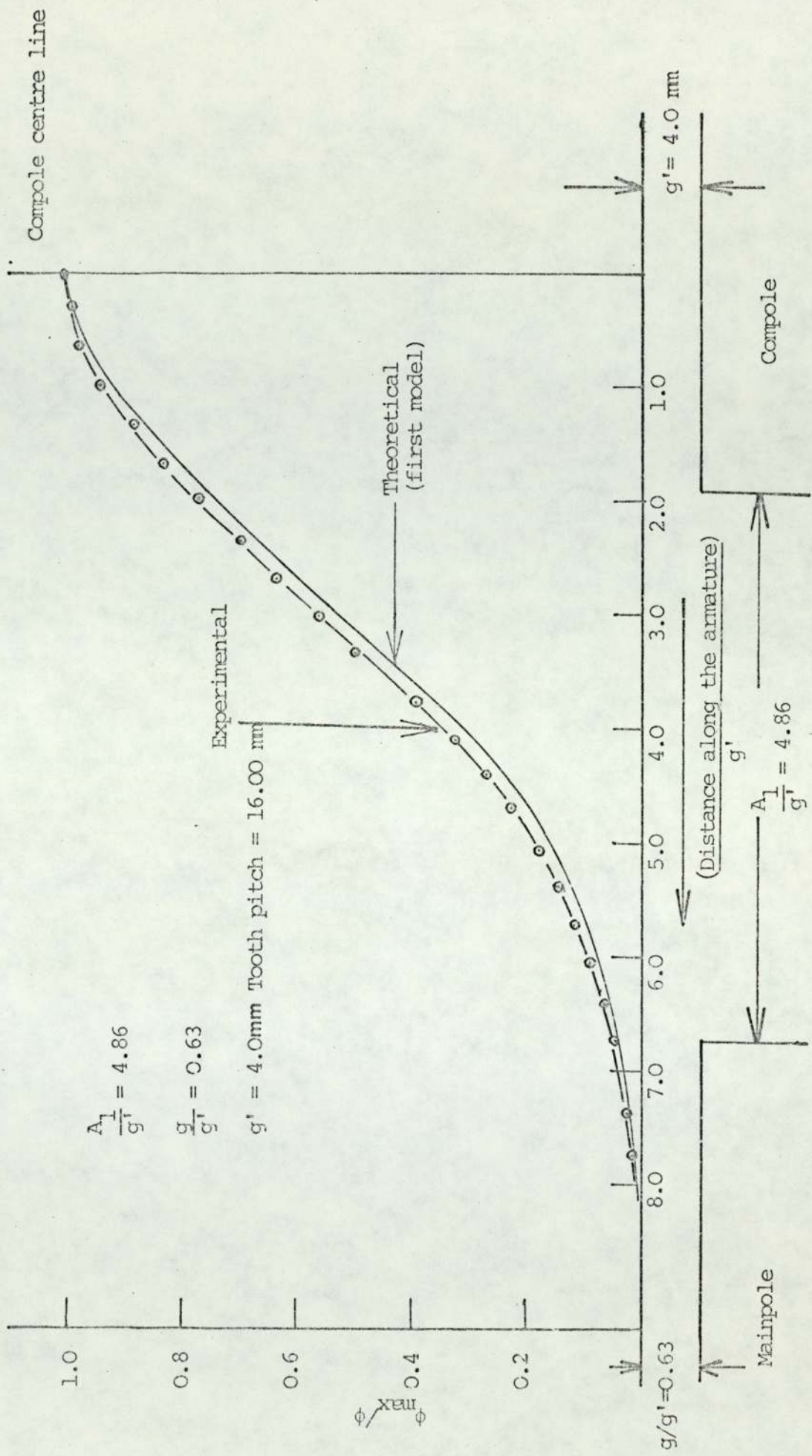
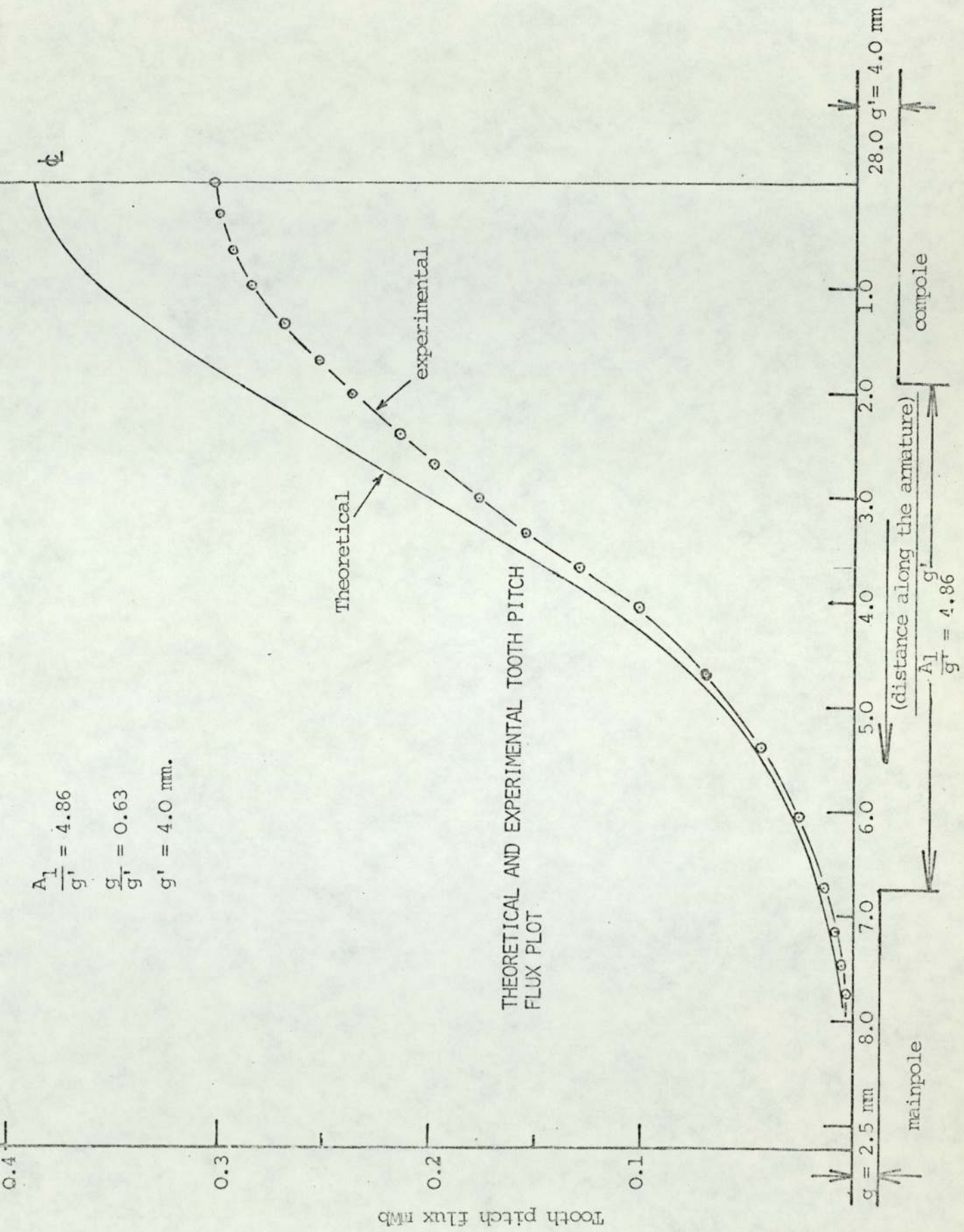


FIG. 2.20 THEORETICAL AND EXPERIMENTAL TOOTH PITCH FLUX DISTRIBUTION ON PER UNIT BASIS.

$$\frac{A_1}{g'} = 4.86$$

$$\frac{g}{g'} = 0.63$$

$$g' = 4.0 \text{ mm.}$$



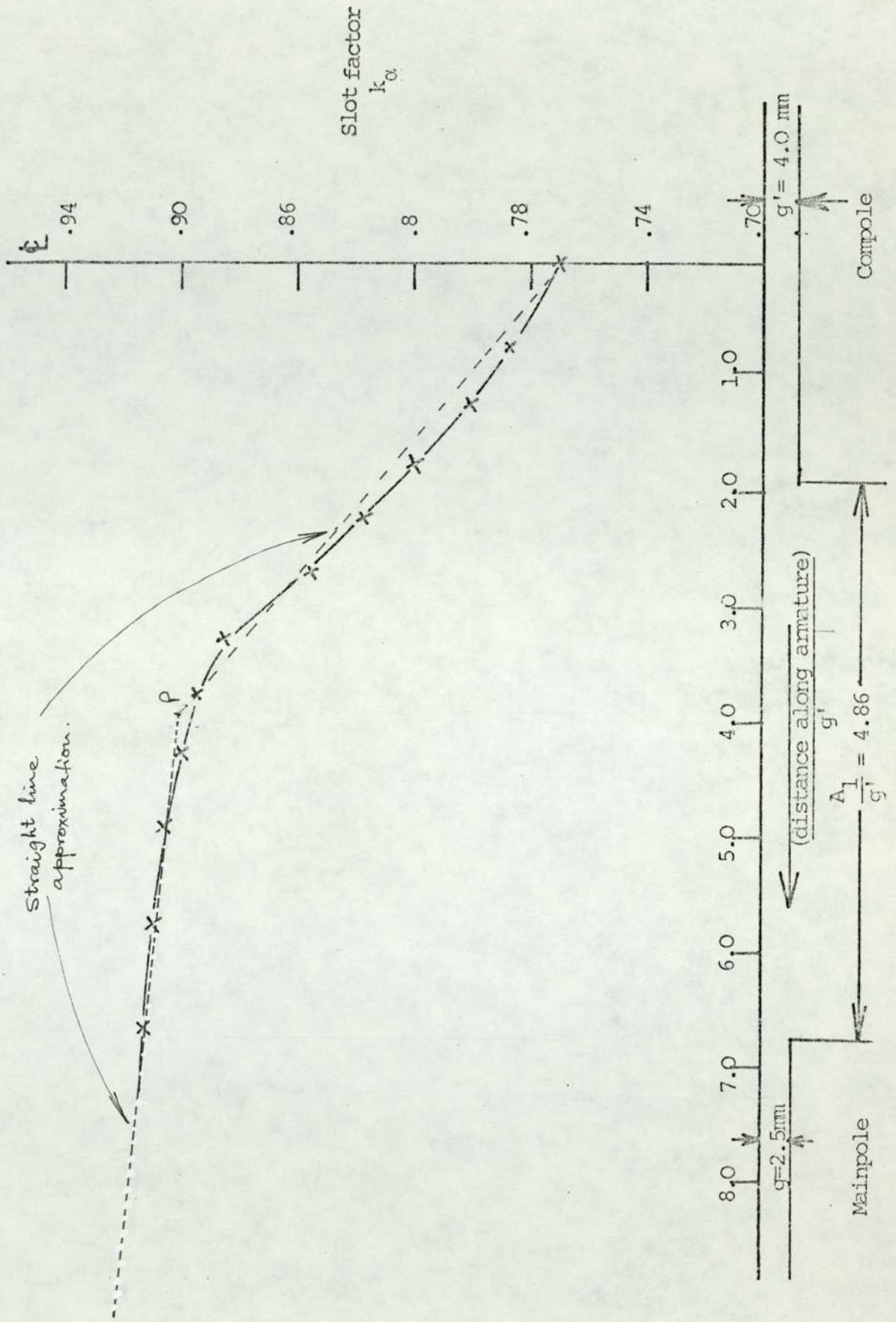


FIG. 2.22 THE VARIATION OF SLOT FACTOR k_{α} WITH DISTANCE ALONG THE ARMATURE

FIGURES FOR CHAPTER 4

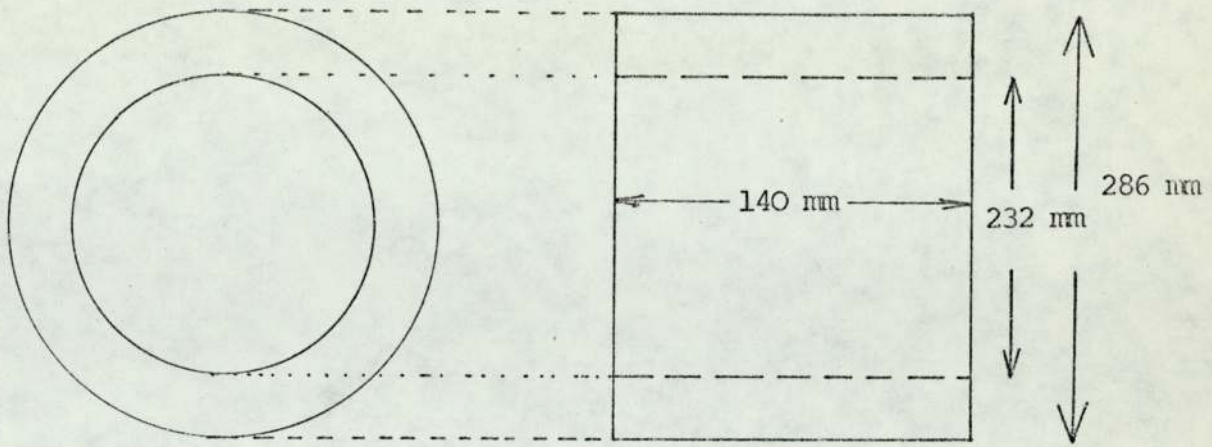


FIG. 4.1 THE SOLID SHELL OF THE EXPERIMENTAL MACHINE

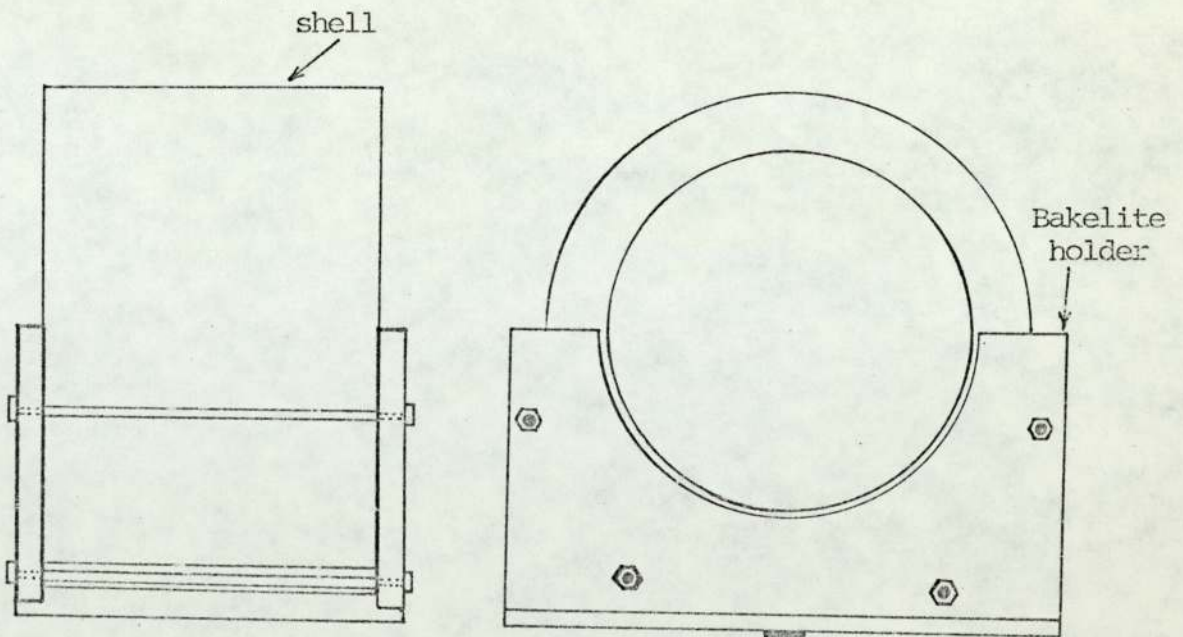


FIG. 4.2 THE SOLID SHELL AND BAKELITE HOLDERS

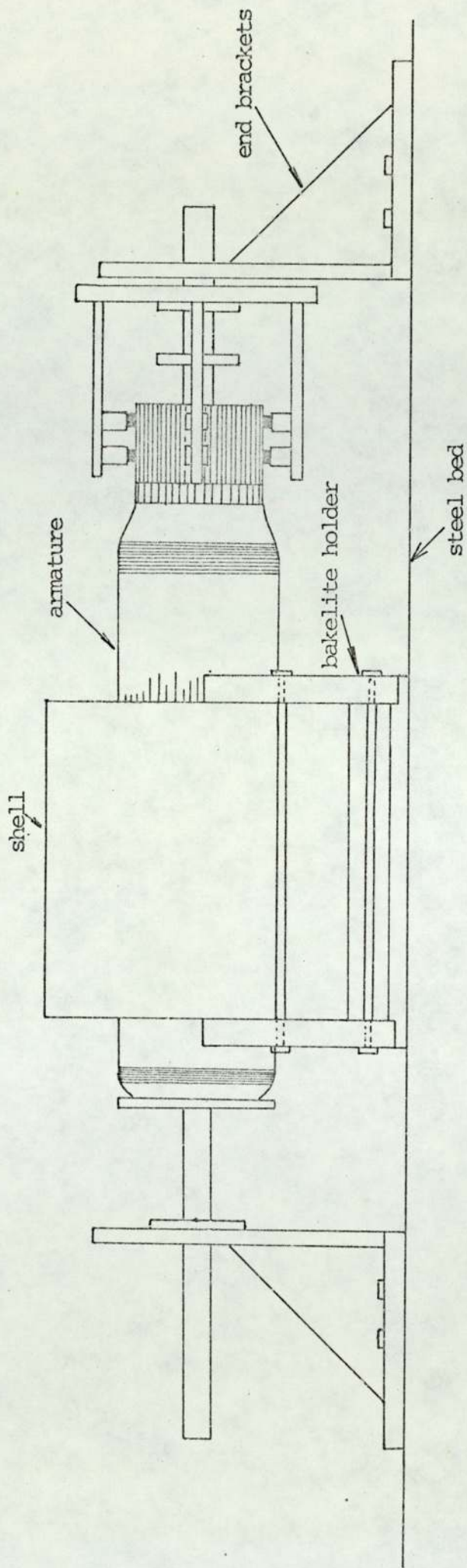
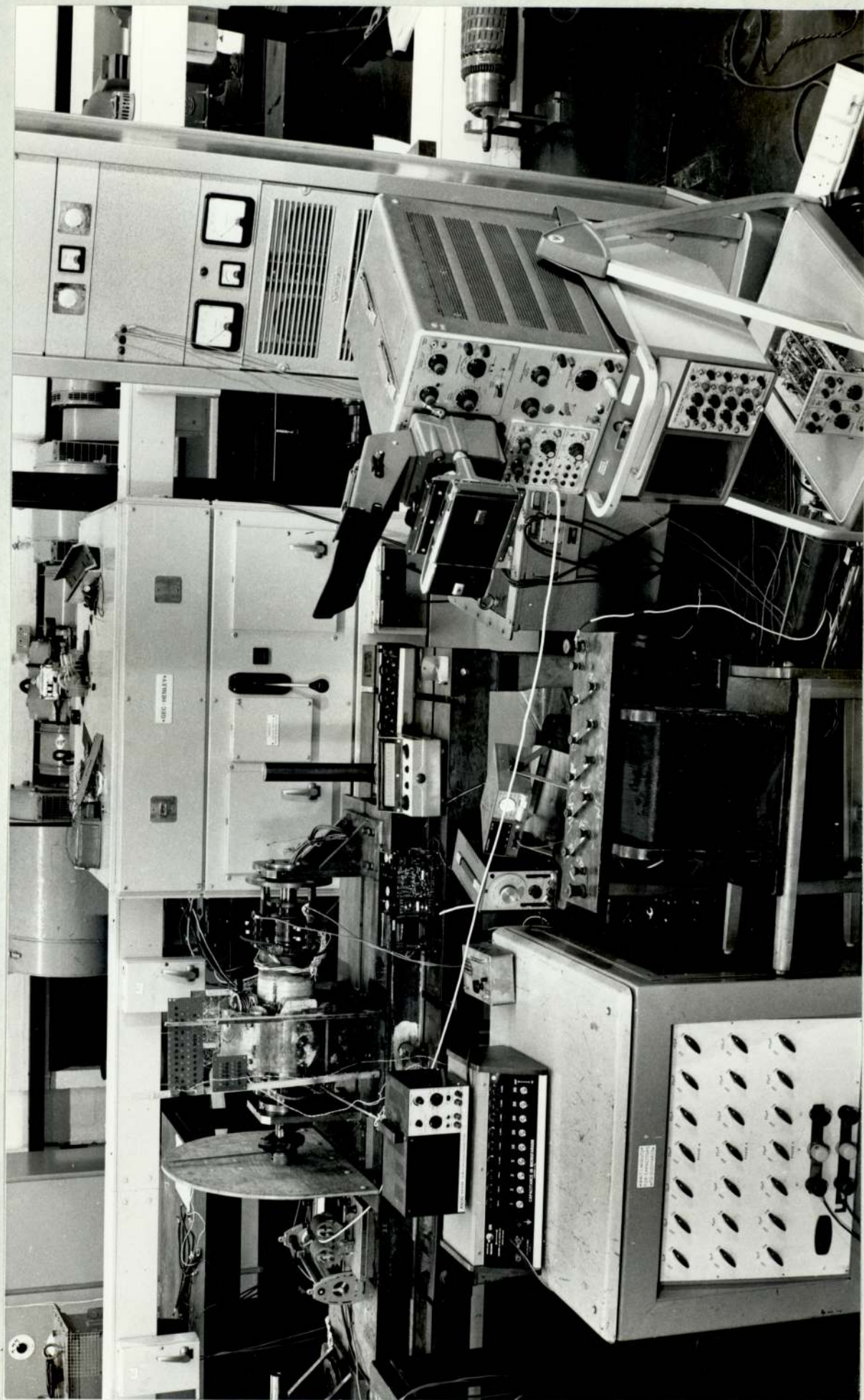
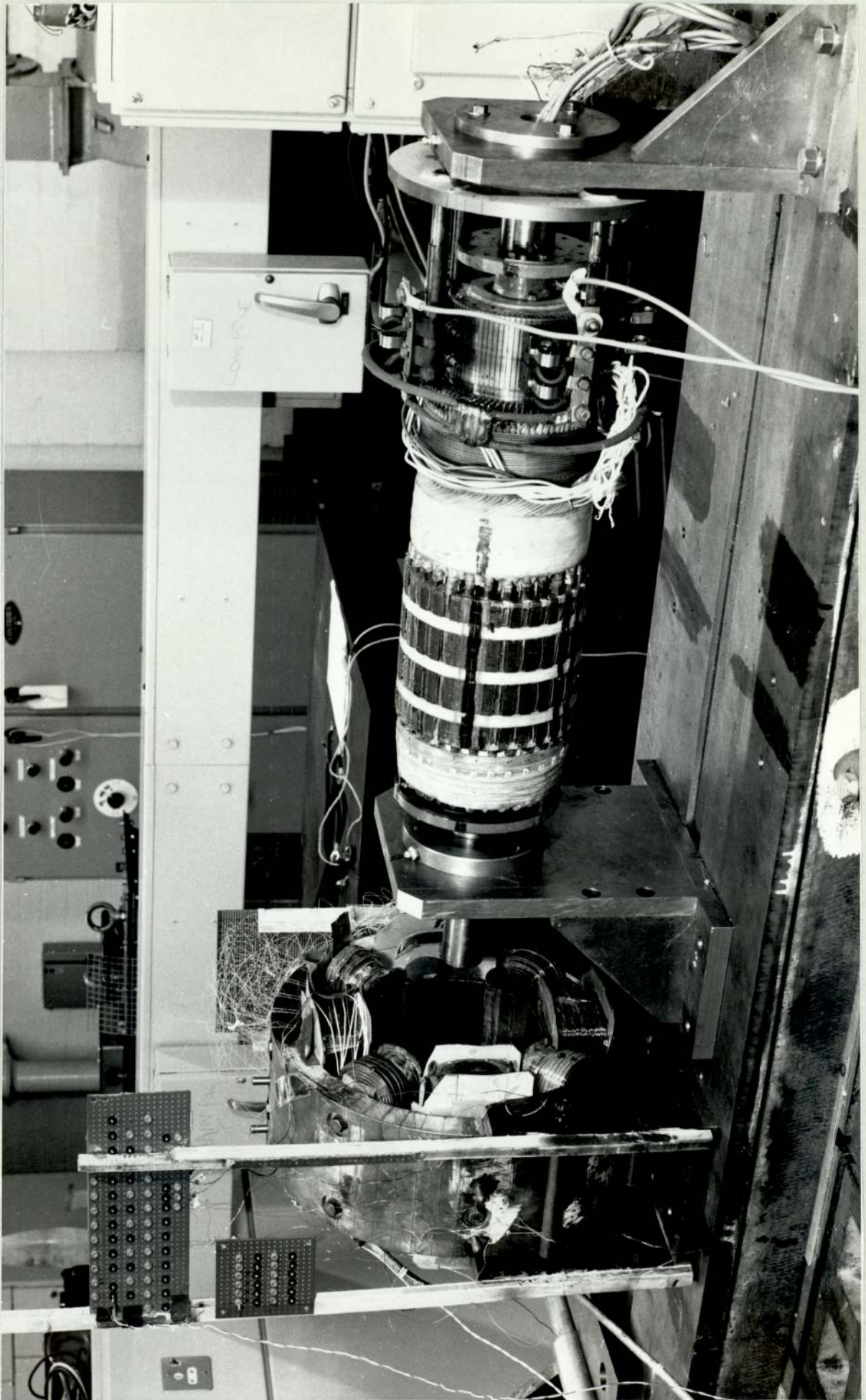


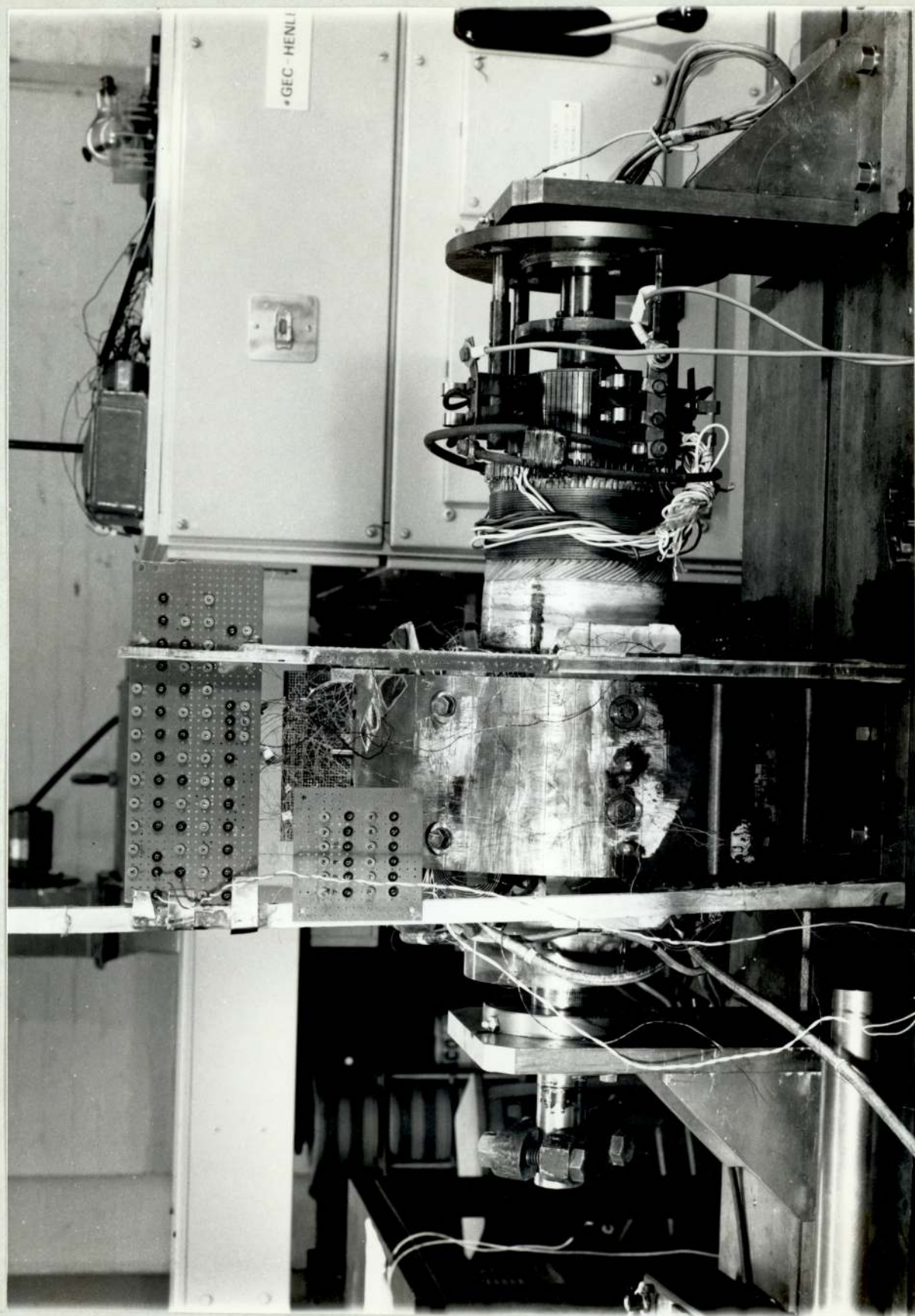
FIG. 4.3 SCHEMATIC DIAGRAM OF THE TEST RIG.



4.4a THE WHOLE EXPERIMENTAL SET UP



4.4b THE TEST MACHINE



4.4c THE TEST MACHINE WITH ARMATURE IN POSITION

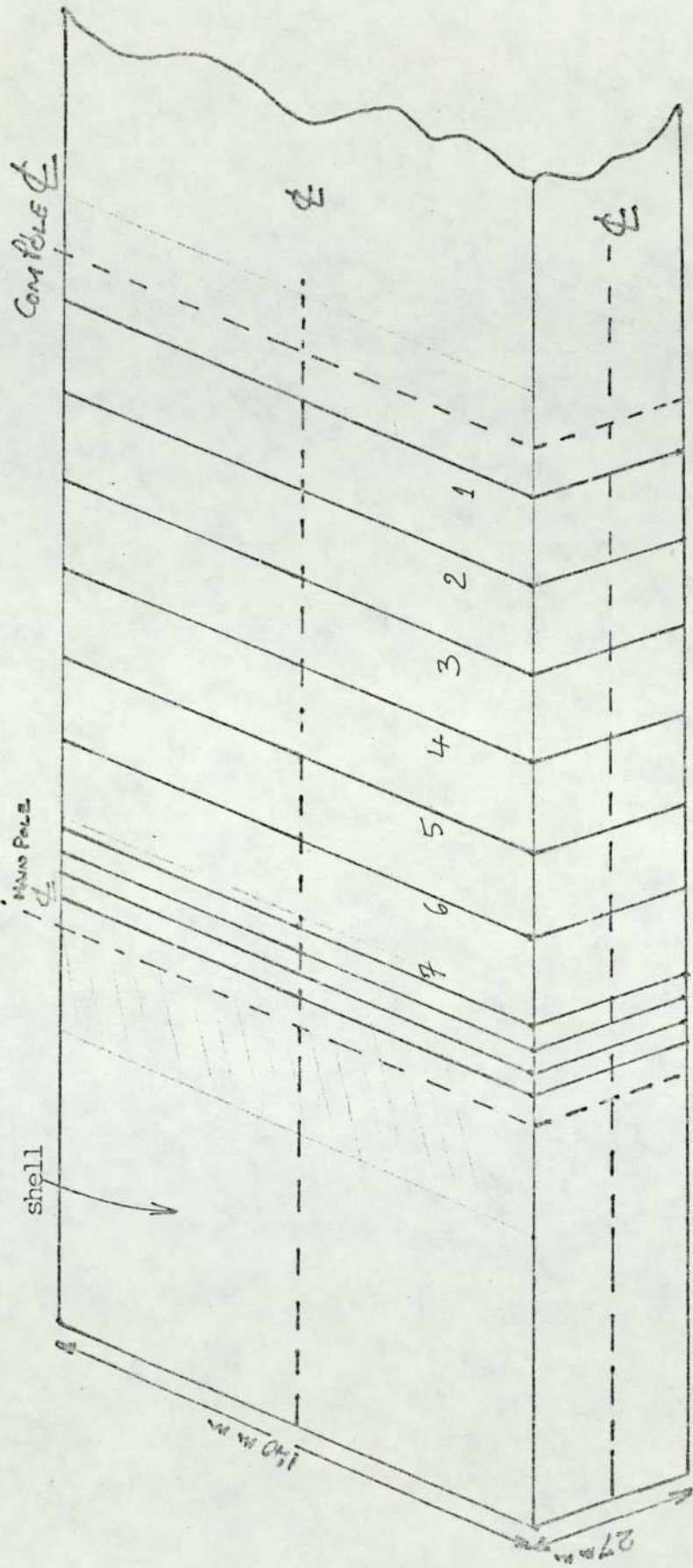


FIG. 4.5 SHELL LOOP SEARCH COILS

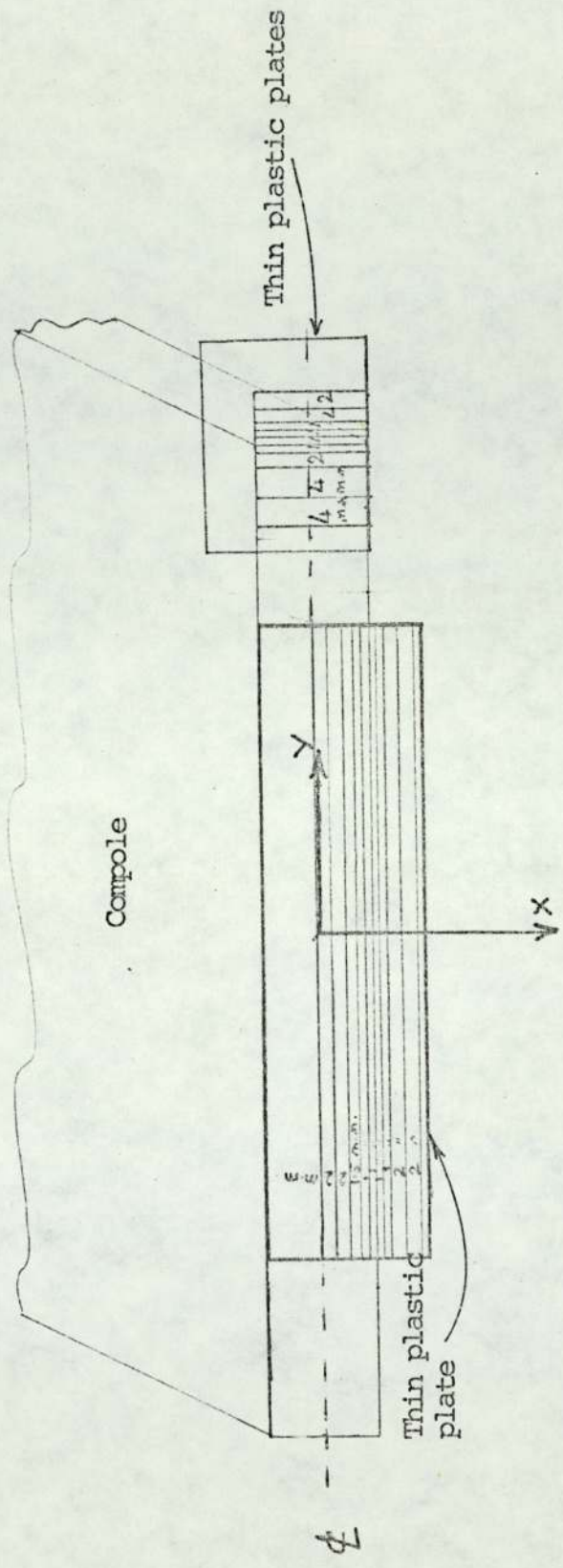


FIG. 4.6 SEARCH COILS FOR THE MEASUREMENTS OF THE FLUX DENSITY IN THE AIRGAP AT THE BACK OF THE COMPOLET (TOWARDS THE SHELL).

FIG. 4.7 TOOTH PITCH SEARCH COIL ON THE ARMATURE SURFACE

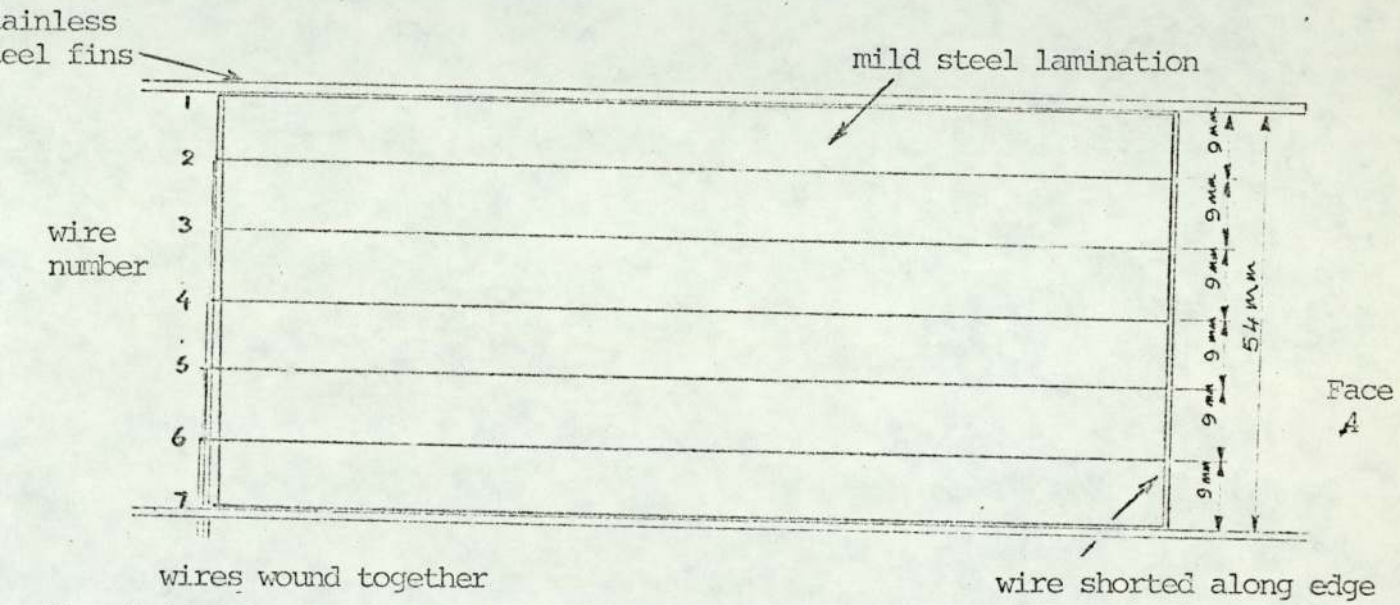
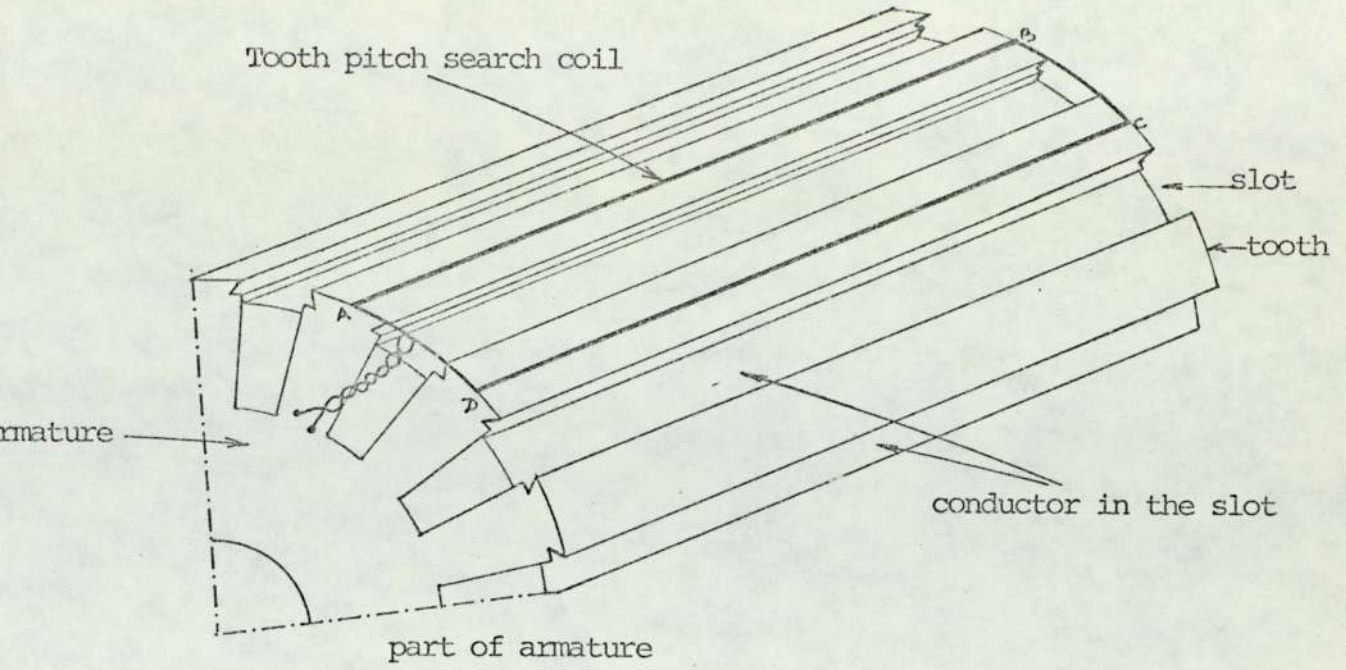


FIG. 4.8a 6 RECTANGULAR SEARCH COILS ON THE FACE A OF THE CORE OF THE COMPOLE

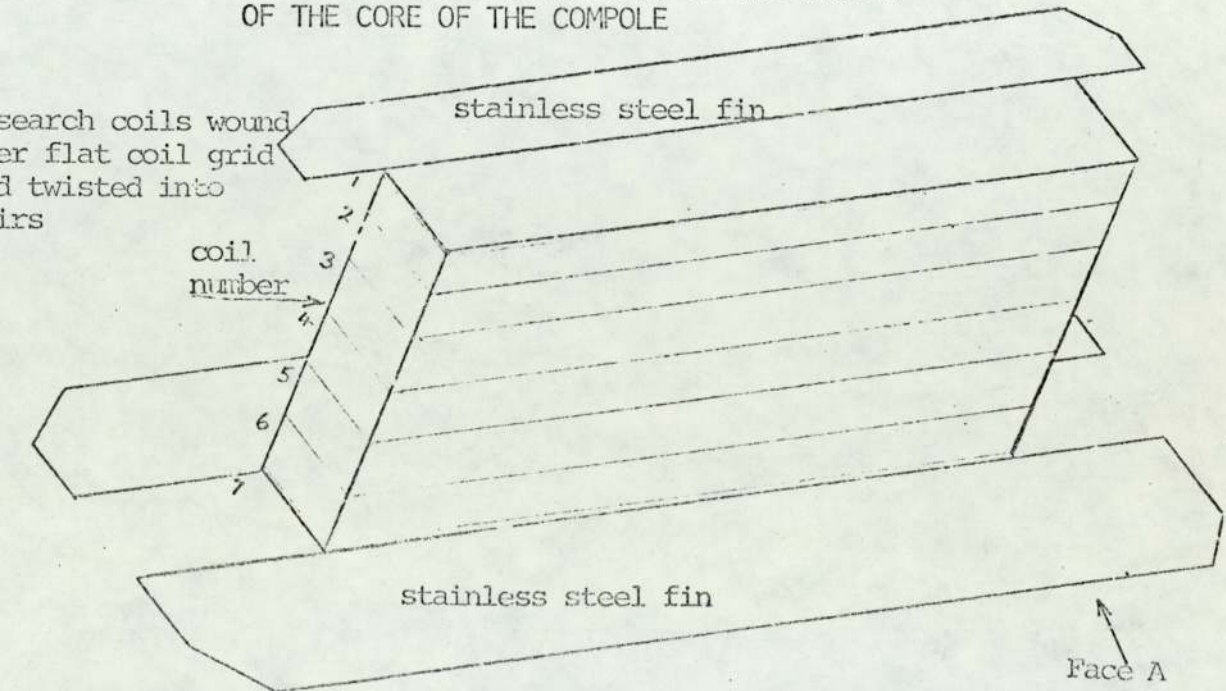


FIG. 4.8b SEARCH COILS AROUND THE CORE OF THE COMPOLE

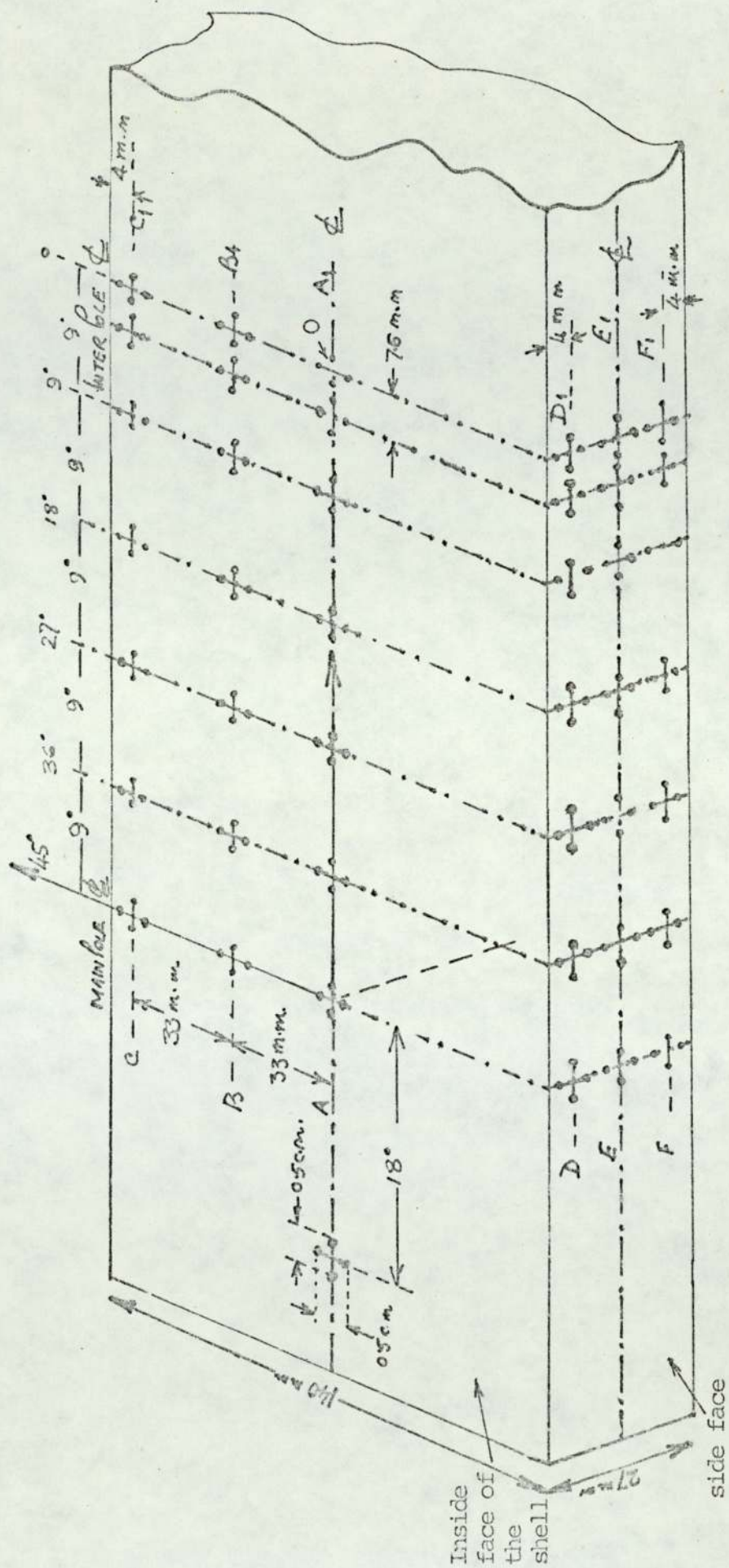


FIG. 4.9a J - PROBE ARRANGEMENT ON THE SIDE AND INNER SURFACE OF THE SHELL.

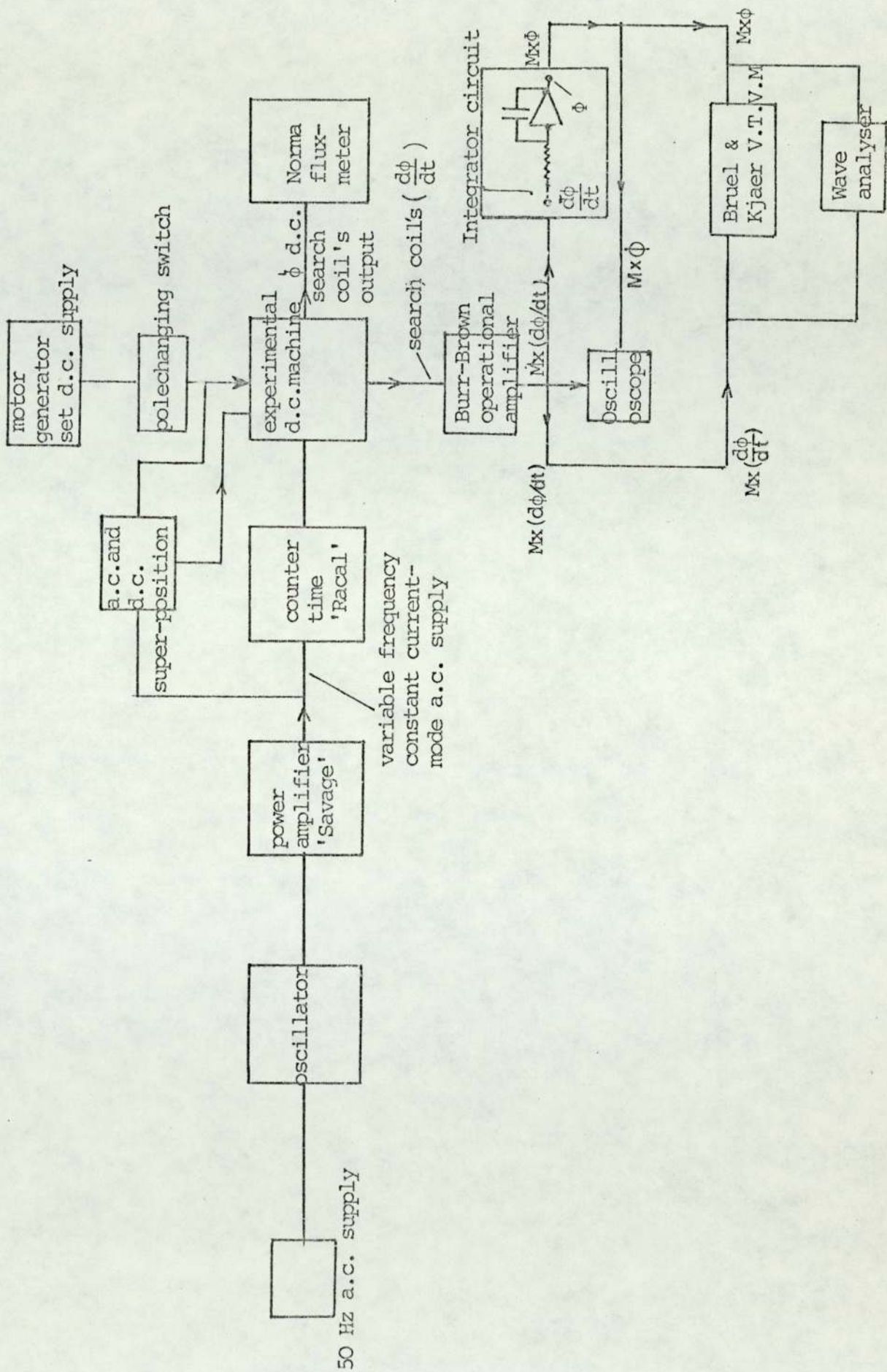


FIG. 4.18 THE SCHEMATIC ELECTRICAL CIRCUIT DIAGRAM FOR THE EXPERIMENTAL WORK

FIGURES FOR CHAPTER 5

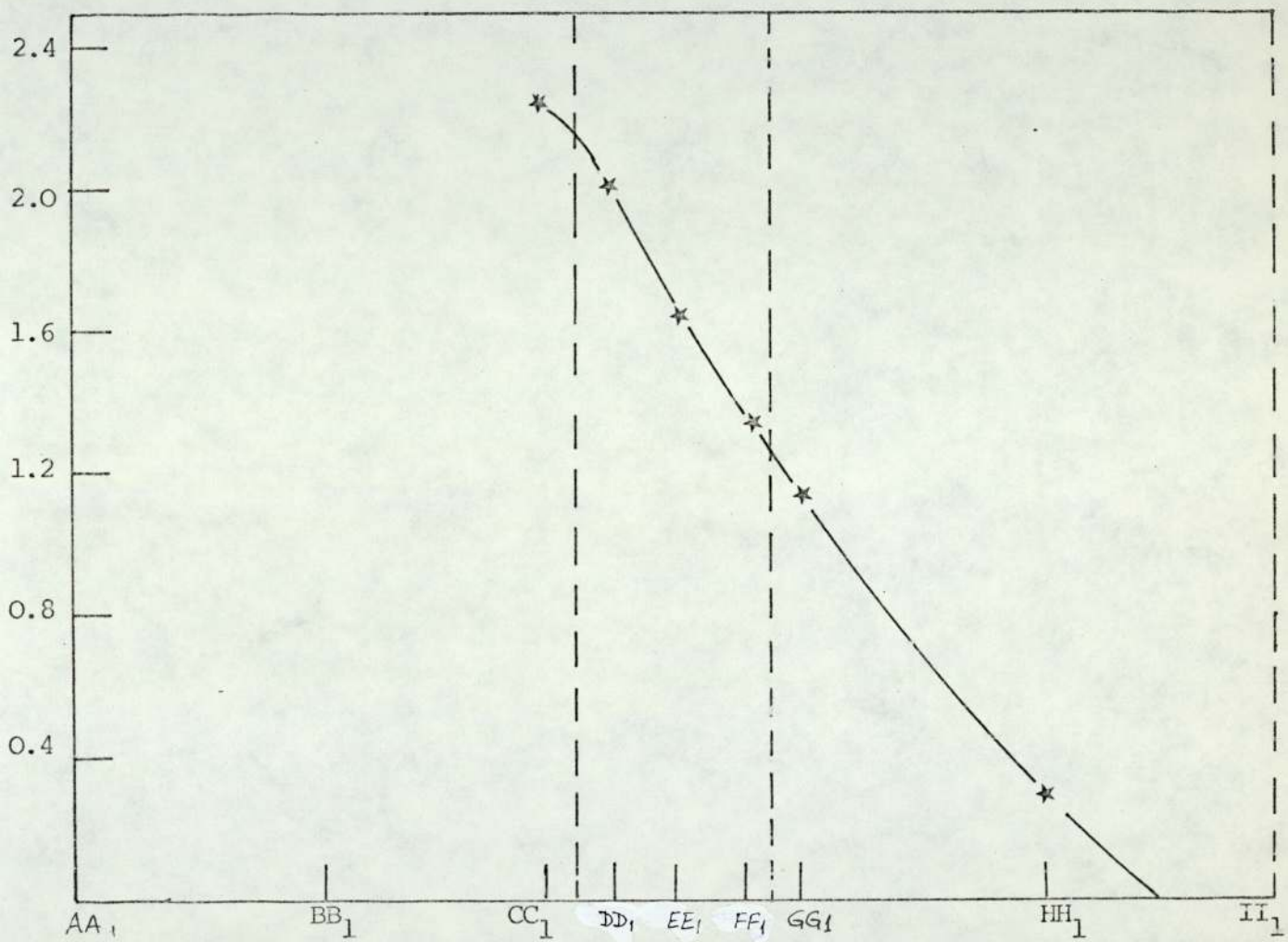


FIG. 5.1 EXPERIMENTAL CURRENT DENSITY DISTRIBUTION ALONG 0° LINE.

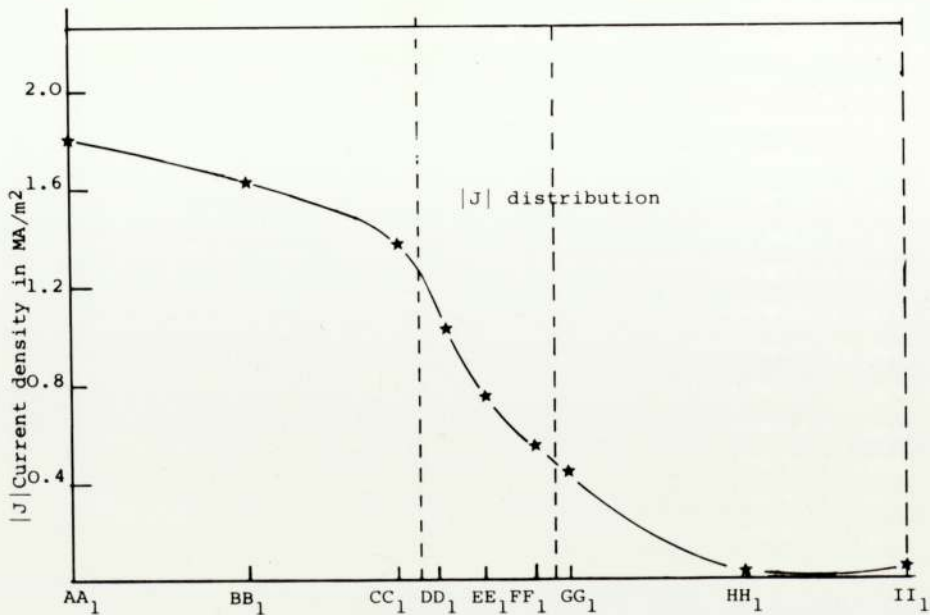
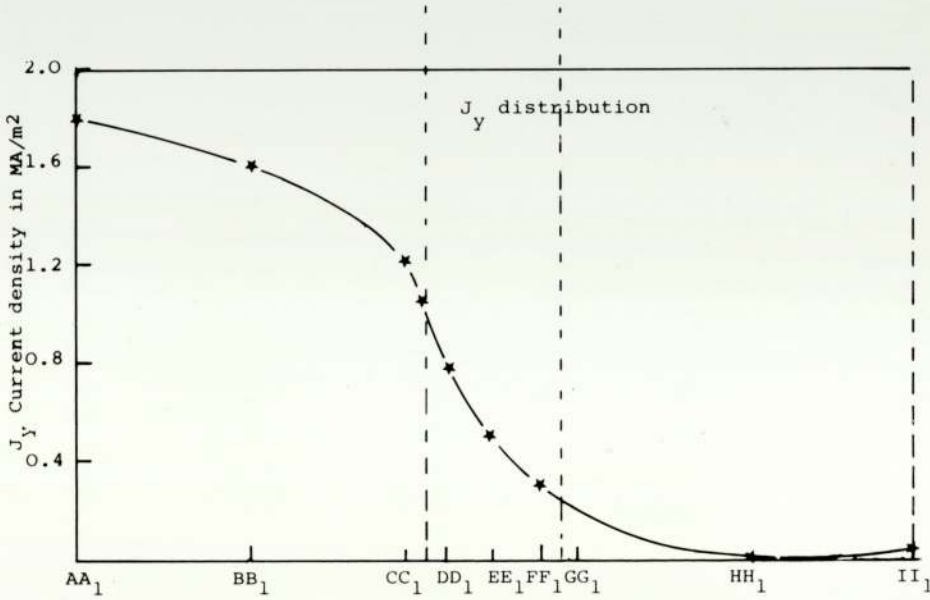
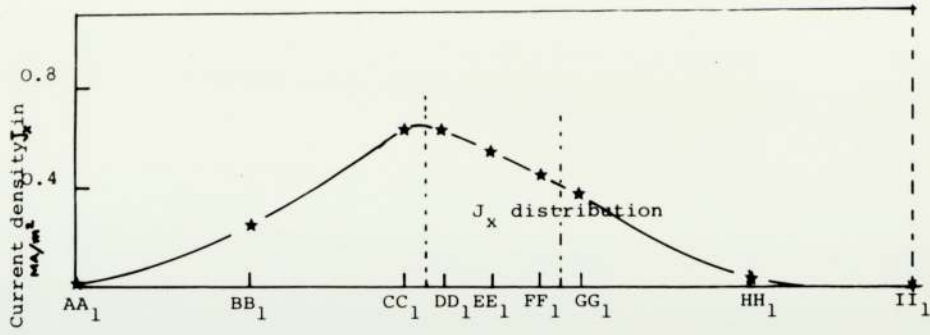


FIG. 5.2 EXPERIMENTAL EDDY CURRENT DISTRIBUTION ALONG 90° LINE ON THE SURFACE OF THE SHELL.

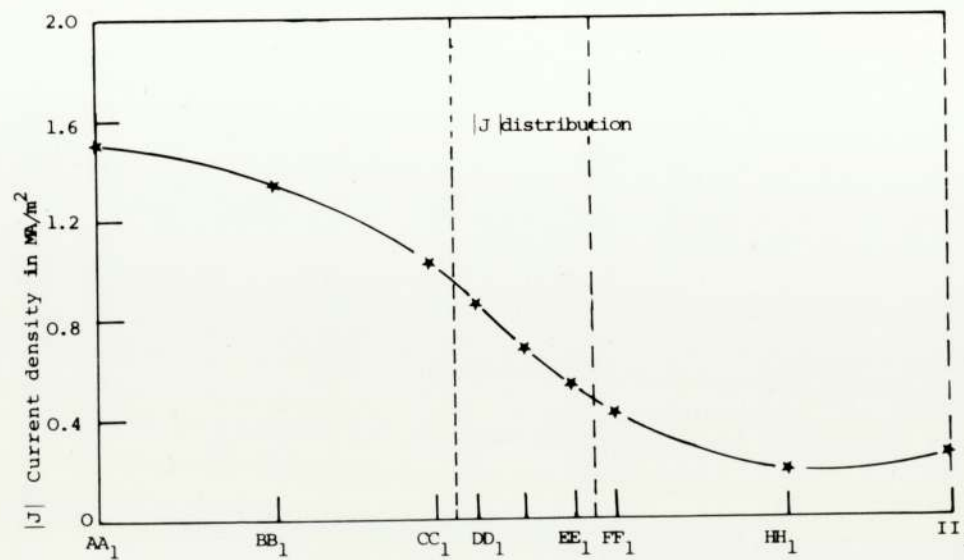
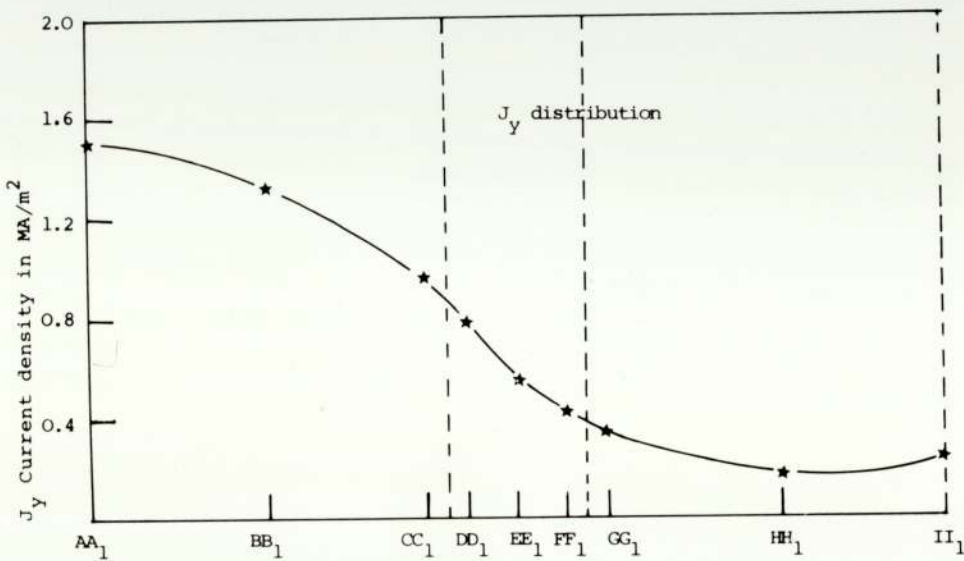
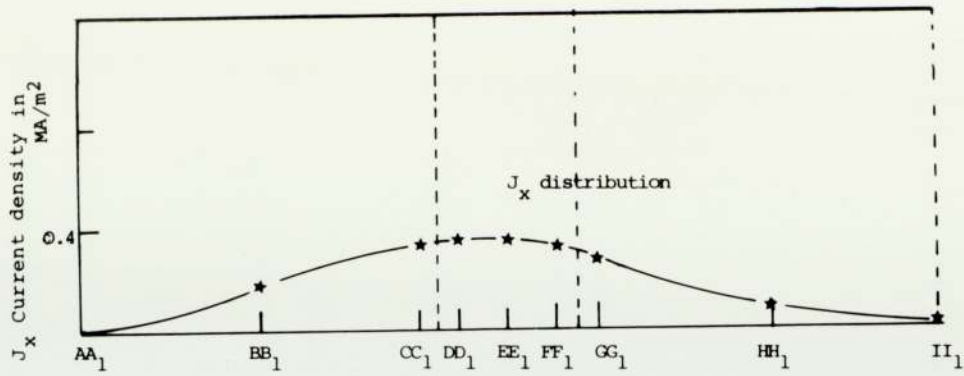


FIG. 5.3 EXPERIMENTAL EDDY CURRENT DISTRIBUTION ALONG 18° LINE ON THE SURFACE OF THE SHELL

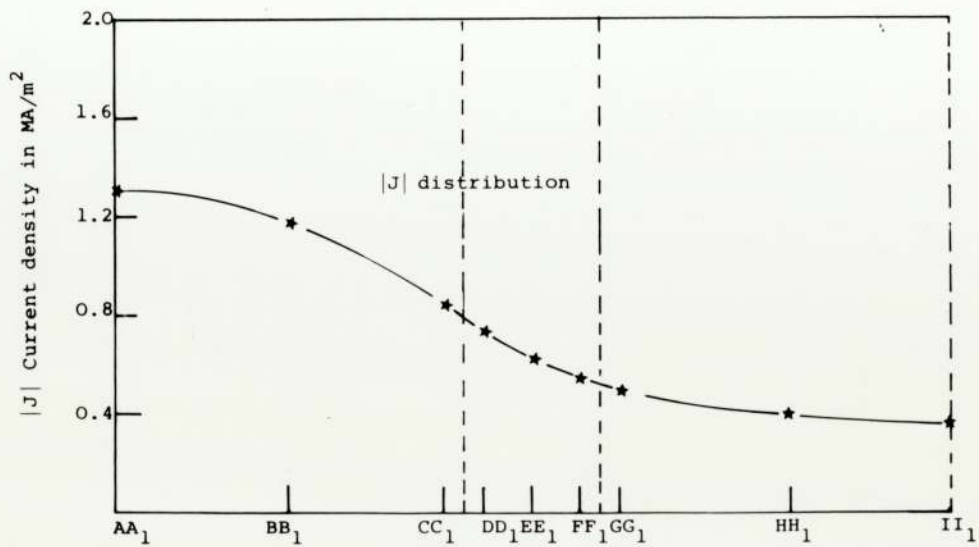
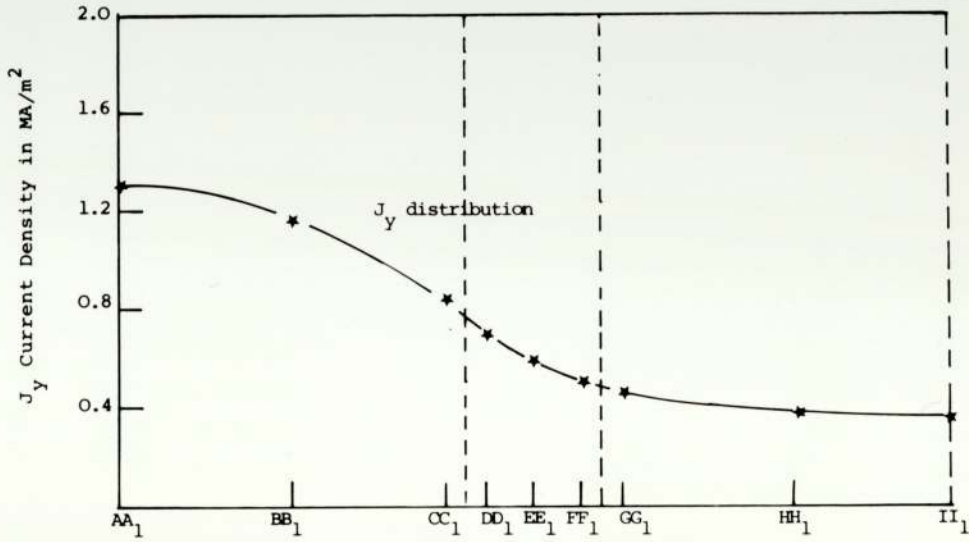
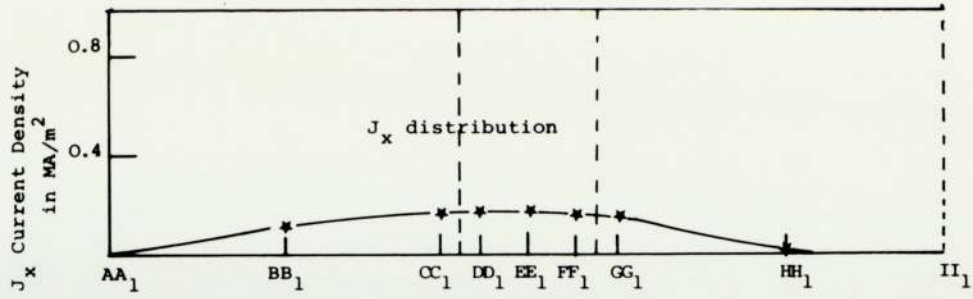


FIG.5.4 EXPERIMENTAL EDDY CURRENT DISTRIBUTION ALONG 27° LINE ON THE SURFACE OF THE SHELL

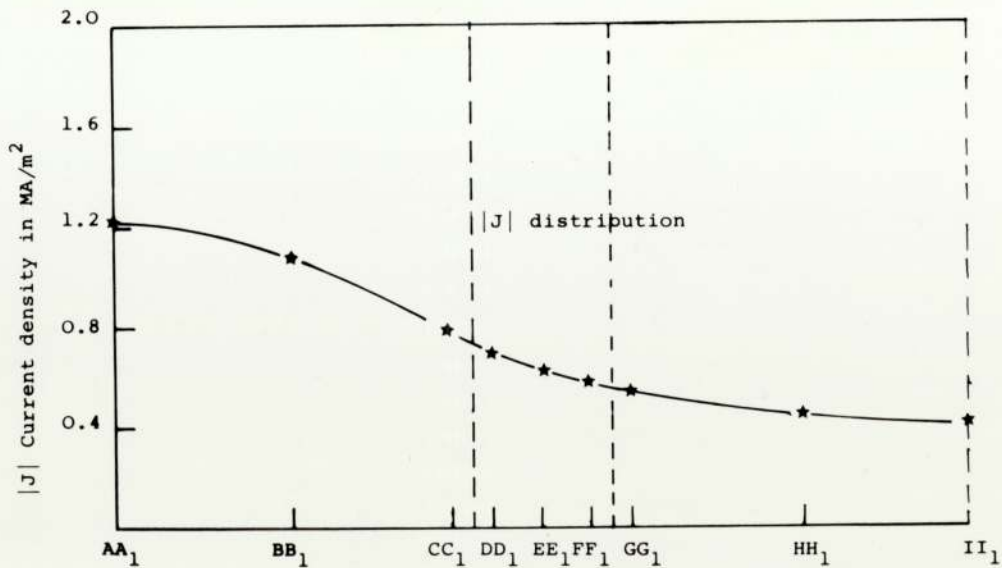
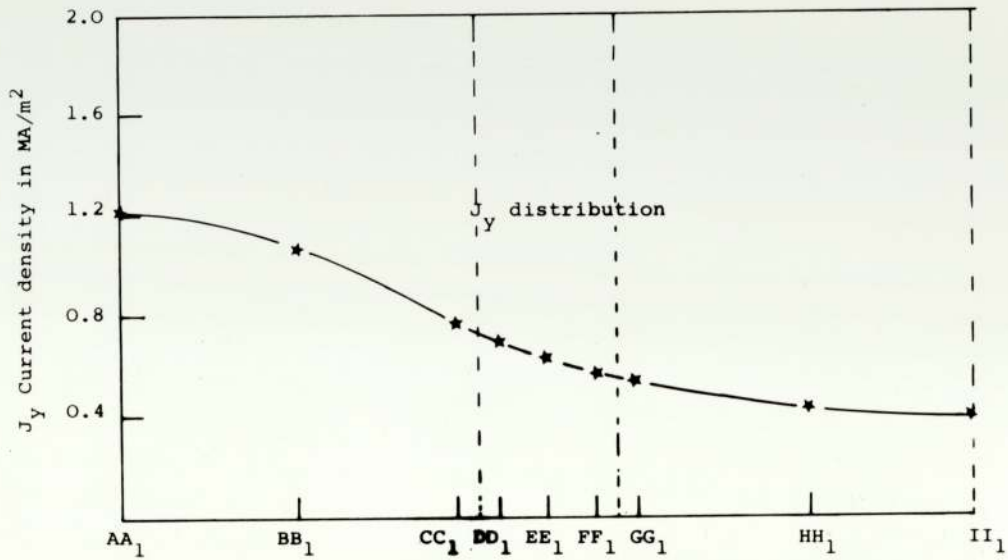
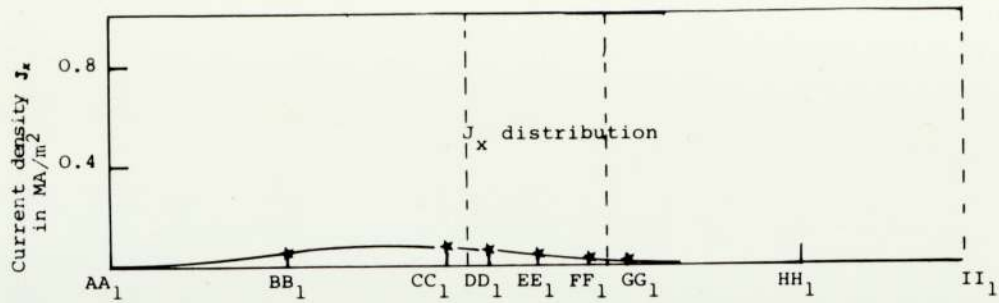


FIG. 5.5 EXPERIMENTAL EDDY CURRENT DISTRIBUTION ALONG 36° LINE ON THE SURFACE OF THE SHELL.

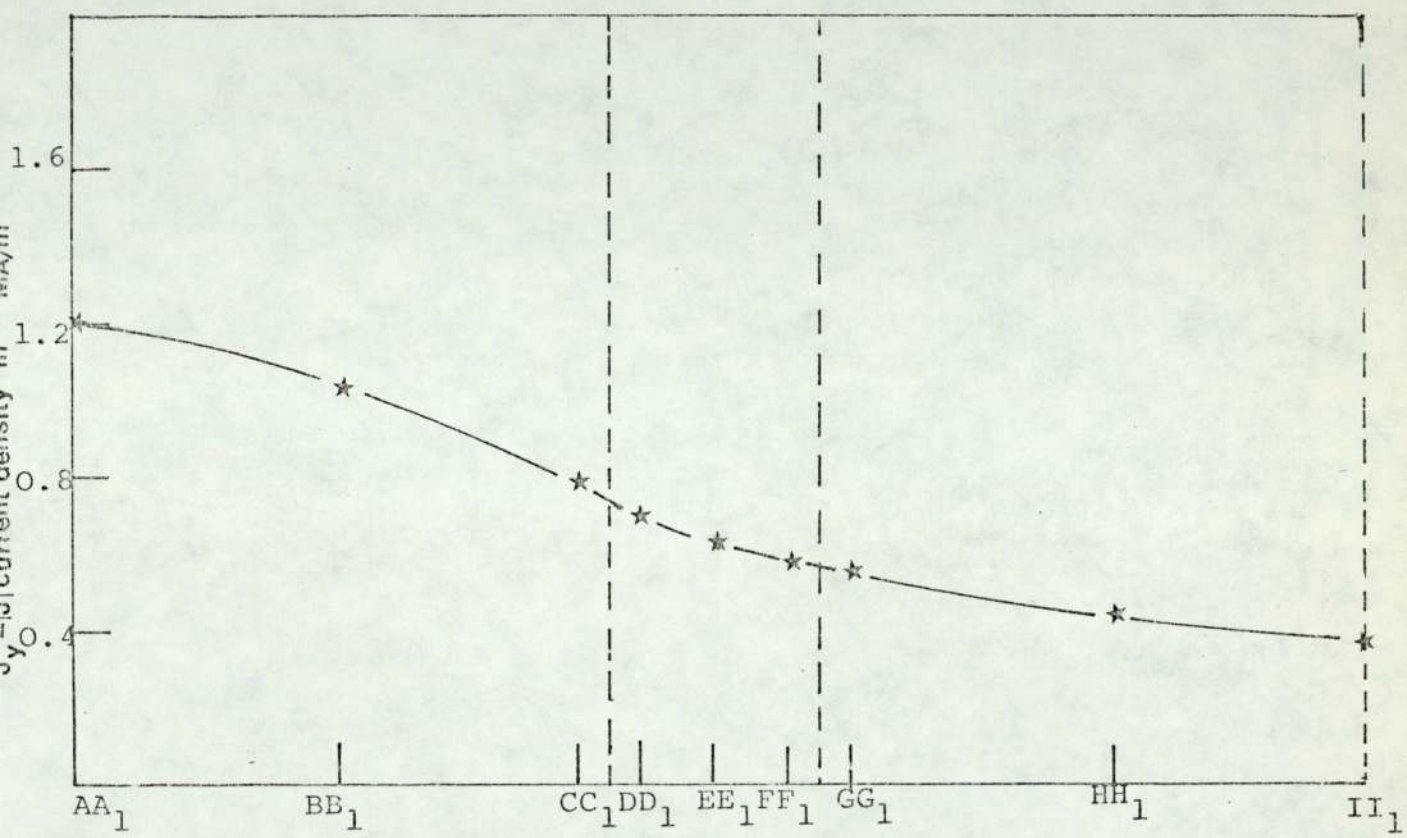


FIG. 5.6 EXPERIMENTAL CURRENT DENSITY DISTRIBUTION ALONG 45° LINE ALONG THE SURFACE OF THE SHELL.

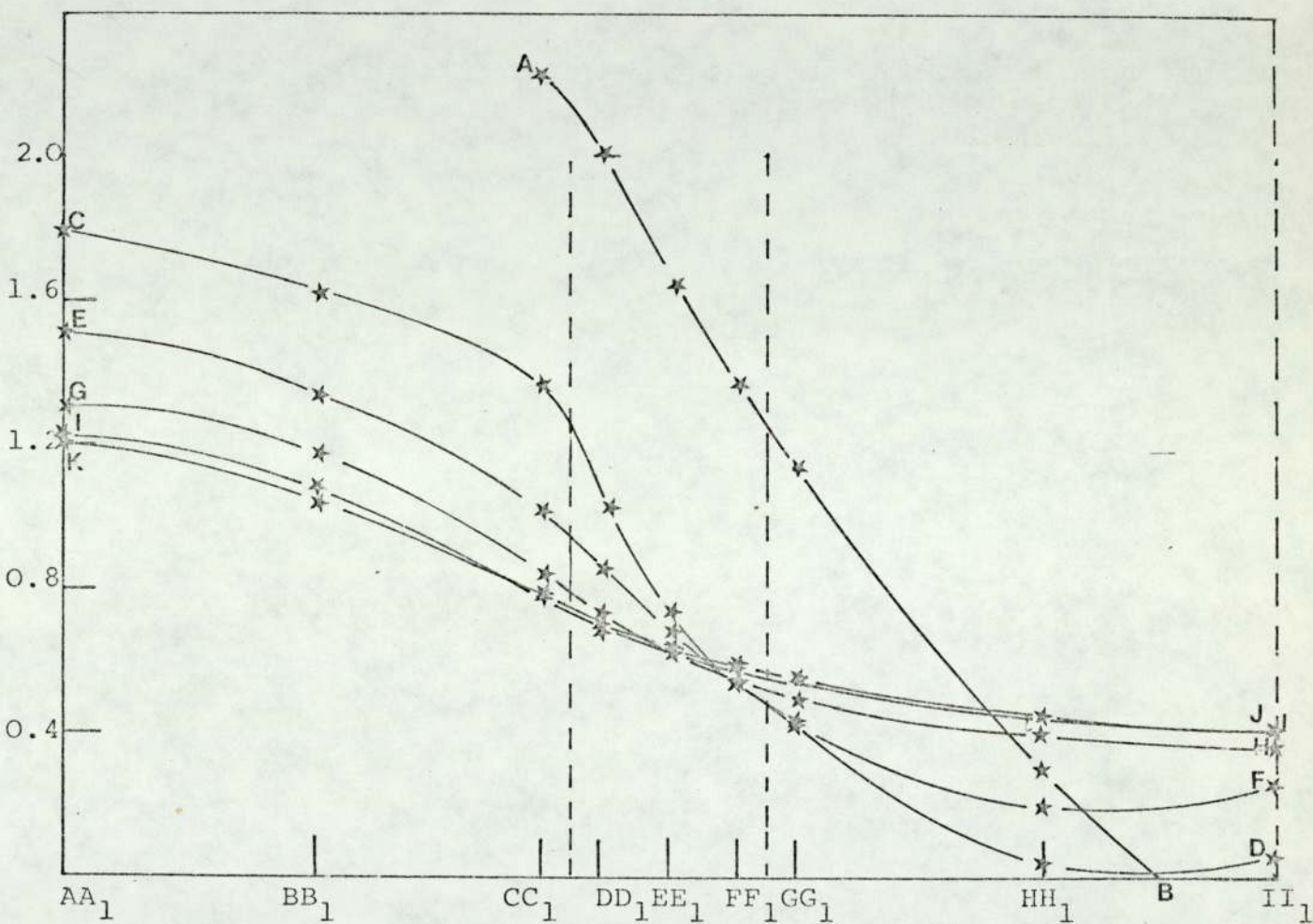


FIG. 5.7 EXPERIMENTAL CURRENT DENSITY DISTRIBUTION $|J|$ ON THE SURFACE OF THE SHELL.

- AB along 0° line
- CD along 9° line
- EF along 18° line
- GH along 27° line
- IJ along 36° line
- KL along 45° line

●-●-● Shellloop search coil's $(\frac{d\phi}{dt})_{av}$ plot
 ★-★-★ $\oint |\hat{E}_Y|_{av} \cdot d\hat{l}$ from the J-probe measurements

Centre line

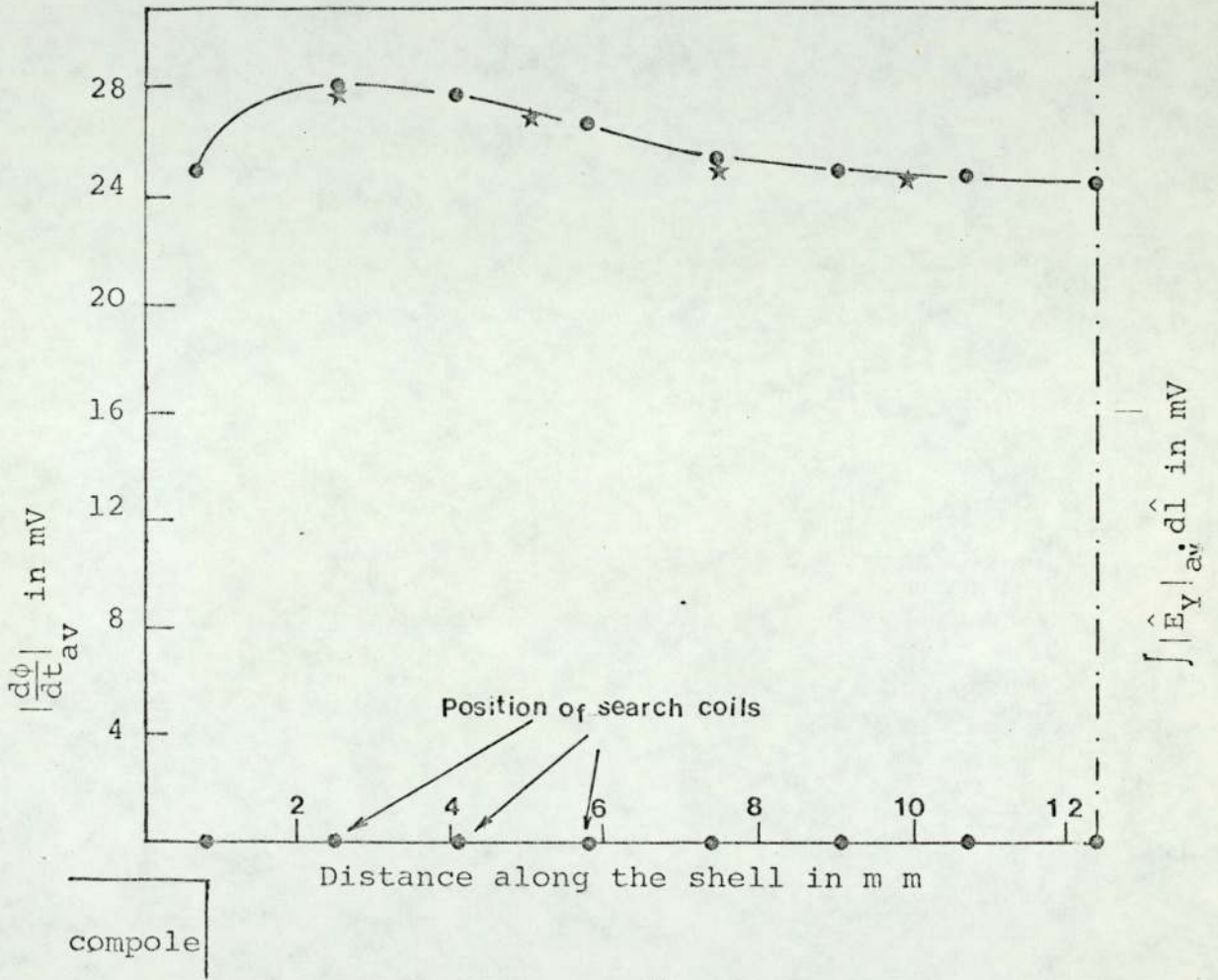


FIG. 5.8 COMPARISON BETWEEN VOLTAGES FROM THE SHELL LOOP SEARCH COILS AND J-PROBE MEASUREMENTS.

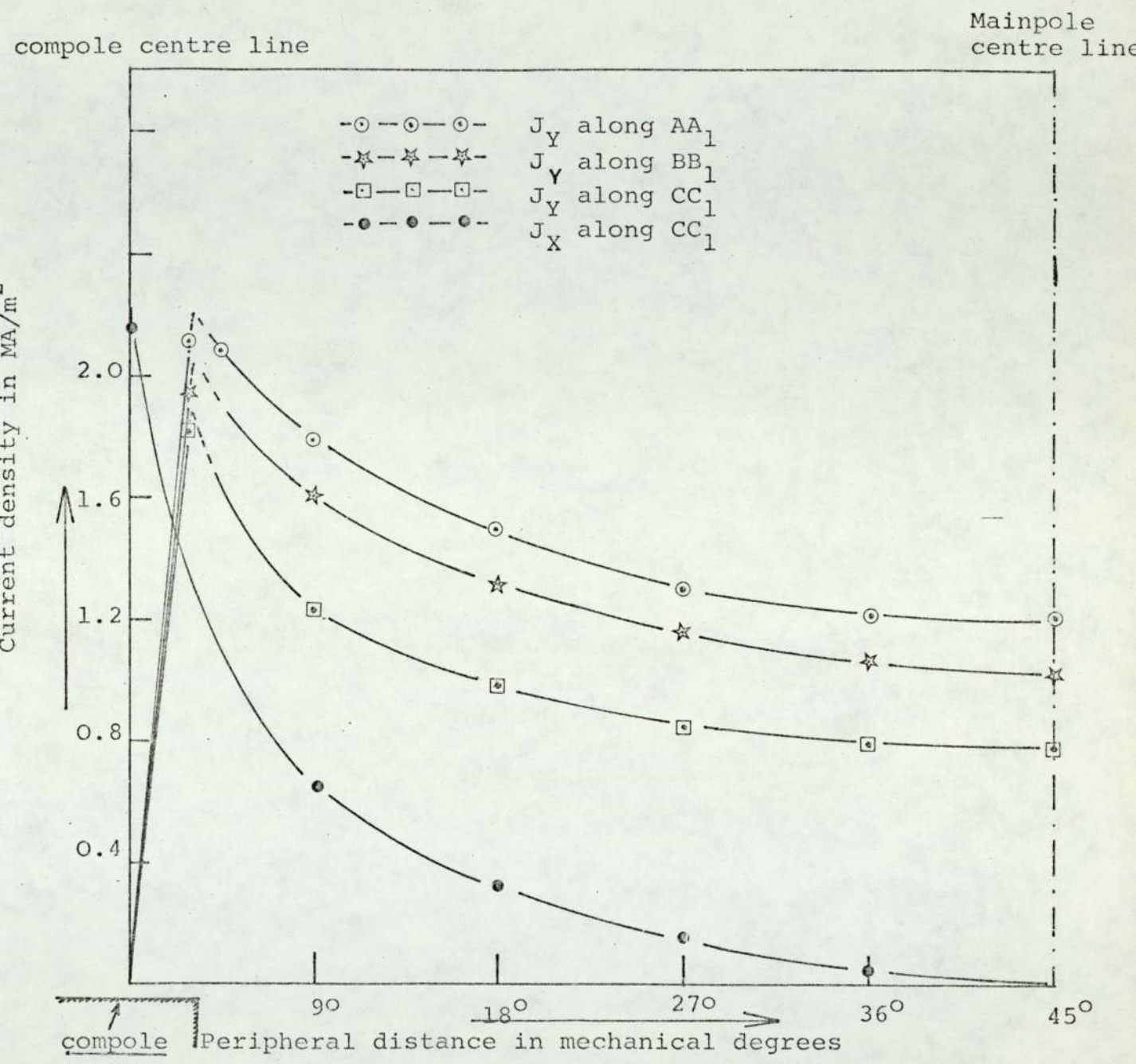


FIG. 5.9 MEASURED CURRENT DENSITY DISTRIBUTION ON THE INNER SURFACE OF THE SHELL.

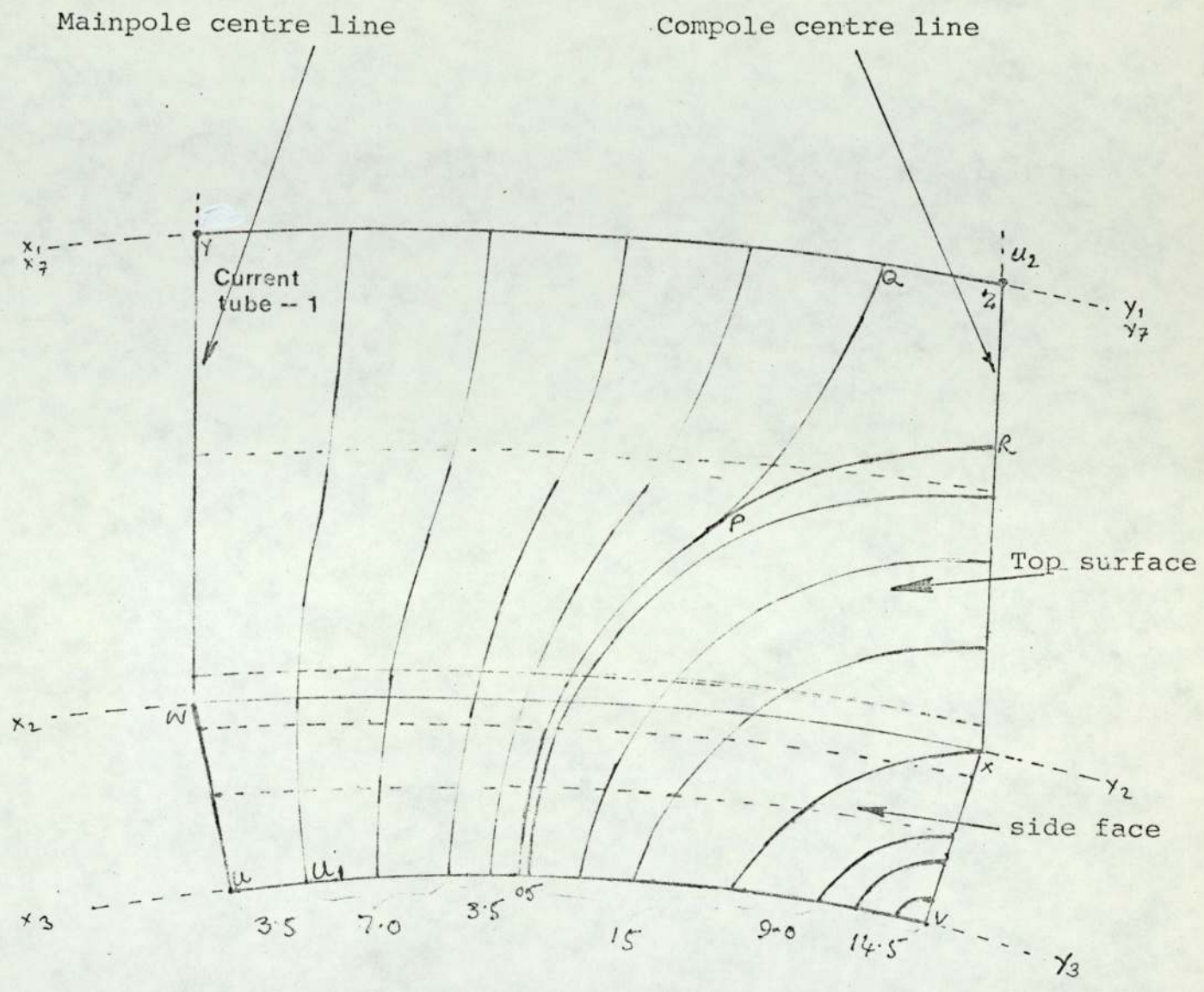


FIG. 5.10 J-DISTRIBUTION ON THE SIDE FACE AND TOP SURFACE OF THE SHELL.

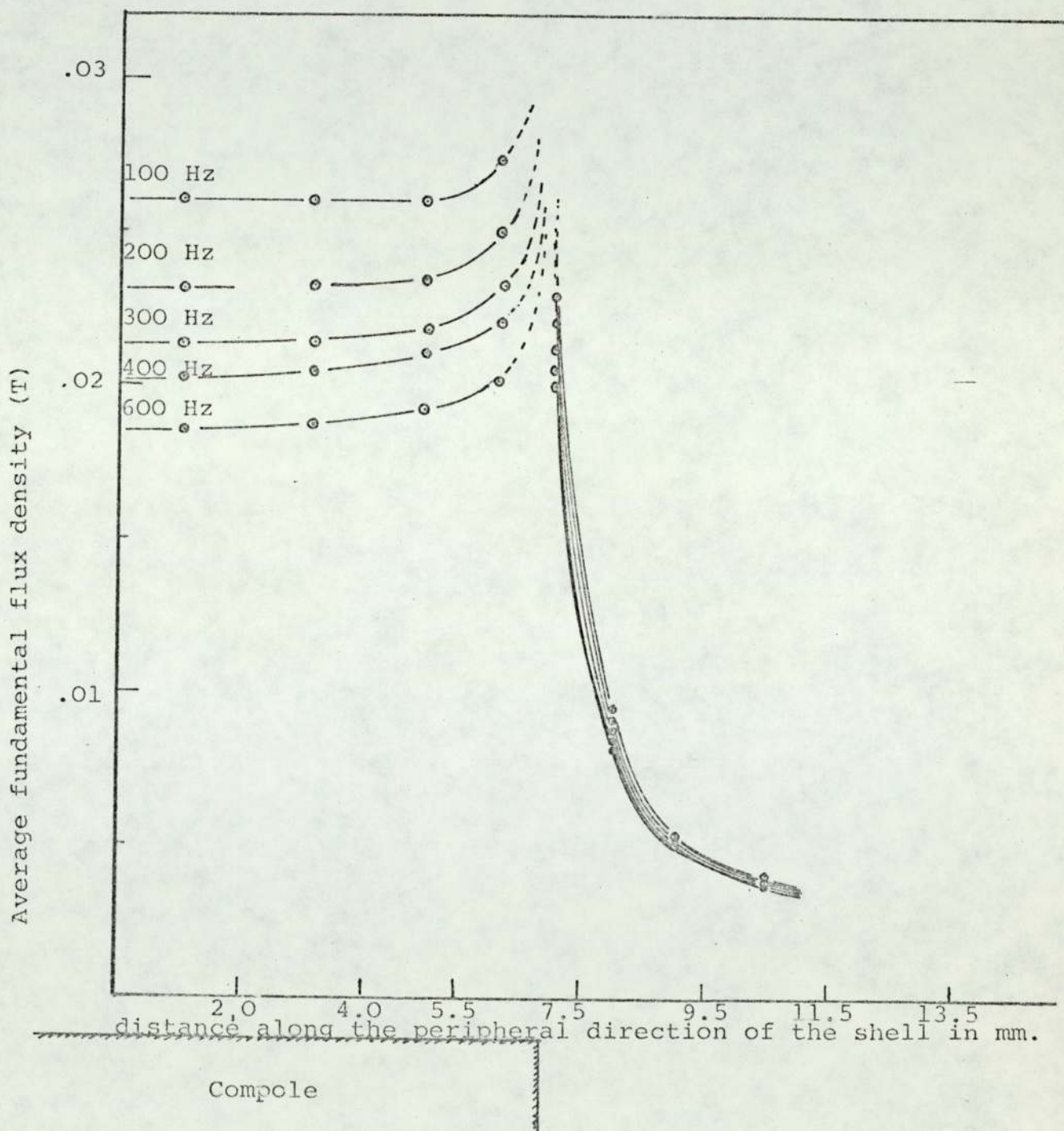


FIG. 5.13 EXPERIMENTAL A.C. FLUX DENSITY DISTRIBUTION IN THE PERIPHERAL DIRECTION IN THE AIRGAP AT THE BACK OF THE COMPOLE.

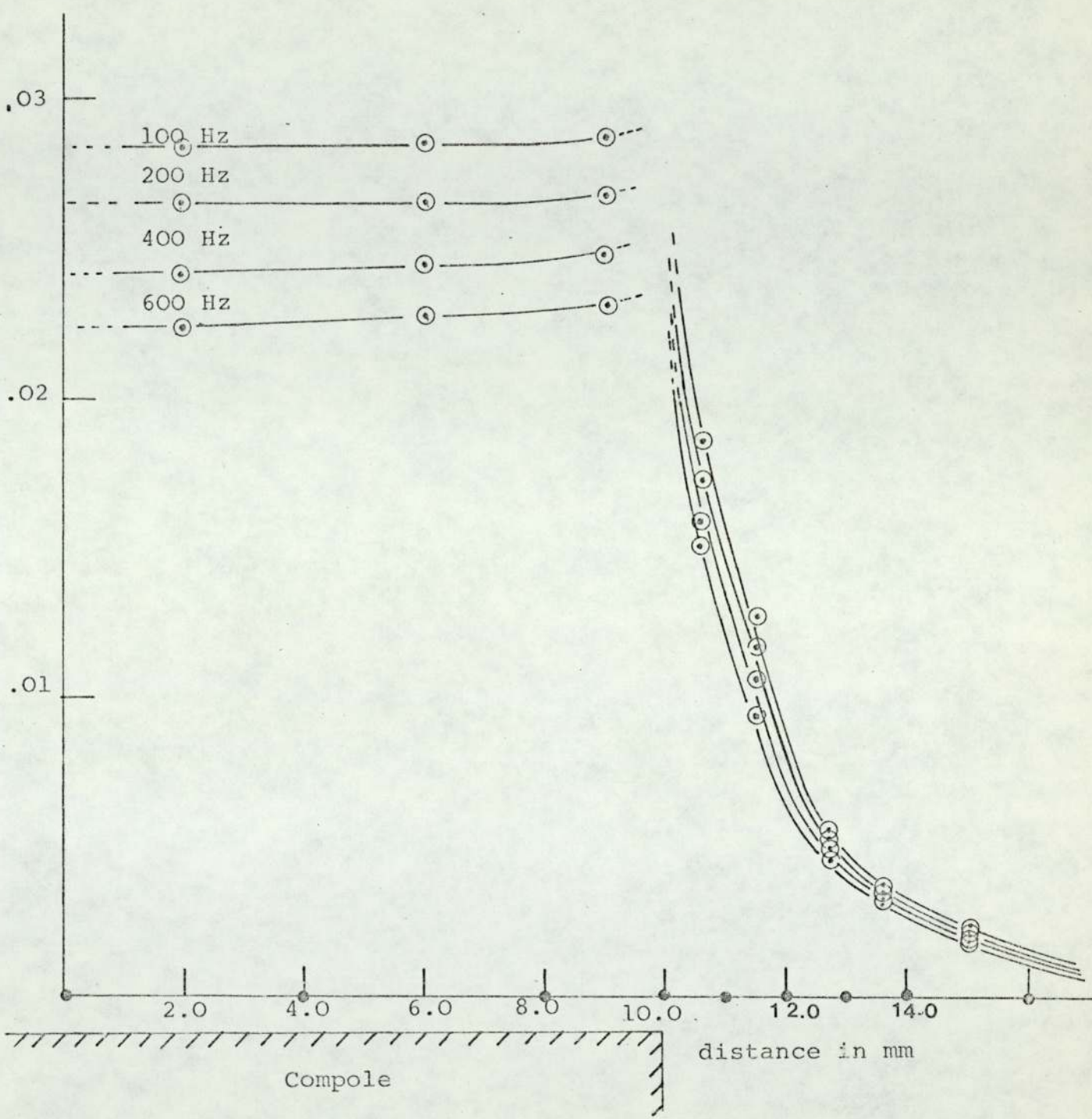


FIG. 5.14 EXPERIMENTAL A.C. FLUX DENSITY DISTRIBUTION IN THE AXIAL DIRECTION IN THE AIRGAP AT THE BACK OF THE COMPOLE

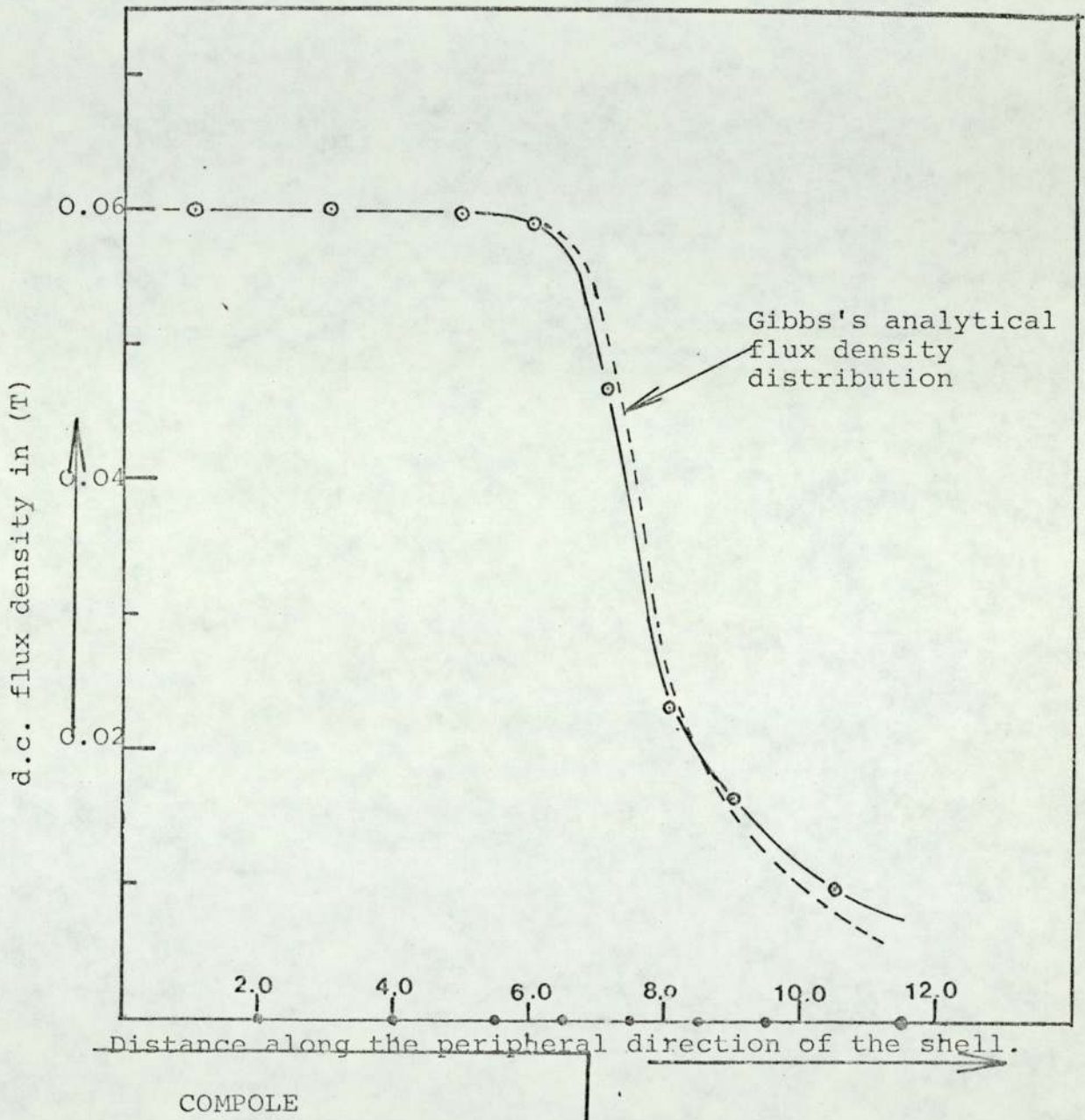


FIG. 5.15 EXPERIMENTAL D.C. FLUX DENSITY DISTRIBUTION IN THE AIRGAP AT THE BACK OF THE COMPOLE.

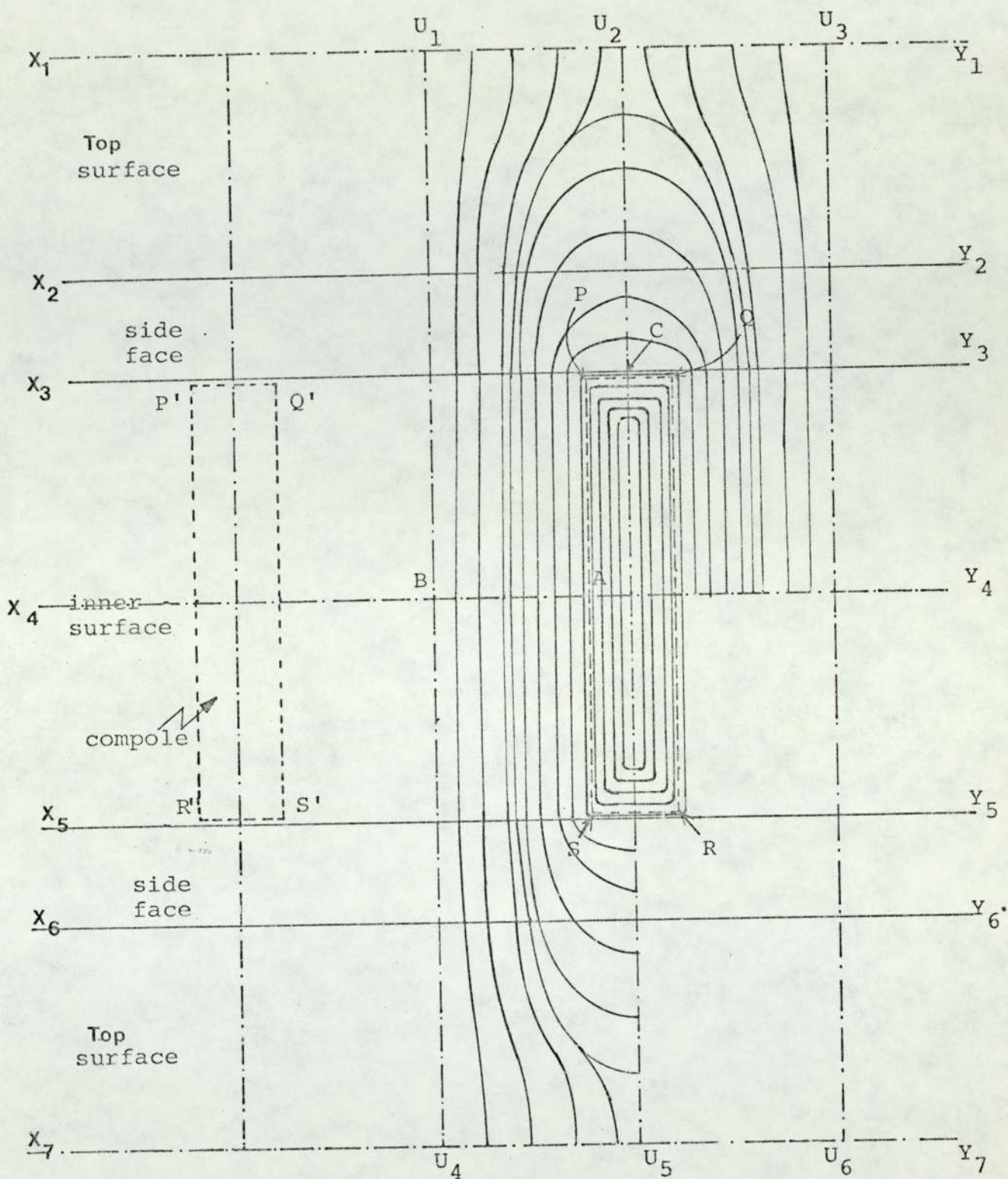


FIG. 5.18 EDDY CURRENT DISTRIBUTION ON THE SURFACE OF THE SHELL.

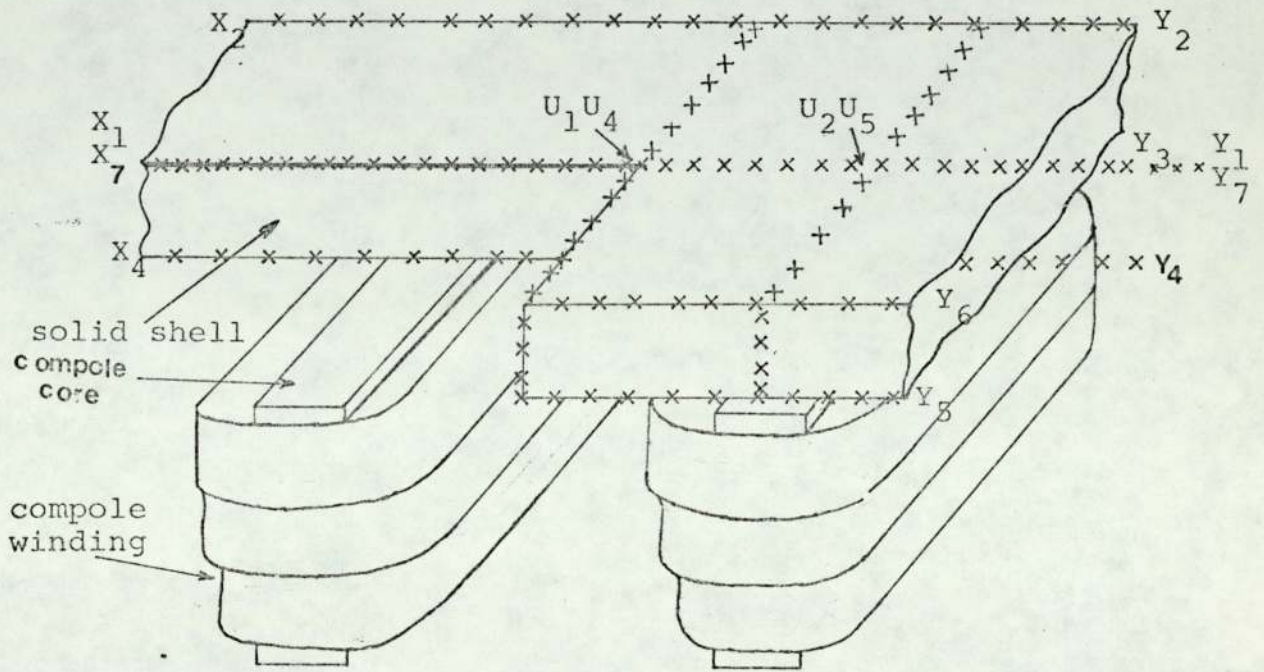


FIG. 5.19 SHELL AND COMPOLES.

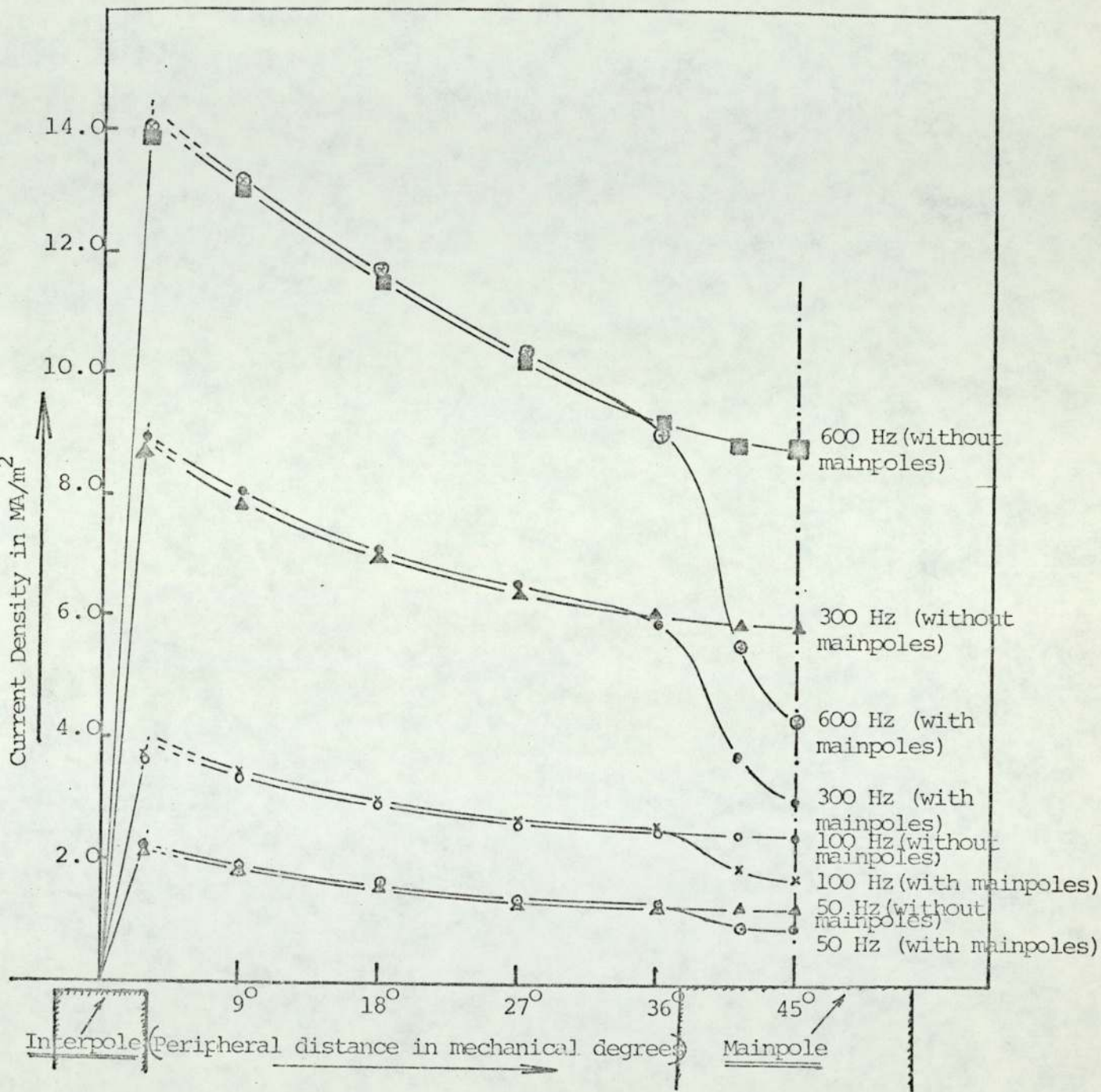


Fig. 5.20 CURRENT DENSITY DISTRIBUTION ALONG THE CENTRE LINE OF THE INNER SURFACE OF THE SHELL, WITH AND WITHOUT MAINPOLES AT DIFFERENT FREQUENCIES WITH CONSTANT COMPOLE EXCITATION.

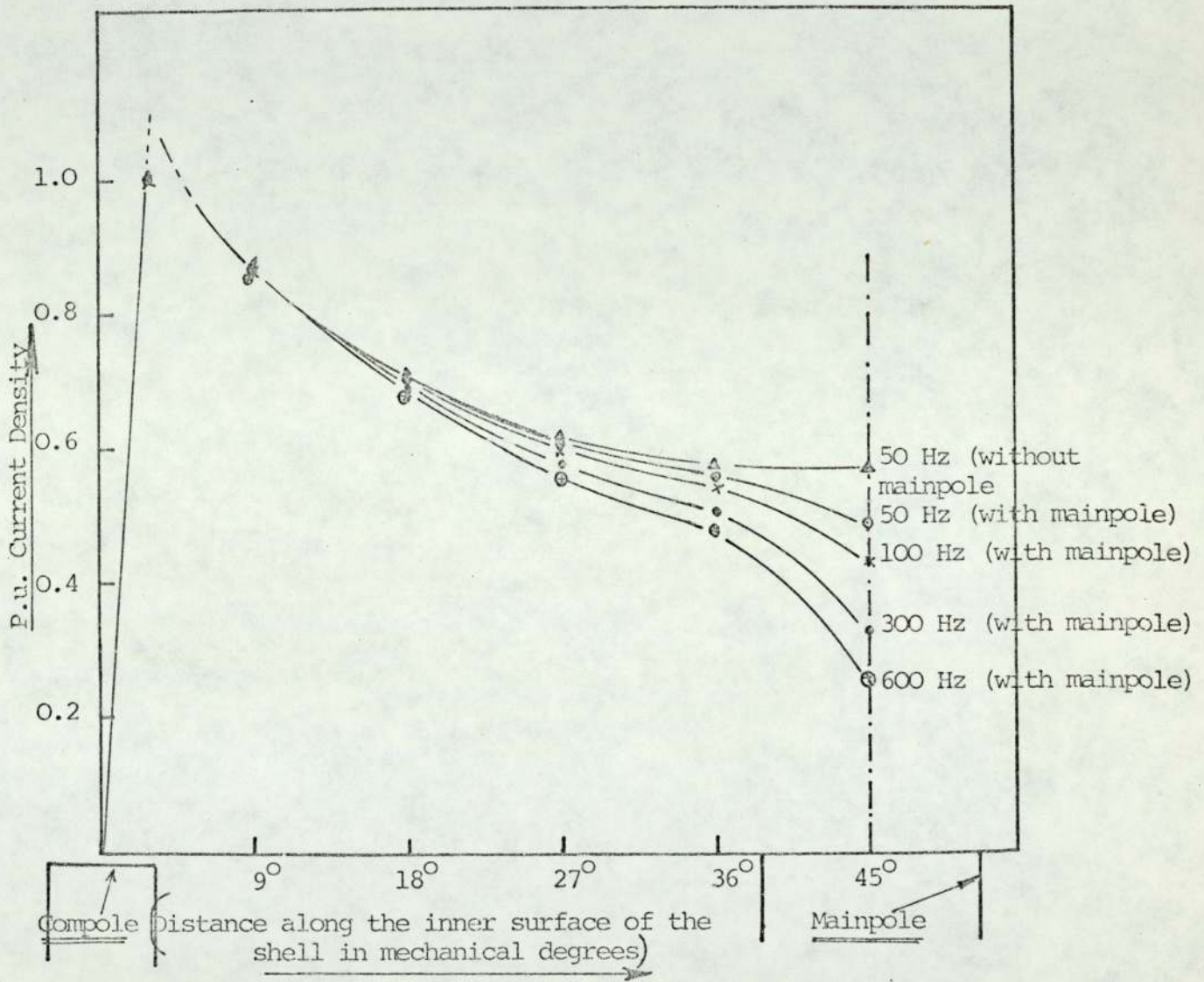


FIG. 5.21 P.U. CURRENT DENSITY DISTRIBUTION ALONG THE INNER SURFACE OF THE SHELL AT DIFFERENT FREQUENCIES, WITH CONSTANT COMPOLE EXCITATION.

(1 P.U. = J AT COMPOLE EDGE, FOR EACH CURVE)

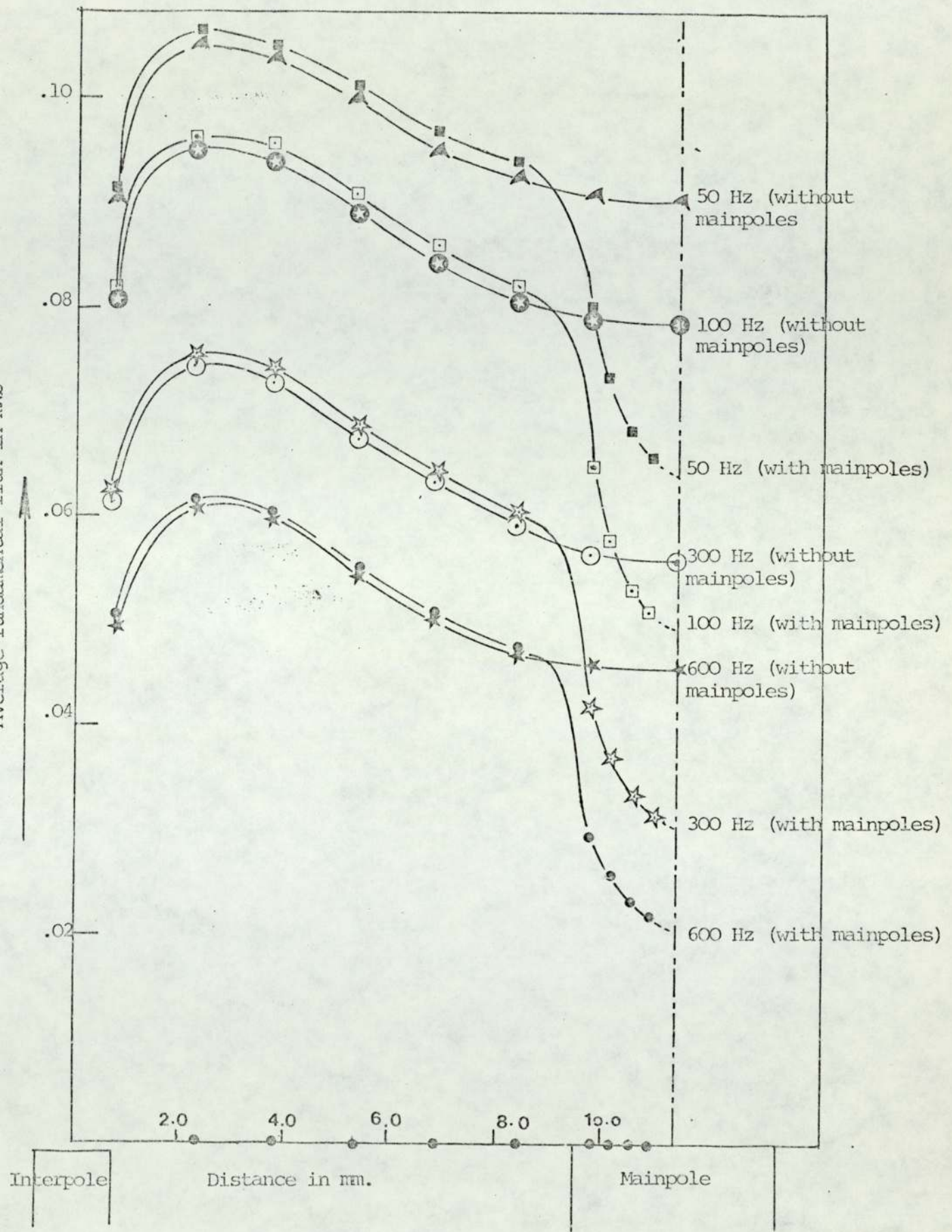


Fig. 5.22 AVERAGE FUNDAMENTAL FLUX DISTRIBUTION FROM THE SHELL LOOP SEARCH COILS WITH AND WITHOUT MAINPOLES AT DIFFERENT FREQUENCIES WITH CONSTANT EXCITATION.

FIGURES FOR CHAPTER 6

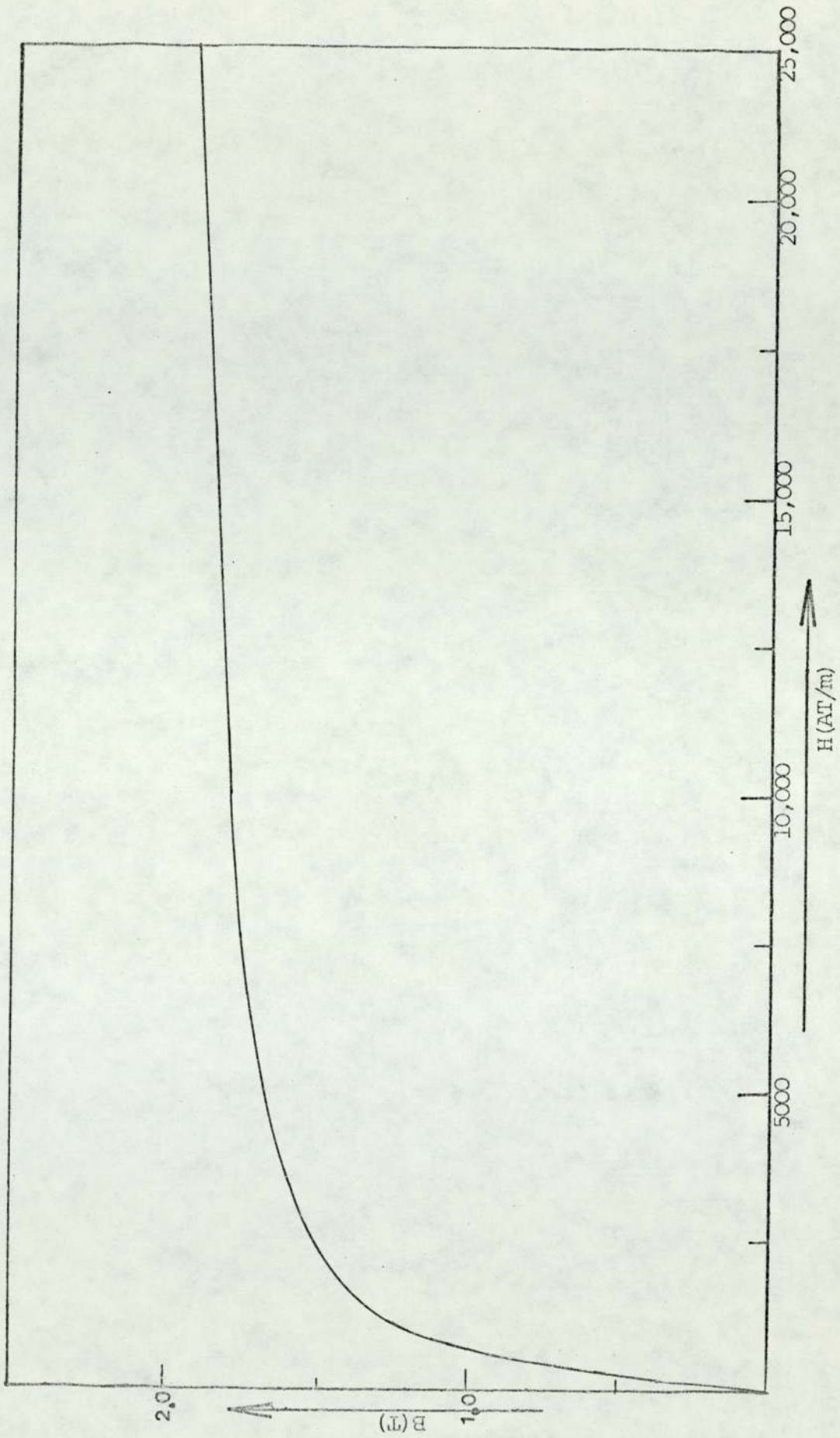


FIG. 6.6 MAGNETISATION CURVE FOR MILD STEEL PLATE (BS 4360 GRADE 43A, EN3)

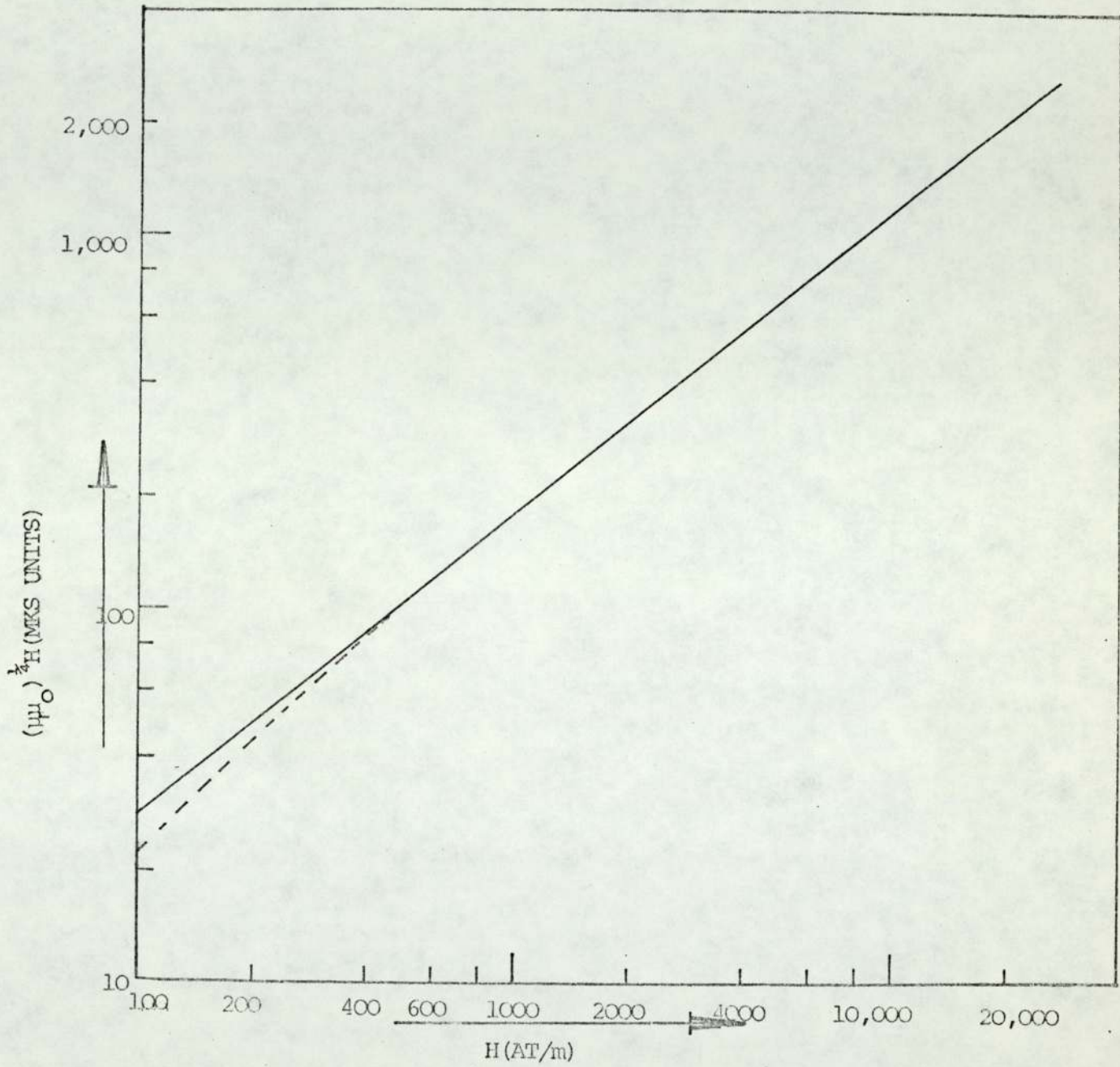


FIG. 6.7 LOG LOG PLOTS OF $(\mu_r \mu_0)^{1/2} H$ AGAINST MAGNETIC FIELD STRENGTH H FOR EN3 STEEL.

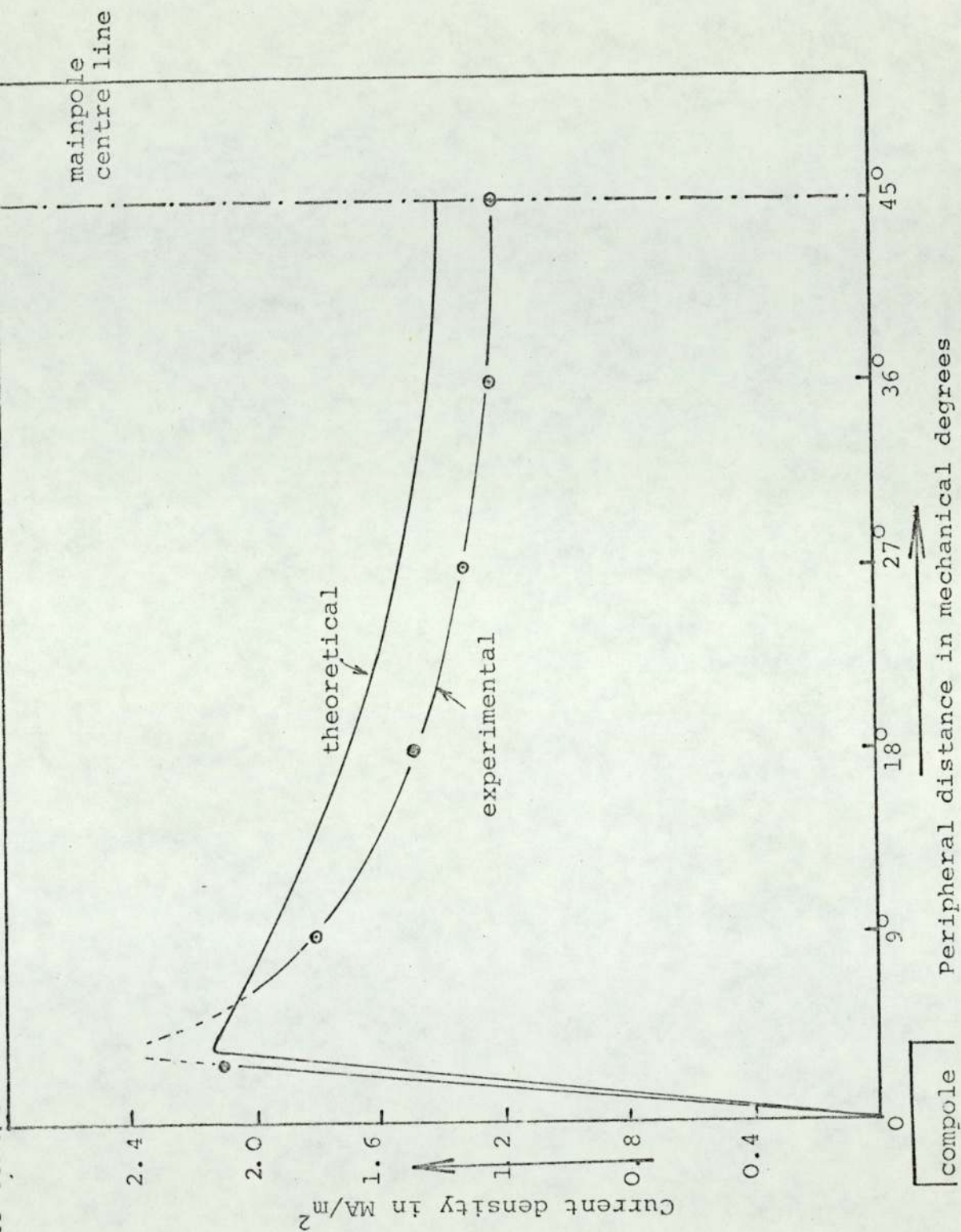


FIG. 6.8 THEORETICAL AND EXPERIMENTAL CURRENT DENSITY DISTRIBUTIONS ALONG THE CENTRAL LINE OF THE INNER SURFACE OF THE SHELL.

- (1) SUPPLY FREQUENCY 50 HZ.
- (2) EXCITATION TO THE COMPOLE 8A P-P.

FIGURES FOR CHAPTER 7

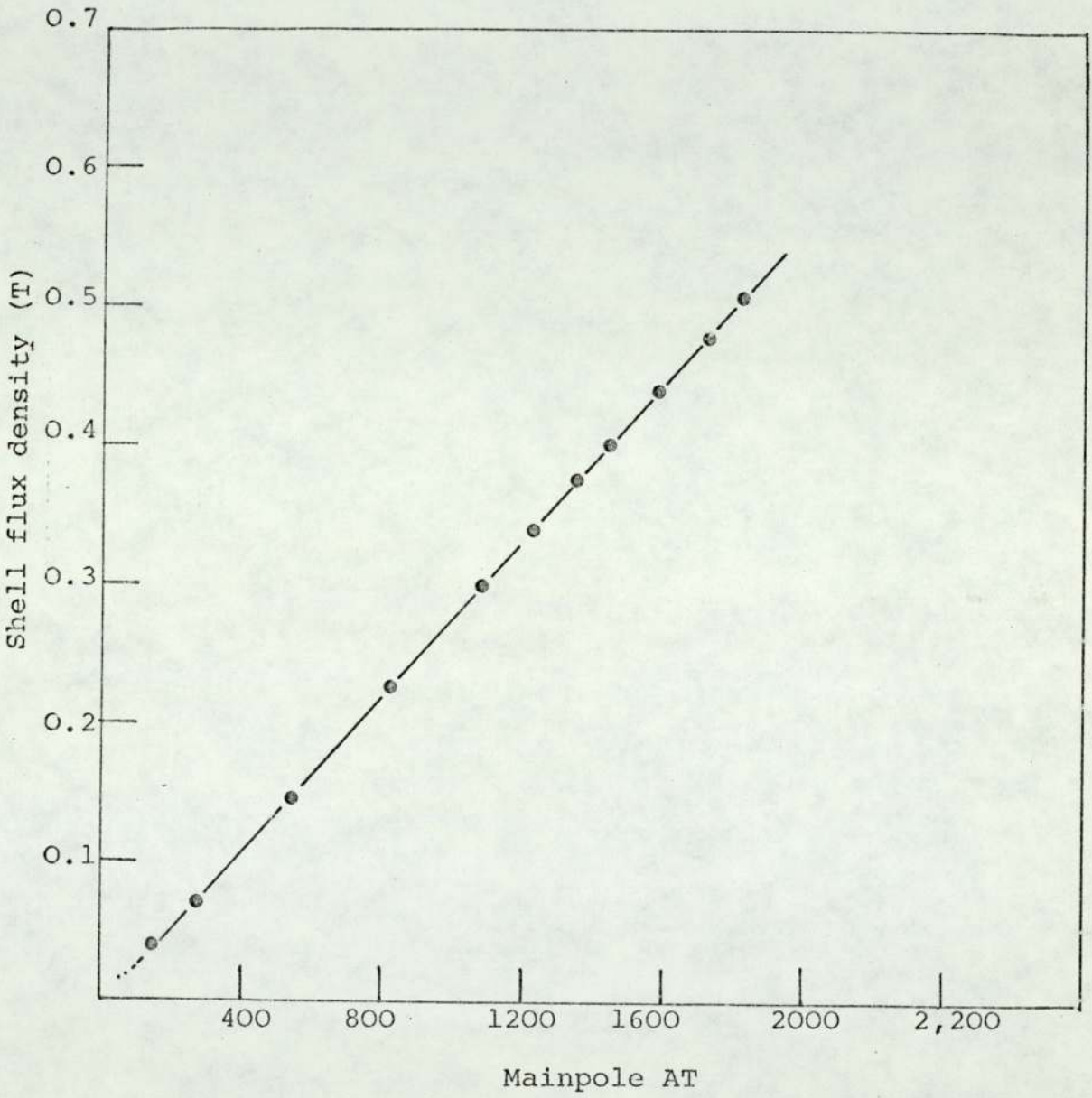


FIG. 7.1 MAINPOLE AT VS. SHELL FLUX DENSITY.

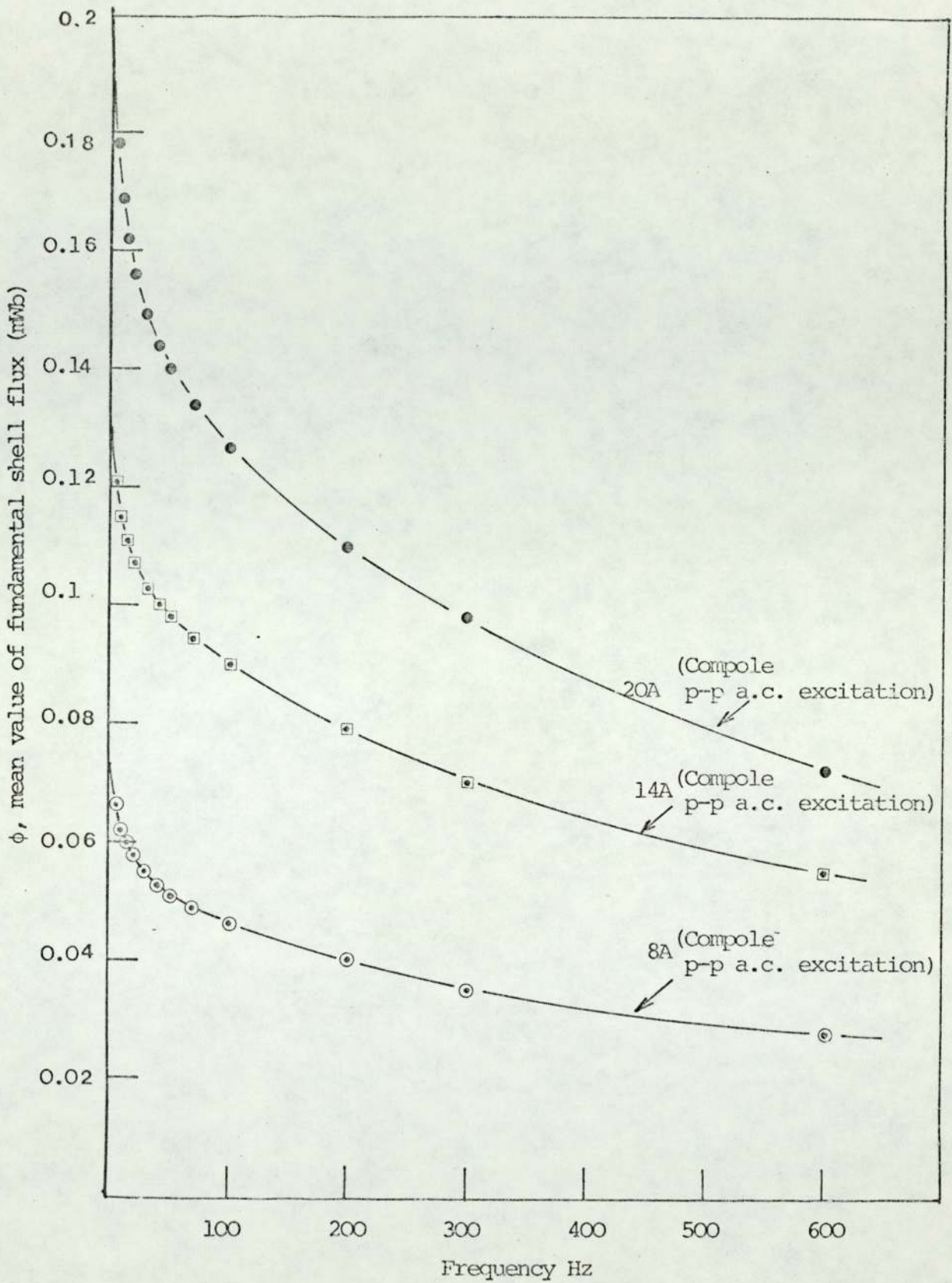


FIG. 7.2 VARIATION OF FUNDAMENTAL SHELL FLUX WITH SUPPLY FREQUENCY

(1) COMPOLE D.C. EXCITATION 9A.

(2) MAINPOLE D.C. EXCITATION 0.68A

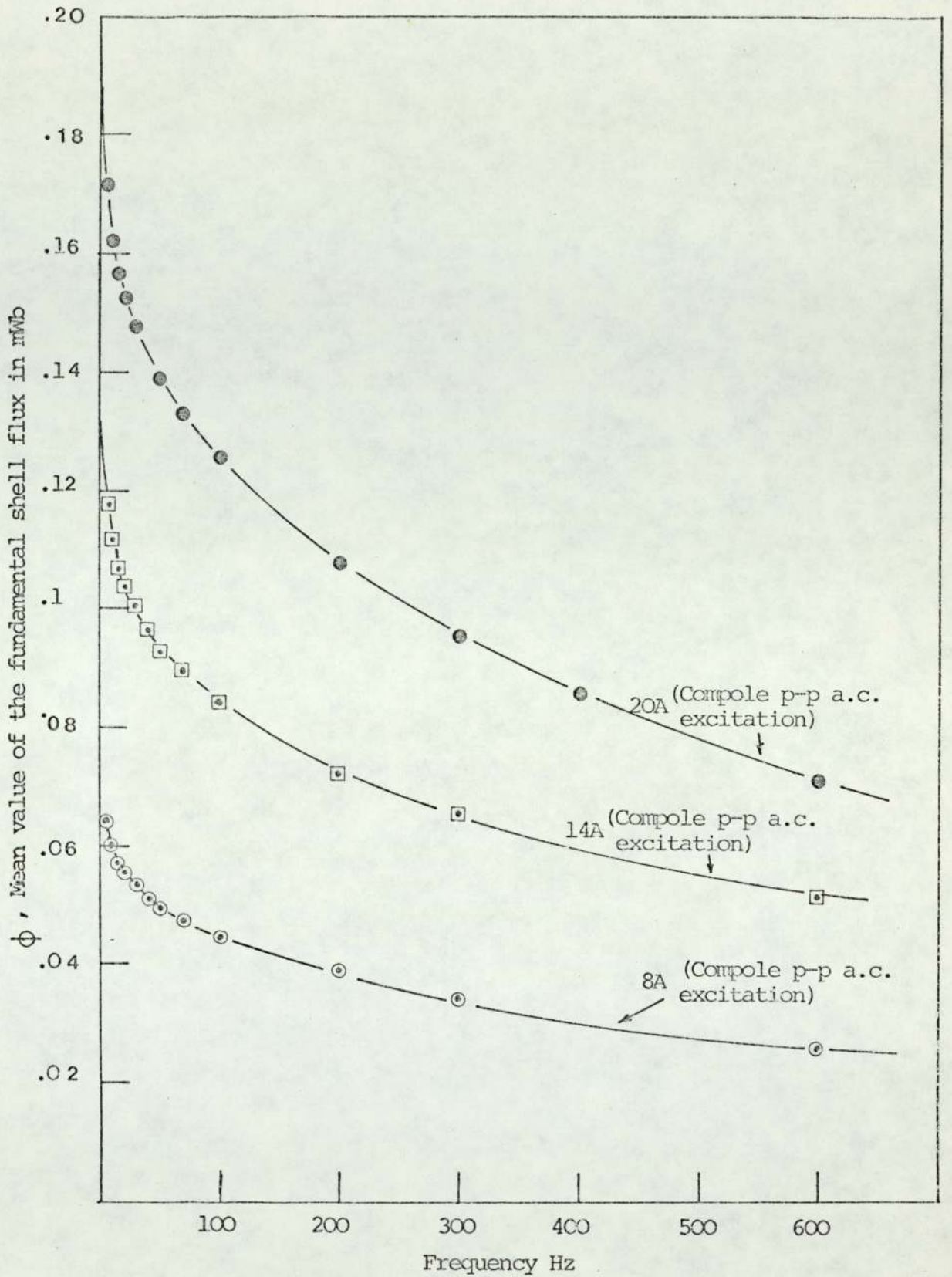


FIG. 7.3 VARIATION OF FUNDAMENTAL SHELL FLUX WITH SUPPLY FREQUENCY

(1) COMPOLE D.C. EXCITATION 11.25A

(2) MAINPOLE D.C. EXCITATION 0.68A

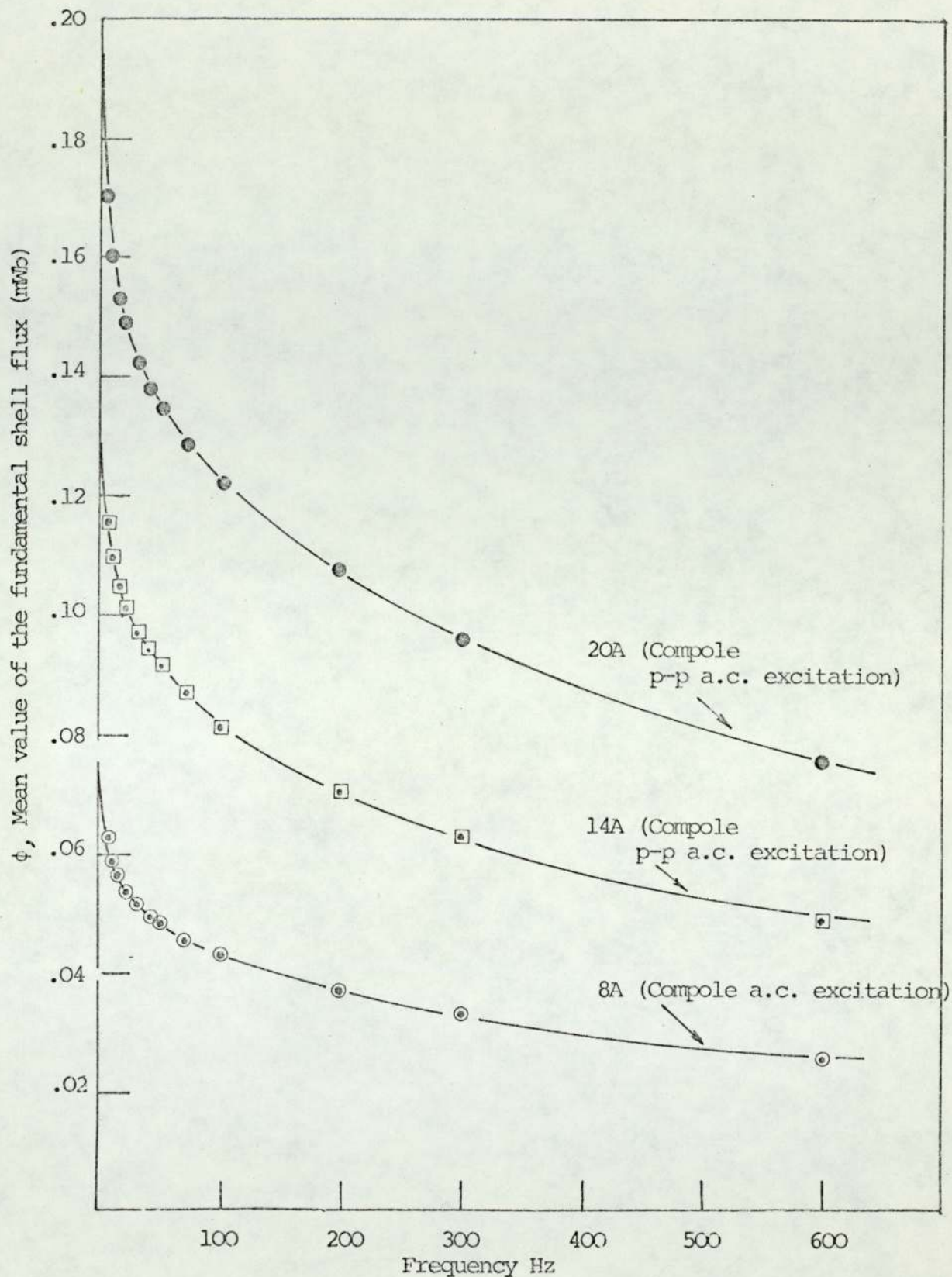


FIG. 7.4 VARIATION OF FUNDAMENTAL SHELL FLUX WITH FREQUENCY.

(1) COMPOLE D.C. EXCITATION 13.5A.

(2) MAINPOLE D.C. EXCITATION .68A.

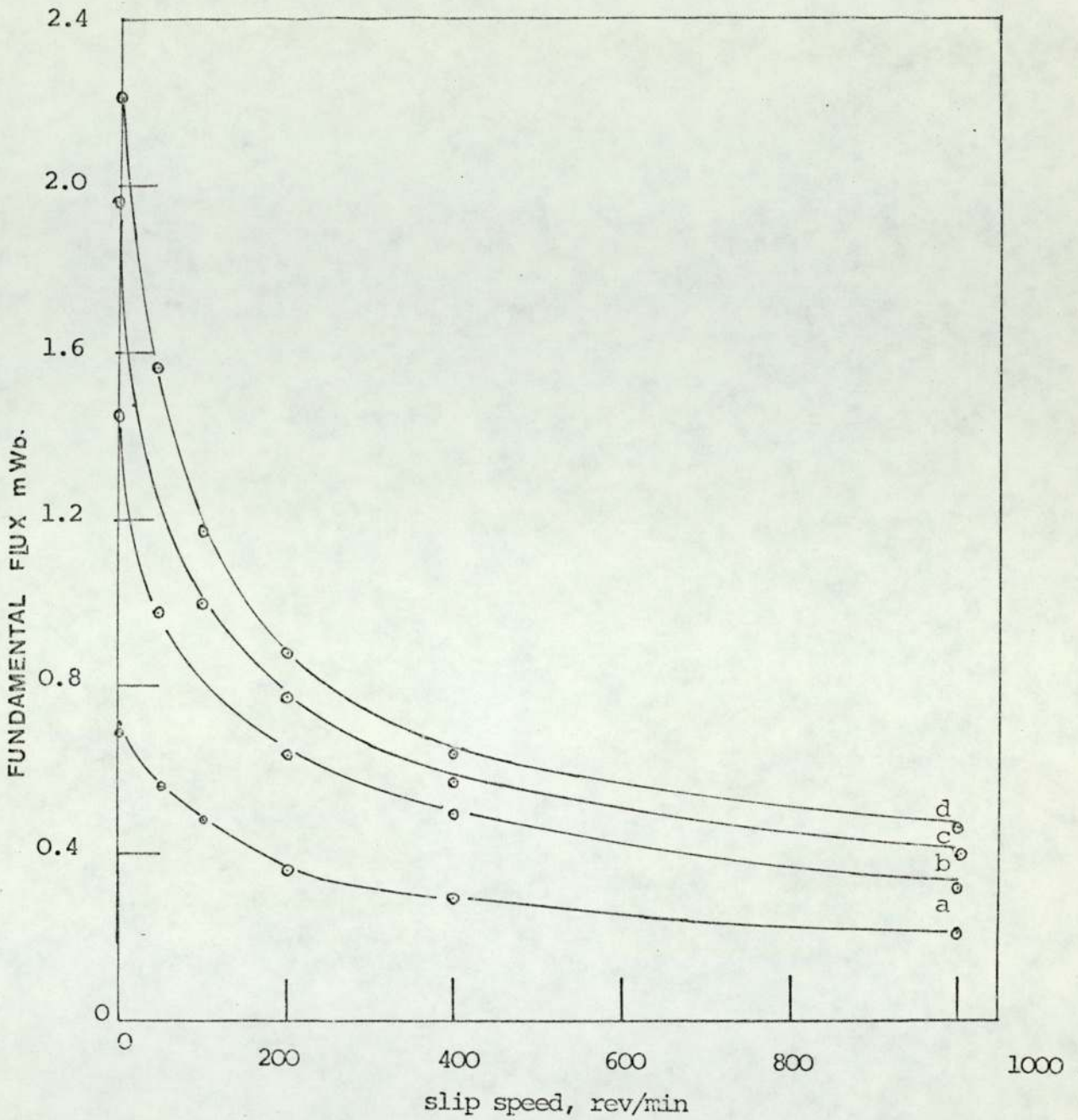


FIG. 7.5 VARIATION OF FUNDAMENTAL FLUX WITH SLIP SPEED FOR VARIOUS EXCITATIONS. (FROM WRIGHT'S THESIS)

Excitation m.m.f.s:

a: 100 AT/pole b: 200 AT/pole
 c: 300 AT/pole d: 400 AT/pole

o: values of total flux/pole

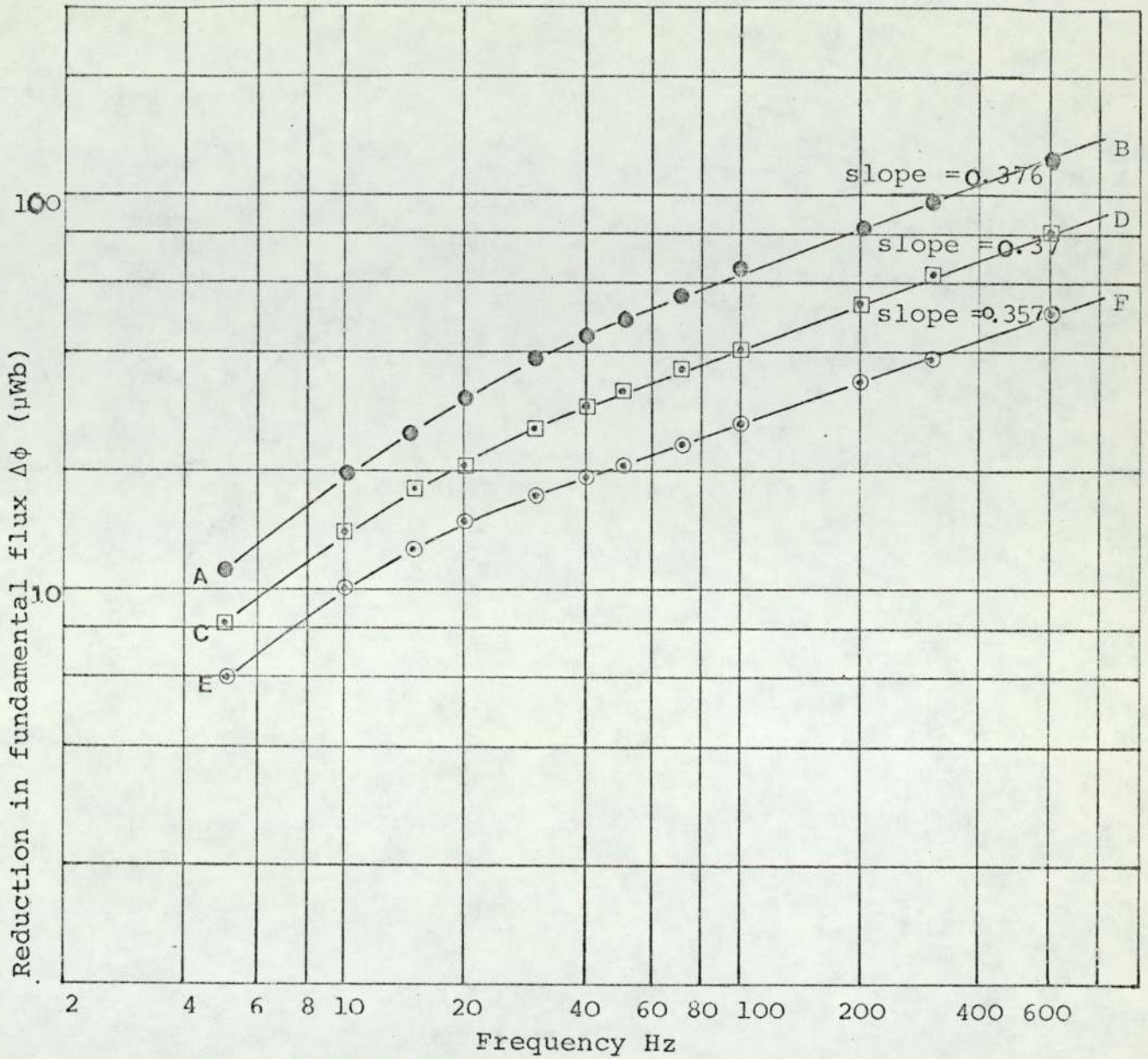


FIG. 7.6 VARIATION OF $\Delta\phi$ WITH SUPPLY FREQUENCY.

(1) COMPOLE D.C. EXCITATION 4.5A.

(2) MAINPOLE D.C. EXCITATION 0.68A.

COMPOLE A.C. EXCITATION

AB 20A P-P

CD 14A P-P

EF 8A P-P

AVERAGE SLOPE 0.367

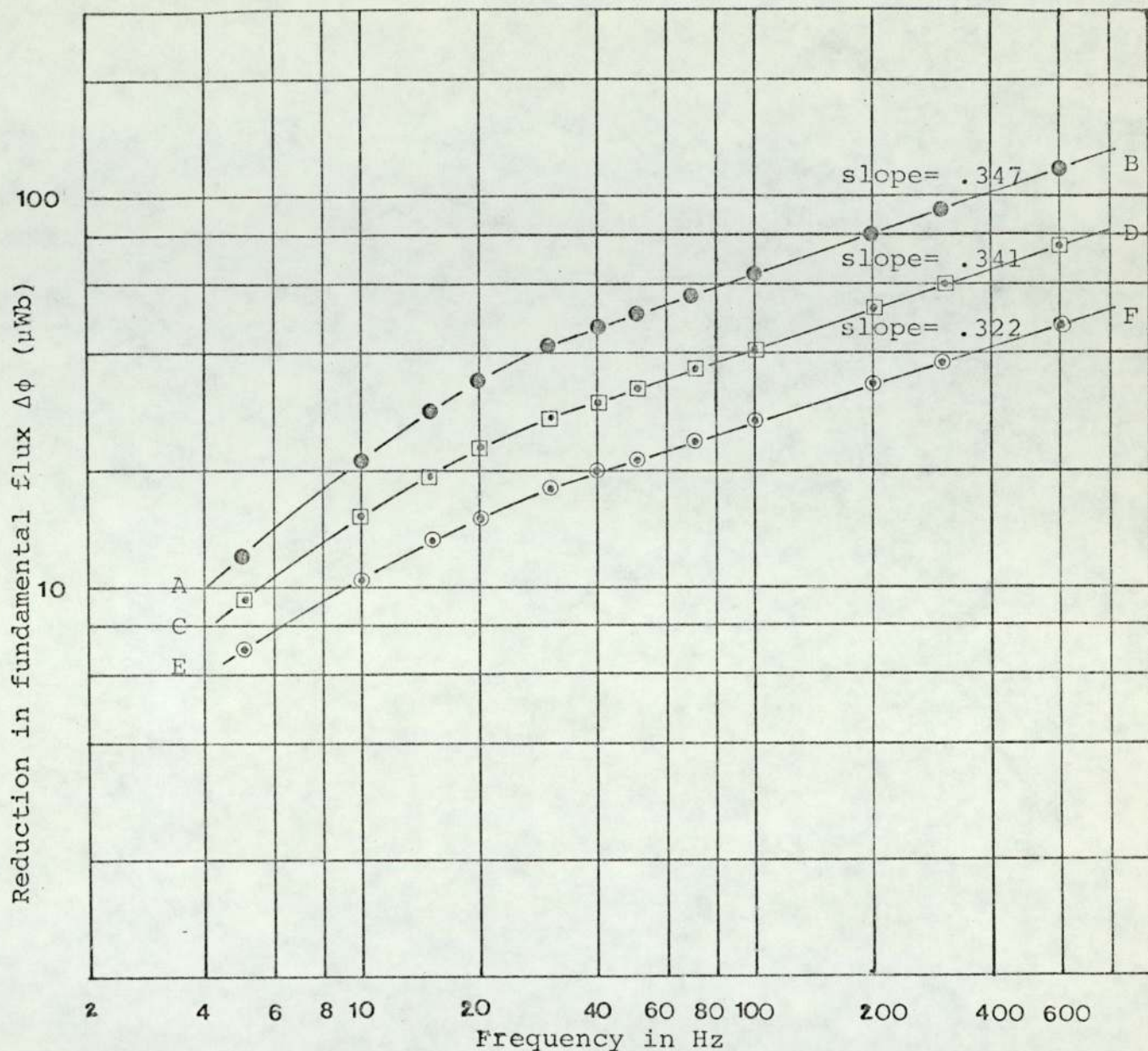


FIG. 7.7 VARIATION OF $\Delta\phi$ WITH SUPPLY FREQUENCY.

(1) COMPOLE D.C. EXCITATION 9A.

(2) MAINPOLE D.C. EXCITATION 0.68A.

COMPOLE A.C. EXCITATIONS

AB 20A P-P

CD 14A P-P

EF 8A P-P

AVERAGE SLOPE = .336.

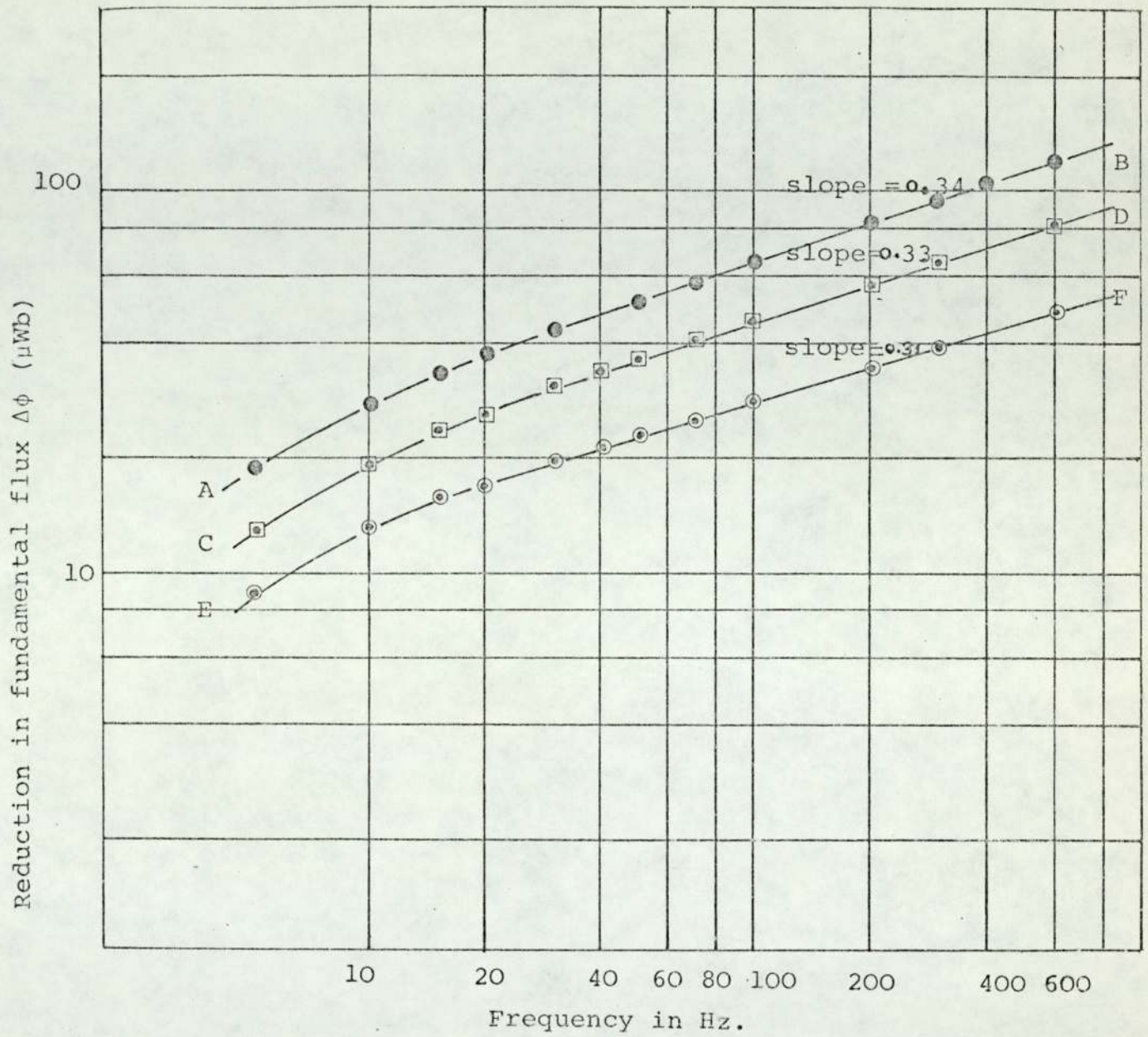


FIG. 7.8 VARIATION OF $\Delta\phi$ WITH SUPPLY FREQUENCY.

(1) COMPOLE D.C. EXCITATION 11.25A.

(2) MAINPOLE D.C. EXCITATION 0.68A.

COMPOLE A.C. EXCITATIONS

AB 20A P-P

CD 14A P-P

EF 8A P-P

AVERAGE SLOPE = .328

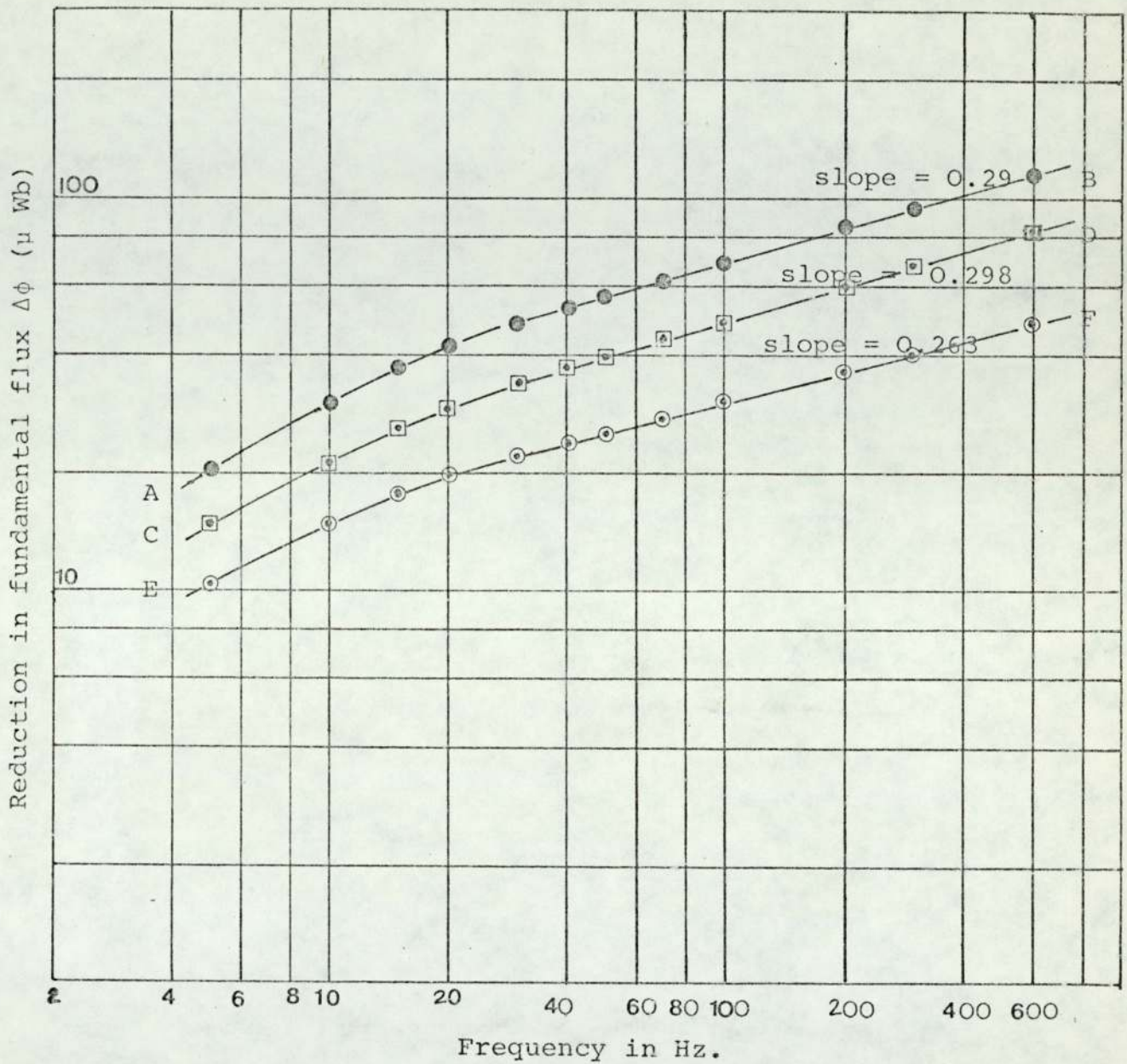


FIG. 7.9 VARIATION OF $\Delta\phi$ WITH SUPPLY FREQUENCY.

(1) COMPOLE D.C. EXCITATION 13.5A.

(2) MAINPOLE D.C. EXCITATION 0.68A.

COMPOLE A.C. EXCITATIONS

AB 20A P-P
 CD 14A P-P
 EF 8A P-P

AVERAGE SLOPE = .284.

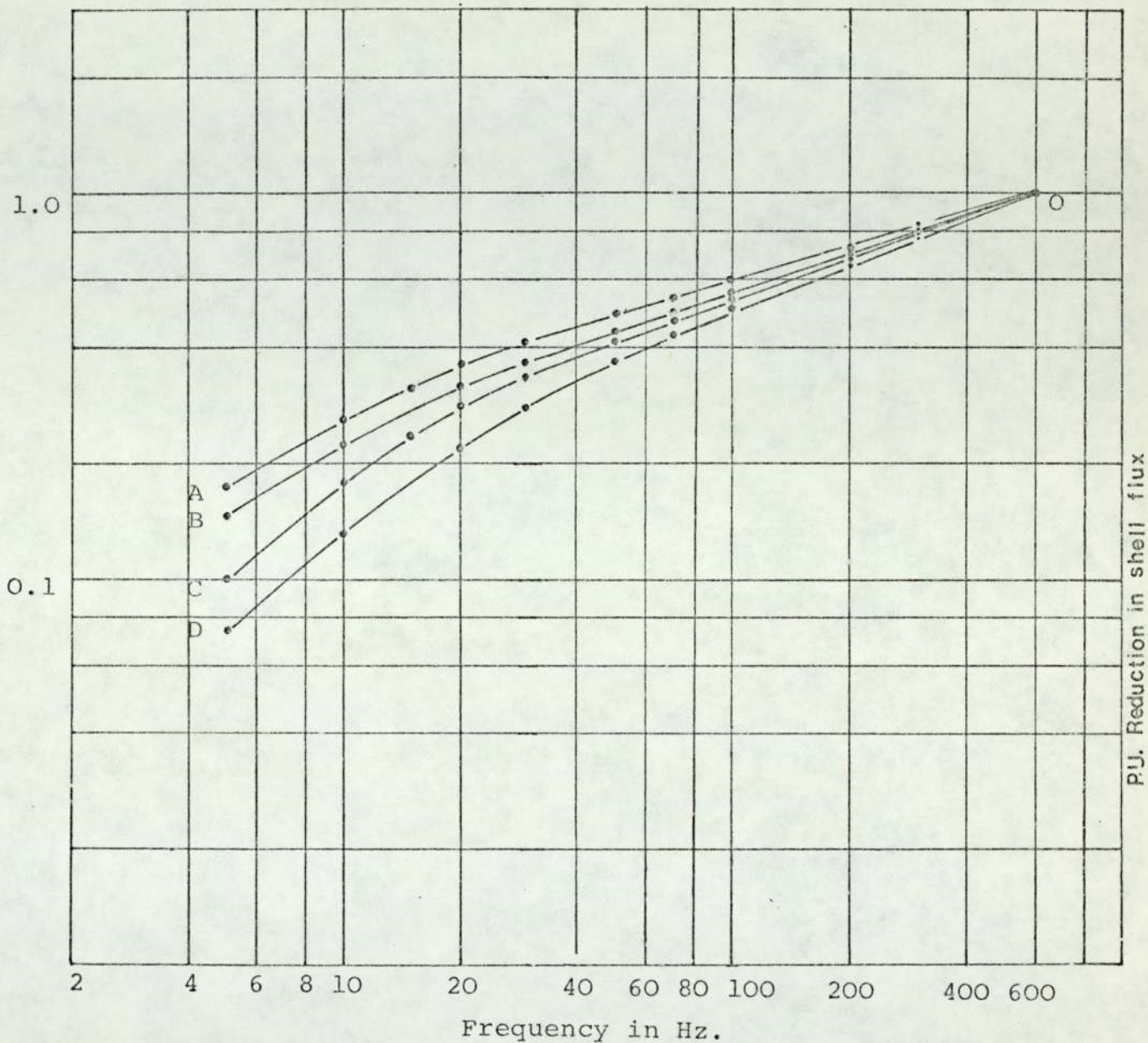


FIG.7.10 VARIATION OF MEASURED $\Delta\phi$ WITH SUPPLY FREQUENCY FOR VARIOUS D.C. FLUX LEVELS IN THE SHELL.

- A.C. EXCITATION TO THE COMPOLE = 20A P-P.
D.C. EXCITATION TO THE MAINPOLE = .68A.
- OA D.C. EXCITATION TO THE COMPOLE = 13.5A.
OB D.C. EXCITATION TO THE COMPOLE = 11.25A.
OC D.C. EXCITATION TO THE COMPOLE = 9A.
OD (1) D.C. EXCITATION TO THE COMPOLE = 20A
(2) D.C. EXCITATION TO THE ARMATURE = 20A.
(3) D.C. EXCITATION TO THE MAINPOLE = .39A.

VALUE OF $\Delta\phi$ AT 600 HZ IS TAKEN AS UNITY FOR ALL THE CURVES.

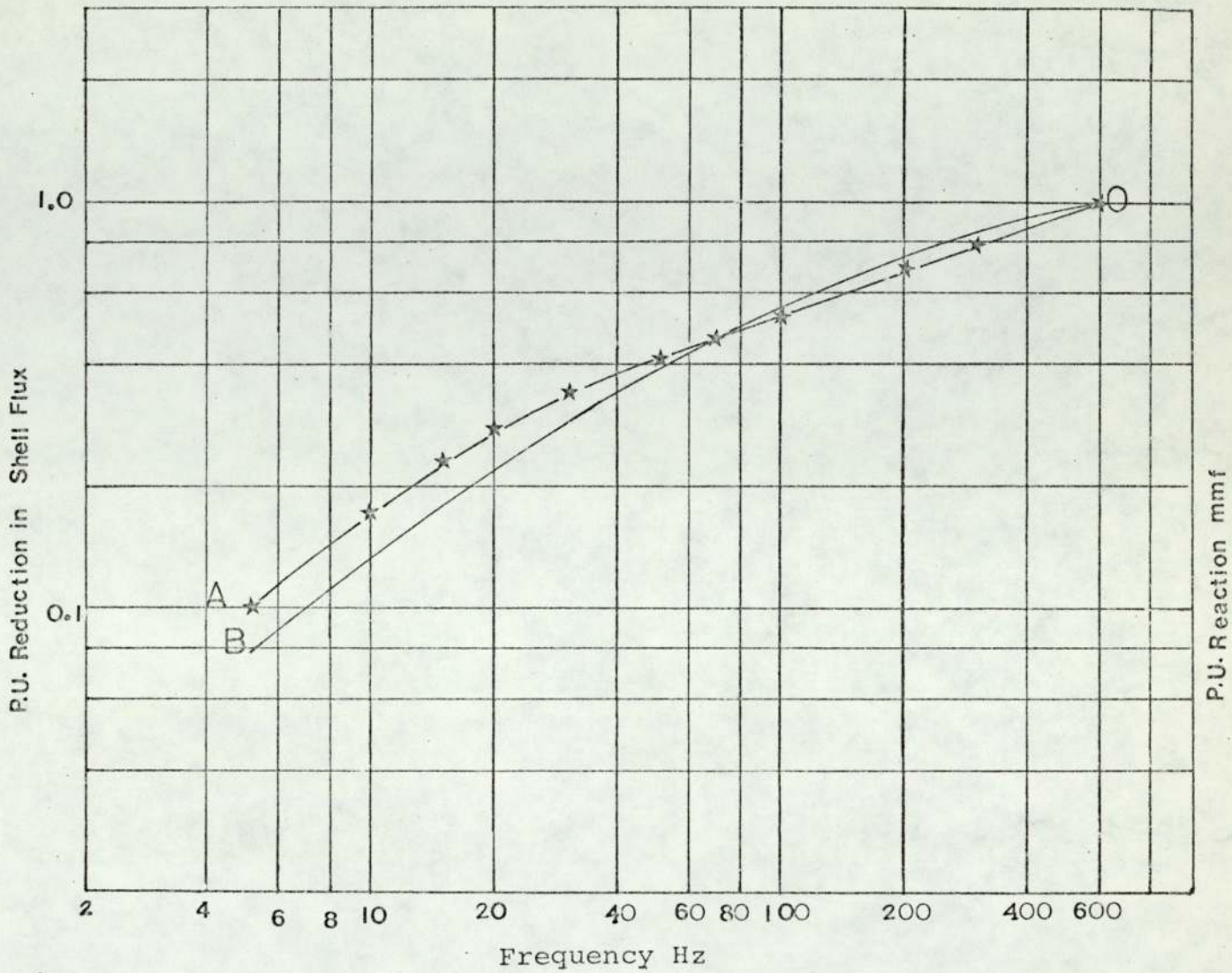


Fig. 7.11 $\star \rightarrow \star \rightarrow \star$ OA PLOT OF MEASURED $\Delta\phi$ AGAINST SUPPLY FREQUENCY WITH
 (A) D.C. EXCITATION TO THE COMPOLE 9A.
 (B) D.C. EXCITATION TO THE MAINPOLE 0.68A.

— O B PLOT OF CALCULATED REACTION MMF'S AGAINST FREQUENCY WITH $m = .758$.

VALUES OF $\Delta\phi$ AND REACTION MMF'S AT 600 HZ ARE TAKEN AS UNITY.

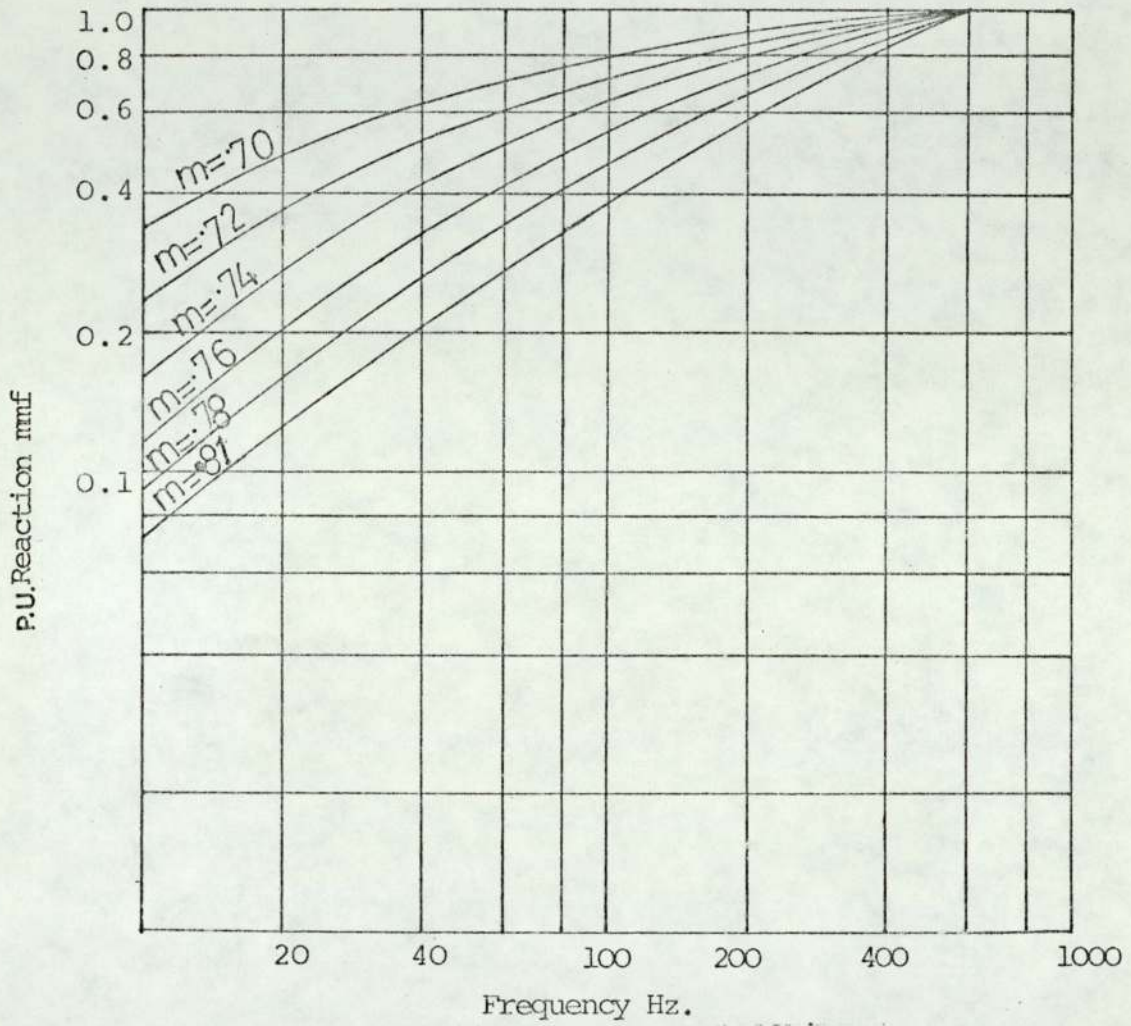


FIG. 7.12 PLOT OF CALCULATED REACTION MMF'S AGAINST FREQUENCY FOR VARIOUS VALUES OF INDEX m REACTION MMF AT 600 HZ IS TAKEN AS UNIT FOR EACH CURVE.

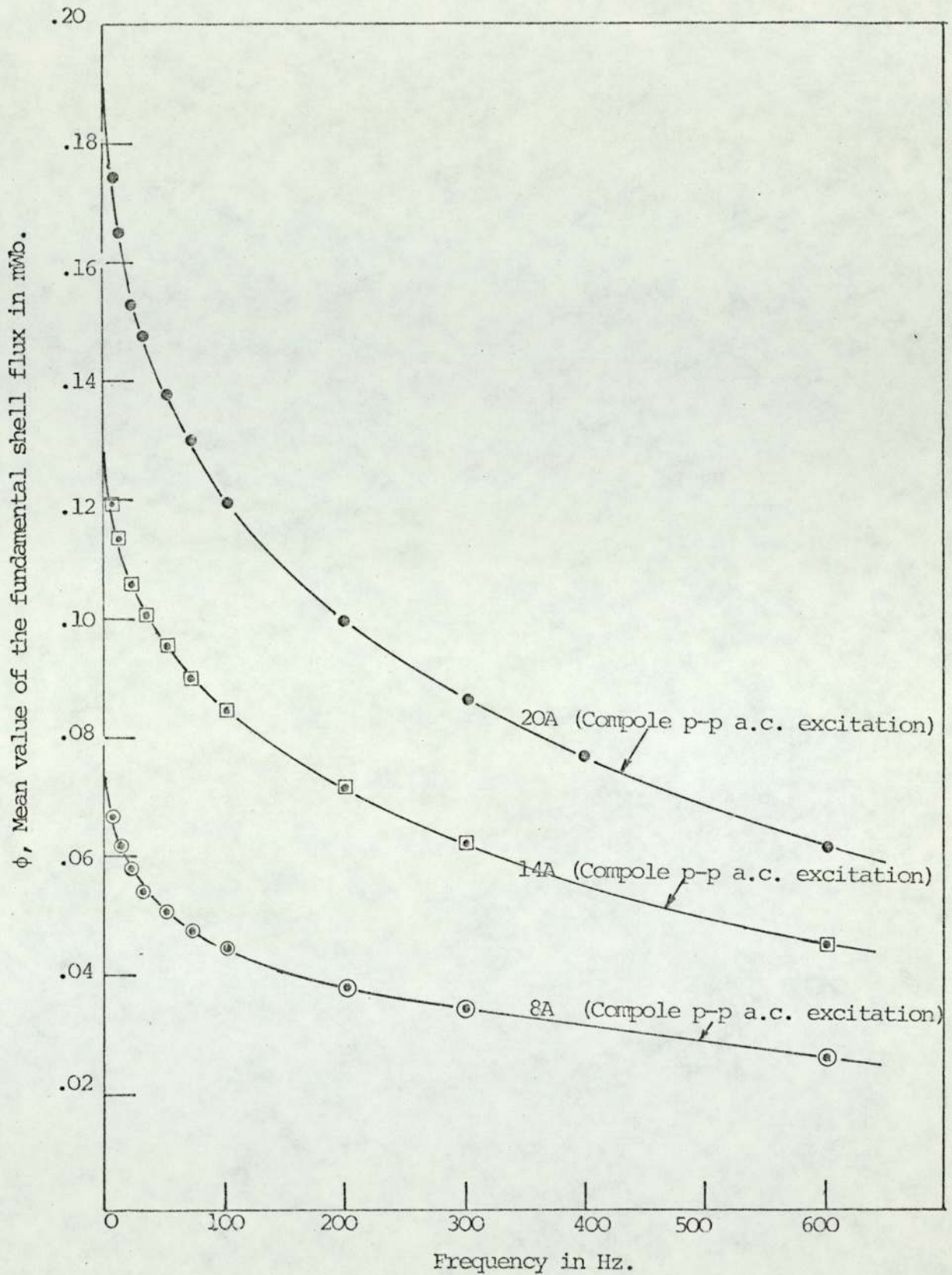


FIG. 7.13 VARIATION OF FUNDAMENTAL SHELL FLUX WITH FREQUENCY.

- (1) COMPOLE D.C. EXCITATION 20A.
- (2) MAINPOLE D.C. EXCITATION 0.68A.
- (3) ARMATURE D.C. EXCITATION 20A.

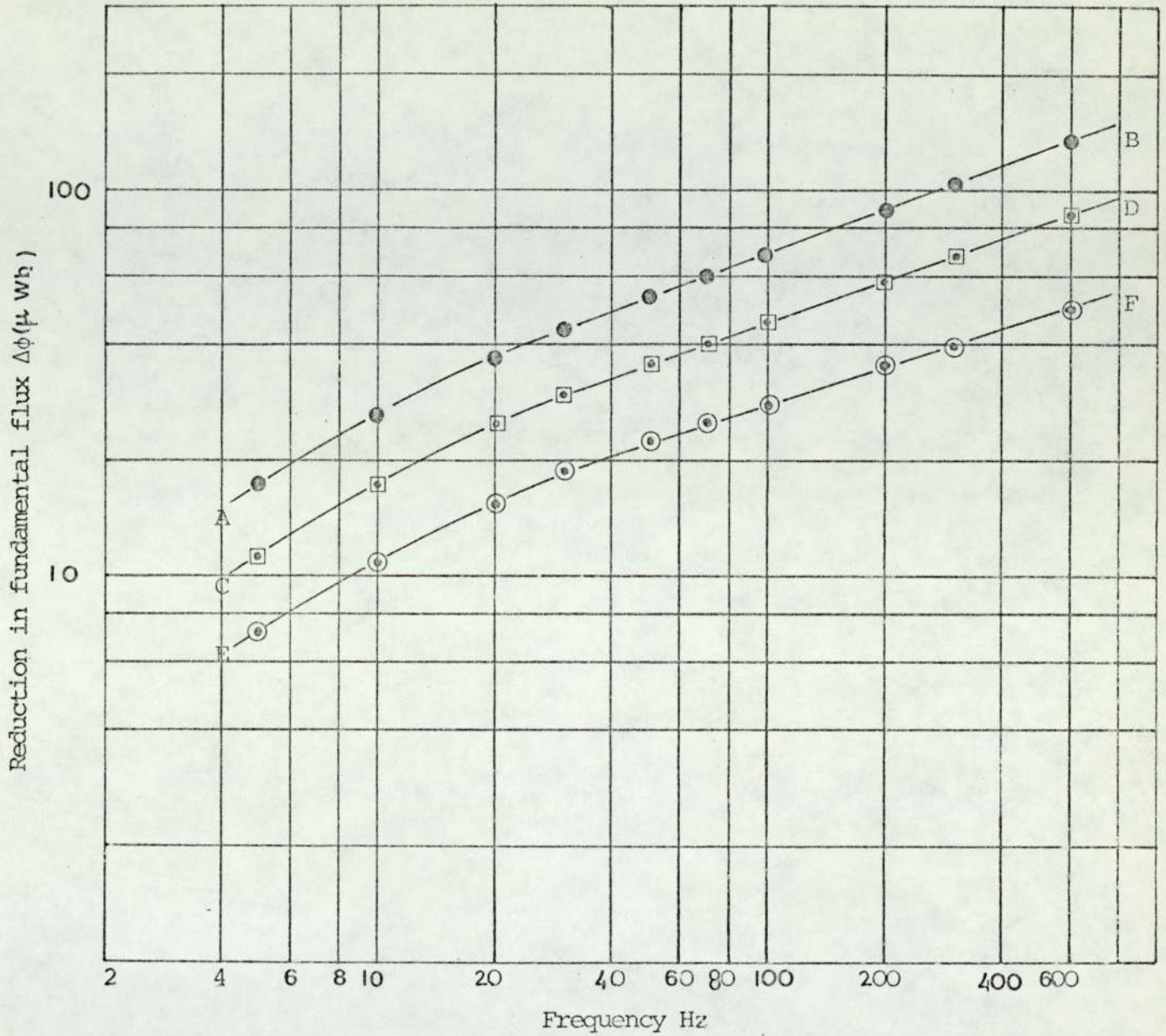


FIG. 7.14 VARIATION OF $\Delta\phi$ WITH SUPPLY FREQUENCY.

- (1) COMPOLE D.C. EXCITATION 20A.
- (2) MAINPOLE D.C. EXCITATION .68A.
- (3) ARMATURE D.C. EXCITATION 20A.

COMPOLE A.C. EXCITATION

AB - 20A P-P
 CD - 14A P-P
 EF - 8A P-P

AVERAGE SLOPE = .345

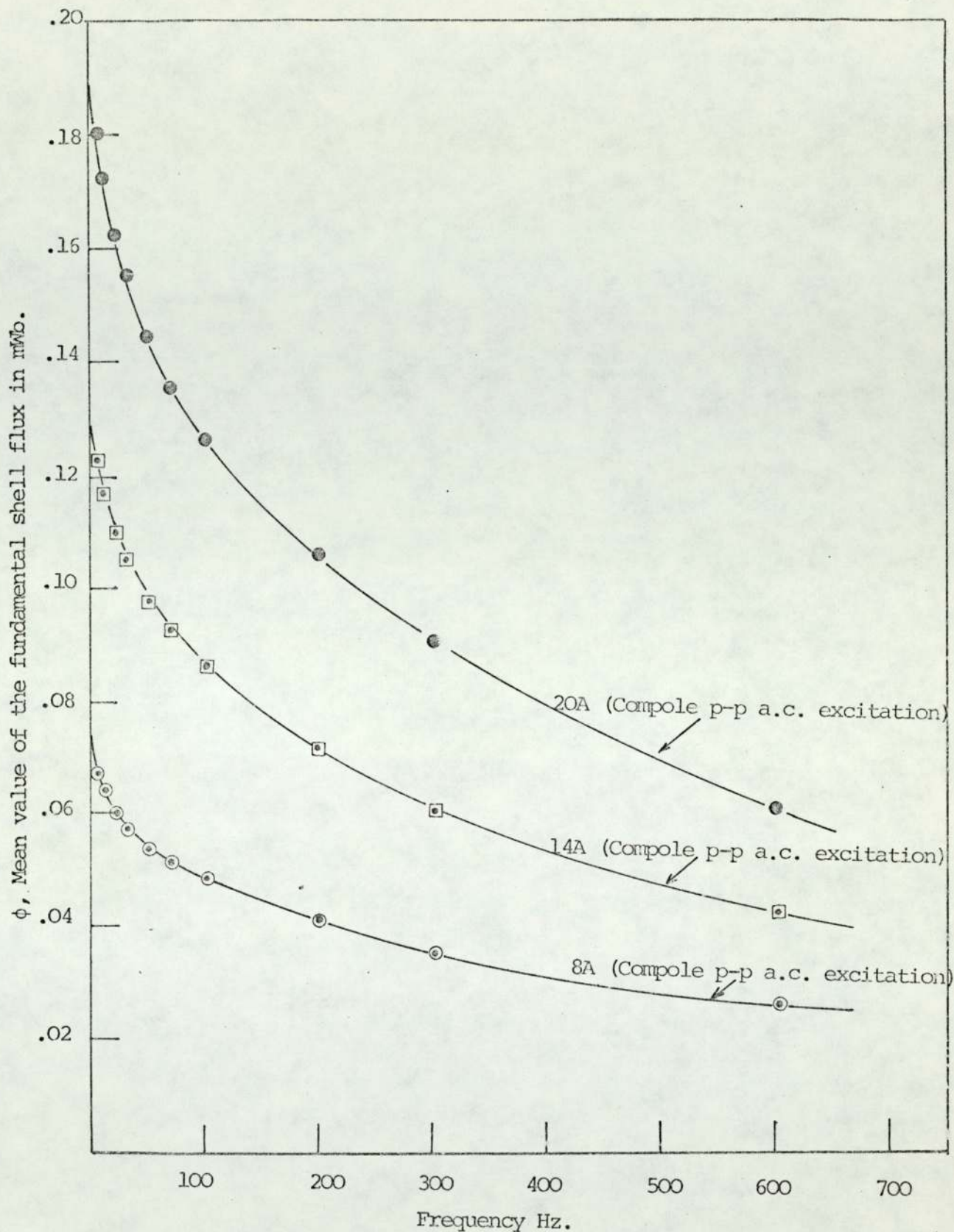


FIG. 7.15 VARIATION OF FUNDAMENTAL SHELL FLUX WITH SUPPLY FREQUENCY.

- (1) COMPOLE D.C. EXCITATION 20A.
- (2) MAINPOLE D.C. EXCITATION 0.39A.
- (3) ARMATURE D.C. EXCITATION 20A.

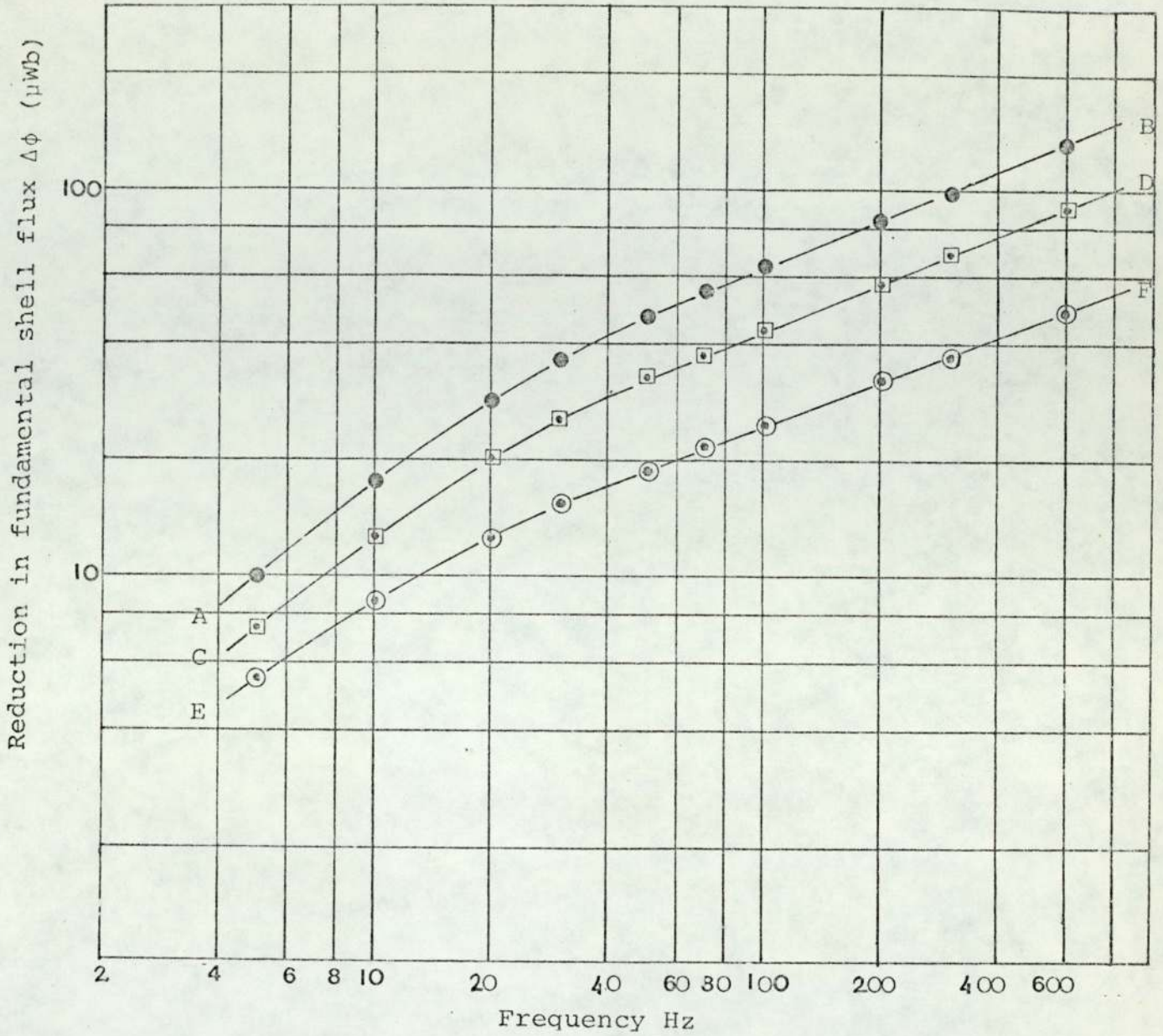


FIG. 7.16 VARIATION OF $\Delta\phi$ WITH SUPPLY FREQUENCY.

- (1) COMPOLE D.C. EXCITATION 20A.
- (2) MAINPOLE D.C. EXCITATION 39A.
- (3) ARMATURE D.C. EXCITATION 20A.

COMPOLE A.C. EXCITATION

AB 20A P-P
 CD 14A P-P
 EF 8A P-P

AVERAGE SLOPE = .41

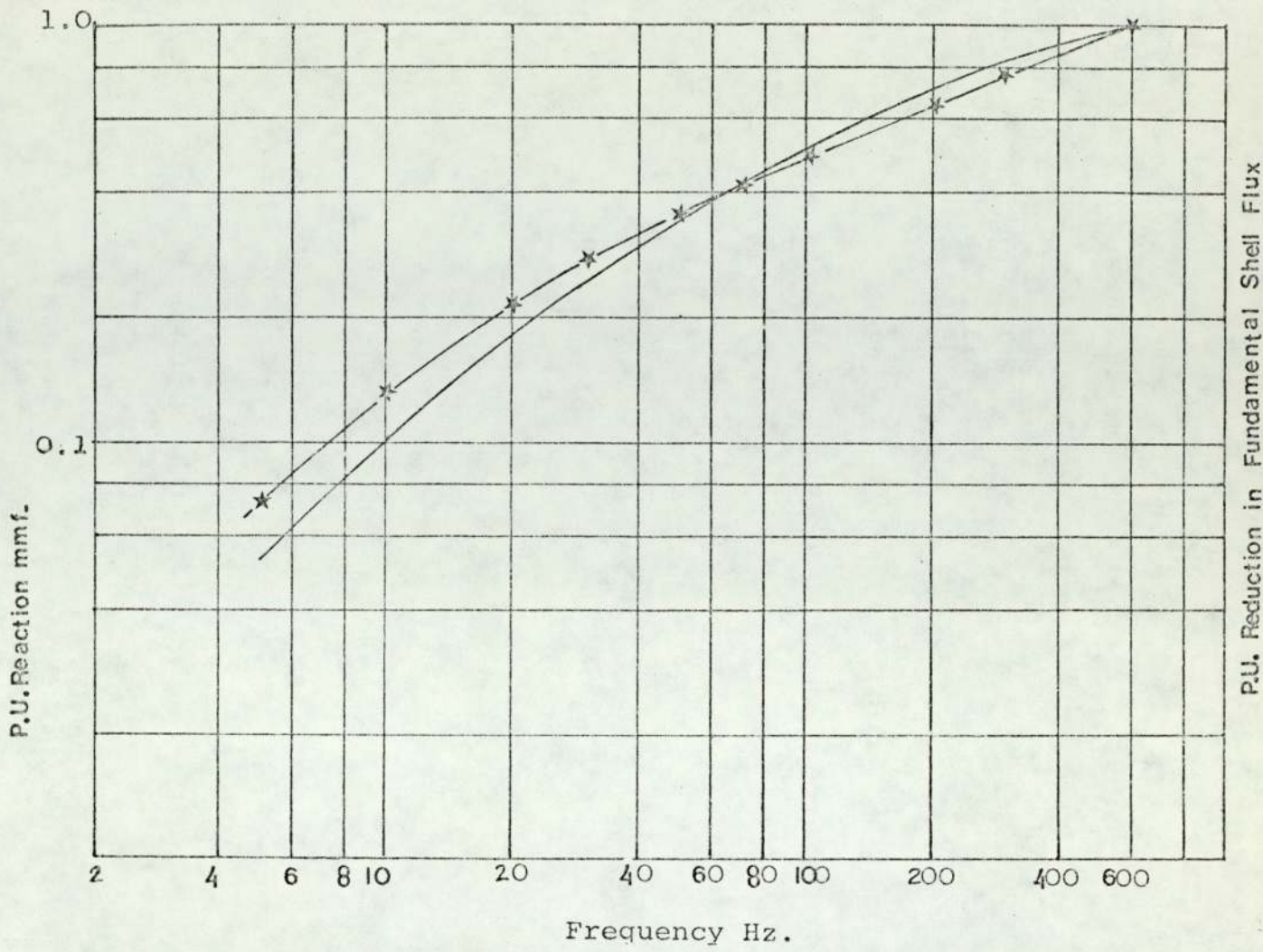


FIG. 7.17

CALCULATED REACTION MMF AGAINST SUPPLY FREQUENCY WITH THE VALUE AT 600 HZ AS UNITY AND WITH $m = 0.77$

★—★—★ MEASURED $\Delta\phi$ AGAINST FREQUENCY WITH THE VALUE AT 600 HZ AS UNITY.

- (1) COMPOLE D.C. EXCITATION = 20A
- (2) ARMATURE D.C. EXCITATION = 20A
- (3) MAINPOLE D.C. EXCITATION = .39A

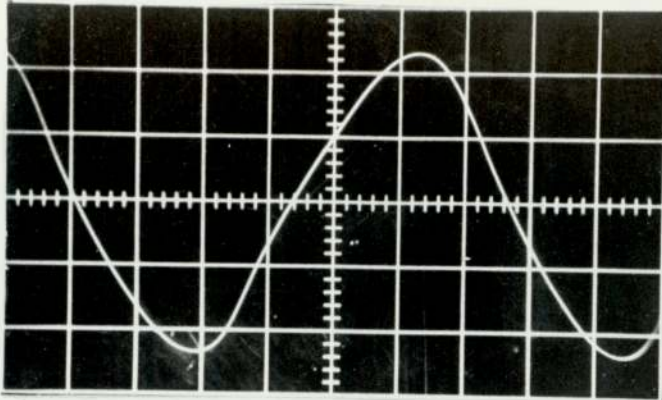


Fig. OS.7.1

- (a) Compole a.c. excitation 20A, p-p.
- (b) Compole d.c. excitation 0A.
- (c) Main pole d.c. excitation 0A
- (d) Frequency of a.c. excitation 100 Hz.

0.05V/cm.

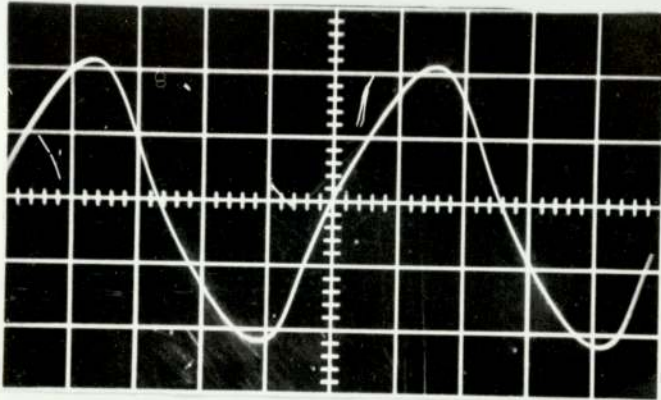


Fig. OS.7.2

- (a) Compole a.c. excitation 20A, p-p.
- (b) Compole d.c. excitation 0A.
- (c) Main pole d.c. excitation 0A.
- (d) Frequency of a.c. excitation 300 Hz.

0.1V/cm

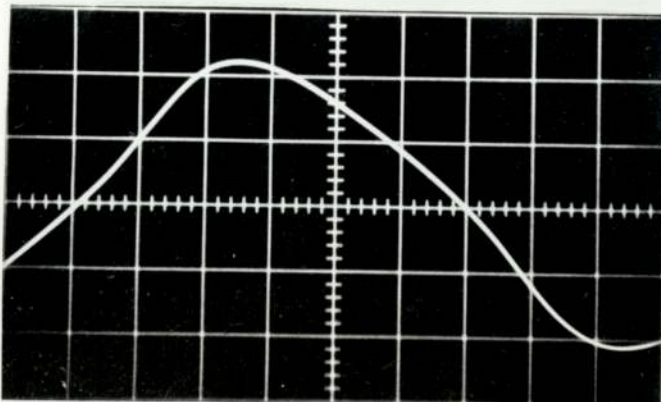


Fig. OS.7.3

- (a) Compole a.c. excitation 14A, p-p.
- (b) Compole d.c. excitation 0A.
- (c) Main pole d.c. excitation 0A.
- (d) Frequency of a.c. excitation 600 Hz.

0.1V/cm.

OSCILLOGRAMS OF VOLTAGES FROM A SHELL LOOP SEARCH COIL

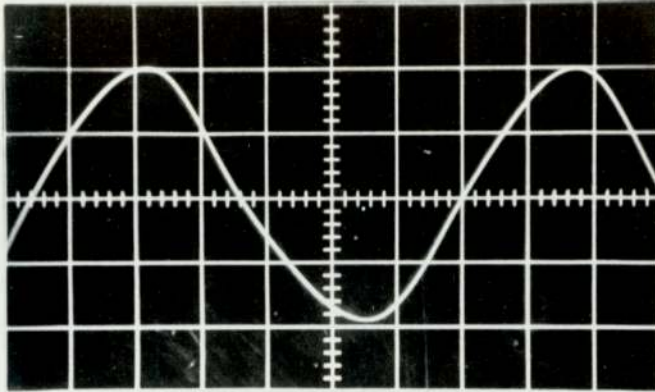


Fig. OS.7.4

- (a) Compole a.c. excitation 20A, p-p.
 - (b) Compole d.c. excitation 8A.
 - (c) Main pole d.c. excitation 0.675A.
 - (d) Frequency of a.c. excitation 100 Hz.
- 0.05V/cm.

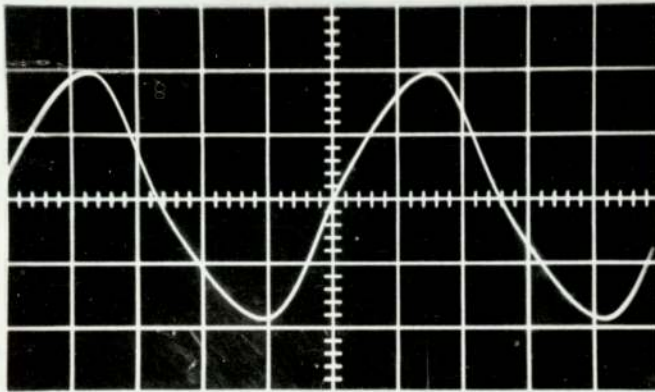


Fig. OS.7.5

- (a) Compole a.c. excitation 20A, p-p.
 - (b) Compole d.c. excitation 8A.
 - (c) Main pole d.c. excitation 0.675A.
 - (d) Frequency of a.c. excitation 300 Hz.
- 0.1V/cm.

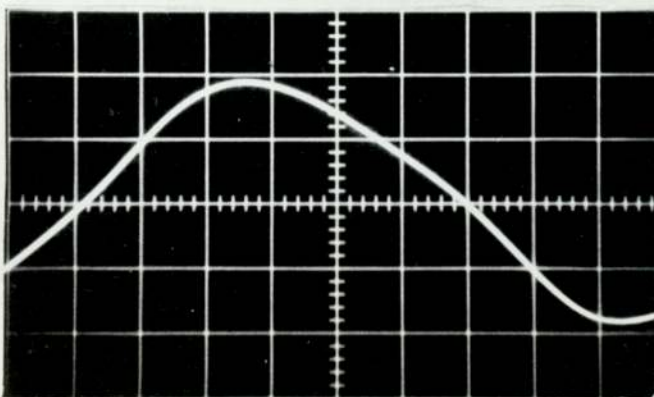


Fig. OS.7.6

- (a) Compole a.c. excitation 14A, p-p.
 - (b) Compole d.c. excitation 8A.
 - (c) Main pole d.c. excitation 0.675A.
 - (d) Frequency of a.c. excitation 600 Hz.
- 0.1V/cm.

OSCILLOGRAMS OF VOLTAGES FROM A SHELL LOOP SEARCH COIL

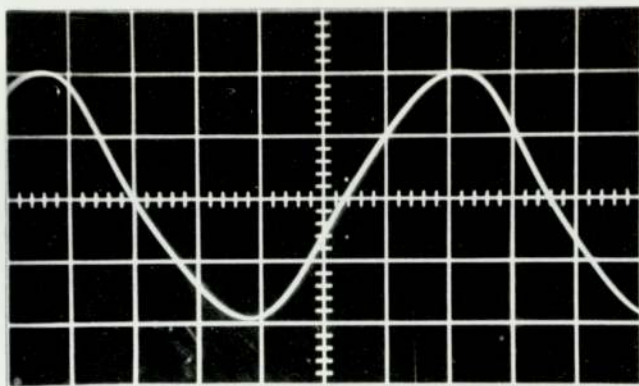


Fig.OS.7.7

- (a) Compole a.c. excitation 20A, p-p.
 - (b) Compole d.c. excitation 16A.
 - (c) Main pole d.c. excitation 0.675A.
 - (d) Frequency of a.c. excitation 100 Hz.
- 0.05V/cm.

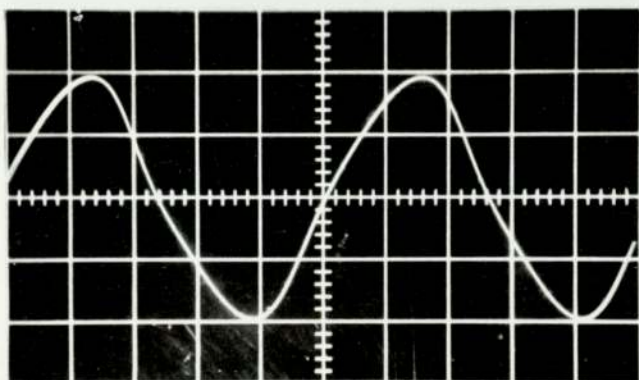


Fig.OS.7.8

- (a) Compole a.c. excitation 20A, p-p.
 - (b) Compole d.c. excitation 16A.
 - (c) Main pole d.c. excitation 0.675A.
 - (d) Frequency of a.c. excitation 300 Hz.
- 0.1V/cm

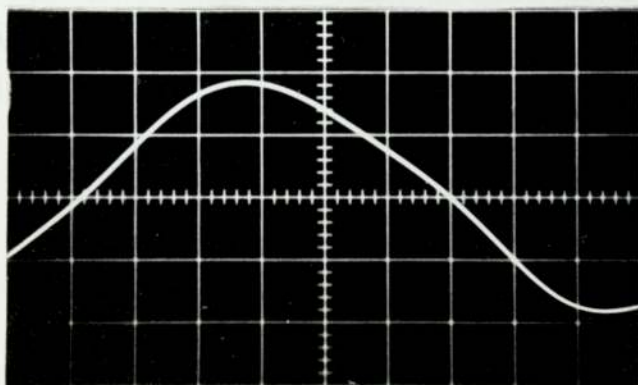


Fig. OS.7.9

- (a) Compole a.c. excitation 14A, p-p.
 - (b) Compole d.c. excitation 16A.
 - (c) Main pole d.c. excitation 0.675A.
 - (d) Frequency of a.c. excitation 600 Hz.
- 0.1V/cm

OSCILLOGRAMS OF VOLTAGES FROM A SHELL LOOP SEARCH COIL

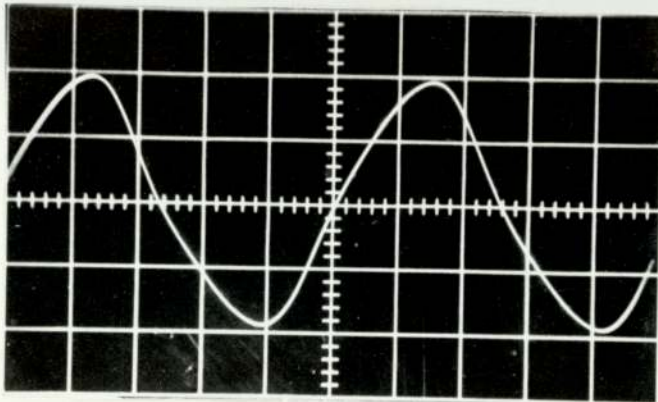


Fig. OS.7.10

- (a) Compole a.c. excitation
20A, p-p.
 - (b) Compole d.c. excitation 12A.
 - (c) Main pole d.c. excitation
0.675A.
 - (d) Frequency of a.c. excitation
300 Hz.
- 0.1V/cm.

OSCILLOGRAMS OF VOLTAGES FROM A SHELL LOOP SEARCH COIL.